Available online at www.sciencedirect.com

ScienceDirect

Procedia Engineering00 (2015) 000–000

Procedia Engineering

www.elsevier.com/locate/procedia

6th BSME International Conference on Thermal Engineering (ICTE 2014)

MHD free convection fluid flow through parallel plates with hall current in a rotating system

Rina Perven, Md. Mahmud Alam*

Mathematics Discuipline,Science, Engineering and Technology School, Khulna University, Khulna-9208, Bangladesh

---

Abstract

An attempt has been made to study the influence of inclined magnetic field with hall current of a viscous incompressible electrically conducting free convection fluid flow through the parallel plates in a rotating system. The channel is rotating with uniform angular velocity about an axis normal to the plates. For numerical solution, the problems have been transferred into dimensionless form and then the explicit finite difference technique has been used. The stability conditions and convergence criteria of the explicit finite difference scheme are established for finding the restriction of the values of various parameters to get more accuracy. The effects of Rotation parameter (R) , Hall parameter (m), Magnetic parameter (M^2) and Angle of inclination (θ) on primary and secondary velocities have been shown in graphical representations. Finally the effects of these parameters have been analyzed by the figures of local shear stress and average current density at the moving plates of channel.

Keywords: Hartmann number; Rotating system; MHD free convection; Inclined magnetic field; Finite difference technique

---

1. Introduction

In the case of an electrically conducting rotating gas at low pressure, there has an interaction of the magnetic field with the electric field of both the electrons and the ionized atoms of the gas. If the magnetic field is perpendicular to the electric field, a current is induced in the conductive rotating gas whose direction is perpendicular to the both the electric field and the magnetic field. This current is called Hall current. The combined effect of Hall and ion-slip

---

* Corresponding author: Md. Mahmud Alam. Tel.: +88-041-725741; Cell: +8801912982811; fax: +88-041-731244.
E-mail address: alam_mahmud2013@ku.ac.bd

currents on unsteady MHD Couette flows in a rotating system has been investigated by Jha and Apere [1]. Keeping in view this fact, Attia [2] has obtained the analytical solution for flow of a dusty fluid in a circular pipe with Hall and ion-slip effect. Edmad et al. [3] studied the effects of Hall current on magneto hydrodynamic free convection flow past a semi-infinite vertical plate with mass transfer. Seth et al. [4] studied the Hartmann flow in a rotating system in the presence of inclined magnetic field with Hall effects.

The purpose of the present investigation is to extend the work studied by Seth et al. [4] and to solve numerically the effect of hall current through MHD free convection fluid flow with the presence of inclined magnetic field. The explicit finite difference method is applied to find the numerical solution and the results for different values of the well-known parameters are shown graphically.

Nomenclature

q	fluid velocity	**E**	electric field
Ω	angular velocity	$\hat{k}$	unit vector along z-axis
P'	fluid pressure including centrifugal force	θ	angle of inclination
B	inclined magnetic field vector	μ_e	magnetic permeability
ρ	fluid density	ω_e	cyclotron frequency
J	current density	τ_e	electron collision time
t	the time	σ	electrical conductivity of the fluid
R	rotation parameter	M^2	magnetic parameter
P_m	magnetic prandtl number	m	hall parameter
ξ, η	dimensionless cartesian coordinates	P_{r_g}	constant pressure gradient

2. Mathematical formulations

Consider a viscous incompressible electrically conducting MHD free convection fluid flow in a rotating system with hall current with the influence of inclined magnetic field. The $x-$axis is taken in the flow direction between two parallel plates where $z = \pm L$. A constant pressure gradient is applied to the direction of the flow. The $z-$axis is perpendicular to the plates. Both the fluid and the channel are in a state of rigid body rotation with uniform angular velocity Ω about $z-$axis. The fluid is permeated by a uniform magnetic field B_0 applied in a direction, which is inclined at an angle θ with the positive direction of $z-$axis in $xz-$plane. The geometrical interpretation of the model is represented physically in Figs. (1) and (2).

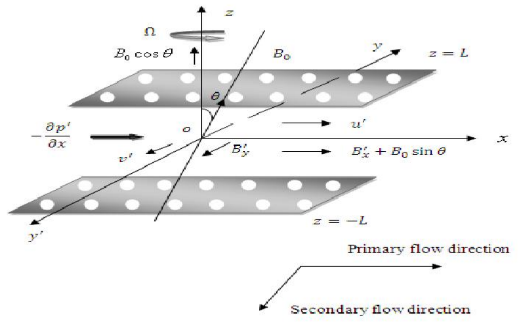

Fig.(1). Physical configuration and coordinate system

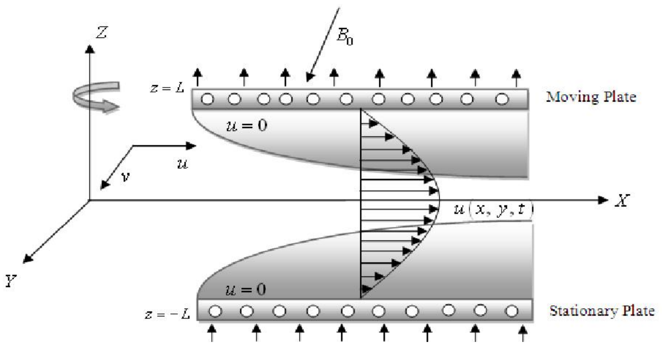

Fig. (2). Geometrical configuration and coordinate system

Since the solutions of the problem will be based on a finite difference method, it is required to make the said equations dimensionless. For this purpose the following dimensionless variables are introduced as;

$$\xi = \frac{x}{L}, \eta = \frac{z}{L}, u = \frac{u'L}{\upsilon}, v = \frac{v'L}{\upsilon}, w = \frac{w'L}{\upsilon}, p = \frac{L^2 p'}{\rho \upsilon^2},$$

$$B_x = \frac{B_x^{'}}{\sigma \mu_e \upsilon B_0}, B_y = \frac{B_y^{'}}{\sigma \mu_e \upsilon B_0}, \tau = \frac{tU_0^2}{\upsilon}$$

Considering the physical configuration of this problem, the governing equations with the boundary conditions in dimensionless form are;

$$\frac{\partial u}{\partial \xi} + \frac{\partial w}{\partial \eta} = 0 \qquad (1)$$

$$\frac{\partial u}{\partial \tau} + u\frac{\partial u}{\partial \xi} + w\frac{\partial u}{\partial \eta} - 2Rv = \frac{\partial^2 u}{\partial \eta^2} + P_{r_g} + M^2 cos\theta \frac{\partial B_x}{\partial \eta} \qquad (2)$$

$$\frac{\partial v}{\partial \tau} + u\frac{\partial v}{\partial \xi} + w\frac{\partial v}{\partial \eta} + 2Ru = \frac{\partial^2 v}{\partial \eta^2} + M^2 cos\theta \frac{\partial B_y}{\partial \eta} \qquad (3)$$

$$P_m \frac{\partial B_x}{\partial \tau} = cos\theta \frac{\partial u}{\partial \eta} + \frac{\partial^2 B_x}{\partial \eta^2} + mcos\theta \frac{\partial^2 B_y}{\partial \eta^2} \qquad (4)$$

$$P_m \frac{\partial B_y}{\partial \tau} = cos\theta \frac{\partial v}{\partial \eta} + \frac{\partial^2 B_y}{\partial \eta^2} - m\left[cos\theta \frac{\partial^2 B_x}{\partial \eta^2} + P_m \frac{\partial B_x}{\partial \xi}\frac{\partial B_x}{\partial \eta} \right] \qquad (5)$$

The corresponding boundary conditions are;

$$u = 0,\ v = 0,\ \frac{\partial B_x}{\partial \eta} = 0, \frac{\partial B_y}{\partial \eta} = 0 \ at\, \eta = \pm 1 \qquad (6)$$

where τ represents the dimensionless time, ξ and η are the dimensionless Cartesian coordinates of x and z respectively, $u, v\, and\, w$ are the dimensionless velocity components, B_x, B_y are the dimensionless primary and secondary inclined magnetic field.

$R = \frac{\Omega L^2}{\upsilon}$ (Rotation parameter), $P_{r_g} = -\frac{\partial p}{\partial \xi}$ (Non-dimensional constant pressure gradient), $M^2 = \frac{B_0^2\, L^2 \sigma}{\rho \upsilon}$ (Magnetic parameter), $P_m = \sigma \mu_e \upsilon$ (Magnetic Prandtl number), $m = \omega_e \tau_e$ (Hall parameter).

3. Shear stress and Current density

For primary velocity, the local shear stress, $\tau_L = \mu\left(\frac{\partial u'}{\partial z}\right)_{z=0}$ is proportional to $\left(\frac{\partial u}{\partial \eta}\right)_{\eta=0}$. For secondary velocity, the local shear stress, $\tau_L = \mu\left(\frac{\partial v'}{\partial z}\right)_{z=0}$ is proportional to $\left(\frac{\partial v}{\partial \eta}\right)_{\eta=0}$.

From the inclined magnetic field, the effects of various parameters on average current density have been calculated. The average current density $J_A = \mu\int\left(-\frac{\partial B'_x}{\partial z}\right)_{z=0} dx$ in $x-$ direction is proportional to $\int_0^{100}\left(-\frac{\partial B_x}{\partial \eta}\right)_{\eta=0} d\xi$. The average current density $J_A = \mu\int\left(-\frac{\partial B'_y}{\partial z}\right)_{z=0} dx$ in $y-$ direction is proportional to $\int_0^{100}\left(-\frac{\partial B_y}{\partial \eta}\right)_{\eta=0} d\eta$.

4. Numerical technique

For simplicity the explicit finite difference method has been used to solve equations (1) - (5) subject to the conditions given by (6). To obtain the solution of the difference equations, the region of the flow is divided into a grid of lines parallel to ξ and $\eta-$ axes where $\xi-$ axes is taken along the plates and $\eta-$ axes is normal to the plates. Here the plates are considered of height $\xi_{\max} = 100$ i.e. ξ varies from 0 to 100 and regard $\eta_{\max} = 2$ i.e. η varies from -1 to 1. There are $m = 44$ and $n = 44$ grid spacing in the ξ and η directions respectively and taken as follows, $\Delta\xi = 2.273(0 \le \xi \le 44)$ and $\Delta\eta = 0.0455(-1 \le \eta \le 1)$ with the smaller time step, $\Delta\tau = 0.001$.
These mesh steps are shown in Fig. (3).

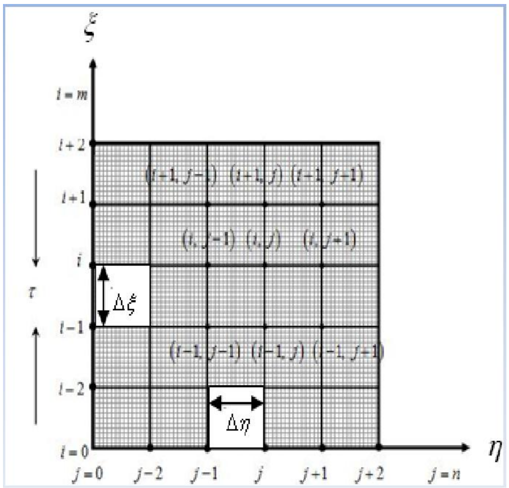

Fig. (3). Explicit finite difference system grid

Using the explicit **finite difference approximation** an appropriate set of finite difference equations are obtained as;

$$w'_{i,j+1} = w_{i,j} - \left(\frac{u_{i,j} - u_{i-1,j}}{\Delta\xi}\right)\Delta\eta \tag{7}$$

$$\frac{u^{'}_{i,j} - u_{i,j}}{\Delta\tau} + u_{i,j}\frac{u_{i,j} - u_{i-1,j}}{\Delta\xi} + w_{i,j}\frac{u_{i,j+1} - u_{i,j}}{\Delta\eta} - 2Rv_{i,j} = \frac{u_{i,j+1} - 2u_{i,j} + u_{i,j-1}}{(\Delta\eta)^2} + P_{r_g} + M^2 cos\theta\frac{B_{x_{i,j+1}} - B_{x_{i,j}}}{\Delta\eta} \tag{8}$$

$$\frac{v^{'}_{i,j} - v_{i,j}}{\Delta\tau} + u_{i,j}\frac{v_{i,j} - v_{i-1,j}}{\Delta\xi} + w_{i,j}\frac{v_{i,j+1} - v_{i,j}}{\Delta\eta} + 2Ru_{i,j} = \frac{v_{i,j+1} - 2v_{i,j} + v_{i,j-1}}{(\Delta\eta)^2} + M^2 cos\theta\frac{B_{y_{i,j+1}} - B_{y_{i,j}}}{\Delta\eta} \tag{9}$$

$$P_m \frac{B'_{x_{i,j}} - B_{x_{i,j}}}{\Delta\tau} = cos\theta \frac{u_{i,j+1} - u_{i,j}}{\Delta\eta} + \frac{B_{x_{i,j+1}} - 2B_{x_{i,j}} + B_{x_{i,j-1}}}{(\Delta\eta)^2} + mcos\theta \frac{B_{y_{i,j+1}} - 2B_{y_{i,j}} + B_{y_{i,j-1}}}{(\Delta\eta)^2} \tag{10}$$

$$\begin{aligned} P_m \frac{B'_{y_{i,j}} - B_{y_{i,j}}}{\Delta\tau} = cos\theta \frac{v_{i,j+1} - v_{i,j}}{\Delta\eta} + \frac{B_{y_{i,j+1}} - 2B_{y_{i,j}} + B_{y_{i,j-1}}}{(\Delta\eta)^2} - mcos\theta \frac{B_{x_{i,j+1}} - 2B_{x_{i,j}} + B_{x_{i,j-1}}}{(\Delta\eta)^2} \\ - P_m \frac{B_{x_{i,j+1}} - B_{x_{i,j}}}{\Delta\eta} \frac{B_{x_{i,j}} - B_{x_{i-1,j}}}{\Delta\xi} \end{aligned} \tag{11}$$

The boundary conditions with the finite difference scheme are;

$$u_{i.j} = 0,\ v_{i,j} = 0,\ B'_{x_{i,j}} = 0, B'_{y_{i,j}} = 0 \quad at\,\eta = \pm 1 \tag{12}$$

The stability condition of the finite difference method is;

$$\left| \frac{2\Delta\tau}{(\Delta\eta)^2} \times \frac{1}{P_m} \right| \le 1$$

And convergence limitation of the problem is $P_m \ge 0.966$ (details are not shown for briefly).

5. Results and Discussion

To analyze the physical situation of the model, the graphs of non-dimensional primary velocity (u), secondary velocity (v), local shear stress and average current densities (in case of moving plate) on some parameters are plotted using the numerical values of the equations of this model obtained by finite difference technique. To obtain the steady-state solutions, the computation has been carried out up to $\tau = 80$.

The comparison of the present results and the results of Seth et al.[4] are shown in Figs. (4) and (5) (scanned from Seth et al.[4]). In case of primary velocity profiles the effects are same but for secondary velocity profiles, they are qualitatively same but quantitatively different.

Figures (6) and (7) are plotted for the primary velocity profiles and the steady state local shear stress profiles in case of moving plate in $x-$direction for different values of magnetic parameter $\left(M^2\right)$. Here the primary velocity profiles increase with the increase of M^2 and this effect is justified by the local shear stress profiles.
As seen in Figs. (8) and (9), the secondary velocity profiles as well as the local shear stress profiles in case of moving plate in $y-$direction show decreasing effect with the increase of rotation parameter (R).

The steady-state average current density profiles in case of moving plate in x – direction increase with the increase of rotation parameter (R) , hall parameter (m) and angle of inclination (θ) but decrease with the increase of magnetic parameter $\left(M^2\right)$ as presented in Figs. (10-13).
As illustrated in Figs. (14-17), the average current density profiles in case of moving plate in $y-$direction increase with the increase of R and θ but show decreasing effect with the increase of m and M^2 .

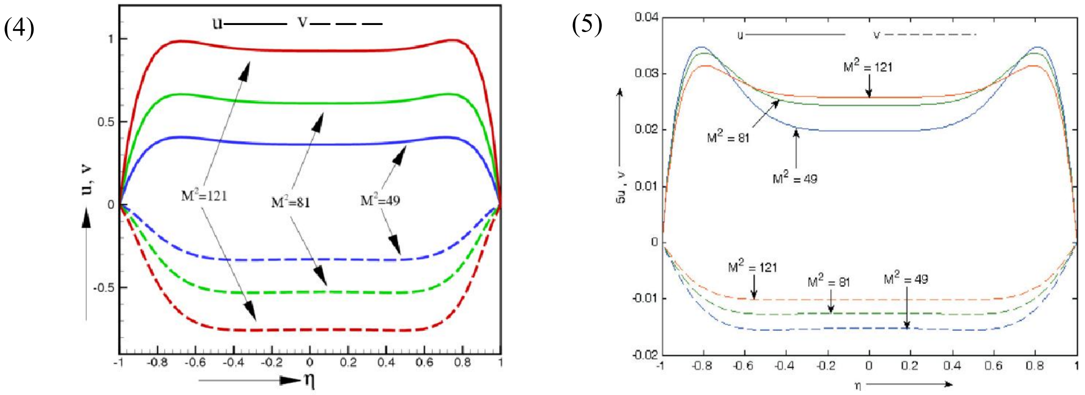

Fig. (4) and (5). Velocity profiles for present work and Seth et al. [4] respectively for large M^2 when $R = 25, m = 1$ and $\theta = 45^0$

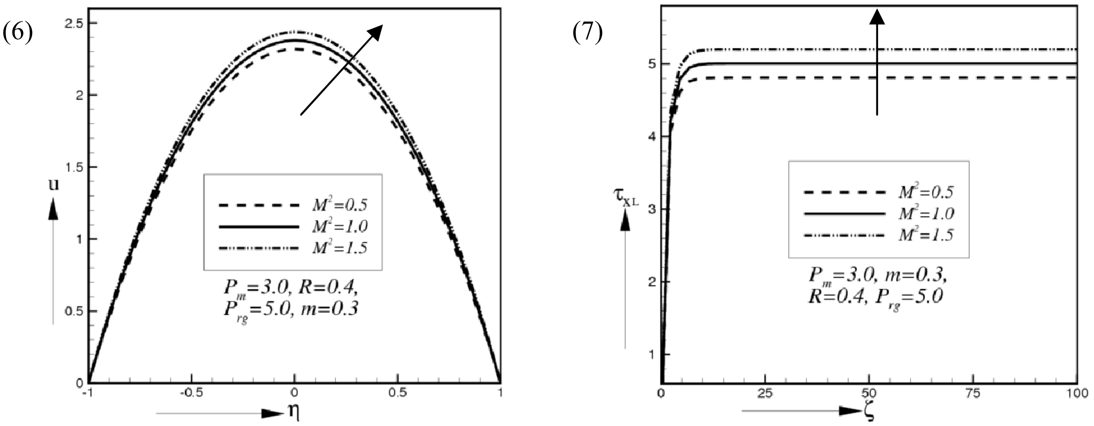

Fig.(6) and(7). Primary velocity profiles and local shear stress in case of moving plate in $x-$direction for different values of M^2 at $\theta = 45^0$

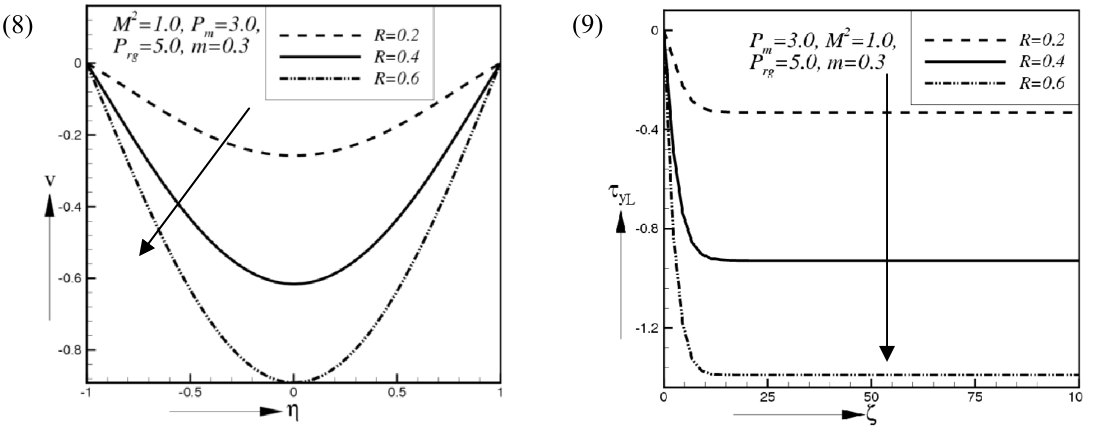

Fig.(8) and (9). Secondary velocity profiles and local shear stress in case of moving plate in $y-$direction for different values of R at $\theta = 45^0$

(10)

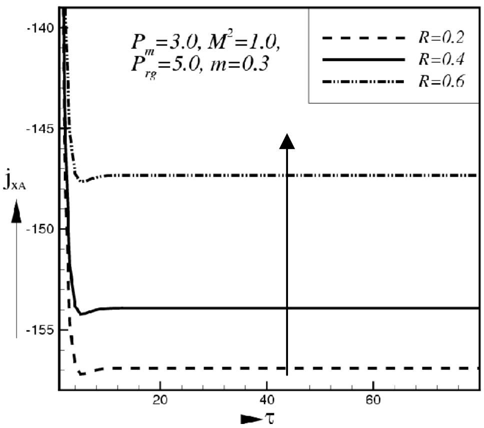

(11)

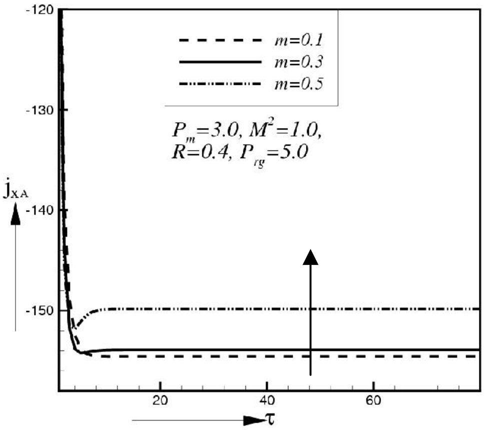

(12)

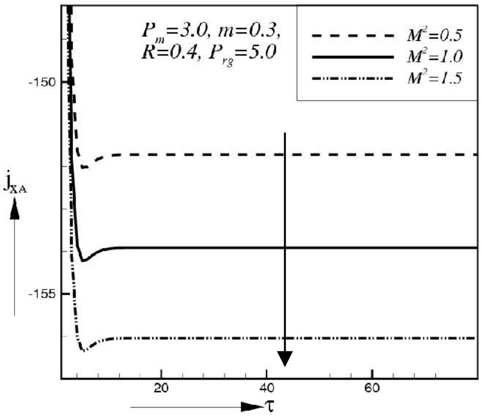

(13)

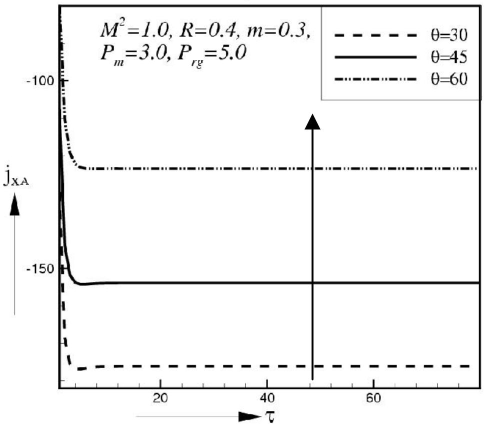

Figs. (10-13). Average current density in case of moving plate in $x-$ direction for different values of R, m, M^2, θ respectively at $\theta = 45^0$

(14)

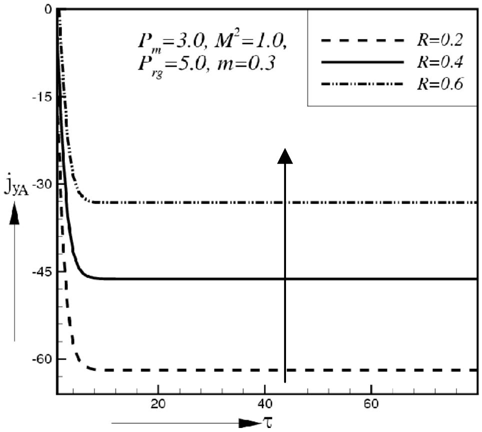

(15)

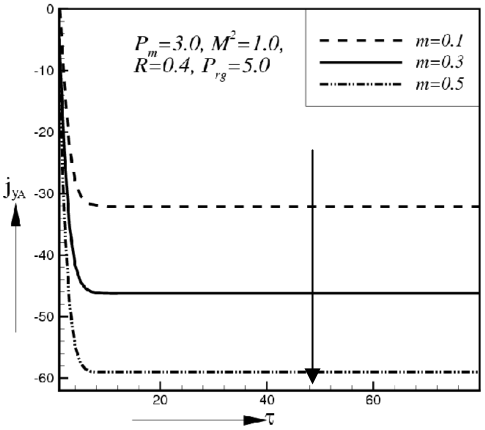

Figs. (14) and (15). Average current density in case of moving plate in $y-$ direction for different values of R, m respectively at $\theta = 45^0$

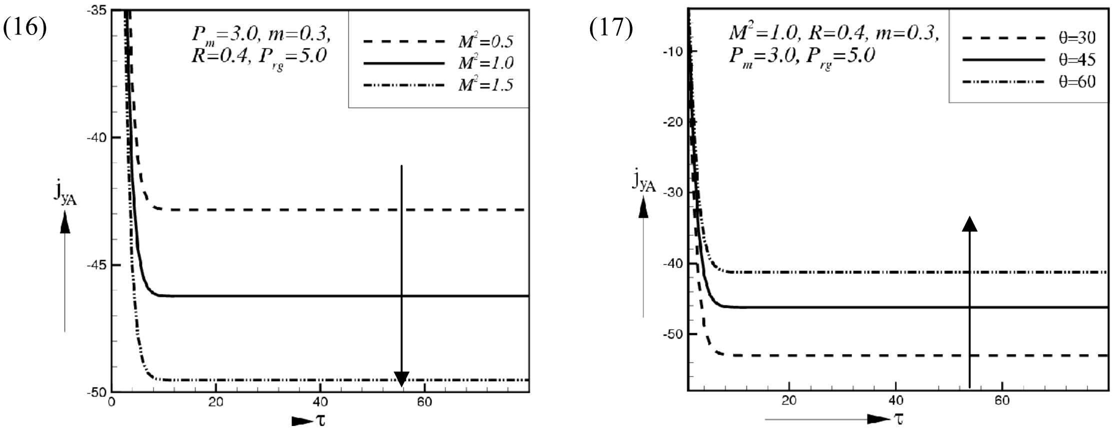

Figs. (16) and (17). Average current density in case of moving plate in $y-$ direction for different values of M^2,θ respectively at $\theta = 45^0$

6. Conclusions

Some important findings of this investigation are: (i) The primary velocity profiles and local shear stress profiles in case of moving plate in $x-$direction increase with the increase of magnetic parameter M^2 . (ii) The secondary velocity profiles and local shear stress profiles in case of moving plate in $y-$direction decrease with the increase of rotation parameter R . (iii) The average current density profiles in case of moving plate in $x-$direction increase with the increase of R , hall parameter m and angle of inclination θ, decrease with the increase of M^2 . (iv) The average current density profiles in $y-$direction increase with the increase of R and θ, decrease with the increase of m and M^2.

It is predicted that the present investigation can be utilized for the movement of oil or gas, producing electricity; these results are also of great interest in geophysics, astrophysics and fluid engineering.

References

[1] Jha B.K. and Apere C.A., " Combined effect of Hall and Ion-Slip Currents on Unsteady MHD Couette Flows in a Rotating System," journal of Physical Society of Japan, vol. 79, No.10,2010,pp104401-104401-9, (2010)

[2] Attia H.A.,"Transient Hartmann Flow with Heat Transfer Considering the Ion Slip", Physica Scripta, vol.66, 2002, pp.470-475, (2002). doi:10.1238/Physica.Regular.066a00470 .

[3] Edmad M. Aboeldahab, Elsayed M.E Elbarbary: "Hall current effect on magneto hydrodynamic free convection flow past a semi-infinite vertical plate with mass transfer", International Journal of Engineering Science vol. 39, pp.1641-1652, (2005)

[4] Seth G.S., Raj Nandkeolyar and Md. S. Ansari, "Hartmann Flow in a Rotating System in the Presence of Inclined Magnetic Field with Hall Effects", Tamkang Journal of Science and Engineering, vol. 13,No.3, pp.243-252, (2010)

Available online at www.sciencedirect.com

ScienceDirect

Procedia Engineering 00 (2015) 000–000

Procedia Engineering

www.elsevier.com/locate/procedia

6th BSME International Conference on Thermal Engineering (ICTE 2014)

Thermal and hydraulic performance analysis of rectangular fin arrays with perforation size and number

Mehedi Ehteshum*, Mohammad Ali, Md. Quamrul Islam, Muhsia Tabassum

Department of Mechanical Engineering, Bangladesh University of Engineering and Technology, Dhaka-1000, Bangladesh

Abstract

Enhancement of heat removal and reduction of fin size become a major concern in designing heat exchanger equipment. The present paper reports an experimental analysis to investigate the turbulent heat transfer performance of rectangular fin arrays, both solid and circular perforations along the length of the fins. The size and number of circular perforation have been varied. Tests have been conducted in a horizontal wind tunnel equipped with forced draft fan. The data are obtained by varying flow velocities while maintaining constant heat input and taken over a period of time. The Reynolds number is varied between 6×10^4 through 25×10^4. The heat loss due to radiation and convection is taken into account during calculation. Thermal performances and effectiveness of perforation and equivalent surface solid fin arrays have been evaluated and compared. Results show remarkable heat transfer enhancement, lower thermal resistances, pressure drop and higher efficiencies, effectiveness for perforated fins with increasing number of perforations in addition to the considerable reduction in weight in comparison with solid fin arrays.

Peer-review under responsibility of organizing committee of the 6th BSME International Conference on Thermal Engineering (ICTE 2014).

Keywords: Perforated fins; Turbulent flow; Fin effectiveness; Heat transfer; Heat transfer enhancement; Perforation size; Perforation number;

1. Introduction

The heat transfer enhancement is an important topic of thermal engineering. There are new inventions every day and new development in mechanical and electrical devices. As the size and mass of these system components are shrinking, their power consumption rate is constantly increasing. According to Chu [1], heat generation is an irreversible process and heat must be removed in order to maintain the continuous operation and to avoid the

---

* Corresponding author. Tel.: +880-1722073634, +880-1520082543.
E-mail address: mehedi69buet@gmail.com

Peer-review under responsibility of organizing committee of the 6th BSME International Conference on Thermal Engineering (ICTE 2014).

detrimental consequences due to burning and overheating. The heat removal may, in general, be enhanced by increasing the convective heat transfer coefficient between a primary surface and its surrounding fluid, or by increasing heat transfer area of the surface, or by both. For this purpose, extended surfaces that are well known as fins are used to enhance heat transfer in a wide range of engineering applications. In this study, the improvement of heat transfer coefficient, other thermal and hydraulic attributes of rectangular fin arrays with circular perforations has been investigated under turbulent flow condition.

Nomenclature

A_{front}	total area restricting the air flow	Q_T	total heat supplied
A	cross-sectional area of the duct	Q_{loss}	total heat loss from setup
A_h	unused area of the heater	Q_{rad}	total heat radiated from fin array
A_s	total heat transfer area	Q_{conv}	total convection heat from fin array
A_b	total base area	h	convective heat transfer coefficient
d_h	hydraulic diameter of the duct	R_{th}	thermal resistance of the fin
v_{avg}	average effective air flow velocity	η_{fin}	fin efficiency
V	volumetric flow rate of air	ε_{fin}	fin effectiveness
v_d	supplied duct air velocity	Re	Reynolds number
T_s	average surface temperature of fin array	Nu	Nusselt number
T_{surr}	average temperature of the surroundings	K	thermal conductivity of air
T_∞	average temperature of bulk air flow	K_{ins}	thermal conductivity of insulation tape
T_b	average base temperature	ρ	density of air
ΔT	temperature difference across the insulation tape	ν	kinematic viscosity of air
Δx	thickness of the insulation tape	ε	emissivity of heater material
Δp	pressure drop across the fin array	σ	Stefan-Boltzmann constant
Δp^*	dimensionless pressure drop across the fin array		

1.1. Literature review

It is believed that comparing the perforated fins with its solid counterpart is the best means to evaluate improvement or non-improvement in heat transfer brought about by introducing the perforations. Essa et al. [2, 3] and Zan et al. [4] found that the perforation of fins enhances the heat dissipation rates and at the same time decreases the expenditure for fin materials. Shaeri and Yaghoubi [5, 6] conducted numerical study of turbulent fluid flow and convective heat transfer over an array of solid and perforated fins. According to their study temperature drop form fin base to fin top surface increases with additions of perforations and perforated fins have higher fin effectiveness than solid fin that rises remarkably by adding more perforations. They also found that the form drag was the highest and the average friction drag was lowest for solid fin compared to perforated fins and drag decreases with increase of perforations [7].

Essa and Hussain [8] studied the effects of fin with square perforations on the thermal systems. Ali [9] conducted study on the effects of perforations' open area ratio on heat transfer coefficient and the module temperature of the fin. Ismail et al. [10] have performed 3D CFD simulation for rectangular solid and perforated fins under turbulent flow conditions. Bhuiyan et al. [11, 12, 13] studied thermal and hydraulic performance of plate fin, wavy fin and tube heat exchanger for transitional and turbulent flow regime. They found that the heat transfer and pressure drop performance increase with the decrease in the longitudinal, transverse pitch and the increase in fin pitch.

1.2. Present work

The present experimental study investigates the improvement of heat transfer coefficient due to perforations with varying sizes and numbers in rectangular fin arrays placed inside a channel under turbulent flow condition. The turbulent heat transfer performances of perforated fin arrays have been compared with that of equivalent solid fin arrays by studying their Nusselt numbers, thermal resistances, efficiencies, effectiveness and pressure drops across the fins. Diameters of perforations are taken as Φ2, Φ3 mm. The experiment is conducted with varying Reynolds numbers ranging from 6×10^4 to 25×10^4.

2. Experimental Setup

2.1. Heat sinks and heater

In this experiment, five different rectangular fins designs have been used including a solid fin and four perforated fins with varying sizes and numbers of perforations. All fins are shown in Fig. 1 and all fin array data are given in Table 1. Fins are heated by electrical heater which is insulated with 1.6 mm of glass-fiber tape (thermal conductivity 0.04 W/m-K). The heater is further insulated with 20 mm of glass-wool (thermal conductivity 0.04 W/m-K) as shown in Fig. 2 and placed inside a wooden box. So there are some convection and radiation heat losses only through the top surface of the heater and these losses are taken into account. The tested fins and heater are milled from solid aluminum (thermal conductivity 237 W/m-K) and no additional surface treatment is applied. The bottom surface of the heater is grooved where the heater coil is placed. This whole setup of heater box and fin is mounted on a plastic tube stand inside the wind tunnel as shown in Figs. 3 and 4.

Table 1. Fin array data.

Type	No. of fins, n	No of perforations, N	Dia. of perforation, d_p (mm)	Length, l (mm)	Width, w (mm)	Height, h_f (mm)	Channel width, w_{ch} (mm)	Fin width, t (mm)	Fin height, h_t (mm)	Total surface area, A_s (mm^2)	Base area, A_b (mm^2)	Mass (gm)
(a)	4	0	0	34	32	15	3	5.75	9	4742.0	1088	36.6
(b)	4	1	2	34	32	15	3	5.75	9	5571.4	1088	35.5
(c)	4	2	2	34	32	15	3	5.75	9	6400.8	1088	34.3
(d)	4	1	3	34	32	15	3	5.75	9	5967.2	1088	34.0
(e)	4	2	3	34	32	15	3	5.75	9	7192.4	1088	31.4

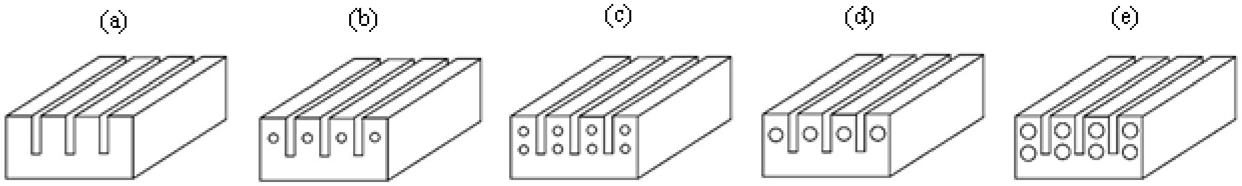

Fig. 1. Schematic view of the fin arrays (a) solid fin, (b) fin with one perforation of 2 mm, (c) fin with two perforations of 2 mm, (d) fin with one perforation of 3 mm, (e) fin with two perforations of 3 mm.

2.2. Wind tunnel

The schematic layout of the wind tunnel is shown in Figs. 4 and 5. The wind tunnel walls are made of plexiglass (thermal conductivity 0.20 W/m-K). The air flow is introduced using a forced draft fan. This fan is driven by two electrical motors and there is a regulator system to control the speed of the fan i.e. the air velocity. The dimensions of the measurement section of the tunnel are 605 x 505 x 495 mm.

2.3. Measurement Equipment

The experiment is operated with air flow velocities of 2, 3.5, 5, 6.5 and 8 m/s. The duct air flow velocities are measured with a digital anemometer. The voltage supplied to the heater coil is controlled by a variac. The electric current is measured using a clamp-on meter. All temperatures are measured using type-K thermocouples with a specified accuracy of ±0.75 ˚C. The pressure drops across the fins are measured using two pitot tubes positioned 50 mm upstream and downstream of the fin respectively and connected to an inclined manometer whose working fluid is kerosene (density 810 kg/m^3).

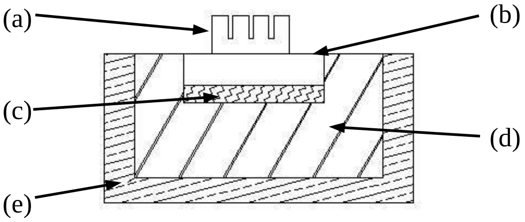

Fig. 2. Sectional view of heat sink assembly (a) fin, (b) heater base insulated with glass-fibre tape, (c) heater coil, (d) glass-wool insulation, (e) wooden box.

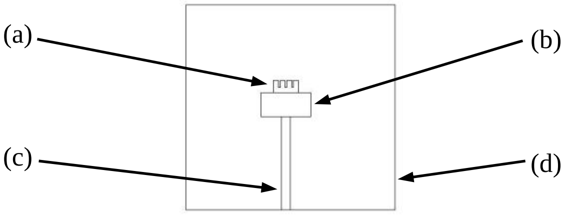

Fig. 3. Front view of setup (a) fin, (b) heater box, (c) plastic tube stand, (d) wind channel.

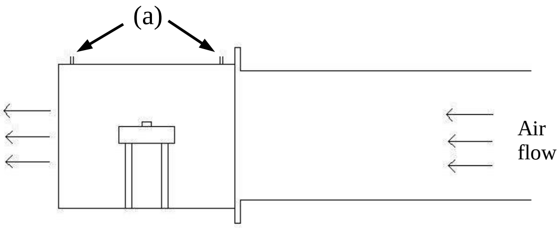

Fig. 4. Side view of setup (a) pitot tube insertion.

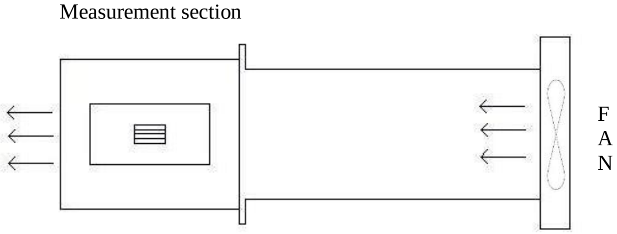

Fig. 5. Top view of wind tunnel.

3. Experiment Procedure

The tests are started by setting up all electrical connections and letting the heater setup being heated for some period to obtain steady state. Then the air flow velocity is adjusted and five sets of data are taken at 5 minutes interval for each velocity. Pressure drops across the fin arrays at 50 mm upstream and downstream are also measured for each velocity. Data are taken corresponding to Reynolds numbers roughly equal to 6x10^4, 10x10^4, 15x10^4, 20x10^4 and 25x10^4 (the above mentioned Reynolds numbers roughly corresponds to the velocities of 2, 3.5, 5, 6.5 and 8 m/s for a tunnel/duct having a height of 495 mm and a width of 505 mm). All properties of associated fluids and materials are taken at average or film temperature of the fin surface and the bulk air.

4. Analytical Method

In order to better reflect the actual effective velocity at the measurement section in the wind tunnel, the average velocity is calculated using the effective fluid flow area, $A - A_{front}$, such as,

$$v_{avg} = \frac{V}{A - A_{front}} \quad \text{[m/s]} \tag{1}$$

Where, $V = Av_d$ [m^3/s]

The duct Reynolds number, Re is defined as,

$$Re = \frac{v_{avg} \cdot d_h}{\nu} \tag{2}$$

Total heat input (Q_T) is calculated from the electrical potential and current supplied to the heater. Conduction loss from the upper surface of the heater setup through the glass-fiber insulation tape (Q_{loss}), which is not contributing to actual heat transfer from the fin, and heat radiated from the fin array (Q_{rad}) are also calculated. Here Q_{rad} is negligible compared to the convective heat transfer rate from the fin (Q_{conv}). Then Q_{conv} can be derived from following relation,

$$Q_{conv} = Q_T - Q_{loss} - Q_{rad} \quad [\mathrm{W}] \tag{3}$$

Now, the convective heat transfer coefficient, h and thermal resistance, R_{th} are calculated as,

$$h = \frac{Q_{conv}}{A_s \,.\, (T_s - T_\infty)} \quad [\frac{\mathrm{W}}{m^2 \,.\, K}] \tag{4}$$

$$R_{th} = \frac{1}{\mathrm{h} \,.\, A_s} \quad [\frac{\mathrm{K}}{\mathrm{W}}] \tag{5}$$

In order to represent heat transfer coefficient in a dimensionless way, Nusselt number, Nu is defined as,

$$Nu = \frac{\mathrm{h} \,.\, \mathrm{l}}{K} \tag{6}$$

Fin efficiency, η_{fin} is defined as the ratio of actual heat transfer rate from the fin to the ideal heat transfer rate from the fin if the entire fin were at base temperature. That is,

$$\eta_{fin} = \frac{\mathrm{h} \,.\, A_s \,.\, (T_s - T_\infty)}{\mathrm{h} \,.\, A_s \,.\, (T_b - T_\infty)} \times 100 \quad [\%] \tag{7}$$

Fin effectiveness, ε_{fin} is the ratio of heat transfer from fin to heat transfer from fin base without fin as,

$$\varepsilon_{fin} = \frac{\mathrm{h} \,.\, A_s \,.\, (T_s - T_\infty)}{\mathrm{h} \,.\, A_b \,.\, (T_b - T_\infty)} = \eta_{fin} \cdot \frac{A_s}{A_b} \tag{8}$$

The dimensionless pressure drop, Δp^* is defined as,

$$\Delta p^* = \frac{\Delta p}{\frac{1}{2} \,.\, \rho \,.\, v_{avg}^2} \tag{9}$$

5. Results and Discussion

The present analysis is performed with all five fins and carried out for Re ranging from 6×10^4 to 25×10^4 .i.e. under turbulent flow conditions with an uncertainty of 3.5%. Constant heat rate is maintained and all heat losses are measured to obtain actual heat dissipated from fin array by convection. These heat transfer rates are used to determine all the heat transfer performance parameters for all conditions. Smooth curves are drawn through the data points.

5.1. Effects of Reynolds number on heat transfer performance parameters

The comparative relations of heat transfer coefficient and Nusselt number for different fins corresponding to different Reynolds number are shown in Figs. 6 and 7. It is found that for all cases perforated fins have higher heat transfer coefficient compared to that of solid fin. It is especially true for fins with larger size and higher number of perforations. It is found that there is a significant rise of heat transfer coefficient values between fins with one perforation of 2 mm compared to that with one perforation of 3 mm. It is also found from Fig. 6 that the increase in value of heat transfer coefficient for fins with one perforation is higher than that for fins with two perforations.

Since Nusselt number is said to be dimensionless heat transfer coefficient, it is more appropriate to compare different fins with respect to this parameter. However, Nusselt number graphs of Fig. 7 also show the similar results stated above. Both Nusselt number and heat transfer coefficient increase whereas thermal resistance decreases with the increase in Reynolds number. Solid fin has maximum thermal resistance than other perforated fins and the decrease in value of thermal resistance is higher for larger perforation and higher number of perforation as shown in Fig. 8.

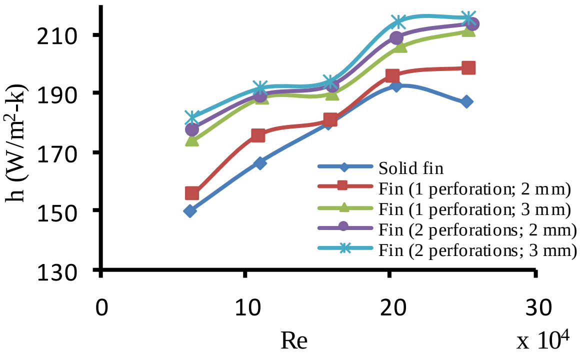

Fig. 6. Effect of Reynolds number on convective heat transfer coefficient.

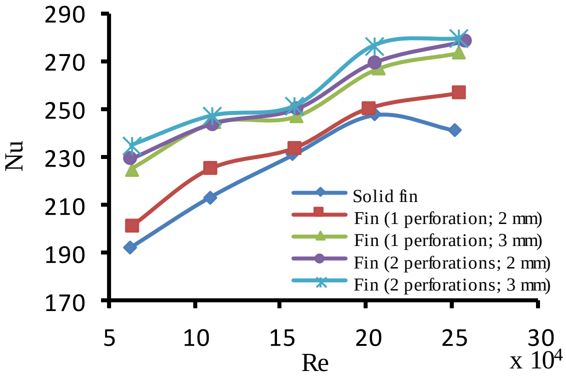

Fig. 7. Effect of Reynolds number on Nusselt number.

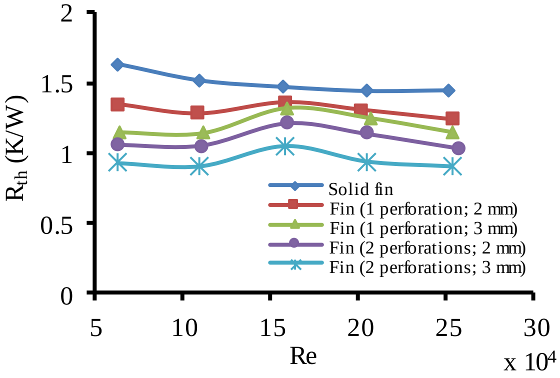

Fig. 8. Effect of Reynolds number on thermal resistance.

5.2. Fin efficiency and effectiveness at various Reynolds numbers

Figure 9 represents the comparative results of efficiencies for different fins. Results show that fins with larger perforation are more efficient and efficiency increases with increasing number of perforations within our experimental limit. Fin effectiveness shows similar relations as shown in Fig. 10. This is because perforated fins have larger effective heat transfer area compared to that of solid fin. However, both efficiencies and effectiveness decrease with increasing air velocity i.e. Reynolds number.

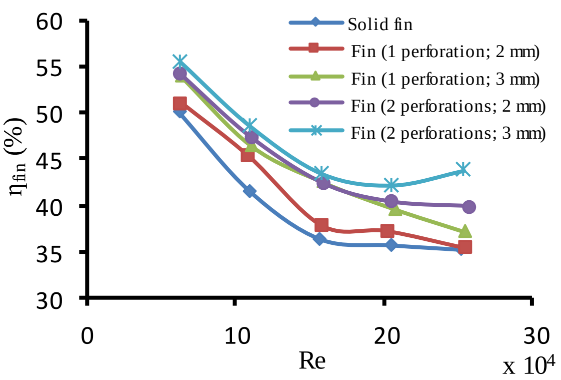

Fig. 9. Effect of Reynolds number on fin efficiency.

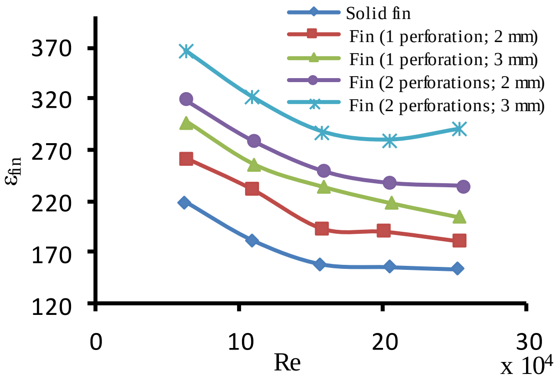

Fig. 10. Effect of Reynolds number on fin effectiveness.

5.3. Effects of Reynolds number on pressure drop

Pressure drop that occurs across the fin array is mainly due to two components of drag – form drag and friction/skin friction drag. Both components increase with the square of velocity. So it is expected that total pressure drop will increase with increasing velocity i.e. Reynolds number which is evident from Fig. 11. For all configurations the pressure drops are almost same, although solid fin has a tendency to have higher value which is quite natural.

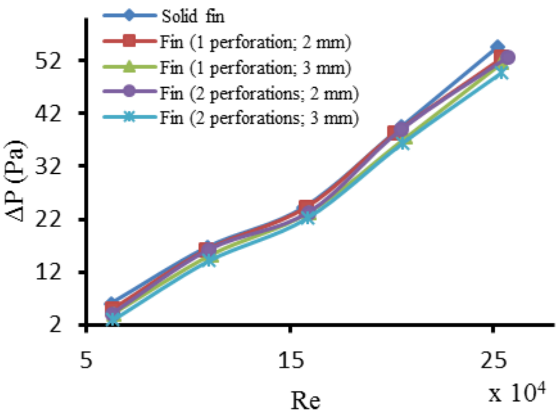

Fig. 11. Effect of Reynolds number on pressure drop.

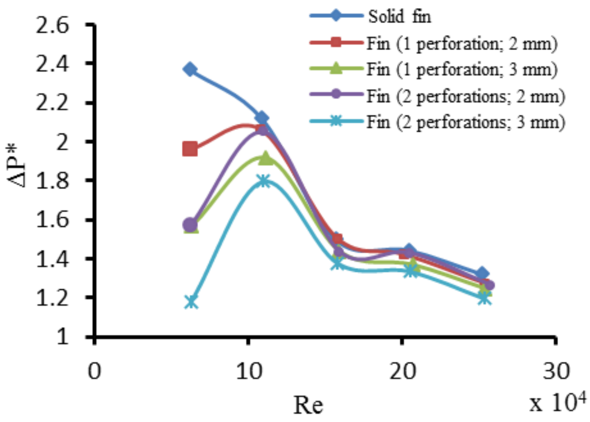

Fig. 12. Effect of Reynolds number on dimensionless pressure drop.

In case of solid fin, air flow interacts with the front surface of the fin and separation occurs. Due to perforation, some parts of the air flow goes through the perforation like flow in a channel. For this reason, the formed wakes are smaller for perforated fins compared to solid fins. And it is also seen from Fig. 11 that perforated fins have smaller pressure drops than that of solid fin for all Reynolds numbers. Figure 12 shows that dimensionless pressure drop generally decreases with increasing Reynolds number i.e. dynamic pressure. This indicates that the significance of pressure drop effect decreases with increasing Reynolds number. For perforated fins, it is found that dimensionless pressure drop initially rises up to a peak value than gradually decreases, however, all the time maintains lower value than that of solid fin. This is because, due to more available surface area of perforated fins, at the beginning the increasing friction drag dominates the decreasing form drag due to perforation and finally the decreasing form drag takes over the domination. This phenomenon is truer for more and larger perforations. In case of solid fins, due to the absence of perforation this parameter decreases constantly.

6. Conclusion:

In this experimental study, five different types of fins are tested to observe different parameters like- Nusselt number, heat transfer coefficient, thermal resistance, efficiency and effectiveness with varying Reynolds numbers. Nusselt number, heat transfer coefficient and pressure drop increase with increasing Reynolds number for all fins. But perforated fins show higher values of Nu and h and lower values of pressure drop than solid fin. The values of thermal resistance, efficiency, effectiveness and dimensionless pressure drop, in general, decrease with the increasing Reynolds number for all the fins. It is found that for more and larger perforations, thermal resistance and dimensionless pressure drop decrease whereas efficiency and effectiveness increase.

Acknowledgements

The authors are grateful to ME Department Library, Central Library and different Laboratories of Bangladesh University of Engineering and Technology (BUET) for providing technical support for this study.

References

[1] R. C. Chu, “Foreword,” in *Air Cooling Technology for Electronic Equipment*, CRC Press, 1996.

[2] A. A. Essa and M. A- Widyan, “Enhancement of natural convection heat transfer from a fin by triangular perforations of bases parallel and towards its tip,” *Applied Mathematics & Mechanics,* vol. 28, no. 8, pp. 1033-1044.

[3] A. A. Essa and M. Q. Al-Odat, “Enhancement of natural convection heat transfer from a fin by triangular perforations of bases parallel and toward its base,” *The Arabian Journal for Science and Engineering,* vol. 34.

[4] Zan WU, Wei LI, Zhi-jian SUN and Rong-hua HONG, “Modeling natural convection heat transfer from perforated plates,” *Journal of Zhejiang University-SCIENCE A (Applied Physics & Engineering),* vol. 13, pp. 353-360, 2012.

[5] M. R. Shaeri and M. Yaghoubi, “Numerical analysis of turbulent convection heat transfer from an array of perforated fins,” *International Journal of Heat and Fluid Flow,* vol. 30, pp. 218-222, 2009.

[6] M. R. Shaeri and M. Yaghoubi, “Thermal enhancement from heat sinks by using perforated fins,” *Energy conservation and management,* vol. 50, pp. 1264-1270.

[7] M. R. Shaeri, M. Yaghoubi and K. Jafarpur, “Heat transfer analysis of lateral perforated fin heat sinks,” *Applied Energy,* vol. 10, pp. 2019-2029, 2009.

[8] A. A. Essa and F. M. S. A. Hussain, “The effect of orientation of square perforation on the heat transfer enhancement from a fin subjected to natural convection,” *Heat and Mass Transfer,* vol. 40, pp. 509-515, 2004.

[9] R. K. Ali, “Heat transfer enhancement from protruding heat sources using perforated zone between the heat sources,” *Applied Thermal Engineering,* vol. 29, pp. 2766-2772, 2009.

[10] M. F. Ismail, M. O. Reza, M. A. Zobaer and M. Ali, “Numerical investigation of turbulent heat convection from solid and longitudinally perforated rectangular fins,” Procedia Engineering, vol. 56, pp. 497-502, 2013.

[11] A. A. Bhuiyan, M. R. Amin, A. K. M. Sadrul Islam, “Three-Dimensional Performance Analysis of Plain Fin Tube Heat Exchangers in Transitional Regime”, Applied Thermal Engineering, Vol 50, Issue 1, pp 445-454, 2013.

[12] A. A. Bhuiyan, M. R. Amin, R. Karim, A. K. M. Sadrul Islam, “Plate fin and tube heat exchanger modeling: Effects of performance parameters for turbulent flow regime”, International Journal of Automotive and Mechanical Engineering (IJAME), 9(1), pp. 1768-1781, 2014.

[13] A. A. Bhuiyan, A. K. M. Sadrul Islam, M. R. Amin, “Numerical study of 3D thermal and hydraulic characteristics of wavy fin-and-tube heat exchanger”, Frontiers in heat and mass Transfer (FHMT) 3 - 033006, 2012.

Available online at www.sciencedirect.com

ScienceDirect

Procedia Engineering00 (2015) 000–000

Procedia Engineering

www.elsevier.com/locate/procedia

6th BSME International Conference on Thermal Engineering (ICTE 2014)

MHD Free Convection and Mass Transfer Flow through a Vertical Oscillatory Porous Plate with Hall, Ion-slip Currents and Heat Source in a Rotating System

Md. Delowar Hossain, Md. Abdus Samad and Md. Mahmud Alam*

Department of Mathematics,University of Dhaka, Dhaka-1000, Bangladesh

**Mathematics Discipline, Khulna University, Khulna-9208, Bangladesh*

Abstract

Unsteady MHD free convection and mass transfer flow through a vertical oscillatory porous plate with hall, ion-slip currents and heat source in a rotating system are studied. The governing equations of the problem contain a system of non-linear coupled partial differential equations. The coupled non-linear partial differential equations are solved by explicit finite difference method and the numerical results have been calculated by Compaq Visual 6.6a. For good accuracy, stability and convergence analysis have been analyzed. The results of this investigation are discussed for the different values of the well-known parameters and are shown graphically.

Peer-review under responsibility of organizing committee of the 6th BSMEInternational Conference on Thermal Engineering (ICTE 2014).

Keywords: MHD flow, Hall current, Ion-slip current, Suction parameter, Heat source parameter.

---

1. Introduction

The MHD mass transfer flow under the action of strong magnetic field plays a decisive role in astrophysical and geophysical problems. Hall and ion-slip currents are likely to be important in flows of laboratory plasma. When the conducting fluid is partially-ionized gas, e.g. water gas seeded with potassium, the Hall and ion-slip currents are also significant. Hence it is now proposed to study the MHD free convection flow of a partially-ionized gas past an

---

* Corresponding author. Tel.:+88-041-725741; Cell: +8801912982811 fax:+88-041-731244
*E-mail address:*alam_mahmud2000@yahoo.com

Peer-review under responsibility of organizing committee of the 6th BSME International Conference on Thermal Engineering (ICTE 2014).

infinite vertical porous plate in a rotating system of reference when a strong magnetic field of a uniform strength is applied perpendicularly to the flow. Combined effects of hall and ion-slip currents on free convective heat generating flow past a semi-infinite vertical flat plate have been investigated by Abo-Eldahab et al. [1]. Attia [2] has discussed the combined effects of hall and ion-slip current of a conducting fluid flow due to a rotating disk. Osalusi et al. [3] have studied the combined effects of hall and ion-slip currents in MHD flow over a porous rotating disk. Ghara et al. [4] studied the effects of hall and ion-slip current on the flow induced by torsional oscillations of a disc in a rotating system. Maji et al. [5] studies Hall effects on hydromagnetic flow on an oscillating porous plate.

In this paper, our aim is to study the effects of hall and ion-slip currents on the unsteady MHD flow through a viscous incompressible electrically conducting fluid with the oscillations of an infinite non-conducting vertical porous plate.

Nomenclature

x, y, z	Cartesian co-ordinates	β_e	Hall parameter
u, v, w	Velocity components	β_i	Ion-slip parameter
γ	Permeability of the Porous Medium	k	Magnetic permeability of the porous medium
R	Rotational parameter	β	Thermal expansion co-efficient
T_w	Temperature at the plate	β^*	Concentration expansion co-efficient
T_∞	Temperature outside the boundary layer.	α	Heat source parameter
C_w	Concentration at the plate	ν	Kinematic viscosity
C_∞	Concentration outside the boundary layer	ρ	Density of the fluid
Ω	Rotational velocity component	σ_e	Electrical conductivity
U	Dimensionless primary velocity	σ	Thermal conductivity
W	Dimensionless secondary velocity	c_p	Specific heat at constant pressure
$\bar{T}$	Dimensionless fluid temperature	D_m	Co-efficient of mass diffusivity
$\bar{C}$	Dimensionless fluid concentration	Q	Heat absorption quantity
$\mathbf{J}$	Current density	k_T	Thermal diffusion ratio
$\mathbf{B}$	Magnetic field	T_m	Mean fluid temperature
B_o	Magnetic component	P_r	Prandtl number
U_0	Uniform velocity	S_0	Soret number
G_r	Grashof number	S_c	Schmidt number
G_m	Modified Grashof number	ε	Arbitrary constant

2. Mathematical formulation

The The unsteady flow of an electrically conducting incompressible viscous fluid past semi-infinite vertical porous plate $y = 0$ has been considered, with the x −axis chosen along the plate, when the plate velocity $U(t)$ oscillates in t with a frequency n and is given as $U(t) = U_0(1 + \cos nt)$. The flow is assumed to be in the x −direction and which is taken along the plate in the upward direction and y −axis is normal to it. Initially the fluids as well as the plate are at rest but for time $t > 0$ the whole system is allowed to rotate with a constant angular velocity Ω about the y −axis. Initially, it is considered that the plate as wall as fluid is at the same temperature $T_w(= T_\infty)$ and concentration level$C_w(= C_\infty)$. Also it is assumed that the temperature of the plate and spices concentration are raised to$T_w(> T_\infty)$ and $C_w(> C_\infty)$ respectively, which are there after maintained constant, where $T_w, C_w$are temperature and species concentration at the wall and T_∞, C_∞ are the temperature and the concentration of the spices outside the boundary layer respectively, the

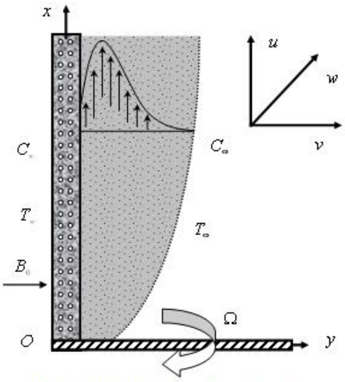

Fig.1 Physical configuration and coordinate system

physical configuration of the problem is shown in Fig. 1. A uniform magnetic field **B** is acting transverse to the plate. Using the relation $\nabla.\mathbf{B}=0$ or the magnetic field $\mathbf{B}=\left(B_x,B_y,B_z\right)$, $B_y=B_0$ has been considered everywhere in the fluid (B_0 is a constant). The induced magnetic field is neglected since the magnetic Reynolds number of a partially-ionized fluid is very small. If $\mathbf{J}=\left(J_x,J_y,J_z\right)$ is the current density, from the relation $\nabla.\mathbf{J}=0, J_y=\text{constant}$ has been obtained. Since the plate is electrically non-conducting, $J_y=0$ at the plate and hence zero everywhere. The dimensional governing equations are;

Continuity equation: $\dfrac{\partial u}{\partial x}+\dfrac{\partial v}{\partial y}=0$ (1)

Momentum equation:

$$\frac{\partial u}{\partial t}+u\frac{\partial u}{\partial x}+v\frac{\partial u}{\partial y}=\nu\frac{\partial^2 u}{\partial y^2}+g\beta(T-T_\infty)+g\beta*(C-C_\infty)+2\Omega w-\frac{\nu}{k}u-\frac{B_0^2\sigma_e(\alpha_e u+\beta_e w)}{\rho(\alpha_e^2+\beta_e^2)} \tag{2}$$

$$\frac{\partial w}{\partial t}+u\frac{\partial w}{\partial x}+v\frac{\partial w}{\partial y}=\nu\frac{\partial^2 w}{\partial y^2}-2\Omega u-\frac{\nu}{k}w+\frac{B_0^2\sigma_e(\beta_e u-\alpha_e w)}{\rho(\alpha_e^2+\beta_e^2)} \tag{3}$$

Energy equation: $\dfrac{\partial T}{\partial t}+u\dfrac{\partial T}{\partial x}+v\dfrac{\partial T}{\partial y}=\dfrac{\sigma}{\rho c_p}\dfrac{\partial^2 T}{\partial y^2}+Q(T_\infty-T)$ (4)

Concentration equation $\dfrac{\partial C}{\partial t}+u\dfrac{\partial C}{\partial x}+v\dfrac{\partial C}{\partial y}=D_m\dfrac{\partial^2 C}{\partial y^2}+\dfrac{D_m k_T}{T_m}\dfrac{\partial^2 T}{\partial y^2}$ (5)

The initial and boundary conditions for the model are;

$$\left.\begin{aligned}&u=0,v=0,w=0,T=T_\infty,C=C_\infty \text{ for } t\le 0\\&u=0,v=0,w=0,T=T_\infty,C=C_\infty \text{ at } x=0,\ t>0\end{aligned}\right\} \tag{6}$$

$$\left.\begin{aligned}&u=U_0\left[1+\frac{\varepsilon}{2}\left(e^{\text{int}}+e^{-\text{int}}\right)\right],v=0,w=0,T=T_w,C=C_w \quad at\ y=0,t>0\\&u=0,v=0,w=0,T=T_\infty,C=C_\infty \quad at\ y\to\infty,t>0\end{aligned}\right\} \tag{7}$$

The dimensionless governing equations have been obtained by using the following dimensionless variables. $X=\dfrac{xU_0}{\nu},Y=\dfrac{yU_0}{\nu},\ U=\dfrac{u}{U_0},\ V=\dfrac{v}{U_0}\ W=\dfrac{w}{U_0},\ \tau=\dfrac{tU_0^2}{\nu},\ \omega=\dfrac{n\nu}{U_0},\ \bar{T}=\dfrac{T-T_\infty}{T_w-T_\infty};\ \bar{C}=\dfrac{C-C_\infty}{C_w-C_\infty}$

The dimensionless governing equations are:

$$\frac{\partial U}{\partial X}+\frac{\partial V}{\partial Y}=0 \tag{8}$$

$$\frac{\partial U}{\partial \tau}+U\frac{\partial U}{\partial X}+V\frac{\partial U}{\partial Y}=\frac{\partial^2 U}{\partial Y^2}+G_r\bar{T}+G_m\bar{C}+2RW-\gamma U-\frac{M\left(\alpha_e U+\beta_e W\right)}{\left(\alpha_e^2+\beta_e^2\right)} \tag{9}$$

$$\frac{\partial W}{\partial \tau}+U\frac{\partial W}{\partial X}+V\frac{\partial W}{\partial Y}=\frac{\partial^2 W}{\partial Y^2}-2RU-\gamma W+\frac{M\left(\beta_e U-\alpha_e W\right)}{\left(\alpha_e^2+\beta_e^2\right)} \tag{10}$$

$$\frac{\partial \bar{T}}{\partial \tau}+U\frac{\partial \bar{T}}{\partial X}+V\frac{\partial \bar{T}}{\partial Y}=\frac{1}{P_r}\frac{\partial^2 \bar{T}}{\partial Y^2}-\frac{\alpha}{P_r}\bar{T} \tag{11}$$

$$\frac{\partial \bar{C}}{\partial \tau}+U\frac{\partial \bar{C}}{\partial X}+V\frac{\partial \bar{C}}{\partial Y}=\frac{1}{S_c}\frac{\partial^2 \bar{C}}{\partial Y^2}+S_0\frac{\partial^2 \bar{T}}{\partial Y^2} \tag{12}$$

The boundary conditions are ;

$$\left.\begin{aligned} &U=0, V=0,\ W=0,\ \bar{T}=0,\ \bar{C}=0 \quad \text{for } \tau \le 0 \\ &U=0, V=0,\ W=0,\ \bar{T}=0,\ \bar{C}=0 \quad \text{at } X=0,\ \tau>0 \end{aligned}\right\} \tag{13}$$

$$\left.\begin{aligned} &U=1+\frac{\varepsilon}{2}\left(e^{\mathrm{i}\omega\tau}+e^{-\mathrm{i}\omega\tau}\right)=1, V=0, W=0, \bar{T}=1,\ \bar{C}=1 \ \ at\ Y=0,\ \tau>0 \\ &U=0, V=0,\ W=0, \bar{T}=0, \bar{C}=0 \qquad at\ Y\to\infty, \tau>0 \end{aligned}\right\} \tag{14}$$

Where, $G_r=\dfrac{g\beta(T_w-T_\infty)\nu}{U_0^3}$ (Grashof Number), $G_m=\dfrac{g\beta^*(C_w-C_\infty)\nu}{U_0^3}$ (Modified Grashof Number), $M=\dfrac{\sigma_e B_0^2\nu}{\rho U_0^2}$ (M agnetic Parameter), $P_r=\dfrac{\rho c_p\nu}{\sigma}$ (Prandtl Number), $S_c=\dfrac{\nu}{D_m}$ (Schmidt Number), $S_0=\dfrac{D_m k_T(T_w-T_\infty)}{\nu T_m(C_m-C_\infty)}$ (Soret Number), $R=\dfrac{\Omega\nu}{U_0^2}$ (Rotational Parameter), $\alpha=\dfrac{Q\nu^2\rho c_p}{U_0^2\sigma}$ (Heat Source Parameter), $\gamma=\dfrac{\nu^2}{kU_0^2}$ (Permeability of the Porous Medium)

3. Shear stress, Nusselt number and Sherwood number

The quantities of chief physical interest are the local shear stress, Nusselt number, Sherwood number. The following equations represent the shear stress $\tau_x=\mu_0\left(\dfrac{\partial u}{\partial y}\right)_{y=0}$ which is proportional to $\left(\dfrac{\partial U}{\partial y}\right)_{y=0}$. Nusselt number $N_u=-\mu_0\left(\dfrac{\partial T}{\partial y}\right)_{y=0}$ which is proportional to $\left(\dfrac{\partial \bar{T}}{\partial y}\right)_{y=0}$ and Sherwood number $S_h=-\mu_0\left(\dfrac{\partial C}{\partial y}\right)_{y=0}$ which is proportional to $\left(\dfrac{\partial \bar{C}}{\partial y}\right)_{y=0}$.

4. Numerical Solution

In this section, the governing second order nonlinear coupled dimensionless partial differential equations have been solved with the associated initial and boundary conditions. For simplicity the explicit finite difference method has been used to solve equation (8) to (12) subject to the initial and boundary conditions (13)-(14). The present problem is required a set of finite difference equation. In this case the region within the boundary layer is divided into grid or meshes of lines parallel to X and Y axes where X-axis is taken along the plate and Y-axis is normal to the plate. Here the plate of height $X_{\max}(=100)$ is considered i.e. X varies 0 to 25 and $Y_{\max}(=25)$ as corresponds to $Y\to\infty$ i.e. Y varies from 0 to 25. There are $m(=150)$ and $n(=150)$ grid spacing in the X and Y direction as shown ΔX, ΔY are constant mesh size along e constant mesh size along X and Y direction as follows $\Delta X=0.67(0\le X\le 100)$ and $\Delta Y=0.17(0\le Y\le 25)$ with smaller time step $\Delta t=0.005$.

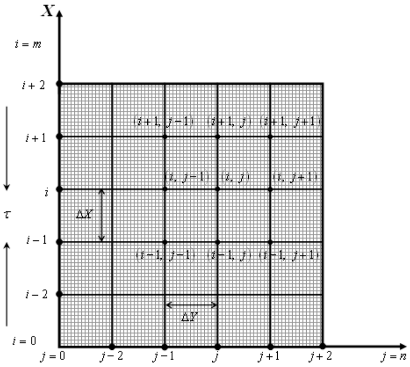

Fig. 2 Finite difference grid space.

Let $U', W', \bar{T}', \bar{C}'$ denoted the values of $U, W, \bar{T}, \bar{C}$ at the end of a time-step respectively. Using the explicit difference approximation these have been mentioned.

From the system of partial differential equations (8) to (12) with substituting the above relations into the corresponding differential equation we obtain an appropriate set of finite difference equations

$$\frac{U'_{i,j}-U'_{i-1,j}}{\Delta X}+\frac{V_{i,j}-V_{i,j-1}}{\Delta Y}=0 \tag{15}$$

$$\begin{aligned}\frac{U'_{i,j}-U_{i,j}}{\Delta\tau}+U_{i,j}\frac{U_{i,j}-U_{i-1,j}}{\Delta X}+V_{i,j}\frac{U_{i,j+1}-U_{i,j}}{\Delta Y}&=\frac{U_{i,j+1}-2U_{i,j}+U_{i,j-1}}{(\Delta Y)^2}+G_rT_{i,j}+G_mC_{i,j}+2RW_{i,j}-\gamma U_{i,j}\\&-\frac{M}{\alpha_e^2+\beta_e^2}\left(\alpha_eU_{i,j}+\beta_eW_{i,j}\right)\end{aligned} \tag{16}$$

$$\begin{aligned}\frac{W'_{i,j}-W_{i,j}}{\Delta\tau}+U_{i,j}\frac{W_{i,j}-W_{i-1,j}}{\Delta X}+V_{i,j}\frac{W_{i,j+1}-W_{i,j}}{\Delta Y}&=\frac{W_{i,j+1}-2W_{i,j}+W_{i,j-1}}{(\Delta Y)^2}-2RU_{i,j}-\gamma W_{i,j}\\&+\frac{M}{\alpha_e^2+\beta_e^2}\left(\beta_eU_{i,j}-\alpha_eW_{i,j}\right)\end{aligned} \tag{17}$$

$$\frac{\overline{T}'_{i,j}-\overline{T}_{i,j}}{\Delta\tau}+U_{i,j}\frac{\overline{T}_{i,j}-\overline{T}_{i-1,j}}{\Delta X}+V_{i,j}\frac{\overline{T}_{i,j+1}-\overline{T}_{i,j}}{\Delta Y}=\frac{1}{P_r}\frac{\overline{T}_{i,j+1}-2\overline{T}_{i,j}+\overline{T}_{i,j-1}}{(\Delta Y)^2}-\frac{\alpha}{P_r}\overline{T}_{i,j} \tag{18}$$

$$\frac{\overline{C}'_{i,j}-\overline{C}_{i,j}}{\Delta\tau}+U_{i,j}\frac{\overline{C}_{i,j}-\overline{C}_{i-1,j}}{\Delta X}+V_{i,j}\frac{\overline{C}_{i,j+1}-\overline{C}_{i,j}}{\Delta Y}=\frac{1}{S_c}\frac{\overline{C}_{i,j+1}-2\overline{C}_{i,j}+\overline{C}_{i,j-1}}{(\Delta Y)^2}+S_0\frac{\overline{T}_{i,j+1}-2\overline{T}_{i,j}+\overline{T}_{i,j-1}}{(\Delta Y)^2} \tag{19}$$

and boundary conditions with the finite difference scheme are

$$\left.\begin{aligned}&U^0_{i,j}=0, V^0_{i,j}=0,\ W^0_{i,j}=0,\ \overline{T}^0_{i,j}=0,\ \overline{C}^0_{i,j}=0\\&U^n_{0,j}=0, V^n_{0,j}=0,\ W^n_{0,j}=0,\ \overline{T}^n_{0,j}=0,\ \overline{C}^n_{0,j}=0 \quad \text{at } X=0\end{aligned}\right\} \tag{20}$$

$$\left.\begin{aligned}&U^n_{i,0}=1,\ V^n_{i,0}=0,\ W^n_{i,0}=0,\ \overline{T}^n_{i,0}=1,\ \overline{C}^n_{i,0}=1 \quad at\ Y=0\\&U^n_{i,L}=0,\ V^n_{i,L}=0,\ W^n_{i,L}=0, \overline{T}^n_{i,L}=0, \overline{C}^n_{i,L}=0 \qquad \text{where } L\to\infty\end{aligned}\right\} \tag{21}$$

Here the subscripts i designate the grid points with Y coordinates and the superscript n represents a value of time, $\tau=n\Delta\tau$ where $n=0,1,2,3,.....$ At the end of any time step $\Delta\tau$, the new primary velocity U' and the new secondary velocity W', the new temperature $\overline{T}'$, the new concentration $\overline{C}'$ at all interior nodal may be obtained by successive applications of equations (16), (17) , (18), (19) respectively.

The stability conditions of the explicit finite difference method are

$$\frac{U\Delta\tau}{\Delta X}+\frac{|V|\Delta\tau}{\Delta Y}+\frac{2\Delta\tau}{(\Delta Y)^2}+\frac{\gamma\Delta\tau}{2}\le 1\ ,\quad \frac{U\Delta\tau}{\Delta X}+\frac{|V|\Delta\tau}{\Delta Y}+\frac{2\Delta\tau}{(\Delta Y)^2}+\frac{\gamma\Delta\tau}{2}\le 1\ ,\quad \frac{U\Delta\tau}{\Delta X}+\frac{|V|\Delta\tau}{\Delta Y}+\frac{2\Delta\tau}{P_r(\Delta Y)^2}+\frac{\alpha\Delta\tau}{2P_r}\le 1\ ,$$

$\frac{U\Delta\tau}{\Delta X}+\frac{|V|\Delta\tau}{\Delta Y}+\frac{2\Delta\tau}{S_c(\Delta Y)^2}\le 1$ and the convergence criteria of the method are $P_r\ge 0.35,\ S_c\ge 0.35$

5. Results and Discussion

For the purpose of discussing the effects of various parameters on the flow behavior, numerical calculations have been carried out for different values of heat source (α), Hall parameter (β_e), ion-slip parameter (β_i) and magnetic parameter (M). The results of numerical calculations are shown in Figs. 3(a)-5(d). The shear stress (τ_x) for x-direction is shown in Figs. 3(a)-3(d). From Figs. 3(a) and 3(d) it is observed that shear stress τ_x decrease with the increase of α and M but it increase with the increases of β_e and β_i which are shown in Figs. 3(b) and 3(c). In Figs.4 (a)-4(d) Nusselt number (N_u) has shown for the effect of heat source parameter α , Hall parameter β_e , ion-slip parameter β_i and magnetic parameter M respectively. The Nusselt number N_u decreases with the increase of heat source parameter, Hall parameter and Ion-slip parameter which are shown in Figs. 4(a)-4(c) while the Nusselt number N_u decreases with the increase of magnetic parameter M which are observed in Fig. 4(d). The profiles for Sherwood number (S_h) for different values of heat source parameter α , Hall parameter β_e, ion-slip parameter β_i and magnetic parameter M are represented in Figs. 5(a)-5(d). From Figs. 5(a) and 5(d) it is seen that Sherwood distribution profiles S_h decrease with the increase of α and M while it increase with the increases of β_e and β_i in Figs. 5(a) and 5(d).

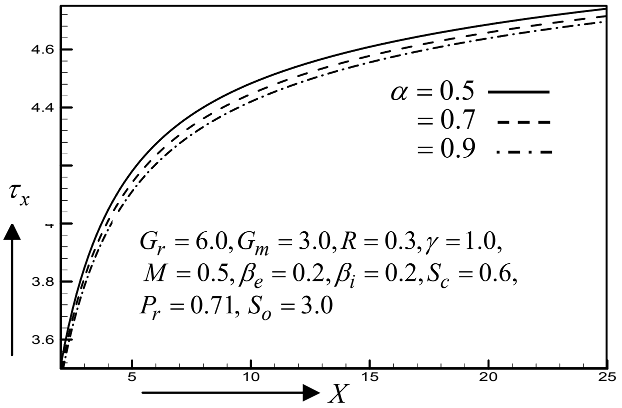

Fig.3(a) Shear stress for different values of heat source parameter α

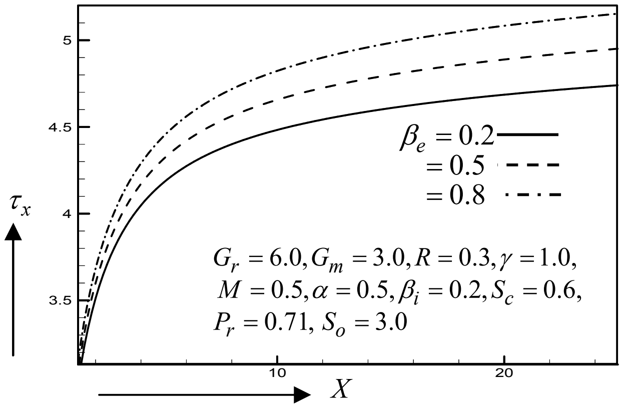

Fig. 3(b) Shear stress for different values of Hall parameter β_e

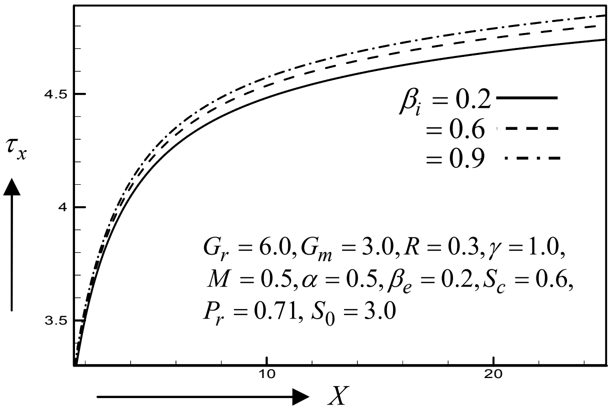

Fig.3(c) Shear stress for different values of Ion-slip parameter β_i

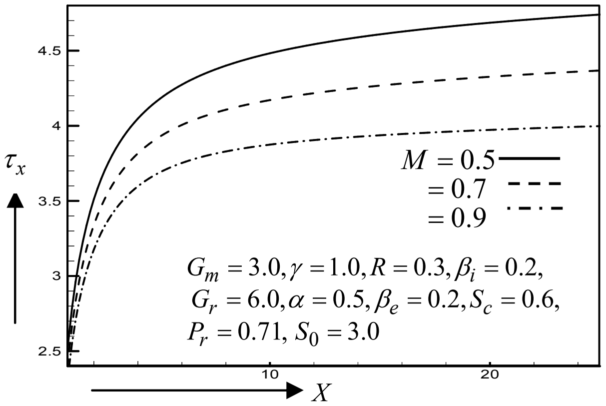

Fig.3(d) Shear stress for different values of magnetic parameter M

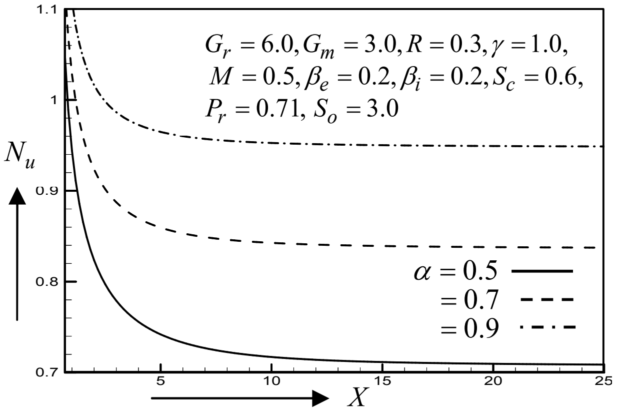

Fig. 4(a) Nusselt number for different values of heat source parameter α

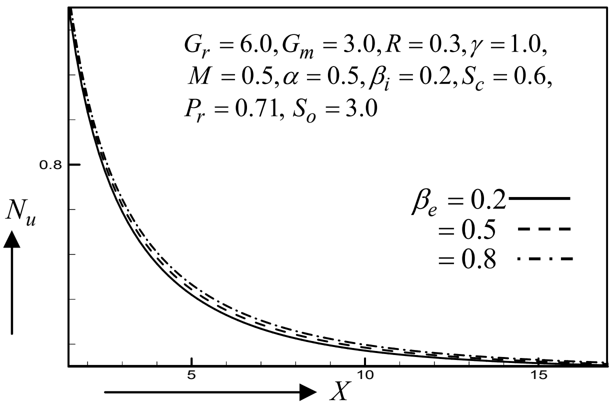

Fig. 4(b) Nusselt number for different values of Hall parameter β_e

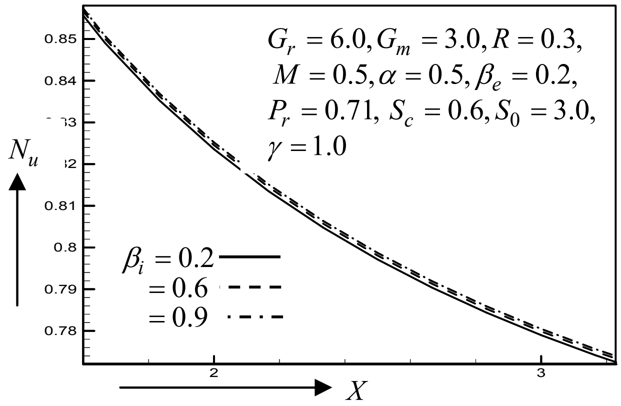

Fig. 4(c) Nusselt number for different values of Ion-slip parameter β_i

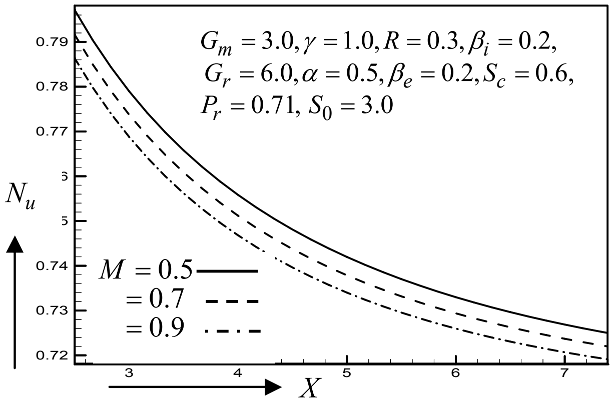

Fig. 4(d) Nusselt number for different values of magnetic Parameter M

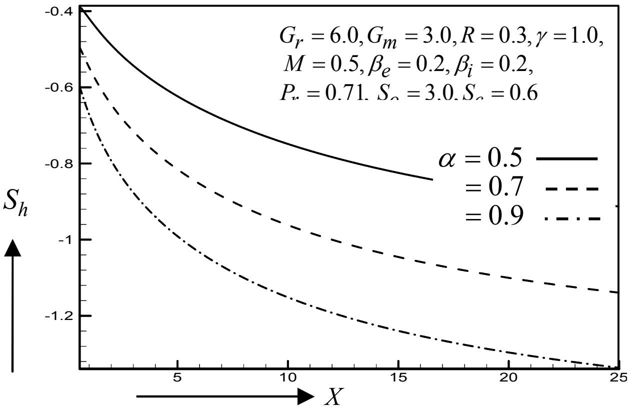

Fig.5(a) Sherwood number for different values of heat source parameter α

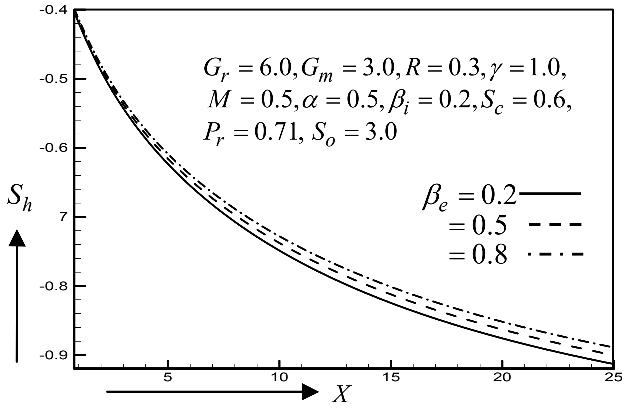

Fig. 5(b) Sherwood number for different values of Hall parameter β_e

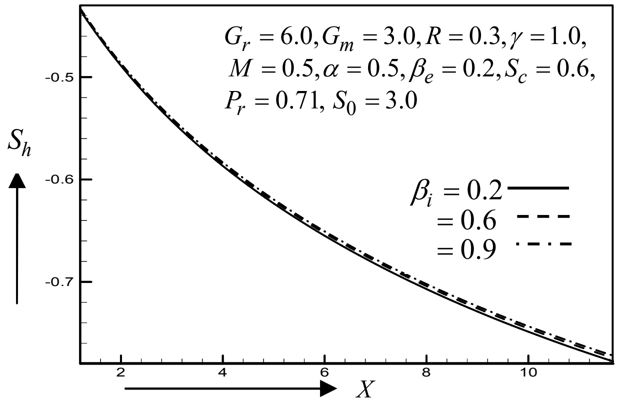

Fig. 5(c) Sherwood number for different values of Ion-slip parameter β_i

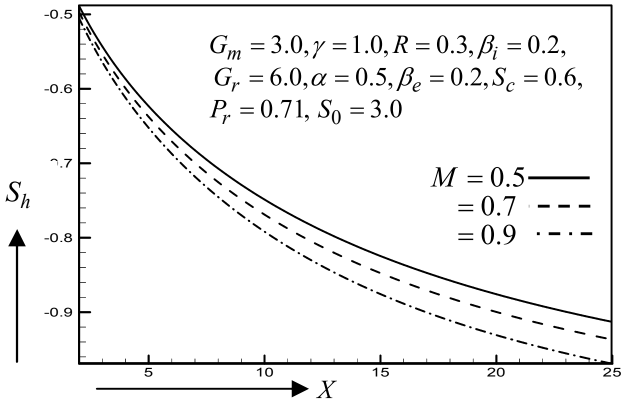

Fig. 5(d) Sherwood number for different values of magnetic parameter M

Conclusions

In this paper, MHD free convection and mass transfer flow through a vertical oscillatory porous plate with Hall, ion-slip currents and heat source in a rotating system is presented. Results are presented graphically to illustrate the variation shear stress, Nusselt number and Sherwood number with various parameters. In this study the following conclusions are set out:

1. The shear stress increases with an increase of Hall and ion-slip parameters while it decreases with the

increase of heat source and magnetic parameters.

2. Nusselt distribution increases with the increase of heat source, Hall and ion-slip parameters. On the other hand, it decreases with an increase in the value of magnetic parameter.
3. Sherwood distribution increases with the increase of Hall and ion-slip parameters while it decreases with the increase of heat source and magnetic parameters.

References:

[1]. Abo-Eldahab, E.M. and Aziz, M.A., "Hall and ion-slip effects on MHD free convective heat generating flow past a semi-infinite vertical plate flat plate", *Physica Scripta*, 61(2000), pp 344-348.

[2]. Attia , H.A., "Ion-slip on the flow due to a rotating disk", *The Arabian Journal of Science Engineering*, 29 (2004), pp 165-172.

[3]. Osalusi E., Side, J. and Harris, R., "The effects of Ohmic heating and viscous dissipation on unsteady MHD and slip flow over a porous rotating disk with variable properties in the presence of hall and ion-slip currents", *International Communication heat and mass transfer*, 34(2007), pp 1017-1029 .

[4]. Ghara, N., Das, S., Maji, S.L., Jana, R.N., "Effects of hall current and ion-slip on MHD low induced by torsional oscillations of a disc in a rotating fluid", *Journal of Mechanics*, Vol. 29(2013), No 2, pp 337-344.

[5]. Maji, S.L., Kanch, A.K., Guria, M., Jana, R.N., "Studies hall effects on hydromagnetic flow on an oscillating porous plate", *Appl. Math. Mech. –Engl. Ed*. 30(4) (2009), 503-512.

6th BSME International Conference on Thermal Engineering (ICTE 2014)

Two-phase frictional multiplier correlation for the prediction of condensation pressure drop inside smooth horizontal tube

Md. Anowar Hossain[a,*], Hasan MM Afroz[a], Akio Miyara[b]

[a]*Department of Mechanical Engineering, Dhaka University of Engineering & Technology, Gazipur, Bangladesh*
[b]*Department of Mechanical Engineering, Saga University, Saga shi 840-8502, Japan*

Abstract

In the present work, a two-phase frictional multiplier (Φ_V) correlation for the prediction of condensation pressure drop inside smooth horizontal tube has been proposed incorporating the effect of mass velocity, tube geometry and surface tension. Other existing correlations and the newly proposed correlation of two-phase frictional multiplier have been used to predict the condensation pressure drop of R1234ze(E), R32, R410A, dimethyl ether (DME) and R1234ze(E)/R32mixtures (30/70 and 45/55 weight %) inside a horizontal smooth tube. The predicted results have been compared with the available experimental data which is done inside a water heated double tube heat exchanger. The test section is a horizontally installed smooth tube with effective length of 3.6m and inner diameter of 4.35mm. The experiment has been carried out under the conditions of mass flux varying from 147 to 403 kgm^{-2}s^{-1} and the saturation temperatures ranging between 30 and 45 °C, over the vapor quality range 0.0065 to 0.9724. From the results of comparison, proposed correlation shows better performance for all refrigerants. Proposed Φ_V correlation can predict all the experimental data within ±11%.

Keywords: Condensation; R1234ze(E); frictional multiplier; R1234ze(E)/R32 mixture.

---

1. Introduction

The refrigerants used in refrigeration systems typically have measurable environmental effects including the ozone depletion potential (ODP) and global warming potential (GWP). Today, either hydrofluorocarbons (HFCs) with high

---

* Corresponding author. Tel.: +88-02-920-4710; +8801821769479; fax: +88-02-920-4711.
*E-mail address:*anowar96me@gmail.com

GWP values or hydrochlorofluorocarbons (HCFCs) with small ODP values are used in stationary air conditioners. Hence, it is crucial to replace these refrigerants with low GWP alternatives. R1234ze(E), a newly developed refrigerant with a GWP of 6, can be used as a drop-in solution for heat pump system.

Only few works have been done for the low GWP refrigerant R1234ze(E) that include the experimental study of heat transfer and pressure drop and comparisons with conventional refrigerants [1-6]. Koyama et al. (2010, 2011) carried out drop-in tests of R410A, R1234ze(E) and the mixtures of R1234ze(E)/R32 at heating mode, using a vapor compression heat pump system developed for R410A. They recommended that mixtures of R1234ze(E) and R32 are strong candidates for replacing R410A in domestic heat pump system.

Experimental condensation heat transfer coefficient (HTC) and pressure drop of R1234ze(E) in a horizontal smooth tube are measured and compared with R32 and R410A by Hossain et al. [3]. They found that HTC of R1234ze(E) is lower than R32 but higher than R410A but pressure gradient of R1234ze(E) is higher than R32 and R410A. Hossain et al. [4] experimentally investigated the effect of vapor quality, mass flux and saturation temperature on the evaporation heat transfer coefficients of R1234ze(E), R32, R410A and a mixture of R1234ze(E) and R32 inside a horizontal smooth tube and found that The local heat transfer coefficient of zeotropic mixture is lower than R32 and R410A for the whole quality range but is higher than R1234ze(E) in low vapor quality region only and The evaporation heat transfer coefficient increases with increasing saturation temperature but the increasing rate is not so significant.

Some works have found that include the prediction correlations of two-phase pressure drop (Φ_V correlation) for smooth horizontal tube [7-10]. But these Φ_V correlations may not be used for prediction of pressure drop of new low GWP refrigerant R1234ze(E). Haraguchi et al. [7] developed the Φ_V correlation as a function of Froude number (*Fr*) and Lockhart-Martinelli parameter (X_{tt}). Haraguchi's Φ_V inferior for low Bond number (*Bo*) region. By considering the effect of *Bo* (i.e. surface tension as well as tube diameter), Miyara et al. [8] developed their Φ_V correlation which is improved the prediction. But still need modification for better prediction of all the refrigerants data considered in the present work. In this paper, an empirical correlation of two-phase frictional multiplier has been proposed to predict condensation pressure drop of R1234ze(E), R32, R410A, dimethyl ether (DME) and R1234ze(E)/R32mixtures (30/70 and 45/55 weight %) inside a horizontal smooth tube.

Nomenclature

Bo	Bond number
d	diameter (m)
Fr	Froude number
f	friction factor
G	mass velocity (kg m^{-2} s^{-1})
g	gravitational acceleration
P	pressure (Pa)
ΔP	pressure drop (Pa)
R_a	arithmetic mean roughness (μm)
R_q	root mean square roughness (μm)
Re	Reynolds number
x	vapor quality
X_{tt}	Lockhart-Martinelli parameter [$\left((1-x)/x\right)^{0.9}\left(\rho_v/\rho_l\right)^{0.5}\left(\mu_l/\mu_v\right)^{0.1}$]
T	temperature
Δz	pressure drop length (m)
Φ	two-phase frictional multiplier
σ	surface tension, (N m^{-1})
μ	viscosity (Pa s)
ρ	density (kg m^{-3})
ε	void fraction

2. Experimental Data

Our previously measured data of condensation pressure drop of R1234ze(E), R32, R410A, dimethyl ether (DME) and R1234ze(E)/R32mixtures (30/70 and 45/55 weight %) inside a horizontal smooth tube have been used for the present analysis. Most of the data have already been published in different publications for different analysis [3, 4, 13, and 14]. The details of the experimental methodology have been described in [3, 4, 13, and 14]. The refrigerant mass flux variation was 147to 503 kg m^{-2} s^{-1}. The range of inlet saturation temperature of the test section was 35°C to 45°C. The test section was horizontally installed double tube heat exchanger with effective length of 3.6 m as shown in Fig.1. Refrigerant flows inside an inner tube and heating water flows through the annular space in a counter current. In order to measure quasi-local heat transfer and pressure drop, the annular channel is divided into 12 and 8 subsections with each subsection length 300 mm and 920 mm, respectively. The inner tube is the smooth test tube made of copper and of 4.35 mm inner diameter and 6.35 mm outer diameter. The surface roughness of copper test tube is R_a=0.666 µm and R_q=0.849 µm. The outer tube is made of poly-carbonated resin and of 9 mm inner diameter and 13 mm outer diameter.

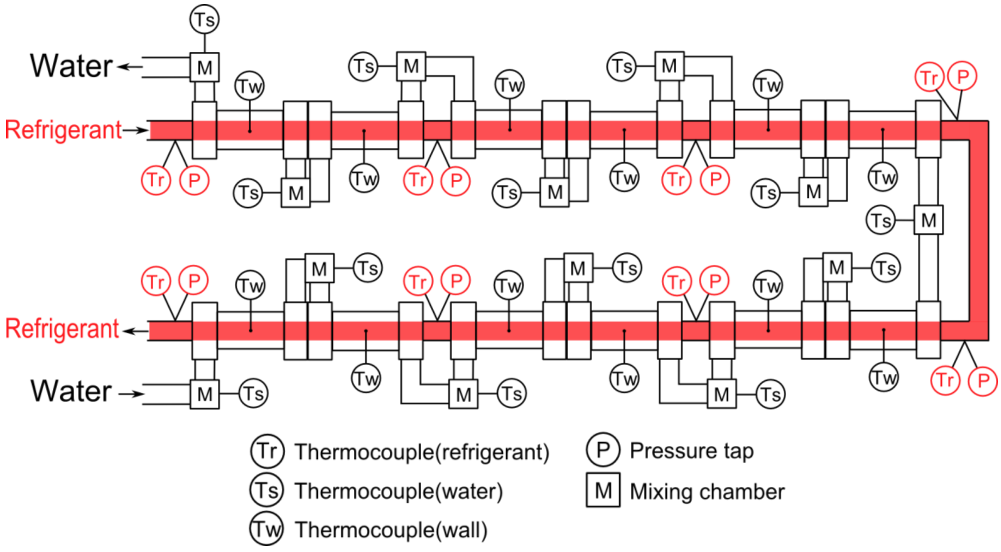

Fig. 1. Test section

3. Proposed correlation

By the using the experimental data of all the refrigerants considered in the present analysis, a correlation of two-phase frictional multiplier has been developed by considering the effect of mass flux, surface tension and tube diameter.

3.1. Developing equation

According to the separated flow model the overall pressure drop expression for Δz length inside a smooth horizontal tube can be obtained as Eq. (1).

$$\Delta p_{\text{total}} = \Delta p_{\text{static}} + \Delta p_{\text{mom}} + \Delta p_{\text{fric}} \tag{1}$$

For a horizontal tube, there is no change in static head so $\Delta p_{\text{static}} = 0$. The momentum pressure drop reflects the change in kinetic energy of the flow and is for the present case given by:

$$\Delta p_{\mathrm{mom}} = G^2\{[\frac{(1-x)^2}{\rho_l(1-\varepsilon)} + \frac{x^2}{\rho_v\varepsilon}]_o - [\frac{(1-x)^2}{\rho_l(1-\varepsilon)} + \frac{x^2}{\rho_v\varepsilon}]_i\} \quad (2)$$

where *G* is the total mass velocity of liquid plus vapour and *x* is the vapour quality. In the present study, the void fraction ε is obtained from the Smith [15] separated flow model as:

$$\varepsilon = \left\{1 + \left(\frac{1-x}{x}\right)\left(\frac{\rho_v}{\rho_l}\right)\left[0.4 + 0.6\sqrt{\frac{\frac{\rho_l}{\rho_v} + 0.4\frac{1-x}{x}}{1 + 0.4\frac{1-x}{x}}}\right]\right\}^{-1} \quad (3)$$

Using the experimental values for the inlet and outlet vapour quality, the momentum pressure drop is calculable. Hence, the experimental two-phase frictional pressure drop is obtainable from Eq. (1) by subtracting the calculated momentum pressure drop from the measured total two-phase pressure drop. Then from the experimental frictional pressure drop, the experimental two-phase frictional multiplier Φ_V is obtained from the following equation as:

$$\left(\frac{dp_{\mathrm{f}}}{dz}\right) = \Phi_{\mathrm{v}}^2\left(\frac{dp_{\mathrm{v}}}{dz}\right) \quad (4)$$

where (dp_{f} / dz) is the frictional pressure gradient for the two-phase flow; (dp_{v} / dz) is the single-phase frictional pressure gradient when only vapour flows through the test tube.

The value of (dp_{v} / dz) is estimated by

$$\left(\frac{dp_{\mathrm{v}}}{\mathrm{dz}}\right) = \frac{2 f_v G^2 x^2}{\mathrm{d_i}\rho_v} \quad (5)$$

where the friction factor f_v is calculated by Colburn's Eq. for single-phase flow in a smooth tube.

$$f_v = \frac{0.046}{\mathrm{Re}_v^{0.2}} \quad (6)$$

By using generalized Φ_V equation given by Lockhart and Martinelli [16]

$$\Phi_{\mathrm{v}}^2 = 1 + CX_{tt}^n + X_{tt}^2 \quad (7)$$

where, *C* and *n* have to be found from the experimental results of two-phase frictional multiplier.

From the experimental values of Φ_v the value of *C* and *n* for the Eq. (7) has been determined by plotting $(\Phi_v^2 - 1 - X_{tt}^2)$ versus X_{tt} graph for different refrigerants at different mass fluxes and then by using curve fitting method.

Fig. 2 shows some examples of finding *C* and *n* for different refrigerants at different mass fluxes. The obtained values of '*C*' for different tubes at different mass fluxes are correlated in terms of Bond number (*Bo*) and Froude number (*Fr*) by assuming

$$C = 21 f(Bo) f(Fr) \quad (8)$$

where,

$Fr = G / \sqrt{\rho_v(\rho_l - \rho_v) g d_i}$, $Bo = (g d_i^2(\rho_l - \rho_v)) / \sigma$ and $f(Bo)$ has been consider as the Eq. (9), which is similar to the analysis of Miyara et al. [8].

$$f(Bo) = \{1 - \exp(-0.28 Bo^{0.5})\} \quad (9)$$

Now plotting the graph of $C / 21 / f(Bo)$ versus *Fr* for all tubes at different mass fluxes and by using curve fitting method as shown in the Fig. 3 expression of $f(Fr)$ in the C has been found as

$$f(Fr) = \{2 - 1.9\exp(-0.016Fr^{1.4})\} \tag{10}$$

So the final form of the C expression in the Eq. (8) becomes as

$$C = 21\{1 - \exp(-0.28Bo^{0.5})\}\{2 - 1.9\exp(-0.016Fr^{1.4})\} \tag{11}$$

The 'n' in the Eq. (7) has been found as Eq. (12) by plotting the graph n versus Fr and using the curve fitting method as shown in the Fig. 4.

$$n = \{2 - 1.5\exp(-0.025Fr)\} \tag{12}$$

The above mentioned expressions of C and n have been developed from the experimental results of pressure drops of following Froude number (Fr) and Bond number (Bo) range:

$$2.0 \le Fr \le 25.3 \text{ and } 1.62 \le Bo \le 54.0 \tag{11}$$

Hence the proposed correlation of two-phase frictional multiplier for refrigerants R1234ze(E), R32, R410A and DME inside smooth horizontal tube becomes the Eq. (7) where the value of C and n can be obtained by the Eq. (11) and Eq. (12), respectively.

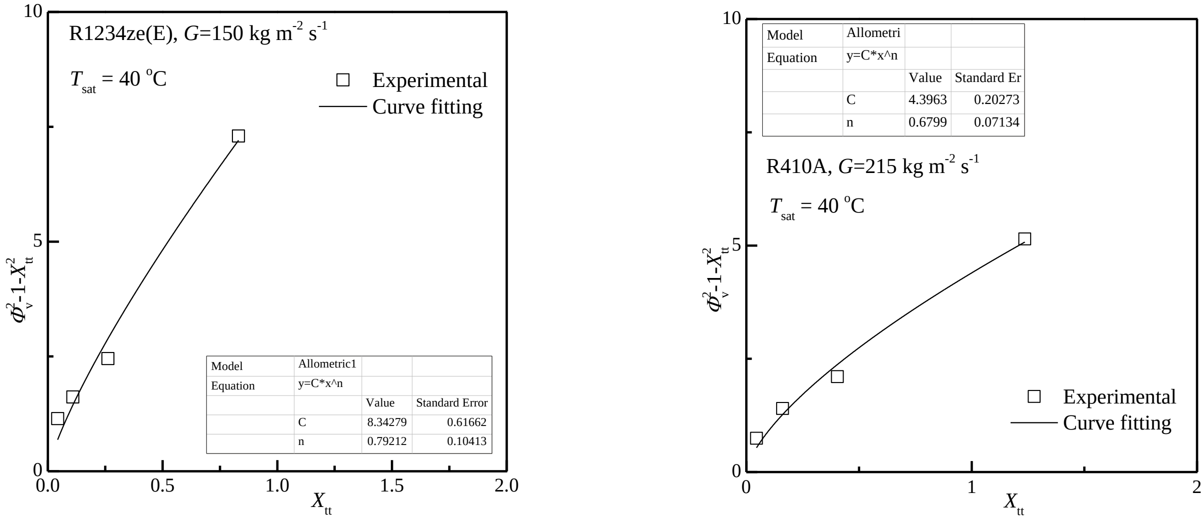

(a) R1234ze(E), G= 150 kg m^{-2} s^{-1}

(b) R410A, G= 215 kg m^{-2} s^{-1}

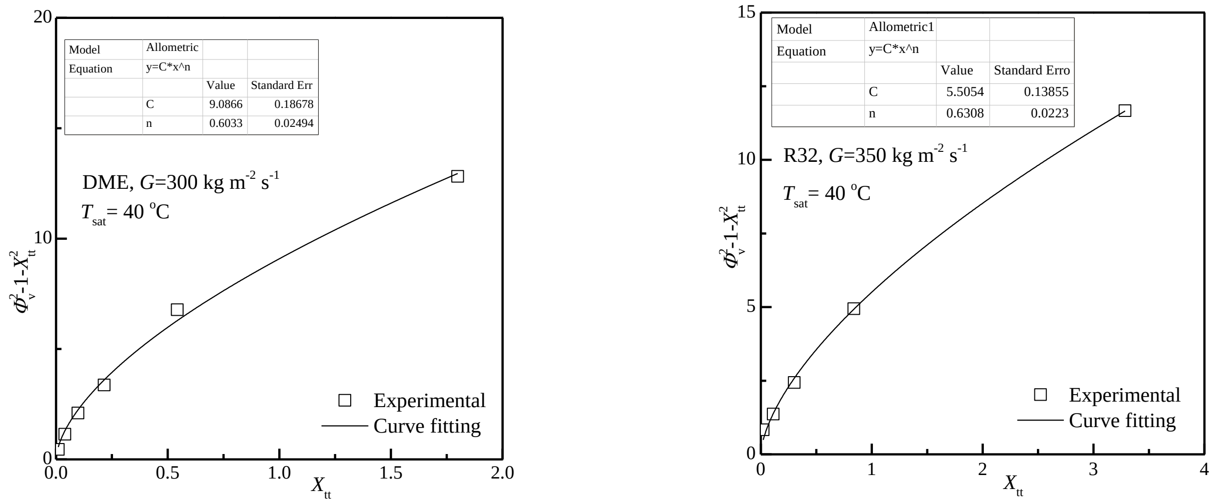

(c) DME, G= 300 kg m^{-2} s^{-1}

(d) R32, G= 350 kg m^{-2} s^{-1}

Fig. 2. Finding of 'C' and 'n' by curve fitting

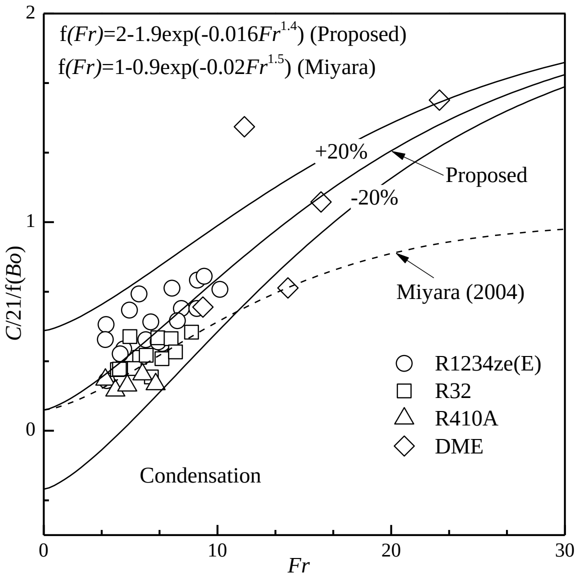

Fig. 3. Finding of the expression of $f(Fr)$ in the Eq. (8) for all the refrigerants at different mass fluxes

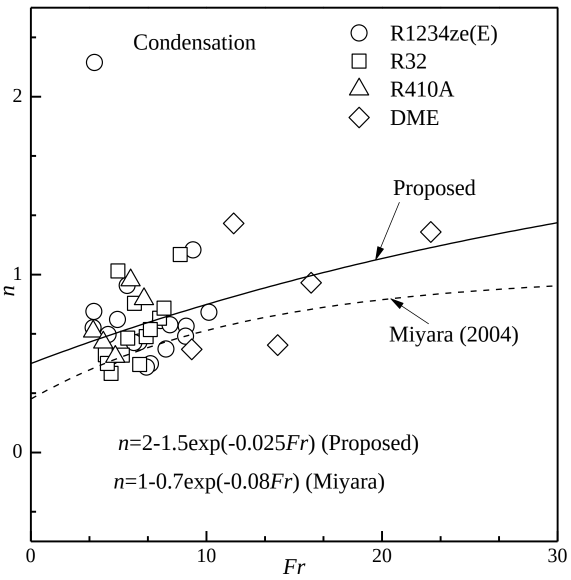

Fig. 4. Finding of the expression of 'n' in the Eq. (7) for all the refrigerants

3.2. Comparison with experimental data

Fig. 5 shows the comparative variation of proposed and Miyara's Φ_V correlations with the experimental results varying with Martinelli parameter (X_{tt}) for condensation of R1234ze(E), R32, R410A, DME and R1234ze(E)/R32 (55/45 mass%), respectively, at mass flux about 250 kg m^{-2} s^{-1}. It is seen that modification of Miyara's Φ_V improved the prediction for all the refrigerants such as R1234ze(E), R32, R410A, DME and R1234ze(E)/R32 mixtures.

Total 257 data of all the refrigerants such as R1234ze(E), R32, R410A, DME and R1234ze(E)/R32 mixtures (55/45 and 70/30 mass%) during condensation inside smooth horizontal tube are analyzed in the present paper. All the predicted data by proposed Φ_V correlation are plotted in Fig. 6 against the all experimental results for all refrigerants within ±30% error band. It is seen that 96% and 98% data are predicted by the proposed Φ_V correlation within ±20% and ±30%, respectively and the mean deviation of the prediction for all the present experimental data is found as 9.50% which is better than any other correlation used in the present analysis.

All the results of deviations of proposed and other various Φ_V correlations against the present experimental condensation data for all the refrigerants are listed in Table 1. It is seen from this table that among all the Φ_V correlations [7-11] the Miyara's Φ_V and proposed Φ_V correlations predicted the condensation experimental data with the minimum mean deviations. The proposed Φ_V correlation gives best results for the new refrigerant R1234ze(E) and even for the mixtures of R1234ze(E) and R32 which will be used as next generation refrigerants.

Table 1 Deviations of various Φ_V correlations against the present condensation data

Refrigerant	Proposed		Haraguchi's Φ_V (1994)		Miyara's Φ_V (2004)		Goto's ΦV (2001)		Jige and Koyama's ΦV (2012)		M-S and Heck's ΦV (1986)	
	AD[a]	MD[b]	AD[a]	MD[b]	AD[a]	MD[b]	AD[a]	MD[b]	AD[a]	MD[b]	AD[a]	MD[b]
R1234ze(E)	-7.31	9.16	3.10	10.57	-10.32	10.32	-22.67	22.75	-8.82	12.24	-10.25	10.71
R32	3.27	8.04	10.64	14.70	-0.74	5.23	-12.59	13.99	-10.29	12.67	-5.23	6.93
R410A	13.60	13.77	12.93	17.85	8.67	9.94	-1.48	10.38	1.72	11.56	2.67	6.65
DME	-6.24	10.47	40.88	42.65	-11.45	12.05	-29.13	29.13	-21.12	21.72	-14.03	14.99
ze/R32	0.47	6.12	3.98	12.62	-3.86	5.56	-16.40	16.48	-18.58	18.85	-6.98	8.15
Total	0.76	9.51	14.31	19.68	-3.54	8.62	-16.45	18.55	-11.42	15.41	-6.76	9.49

[a] Average deviation = $(1/n)\Sigma_1^n\left[\left(\Phi_{V,\mathrm{Pred}}-\Phi_{V,Exp}\right)/\Phi_{V,Exp}\right]\times 100$ [b] Mean deviation = $(1/n)\sum_1^n ABS\left[\left(\Phi_{V,\mathrm{Pred}}-\Phi_{V,Exp}\right)/\Phi_{V,Exp}\right]\times 100$

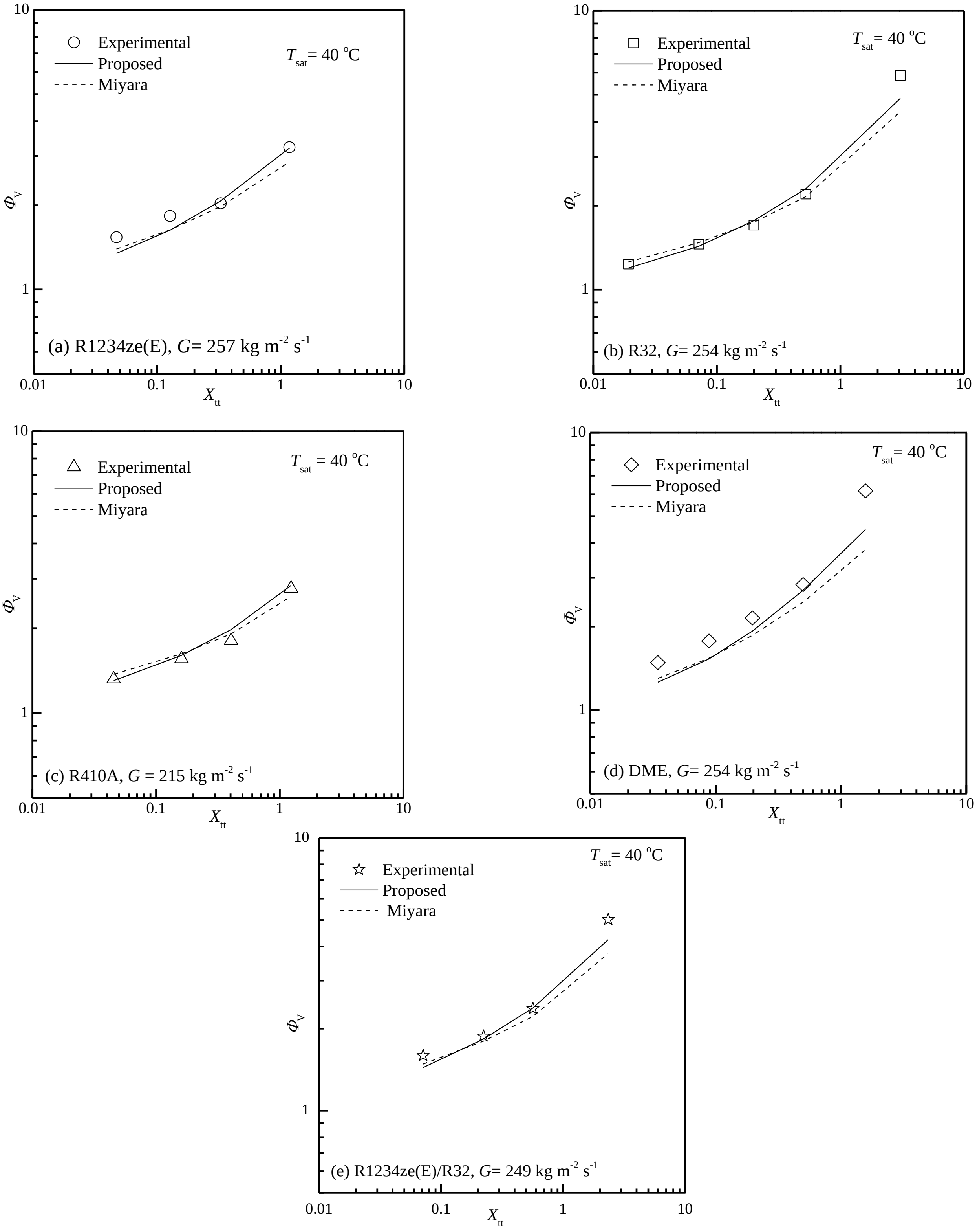

Fig.5. Comparison of proposed and Miyara's Φ_v correlation with experimental results of different refrigerants

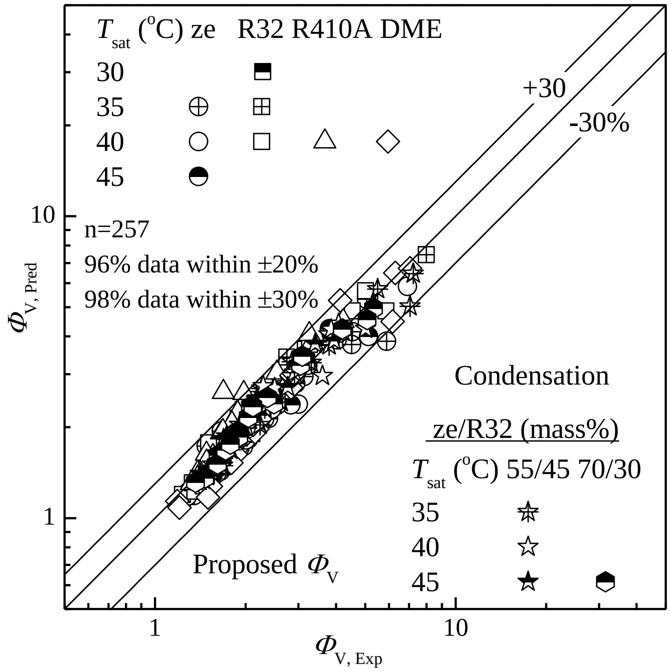

Fig. 6. Prediction versus experimental results by proposed Φ_V correlation for all refrigerants data

4. Conclusions

For the prediction of condensation pressure drop of R1234ze(E), R32, R410A, dimethyl ether (DME) and R1234ze(E)/R32mixtures (30/70 and 45/55 weight %) inside a horizontal smooth tube an empirical two-phase frictional multiplier correlation has been proposed considering the effects of refrigerant mass velocity, tube diameter and property. The predictions of previous existing correlation and newly proposed correlation of condensation pressure drop inside smooth horizontal tube have been compared with available experimental data of R1234ze(E), R32, R410A, dimethyl ether (DME) and R1234ze(E)/R32mixtures (30/70 and 45/55 weight %). From the results of comparison, proposed correlation shows better performance for all the refrigerants considered in this paper.

Proposed correlations can predict 96% and 98% experimental data within ±20% and ±30%, respectively for all the pure and mixture refrigerants.

The proposed two-phase frictional multiplier correlation can be used for the prediction of condensation pressure drop of newly developed low GWP refrigerant R1234ze(E) and mixtures of R1234ze(E)/R32.

References

[1] S. Koyama, N. Takata and S. Fukuda, Drop-in Experiments on Heat Pump Cycle Using HFO-1234ze(E) and Its Mixtures with HFC-32, Int. Refr. A/C Conf. at Purdue, July 12-15 (2010).

[2] S. Koyama, N. Takata, S. Fukuda, An experimental study on heat pump cycle using zeotropic binary refrigerant of HFO-1234ze(E) and HFC-32, 10th IEA Heat Pump Conference, Japan (2011).

[3] M.A. Hossain, Y. Onaka, A. Miyara, Experimental study on condensation heat transfer and pressure drop in horizontal smooth tube for R1234ze(E), R32 and R410A, Int. J. Refrigeration 35 (2012) 927-938.

[4] M.A. Hossain, Y. Onaka, H.M.M. Afroz, A. Miyara, Heat transfer during evaporation of R1234ze(E), R32, R410A and a mixture of R1234ze(E) and R32 inside a horizontal smooth tube, Int. J. Refrigeration, 36 (2013) 465-477.

[5] G. A. Longo, C. Zilio, G. Righetti, J. S. Brown, Condensation of the low GWP refrigerant HFO1234ze(E) inside a Brazed Plate Heat Exchanger, Int. J. Refrigeration, 38 (2014) 250-259.

[6] S. Fukuda, C. Kondoua, N. Takata, S. Koyama, Low GWP refrigerants R1234ze(E) and R1234ze(Z) for high temperature heat pumps, Int. J. Refrigeration, 40 (2014) 161-173.
[7] H. Haraguchi, S. Koyama, T. Fujii, Condensation of refrigerants HCFC 22, HFC 134a and HCFC 123 in a horizontal smooth tube [2nd report, proposal of empirical expressions for local heat transfer coefficient], Trans JSME, 60(574) (1994)245–52
[8] A. Miyara, K. Kuwahara, S. Koyama, Correlation of frictional pressure loss of two-phase flow including effects of tube diameter and mass velocity. In: Proceedings of JSME, 57th Kyushu Conference No. 048-1 (2004) 117–118 (in Japanese).
[9] H. Muller-Steinhagen, K. Heck, A simple friction pressure drop correlation for two-phase flow in pipes, Chem. Eng. Processing, Vol. 20 (1986) 297-308.
[10] L. Friedel, Improved friction pressure drop correlations for horizontal and vertical two-phase pipe flow, Eur. Two-phase Flow Group Meet., Paper E2, Ispra (1979).
[11] M. Goto, N. Inoue, N. Ishiwatari, Condensation and evaporation heat transfer of R410A inside internally grooved horizontal tubes. Int. J. Refrigeration 24 (2001) 628-638.
[12] D. Jige, S. Koyama, Condensation of pure refrigerants in horizontal mini-channels-proposal of frictional pressure drop correlation, JSRAE conference, Japan (2012).
[13] Y. Onakaa, A. Miyara, K. Tsubaki, Experimental study on evaporation heat transfer of CO_2/DME mixture refrigerant in a horizontal smooth tube, Int. J. Refrigeration, 33 (2010) 1277-1291.
[14] H.M.M. Afroz, A. Miyara, K. Tsubaki, Heat transfer coefficients and pressure drops during in-tube condensation of CO2/DME mixture refrigerant, Int. J. Refrigeration, 31 (2008) 1458-1466.
[15] S.L. Smith, Void fraction in two-phase flow: a correlation based upon an equal velocity heat model, Proc. Instn. of Mech. Engrs., London, 184 (1970) 647-664
[16] R.W. Lockhart, R.C. Martinelli, Proposed Correlation of Data for Isothermal Two-Phase, Two-Component Flow in Pipes. Chem. Eng. Prog. 45 (1949) 39-48.

Available online at www.sciencedirect.com

ScienceDirect

Procedia Engineering 00 (2015) 000–000

Procedia Engineering

www.elsevier.com/locate/procedia

6th BSME International Conference on Thermal Engineering (ICTE 2014)

Geometric effect on magnetohydrodynamic convection in a half-moon shaped cavity filled with water having semi-circular bottom heater

Khan. Md. Rabbi*, Towkir Ahmad, Satyajit Mojumder, Sourav Saha, Md. Zobayer Hossain

Department of Mechanical Engineering, Bangladesh University of Engineering & Technology, Dhaka-1000, Bangladesh

---

Abstract

Magneto-hydrodynamic convection has been gaining attention due to its wide range of application. In this paper magneto-hydrodynamic convection in a half-moon (semi-circular) shaped cavity has been analysed. The cavity has two semi-circular bottom heaters and effect of distance between this two heaters has been thoroughly investigated for two different cases (λ = 0.1, 0.4). Numerical simulation has been carried out for a wide range of Rayleigh number ($Ra = 10^3 \sim 10^7$) and for Hartmann number ($Ha = 0 \sim 100$) to understand the flow and thermal field. Galerkin weighted residual method of finite element analysis has been adopted for numerical solution along with code validation and grid independency test to ensure the numerical accuracy. It has been found that strengthening of magnetic field tries to reduce the heat transfer rate, whereas increment of heater distance augments the heat transfer rate. Results analysed on the basis of Nusselt number and average fluid temperatures are shown by related contours, plots and graphical analysis. Therefore, higher heat transfer rate has been achieved for λ = 0.4.

Peer-review under responsibility of organizing committee of the 6th BSME International Conference on Thermal Engineering (ICTE 2014).

Keywords: MHD convection; Bottom heater; Rayleigh Number; Hartmann Number; Magnetic Field.

---

1. Introduction

Magneto-hydrodynamic convection has turned out to be a matter of great importance due to its scientific, technological and industrial applications in petroleum industries, plasma physics, geophysics, MHD pump, MHD

---

* Corresponding author. Tel.: +8801672471959
E-mail address: khanrabbi92@gmail.com

Peer-review under responsibility of organizing committee of the 6th BSME International Conference on Thermal Engineering (ICTE 2014).

flow meter and cooling of nuclear reactors. To keep harmony with its wide range of applications, a considerable amount of research works have been done in this field. A comprehensive review of the early stage work on magneto-hydrodynamic convection can be found in [1-7]. Rudraiah et al. [8] investigated numerically the effect of magnetic field on natural convection in a rectangular enclosure. They found that the effect of the magnetic field reduced the rate of heat transfer. Oztop et al. [9] investigated numerical simulation of magneto-hydrodynamic buoyancy flow in an enclosure when the bottom wall was non-uniformly heated. Magneto-hydrodynamic natural convection in a vertical cylindrical cavity with sinusoidal upper wall temperature was investigated by Kakarantzas et al. [10]. The authors reported that the increment of Rayleigh number promoted heat transfer by convection. The increment of Hartmann number favoured heat conduction and the vertical magnetic field reduced the Nusselt number more than the horizontal. Oztop et al. [11] also studied MHD mixed convection in a lid-driven cavity with corner heater. Rahman et al. [12] investigated MHD natural convection in an enclosure from two semi-circular heaters on the bottom wall. It was reported that the distance between the semi-circular heaters was the most important parameter affecting the heat and fluid flow fields. It was also found that Hartmann number had an adverse effect on heat transfer. Al-Salem et al. [13] investigated the effects of moving lid direction on MHD convection in a linearly heated cavity with the bottom wall. Hossain et al. [14] analysed MHD free convection within trapezoidal cavity with non-uniformly heated bottom wall. The authors found out that the average and local Nusselt number at the non-uniform heating bottom wall of the cavity was dependent on the dimensionless parameters and also tilts angles. Sheikholeslami et al. [15] investigated MHD free convection in an eccentric semi-annulus filled with nanofluid. They reported that the heat transfer enhancement increased with increase of Hartmann number and decreased with augment of Rayleigh number. Islam et al. [16] studied mixed convection and entropy generation characteristics inside a porous cavity with viscous dissipation effect.

Half-moon shaped cavity is considered to understand the model and heat transfer increment of heat exchanger numerically. The objective of this research is to study the geometric effect on magneto-hydrodynamic convection in a Half-moon cavity filled with water having two semi-circular bottom heaters. The effect of distance between this two heater has been thoroughly investigated for two different cases (λ = 0.1, 0.4). Numerical simulation has been carried out for a wide range of Rayleigh number ($Ra = 10^3 \sim 10^7$) and for Hartmann number ($Ha = 0 \sim 100$) to understand the flow and thermal field.

Nomenclature

a	dimensional distance between semi-circular heaters(m)
A	area of the enclosure(m^2)
b	radius of the semi-circular cavity(m)
B_0	magnetic induction
c_p	specific heat at constant pressure (J/kg K)
D	dimensionless distance between semi-circular heaters
g	gravitational acceleration (m/s^2)
Ha	Hartmann number
H	semi-circular heater
k	fluid conductivity (W/m K)
L	length of the bottom wall(m)
Nu	average Nusselt number
p	dimensional pressure (N/m^2)
P	non-dimensional pressure
Pr	Prandtl number
Ra	Rayleigh number
r	dimensionless radius of semi-circular cavity
s	circumference(m)
T	temperature (K)
u, v	dimensional velocity components (m/s)
U,V	dimensionless velocity components
x, y	dimensional coordinates (-)
X,Y	dimensionless coordinates (-)
Greek symbols	
α	thermal diffusivity (m^2/s)
β	thermal expansion coefficient (1/K)
σ	electrical conductivity
μ	dynamic viscosity (Pa s)
ν	kinematic viscosity (m^2/s)
Θ	non-dimensional temperature
ρ	density (kg/m^3)
ψ	stream function
λ	dimensionless distance between semi-circular heaters
Subscripts	
av	average
h	hot
c	cold

2. Problem formulation

2.1. Physical modeling

The physical model under this investigation is shown in Fig. 1 with necessary boundary conditions. A semi-circular enclosure of diameter *L* having two semi-circles at the distance of *a* is considered for this investigation. The two dimensional co-ordinate system is defined and the effect of the gravity is shown on the negative y-axis. The upper portion of enclosure is kept at low temperature ($T = T_c$). The horizontal wall of the enclosure is insulated whereas the two semi-circles situated at the horizontal line are heated ($T = T_h$). The whole environment is permeated with magnetic flux density B_0. The density variation is considered according to the Boussinesq approximation [17]. Radiation mode of heat transfer and viscous dissipation are considered to be negligible. All solid boundaries are assumed to be rigid no-slip walls.

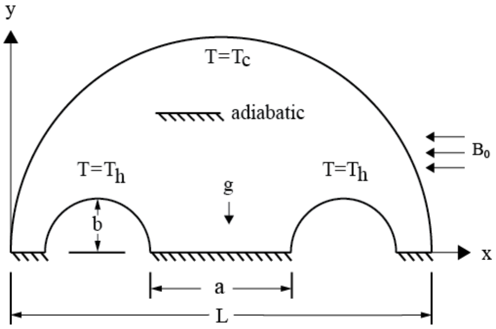

Fig. 1. Schematic diagram of the Half-moon cavity with semi-circular bottom heater

3. Mathematical formulation

The flow in this system is considered to be two-dimensional, steady, incompressible and laminar. The governing equations which define the system behaviour are conservation of mass, energy and momentum. Under these considerations non-dimensional variables can be written as-

$$X = \frac{x}{L}; Y = \frac{y}{L}; U = \frac{u}{U_0}; V = \frac{v}{U_0}; P = \frac{p}{\rho U_0^2}; \Theta = \frac{T - T_c}{T_h - T_c} \tag{1}$$

Based on these non-dimensional variables, two dimensional governing equations can be written as follows:
The continuity equation-

$$\frac{\partial U}{\partial X} + \frac{\partial V}{\partial Y} = 0 \tag{2}$$

The momentum equations-

$$U\frac{\partial U}{\partial X} + V\frac{\partial U}{\partial Y} = -\frac{\partial P}{\partial X} + Pr\left(\frac{\partial^2 U}{\partial X^2} + \frac{\partial^2 U}{\partial Y^2}\right) \tag{3}$$

$$U\frac{\partial V}{\partial X} + V\frac{\partial V}{\partial Y} = -\frac{\partial P}{\partial X} + Pr\left(\frac{\partial^2 V}{\partial X^2} + \frac{\partial^2 V}{\partial Y^2}\right) + Ra\,Pr\,\Theta - Ha^2 Pr\,V \tag{4}$$

The energy equation-

$$U\frac{\partial \Theta}{\partial X} + V\frac{\partial \Theta}{\partial Y} = \left(\frac{\partial^2 \Theta}{\partial X^2} + \frac{\partial^2 \Theta}{\partial Y^2}\right) \tag{5}$$

The dimensionless parameters which have been appeared in the above governing equations are-

$$Pr = \frac{v}{\alpha}; Ha = \sqrt{\frac{\sigma {B_0}^2 L^2}{\mu}}; Ra = \frac{g\beta(T_h - T_c)L^3}{\alpha v} \tag{6}$$

Here, *Pr*, *Ha* and *Ra* refer to Prandtl, Hartmann and Rayleigh number respectively. The non-dimensional form of the boundary conditions are mentioned in Table 1.

Table 1. Boundary conditions in non-dimensional form.

Boundary Wall	Flow Field	Thermal Field
Semi-circular upper wall	$U = 0, V = 0$	$\Theta = 0$
Semi-circular bottom wall	$U = 0, V = 0$	$\Theta = 1$
Horizontal bottom Wall	$U = 0, V = 0$	$\partial\Theta / \partial Y = 0$

The average Nusselt number at the heated semi-circular cavity can be expressed by

$$Nu = \frac{1}{s}\int_{0}^{s} \overline{Nu} ds \tag{7}$$

Circumference of the Half-moon cavity can be described as

$$s = \pi r \tag{8}$$

Local Nusselt number can be expressed as

$$\overline{Nu} = \frac{hL}{k} = -\frac{\partial\Theta}{\partial n} L \tag{9}$$

$$\frac{\partial\Theta}{\partial n} = \frac{1}{L}\sqrt{\left(\frac{\partial\Theta}{\partial X}\right)^2 + \left(\frac{\partial\Theta}{\partial Y}\right)^2} \tag{10}$$

The average temperature of the fluid can be expressed by,

$$\Theta_{av} = \frac{1}{A}\int \Theta dA \tag{11}$$

Whereas non-dimensional area can be expressed as

$$A = \frac{\pi}{8} - \frac{\pi(b / L)^2}{4} \tag{12}$$

The non-dimensional stream function can be expressed by,

$$U = \frac{\partial\psi}{\partial Y}, V = -\frac{\partial\psi}{\partial X} \tag{13}$$

Here, the fluid motion is displayed by stream function ψ acquired from velocity components *U* and *V*.

4. Numerical procedure

4.1. Grid independency test

A grid independency test has been executed to examine the numerical solution of the study. Table 1 has been formed showing outcomes of the grid independency test. The test is performed for *Ha* = 50 and *Ra* = 10^5. From Table 1, it is apparent that for number of elements 429 the average Nusselt number is the lowest and with the improvement of mesh size by increasing number of elements, average Nusselt number increases gradually. But for number of elements 3896 average Nusselt number becomes nearly constant. Additional increment in number of elements does not initiate any significant deviation of average Nusselt number. Therefore, a number of 3896 elements is selected as the ideal mesh size for all conditions of the numerical simulations for this present study.

Table 2. Grid independency test for *Ha* = 50 and *Ra* = 10^5

No of Elements	429	558	930	1716	2904	3896	6864
Nu	8.313	8.316	8.299	8.323	8.322	8.326	8.328

4.2. Code validation

The code of this present study is validated with the previous study of Ghashemi et al. [18].Validation is accomplished through average Nusselt number plots against solid volume fraction of nanofluid. Comparison of average Nusselt number for different solid volume fraction for *Ha*=0 and *Ha*=30 at *Ra*=10^5 is shown in Fig. 2. It is also noticeable from the illustration that the code of the present study is definitive enough to perform numerical simulation for the given cases.

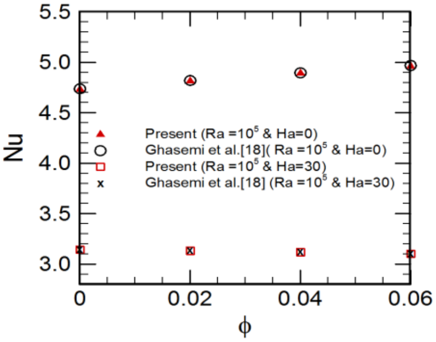

Fig. 2. Comparison of average Nusselt number for different solid volume fraction for *Ha*=0 and *Ha*=30 at *Ra*=10^5 with Ghasemi et al. [18]

5. **Results and Discussion**

A computational analysis has been done to inspect the effect of magnetic field on natural convection with semi-circular bottom heater in an enclosure using finite element method. The considered parameters are Hartmann number, Rayleigh number and distance between heaters. Results are presented by means of streamlines, isotherms, average Nusselt number and average temperature of flow field.

5.1. Effect of Hartmann number on streamlines and isotherm contours

Consequences of magnetic field on streamlines and isotherm contours are illustrated in Fig. 3 with different Hartmann number for λ = 0.1 and λ = 0.4. From the figure it is seen that the strength of the streamline contour is decreased with the increment of Hartmann number for both the values of λ. For *Ha* = 10 the streamlines fully inhabit in the enclosure. As the Hartmann number goes up, streamlines start to move to the corner of the enclosure and the strength of flow field decreases. For all the cases, the flow field and temperature distribution are symmetric. Strength of flow field for λ = 0.4 is almost one-third of that for λ = 0.1. Isotherm contours indicate conduction mode of heat transfer becoming more dominant as the isotherms become more parallel with the increment of Hartmann number which results in lower heat transfer rate.

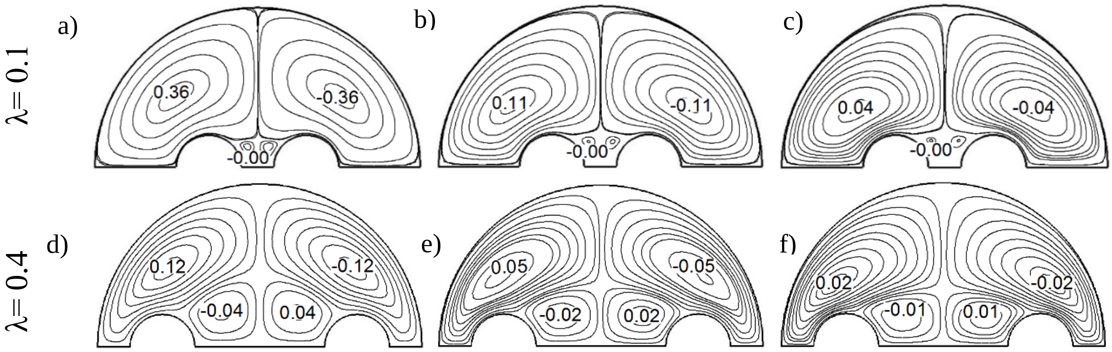

Fig. 3. Comparison of streamline contours for (a), (d) *Ha* = 10; (b), (e) *Ha* = 50; (c), (f) *Ha* = 100. Figures in the upper row represent streamlines for λ = 0.1 and lower row represents the same for λ = 0.4.

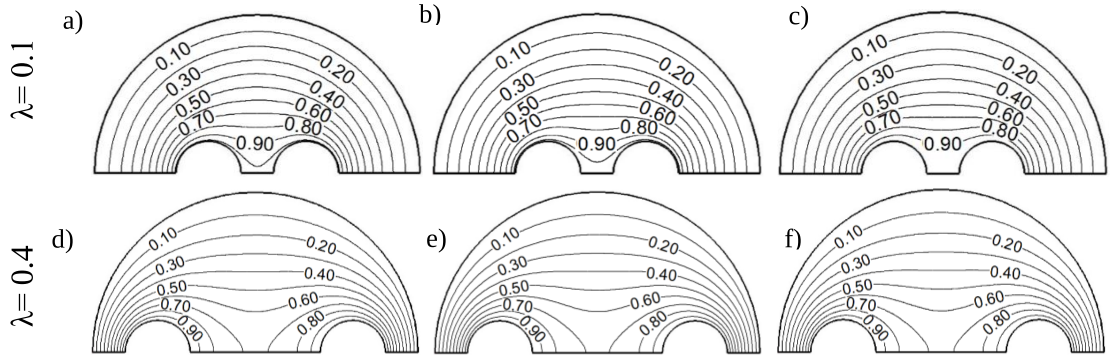

Fig. 4. Comparison of isotherm contours for (a), (d) *Ha* =10; (b), (e) *Ha* = 50; (c), (f) *Ha* = 100. Figures in the upper row represent isotherms for λ = 0.1 and lower row represents the same for λ = 0.4.

5.2. *Effect of Rayleigh number on streamline and isotherm contours*

Effects of Rayleigh number on streamlines and isotherm contours are illustrated respectively in Fig. 5 and 6 for λ = 0.1 and λ = 0.4. From the figure it is obvious that the strength of the streamline contour varies proportionally with the increment of Rayleigh number. As the value of Rayleigh number is increased, streamlines start to move to the corner. From Fig. 7 (a) slight distortion is found along with parallel lines at $Ra = 10^5$ which indicates heat transfer takes place in both conduction and convection mode of heat transfer. With the increment of Rayleigh number increased amount of distortions are found, which resembles the dominance of convection mode of heat transfer.

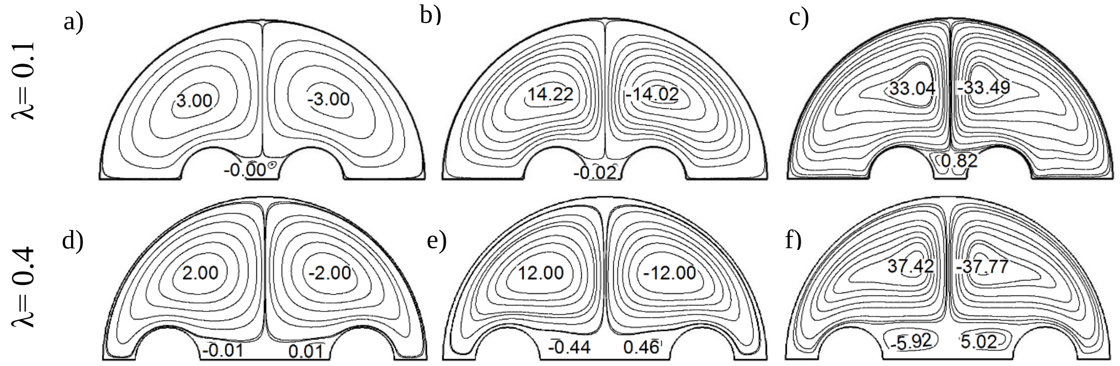

Fig. 5. Comparison of streamline contours for (a), (d) $Ra = 10^5$; (b), (e) $Ra = 10^6$; (c), (f) $Ra = 10^7$. Figures in the upper row represent streamlines for λ = 0.1 and lower row represents the same for λ = 0.4.

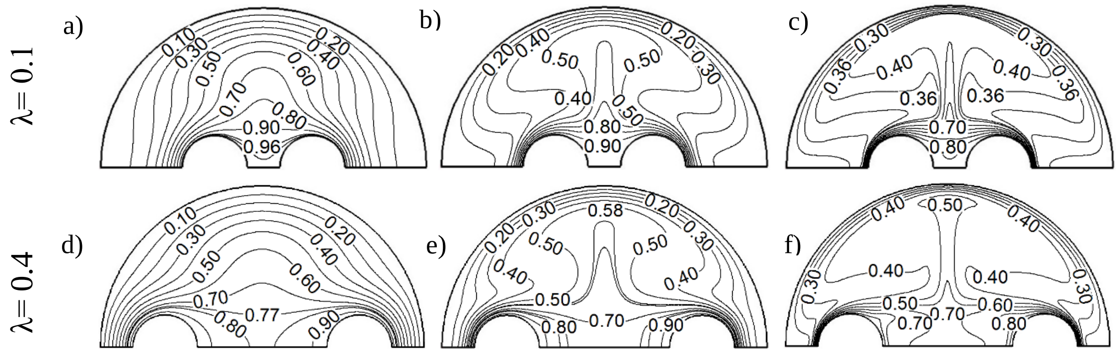

Fig. 6. Comparison of isotherm contours for (a), (d) $Ra = 10^5$; (b), (e) $Ra = 10^6$; (c), (f) $Ra = 10^7$. Figures in the upper row represent isotherms for λ = 0.1 and lower row represents the same for λ = 0.4.

5.3. Effect of Rayleigh number on Nusselt number and average temperature of flow field

The effects of Rayleigh number on average Nusselt number (*Nu*) of the heated bottom wall are illustrated in Fig. 7(a) for λ = 0.1 and λ= 0.4. From the figure it can be seen that the Nusselt number increases with the increment of Rayleigh number. Comparing two different curves for λ = 0.1 and λ = 0.4, it can be observed that the curve for λ = 0.1 shows more upturn than the curve for λ = 0.4. Again the effect of Rayleigh number on average temperature of fluid inside the cavity is also illustrated in Fig. 7(b) for the same conditions. Initially the average temperature starts to rise slightly with increment of Rayleigh number up to 10^5. With the increasing Rayleigh number up to 10^7, the temperature curve for λ = 0.1 drops rapidly, while the other curve for λ = 0.4 drops slightly. For $10^3 < Ra < 7 \times 10^3$ there is no significant change in average Nusselt number and average temperature. At $Ra = 10^6$ there is no evidence of geometric effect on average Nusselt number.

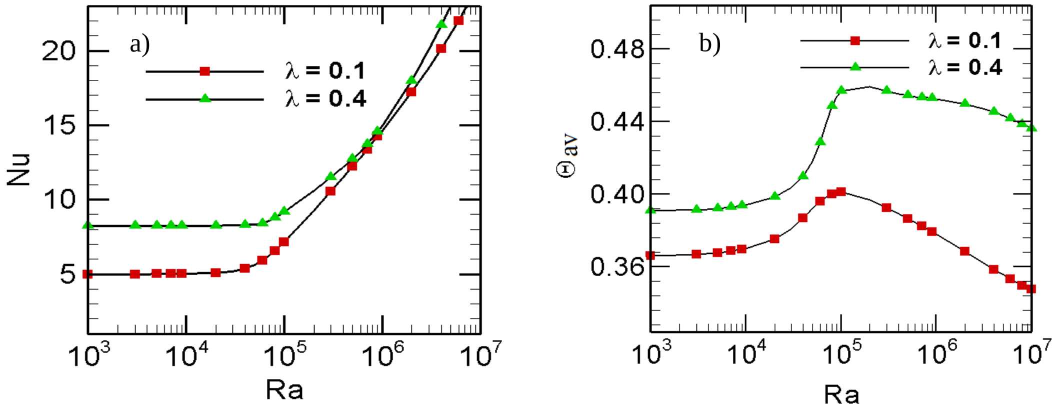

Fig. 7. Variation of (a) average Nusselt number of the heated bottom wall and (b) average temperature of fluid inside the cavity with *Ra*. The red symbols indicate results for λ = 0.1 and green symbols for λ = 0.4.

5.4. Effect of Hartmann number on Nusselt number and average temperature of flow field

The effects of Hartmann number (*Ha*) on average Nusselt number (*Nu*) and average temperature (Θ_{av}) of the heated bottom wall are displayed in Table 2 for two different distances between semi-circular heaters (λ = 0.1 and λ = 0.4). It is observed that the value of Nusselt number and average temperature decrease with the increment of Hartmann number. But in both parameters a higher decrement is found for λ = 0.1 than λ = 0.4 with the increasing Hartmann number. For λ = 0.4, Nusselt number is higher than that of λ = 0.1 and therefore convective dominance takes place ensuring higher heat transfer rate.

Table 3. Variation of average temperature with Nusselt number for λ = 0.1 and λ = 0.4.

Ha	λ = 0.1		λ = 0.4	
	Θ_{av}	*Nu*	Θ_{av}	*Nu*
0	0.373	5.046	0.396	8.240
10	0.372	5.036	0.395	8.239
20	0.371	5.019	0.394	8.2384
30	0.369	5.009	0.393	8.2382
40	0.368	5.003	0.392	8.2377
50	0.367	5.000	0.391	8.2374
60	0.367	4.999	0.3918	8.2372
70	0.366	4.998	0.3916	8.2371
80	0.3664	4.9974	0.3914	8.2370
90	0.3662	4.9972	0.3912	8.2369
100	0.3661	4.9971	0.3910	8.2368

6. Conclusion

The problem considered in this study is to investigate the geometric effect on magneto-hydrodynamic convection by showing flow fields and average temperatures relating to Hartmann numbers, Rayleigh numbers and distance between two semi-circular bottom heaters. The numerical results are discussed and following points have emerged:

- Strength of flow field decreases with the increment of *Ha* and increases with the increment of *Ra*. For any Ha, strength of the streamline contour is maximum at $\lambda = 0.1$ and minimum at $\lambda = 0.4$.
- For any *Ra*, strength of streamline contours is maximum at $\lambda = 0.4$ and minimum at $\lambda = 0.1$. Conduction mode of heat transfer becomes more dominant with increasing of *Ha* and decreasing of *Ra*.
- Again Convection heat transfer rate is greater at $\lambda = 0.1$ than that at $\lambda = 0.4$. Effect of *Ra* on Nusselt number is not evident for any λ up to $Ra = 7\text{x}10^3$. Nusselt number is independent of different geometric conditions at $Ra = 10^6$.
- For $Ra = 10^5$ and geometry of $\lambda = 0.4$, highest average temperature is studied which results in higher heat transfer rate. Increment in magnetic induction decreases average temperature and Nusselt number and thus higher convective environment is evident for $\lambda = 0.4$.

Acknowledgement

Authors would like to thank Multiscale Mechanical Modeling and Research Network (MMMRN) for supporting this study and acknowledge the insightful suggestions for the improvement of this article.

References

[1] V.M. Soundalgekar, Free convection effects on steady MHD flow past a vertical porous plate, *J. Fluid Mech.*, 66 (1974) 541-551.
[2] M.I. Antimirov, E.B. Tabachnik, Unsteady MHD convection in a vertical channel, *MagGi.*, (1976) 27-34.
[3] A. Raptis, MHD natural convection and mass transfer through a horizontal porous channel, *Acta Phys. Hung.*, 54(1-2) (1983) 213-215.
[4] B.K. Jha, R. Prasad, MHD free-convection and mass transfer flow through a porous medium with heat source, *Astrophys. Space Sci.*, 181 (1991) 117-123.
[5] M.A. Hossain, Viscous and Joule heating effects on MHD-free convection flow with variable plate temperature, *Int. J. Heat Mass Tran.*, 35(12) (1992) 3485-3487.
[6] T.K. Aldoss, Y.D. Ali, M.A. Al-Nim, MHD mixed convection from a horizontal circular cylinder, *Numer. Heat Transfer*, 30(4) (1996) 379-396.
[7] T. Alboussière, J.P. Garandet, R. Moreau, Asymptotic analysis and symmetry in MHD convection, *Phys. Fluids*, 8 (1996) 2215.
[8] N. Rudraiah, R.M. Barron, M. Venkatachalappa, C.K. Subbaraya, Effect of magnetic field on free convection in a rectangular enclosure, *Int. J. Eng. Sci.*, 33 (1995) 1075-84.
[9] H.F. Oztop, M. Oztop, Y. Varol, Numerical simulation of magnetohydrodynamic buoyancy-induced flow in a non-isothermally heated square enclosure, *Commun. Nonlinear Sci. Numer. Simul*., 14 (2009) 770–778.
[10] S.C. Kakarantzas, I.E. Sarris, A.P. Grecos, N.S. Vlachos, Magnetohydrodynamic natural convection in a sinusoidal upper heated cylindrical cavity, *Int. J. Heat Mass Tran.*, 52 (2009) 250-259.
[11] H.F. Oztop, K. Al-Salem, I. Pop, MHD mixed convection in a lid driven cavity with a corner heater, *Int. J. Heat Mass Tran.*, 54(15) (2011) 3494-3504.
[12] H.F. Oztop, M.M. Rahman, A. Ahsan, M. Hasanuzzaman, R. Saidur, K. Al-Salem, N.A. Rahim, MHD natural convection in an enclosure from two semi-circular heaters on the bottom wall, *Int. J. Heat Mass Tran.*, 55(7-8) (2012) 1844-1854.
[13] K. Al-Salem, H.F. Oztop, I. Pop, Y. Varol, Effects of moving lid direction on MHD mixed convection in a linearly heated cavity, *Int. J. Heat Mass Tran.*, 55 (2012) 1103-1112.
[14] M.S. Hossain, M.A. Alim, MHD free convection within trapezoidal cavity with non-uniformly heated bottom wall, *Int. J. Heat Mass Tran.*, 69 (2014) 327–336.
[15] M. Sheikholeslami, M. Gorji-Bandpy, D.D. Ganji, MHD free convection in an eccentric semi-annulus filled with nanofluid, *J. Taiwan Inst. Chem. Eng*., 45(4) (2014) 1204-1216.
[16] A.A. Bhuiyan, R. Amin, S.F. Barna, M.H. Banna, A.K.M.S. Islam, Mixed convection and entropy generation characteristics inside a porous cavity with viscous dissipation effect, *ASME Int. Mech. Eng. Congr. & Expo.*, 9 (2009) 533-542.
[17] D.D. Gray, A. Giorgini, The validity of the Boussinesq approximation for liquids and gases, *Int. J. Heat Mass Tran.*, 19 (1976) 545-551.
[18] B. Ghasemi, S.M. Aminossadati, A. Raisi, Magnetic field effect on natural convection in a nanofluid-filled square enclosure, *Int. J. Therm. Sci.*, 50 (2011) 1748 -1756.

Available online at www.sciencedirect.com

ScienceDirect

Procedia Engineering 00 (2015) 000–000

Procedia Engineering

www.elsevier.com/locate/procedia

6th BSME International Conference on Thermal Engineering (ICTE 2014)

The Enhancement of Heat Transfer in a Circular Tube with Insert and without Insert by using the Finite Element Method

Sabbir Hossain[a], Ujjwal Kumar Deb[b], Kazi Afzalur Rahman[a]*

[a]*Mechanical Engineering Department, Chittagong University of Engineering and Technology*
[b]*Department of Mathematics, Chittagong University of Engineering and Technology*

Abstract

This paper presents a Finite Element based model of the heat transfer problem. The Enhancement of heat transfer with mass in a tube has been investigated without insert and with insert i.e. combination of horizontally and vertically arranged rectangular boxes of 5 mm thickness are being fitted perpendicular to the flow direction respectively at equal distance from each other along the length. The combinations are composed of without insert, two inserts, four inserts, six inserts, eight inserts and ten inserts. The purpose of using inserts is to scatter the fluid particles in the laminar flow which increases the heat transfer. An 800 mm long pipe with 26 mm inner diameter and 5 mm thickness is considered in our simulation. The simulations have been completed for both stationary and time dependent conditions with Reynolds number 1600~2400. A constant heat flux is generated at the boundary layer of the tube close to the flowing fluid around the boundary layer. We also have shown the comparisons of heat transfer rate among different combinations of inserts to understand the heat transfer phenomenon for the computational domain.

Peer-review under responsibility of organizing committee of the 6th BSME International Conference on Thermal Engineering (ICTE 2014).

Keywords: *CFD Analysis, Mass transfer, FEM Analysis, Boundary heat flux, Boundary element*

---

* Corresponding author. Tel.:+8801680-453267;
*E-mail address:*afzalur99@yahoo.com

Peer-review under responsibility of organizing committee of the 6th BSME International Conference on Thermal Engineering (ICTE 2014).

1. Introduction

The Heat Transfer Enhancement Technology (HTET) has been developed and commonly applied to heat exchanger applications over last decennium, such as refrigeration, process industry, nuclear reactors, automotive and solar water heaters. The use of relatively complex geometries was initially limited by manufacturing process. However, at the present time new manufacturing methods allow manufacture of much complex surface geometry. Bergles [1] and Webb [2] have shown liberally reviews on techniques for heat transfer enhancement. An experimental investigation was carried out for measuring tube-side heat transfer coefficient, friction factor; heat transfer enhancement efficiency of water for turbulent flow in a circular tube fitted with the stainless steel rectangular [3] and the square-cut twisted tape insert [4].

There have been many techniques proposed over the years for enhancing the heat transfer with mass in tubes by using different types of inserts (i.e.) like combination of non-uniform wire coil and twisted tape inserts [5], counter/co-swirling flow in a tube fitted with twin twisted tapes [6], short-length twisted tape insert [7], regularly spaced twisted tape elements [8], delta-winglet twisted tape inserts [9] have been proposed over the years. Almost all heat exchangers used in the air-conditioning and automotive industries are complex geometries. In these techniques, the fluid flows either laminar or turbulent. As In turbulent flow, unsteady vortices appear on different scales and interact with each other while in laminar flow the fluid particles adhere to with each other and the collision among the particle is very poor. So, heat transfer in turbulent flow is greater than laminar flow though it is burdensome to compute accurately.

If we use such an object or obstacle e.g. insert using perpendicular to the flow direction, that makes the flow laminar to turbulent, the technique becomes reliable or economical, then engineer can executes his design. Usually many experiments related to heat transfer enhancement have done in heat transfer laboratory in mechanical engineering department. So, we can choose the better technique by the theoretical analysis. Though, theoretical result differs from experimental. We get the nearest values and results to experimental results. We also get clear concepts by this technique and able to choose better one.

Finite Element Analysis (FEA) [10] consists of a computer based model of a material or structure that is stressed and analyzed for specific results. It is used for new product design and existing product refinement. A company capable of verifying a proposed design will be able to perform to the client's specifications prior to manufacturing or construction. Modifying an existing product or structure is utilizing to qualify the product or structure for a new service condition. In case of structural failure, FEA may be used for helping to determine the design modifications to meet the desired condition.

In this study, we analyze the heat transfer enhancement in a circular tube with inserts and without insert for laminar flow. Firstly, a non-isothermal flow model is considered. Afterwards water is taken into account in the model and copper is considered as the material of the circular pipe. Using the governing equations of the non-isothermal flow together with continuity equation, the dynamic behavior of the flow can be described which transport heat, the temperature field is affected by the changes in the flow field. Hence, a non-isothermal flow is always a two-way coupling between fluid flow and heat transfer.

The rest of our paper is organized as follows. In section **2**, the mathematical model and the mesh design of the domain is presented. In section **3**, numerical results for this model are shown. Finally, some conclusions are presented in section **4**.

Nomenclature

ρ	Density (Kg/m^3)
T	Absolute temperature (K)
P	Pressure (Pa)
Cp	Specific heat capacity (J/Kg. K)
μ	Dynamic viscosity (Pa·s)
q	Heat flux (W/m^2)
v	Velocity vector (m/s)
τ	Viscous stress tensor (Pa)
S	Strain tensor (1/S)

2. Mathematical Model

The ultimate goal of this study is to improve understanding of the enhancement of heat transfer in a circular pipe using insert and without insert. Our model has been designed as the geometry creates eddies across the flow which enhances the heat transfer. The purpose of using inserts in our design is to decrease layer to layer friction and to scatter the fluid particles carrying heat from the boundary wall, such that the particles near the boundary layer transfer heat to the other particles in the fluid. For example, a design of computational domain with four inserts is shown in Fig.2.1.

2.1 Governing equations

In this study, we have developed a one dimensional model of heat transfer including conduction, convection and mass transfer. Therefore the heat transfer phenomenon is governed by the following equations [11]:

$$\frac{\partial \rho}{\partial t}+\nabla\cdot(\rho v)=0 \tag{1}$$

$$\rho u\cdot\nabla v+\rho\frac{\partial v}{\partial t}=-\nabla p+\nabla\cdot\left(\mu(\nabla v+\nabla v)^T-\frac{2}{3}\mu(\nabla\cdot v)I\right)+F \tag{2}$$

where, ρ is the density (kg/m^3), v is the velocity vector (m/s), p is the pressure (Pa), F is the body force vector (N/m^3), μ is the dynamic viscosity (Pa·s). It also solves the heat transfer through a fluid and governed by the following equation:

$$\rho C_p\left(\frac{\partial T}{\partial t}+(v\cdot\nabla)T\right)=\tau\cdot S-(\nabla\cdot q)-\frac{T}{\rho}\frac{\partial\rho}{\partial T}\Big|\,p\left(\frac{\partial\rho}{\partial t}+(v.\nabla)p\right)+Q \tag{3}$$

where C_p is the specific heat capacity at constant pressure (SI unit: J/(kg·K)), T is absolute temperature (SI unit: K), q is the heat flux by conduction (SI unit: W/m^2), τ is the viscous stress tensor (SI unit: Pa), S is the strain-rate tensor (SI unit: 1/s). The pressure work term:

$\frac{T}{\rho}\frac{\partial\rho}{\partial T}\Big|\,p\left(\frac{\partial\rho}{\partial t}+(v\cdot\nabla)p\right)$ and the viscous heating term $\tau\cdot s$ are not included by default as they are commonly negligible. The interface also describes the heat transfer in solids:

$$\rho C_p\frac{\partial T}{\partial t}=-(\nabla\cdot q)-T\frac{\partial E}{\partial t}+\mathrm{Q}$$

where, E is the elastic contribution to entropy [SI unit: J/(m^3·K)]. As in the case of fluids, the pressure work term is $T\frac{\partial E}{\partial t}$.

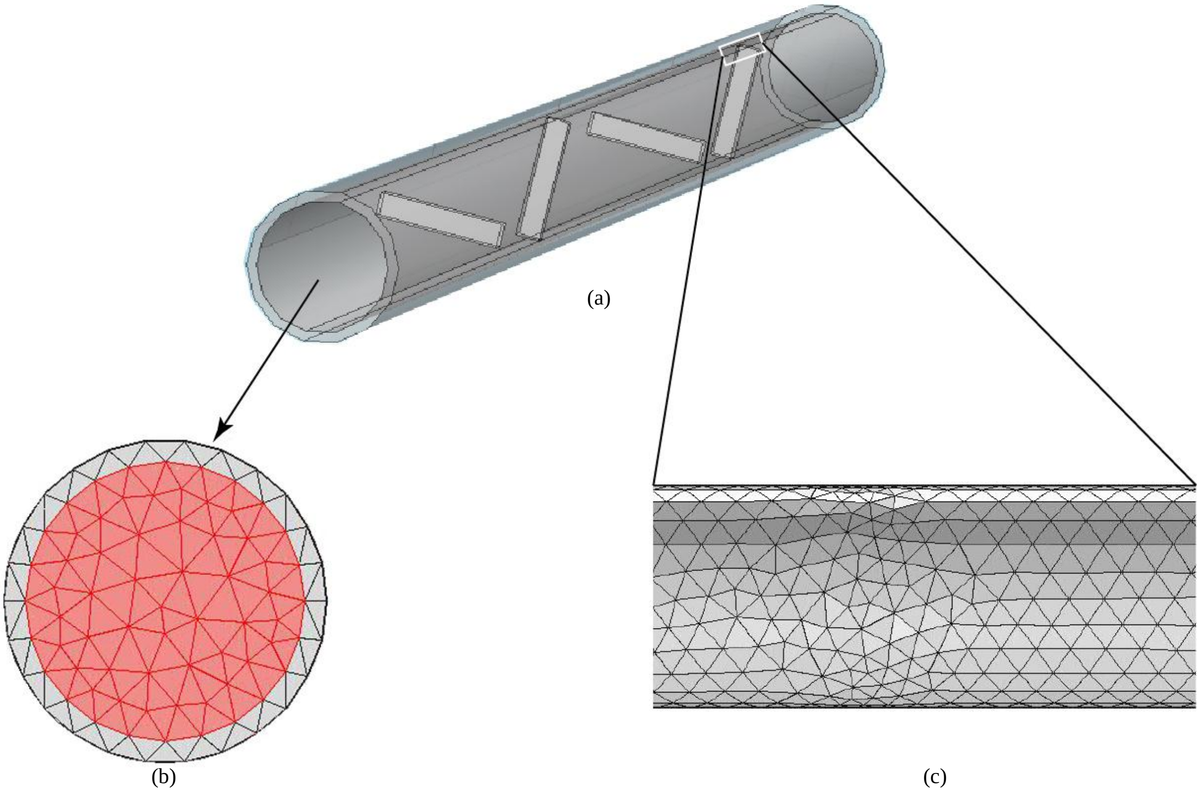
(a)
(b)
(c)

Fig.2.1: Computational domain with four inserts (a) computational domain, (b) mesh design for the inlet and (c) a part from wall of the tube.

2.2. Computational Model and Mesh Design:

In this study, at first we have designed a horizontal circular pipe without insert, two inserts, four inserts, six inserts, eight inserts and ten inserts are equally spaced from the leading edge. An example for four inserts, shown in Fig.2.1 (a). The tube has the total length of 800 mm, the inner and outer diameter of 26 mm and 30 mm respectively. Here, we set up the boundary conditions by selecting boundary layer. It is notable that, perfect meshing plays an important role in terms of accuracy of results. To achieve a satisfactory computational accuracy we continually change mesh design until the results obtained from two trial lead to very close to each other. As our domain length is short and computer processor capacity becomes an important factor for computing the study, we use coarse mesh Shown in Fig.2.1 (b, c) among the entire computational model for numerical simulation. Ash color shows mesh for tube and red color for water domain. Mesh element concentration becomes higher near the insert position have shown in Fig.2.1 (c). A comparison of mesh design among different insert combinations has shown below:

Table 2.1. Comparison of mesh design

Property name	No insert	Two inserts	Four inserts	Six inserts	Eight inserts	Ten inserts
Number of edge elements	374	454	534	606	690	758
Number of boundary elements	1908	2226	2546	2854	3194	3440
Number of elements	4112	5116	6232	7070	8225	8992

3. Numerical Result and Discussion

The main goal of our study is to observe the heat transfer phenomenon in a circular tube for non-isothermal laminar flow assuming time dependent and the flow time is considered for 8 seconds. The results of CFD carried on a flowing water through a plain tube of copper material with inserts and without inserts are shown in the next subsiding topics. For this analysis the tube thickness is neglected and the boundary conditions for the tube are being considered a uniform heat flux adjacent to the water domain wall. We assume that the initial velocity of the water U_{in}= 0.08 *m/s* for laminar flow, the inlet temperature of water is 293.15 K (assuming ambient temperature) and we generate heat source together with boundary heat source sub-feature of highly conductive layer with constant heat flux 32087 W/m^2. As we have only focused on improving the heat transfer rate by the flowing fluid thus we ignored the heat flowing through the solid tube. We also assume that the fluid as water and the tube as copper in our simulation. In this study, we run our simulation using COMSOL Multiphysics version 4.2a. The properties for copper and water are used in simulation that shown in Table-1 and Table-2 respectively.

Table 1. Parameters value for simulation (Copper).

Property name	Symbol	Value (unit)
Density	ρ	870 [kg/m^3]
Thermal conductivity	K	400 [$W/(m\ .k)$]
Heat capacity(at constant-.temperature)	C_p	385 [$J/(kg\ .k)$]
Relative permeability	μ_o	1
Relative permittivity	ε_o	1
Electrical conductivity	σ	5.998×10^7 [S/m]
Coefficient of thermal expansion	α	17×10^{-6} [$1/K$]
Young's modulus	E	110×10^9 [N/m^2]
Poisson's ratio	υ	0.35

Table 2. Parameters value for simulation (Water).

Property name	Symbol	Value (Unit)
Dynamic viscosity	μ	0.798×10^{-3} [$Pa.s$]
Ratio of specific heat	γ	1.0
Electrical conductivity	σ	5.5×10^{-6} [S/m]
Heat capacity(at const. temperature)	C_p	4.2 [$KJ/\ (kg.\ K)$]
Density	ρ	1000 [kg/m^3]
Thermal conductivity	K	0.56 [$W\ /\ (m\ .K)$]

To understand the heat transfer phenomenon, we carried out the simulations by changing the number of inserts. The temperature distributions plot for water domain with transparent view has shown in Fig.3.1. The legends with each figure represent the temperature distribution of water at different positions of the computational domain. As higher heat flux is applied at the boundary layer, hence we observed large change in the temperature at the outlet. We can see the uniform temperature distribution for without insert combination [Fig.3.1. (a)] however after using inserts non-uniform temperature distribution is observed.

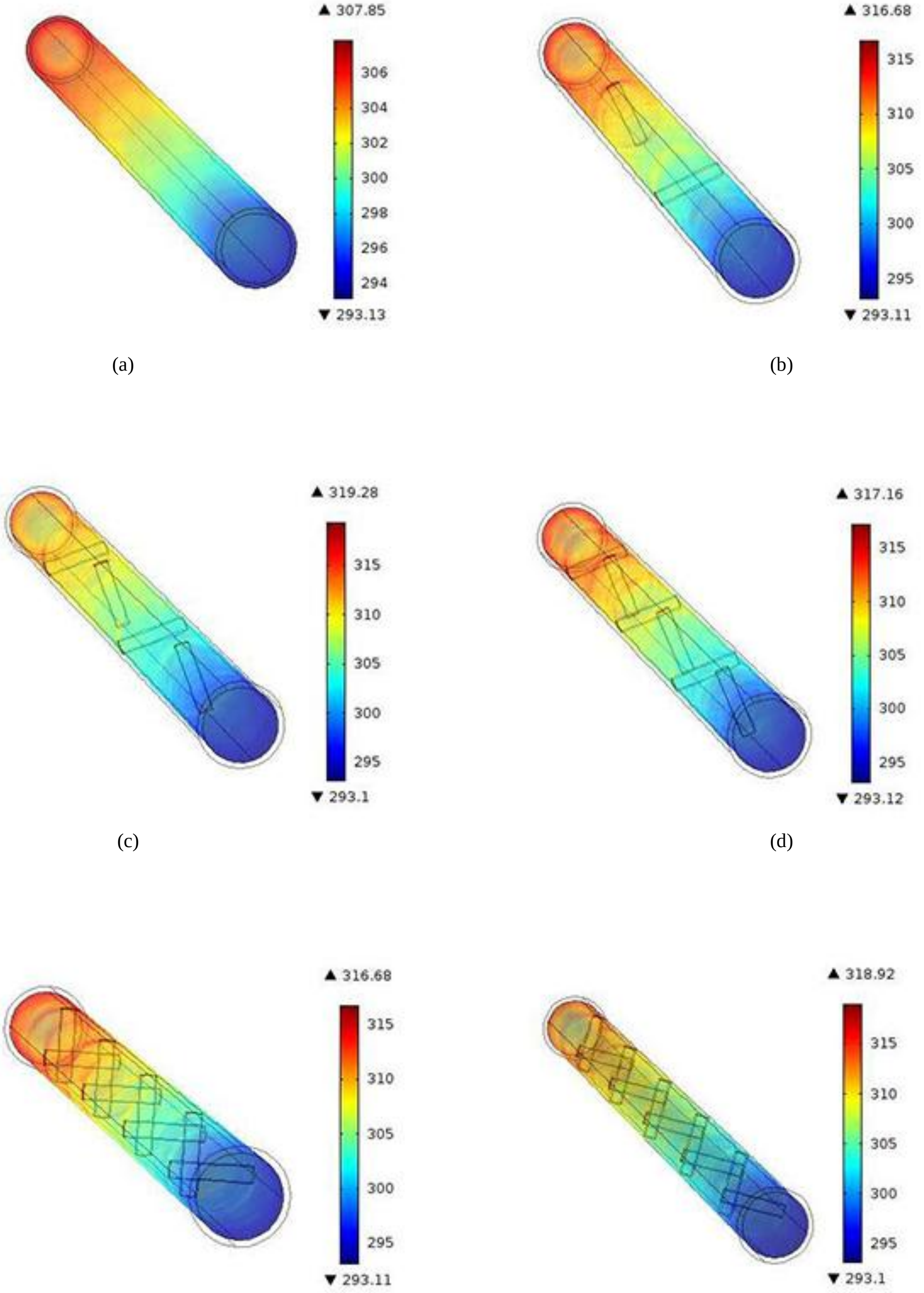

(a) (b)

(c) (d)

(e) (f)

Fig.3.1: Temperature distributions for different number of inserts (a) No insert; (b) two; (c) Four; (d) Six; (e) Eight; (f) Ten inserts.

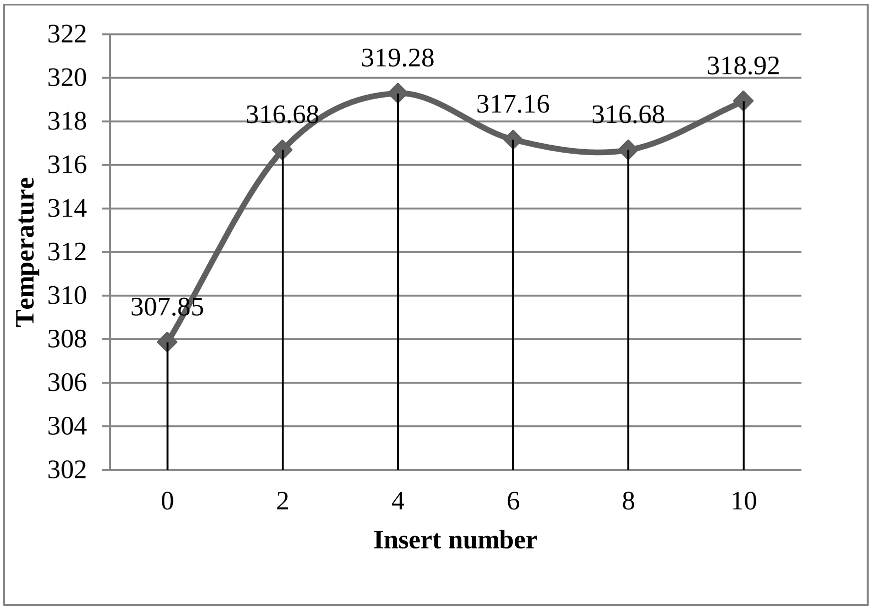

Fig.3.2: The comparison of the outlet temperature relationship for different inserts inside the computational domain.

From Fig.3.1 and 3.2, we have noticed that the outlet temperature increases to 307.85 *K* when there is no insert into the tube. When two inserts [Fig.3.1.(b)] are being fitted into the tube, we find the outlet temperature increases to 316.68 *K*. We get the highest outlet temperature 319.28 *K* for four inserts [Fig.3.1. (c)]. Then again, if we increase the insert number to six [Fig.3.1.(d)] and eight [Fig.3.1.(e)], we find the outlet temperatures are 317.16 *K* and 316.68 *K* respectively which is lower than the four inserts domain. But for ten inserts [Fig.3.1. (f)], we get the outlet temperature 318.92 *K*. Therefore, we noticed that there is an irregular variation of outlet temperature and cannot come to a certain decision to find out the reasons of such irregularities. Then, we changes the insert distance for six and eight inserts which are also simulated for the same physics used before.

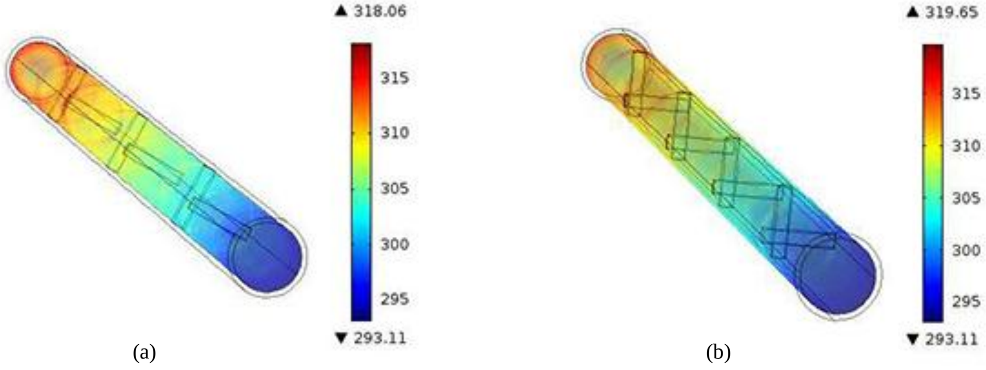

Fig.3.3: Temperature distributions of water domain after changing insert distance (a) Six inserts; (b) Eight inserts.

In this case, the inserts does not arrange at equal distance. Here, we have considered three couples of inserts for six inserts domain and four couples of inserts for eight inserts domain. The distance among those couples are fitted equally. Then, we run our simulation for these domains and temperature distribution have shown in Fig.3.2.We get the outlet temperature 318.06 *K* for six inserts and 319.68 *K* for eight inserts after changing inserts distance which is more than previous designs. Therefore, there is an optimum condition for considering distance among the inserts. It means not only increasing the number of inserts will increase the heat transfer but the distance among the inserts also be considered.

4. Conclusion

A CFD Simulation study on heat transfer characteristics of fluid in a circular tube without insert and with inserts under constant boundary heat flux condition for non-isothermal laminar flow has been presented. The comparison of the outlet temperature for different inserts inside the computational domain has been shown. We found that the higher heat transfer rate is obtained after using inserts compare to without insert. The highest outlet temperature is found for the computational domain with four inserts. After changing inserts position, greater outlet temperature is obtained for six and eight inserts domain. Therefore, optimum distance among the inserts causes greater efficiency of the heat transfer rate. The optimum distance among the inserts should be considered for executing the design which makes it economic and easy to manufacture.

Acknowledgements

The second author gratefully acknowledges for the technical support to Prof. Dr. Benchawan Wiwatanapataphee, Department of Mathematics, Mahidol University, Bangkok-10400, Thailand and the Simulation Lab, Department of Mathematics, Chittagong University of Engineering and Technology, Chittagong-4349.

References

[1] E. Bergles, “Techniques to augment heat transfer,” in Handbook of Heat Transfer Applications, J. P. Hartnett, W. M. Rohsenow, and E. N. Ganic, Eds., chapter 1, McGraw-Hill, New York, NY, USA, 2nd edition, 1985.
[2] R. L. Webb, Principle of Enhanced Heat Transfer, John Wiley, New York, NY, USA, 1994.
[3] B. Salam, S. Biswas, S. Saha and M. M. K. Bhuiya, 2013, “Heat transfer enhancement in a tube using rectangular-cut twisted tape insert”, Procedia Engineering, Vol. 56, pp. 96-103.
[4] Murugesan P, Mayilsamy K and Suresh S. Turbulent heat transfer and pressure drop in tube fitted with square-cut twisted tape. Fluid Flow And Transport Phenomena, 2010; 18(4): 609-617.
[5] Eiamsa-ard S, Nivesrangsan P, Chokphoemphun S and Promvonge P. Influence of combined non-uniform wire coil and twisted tape inserts on thermal performance characteristics. International Communications in Heat and Mass Transfer, 2010a; 37: 850-856.
[6] Eiamsa-ard S, Thianpong C and Eiamsa-ard P. Turbulent heat transfer enhancement by counter/co-swirling flow in a tube fitted with twin twisted tapes. Experimental Thermal and Fluid Science, 2010b; 34:53-62.
[7] Eiamsa-ard S, Thianpong C, Eiamsa-ard P and Promvonge P. Convective heat transfer in a circular tube with short-length twisted tape insert. International Communications in Heat and Mass Transfer, 2009; 36: 365-371.
[8] Eiamsa-ard S, Thianpong C and Promvonge P. Experimental investigation of heat transfer and flow friction in a circular tube fitted with regularly spaced twisted tape elements. International Communications in Heat and Mass Transfer, 2006; 33: 1225-1233.
[9] Eiamsa-ard S, Wongcharee K, Eiamsa-ard P and Thianpong C. Heat transfer enhancement in a tube using delta-winglet twisted tape inserts. Applied Thermal Engineering, 2010c; 30: 310-318.
[10] J. N. Ready, “An introduction to the Finite Element Method”, Third Edition, McGraw-Hill Education Private Limited.
[11] www.comsol.com. Documentation of COMSOL Multiphysics.

Available online at www.sciencedirect.com

ScienceDirect

Procedia Engineering 00 (2015) 000–000

Procedia Engineering

www.elsevier.com/locate/procedia

6th BSME International Conference on Thermal Engineering (ICTE 2014)

The Enhancement of Heat Transfer in a Circular Tube with Insert and without Insert by using the Finite Element Method

Sabbir Hossain[a], Ujjwal Kumar Deb[b], Kazi Afzalur Rahman[a]*

[a]Mechanical Engineering Department, Chittagong University of Engineering and Technology
[b]Department of Mathematics, Chittagong University of Engineering and Technology

Abstract

This paper presents a Finite Element based model of the heat transfer problem. The Enhancement of heat transfer with mass in a tube has been investigated without insert and with insert i.e. combination of horizontally and vertically arranged rectangular boxes of 5 mm thickness are being fitted perpendicular to the flow direction respectively at equal distance from each other along the length. The combinations are composed of without insert, two inserts, four inserts, six inserts, eight inserts and ten inserts. The purpose of using inserts is to scatter the fluid particles in the laminar flow which increases the heat transfer. An 800 mm long pipe with 26 mm inner diameter and 5 mm thickness is considered in our simulation. The simulations have been completed for both stationary and time dependent conditions with Reynolds number 1600~2400. A constant heat flux is generated at the boundary layer of the tube close to the flowing fluid around the boundary layer. We also have shown the comparisons of heat transfer rate among different combinations of inserts to understand the heat transfer phenomenon for the computational domain.

Peer-review under responsibility of organizing committee of the 6th BSME International Conference on Thermal Engineering (ICTE 2014).

Keywords: CFD Analysis, Mass transfer, FEM Analysis, Boundary heat flux, Boundary element

---

* Corresponding author. Tel.:+8801680-453267;
*E-mail address:*afzalur99@yahoo.com

Peer-review under responsibility of organizing committee of the 6th BSME International Conference on Thermal Engineering (ICTE 2014).

1. Introduction

The Heat Transfer Enhancement Technology (HTET) has been developed and commonly applied to heat exchanger applications over last decennium, such as refrigeration, process industry, nuclear reactors, automotive and solar water heaters. The use of relatively complex geometries was initially limited by manufacturing process. However, at the present time new manufacturing methods allow manufacture of much complex surface geometry. Bergles [1] and Webb [2] have shown liberally reviews on techniques for heat transfer enhancement. An experimental investigation was carried out for measuring tube-side heat transfer coefficient, friction factor; heat transfer enhancement efficiency of water for turbulent flow in a circular tube fitted with the stainless steel rectangular [3] and the square-cut twisted tape insert [4].

There have been many techniques proposed over the years for enhancing the heat transfer with mass in tubes by using different types of inserts (i.e.) like combination of non-uniform wire coil and twisted tape inserts [5], counter/co-swirling flow in a tube fitted with twin twisted tapes [6], short-length twisted tape insert [7], regularly spaced twisted tape elements [8], delta-winglet twisted tape inserts [9] have been proposed over the years. Almost all heat exchangers used in the air-conditioning and automotive industries are complex geometries. In these techniques, the fluid flows either laminar or turbulent. As In turbulent flow, unsteady vortices appear on different scales and interact with each other while in laminar flow the fluid particles adhere to with each other and the collision among the particle is very poor. So, heat transfer in turbulent flow is greater than laminar flow though it is burdensome to compute accurately.

If we use such an object or obstacle e.g. insert using perpendicular to the flow direction, that makes the flow laminar to turbulent, the technique becomes reliable or economical, then engineer can executes his design. Usually many experiments related to heat transfer enhancement have done in heat transfer laboratory in mechanical engineering department. So, we can choose the better technique by the theoretical analysis. Though, theoretical result differs from experimental. We get the nearest values and results to experimental results. We also get clear concepts by this technique and able to choose better one.

Finite Element Analysis (FEA) [10] consists of a computer based model of a material or structure that is stressed and analyzed for specific results. It is used for new product design and existing product refinement. A company capable of verifying a proposed design will be able to perform to the client's specifications prior to manufacturing or construction. Modifying an existing product or structure is utilizing to qualify the product or structure for a new service condition. In case of structural failure, FEA may be used for helping to determine the design modifications to meet the desired condition.

In this study, we analyze the heat transfer enhancement in a circular tube with inserts and without insert for laminar flow. Firstly, a non-isothermal flow model is considered. Afterwards water is taken into account in the model and copper is considered as the material of the circular pipe. Using the governing equations of the non-isothermal flow together with continuity equation, the dynamic behavior of the flow can be described which transport heat, the temperature field is affected by the changes in the flow field. Hence, a non-isothermal flow is always a two-way coupling between fluid flow and heat transfer.

The rest of our paper is organized as follows. In section **2**, the mathematical model and the mesh design of the domain is presented. In section **3**, numerical results for this model are shown. Finally, some conclusions are presented in section **4**.

Nomenclature

ρ	Density (Kg/m^3)
T	Absolute temperature (K)
P	Pressure (Pa)
Cp	Specific heat capacity (J/Kg. K)
μ	Dynamic viscosity (Pa·s)
q	Heat flux (W/m^2)
v	Velocity vector (m/s)
τ	Viscous stress tensor (Pa)
S	Strain tensor (1/S)

2. Mathematical Model

The ultimate goal of this study is to improve understanding of the enhancement of heat transfer in a circular pipe using insert and without insert. Our model has been designed as the geometry creates eddies across the flow which enhances the heat transfer. The purpose of using inserts in our design is to decrease layer to layer friction and to scatter the fluid particles carrying heat from the boundary wall, such that the particles near the boundary layer transfer heat to the other particles in the fluid. For example, a design of computational domain with four inserts is shown in Fig.2.1.

2.1 Governing equations

In this study, we have developed a one dimensional model of heat transfer including conduction, convection and mass transfer. Therefore the heat transfer phenomenon is governed by the following equations [11]:

$$\frac{\partial \rho}{\partial t} + \nabla\cdot(\rho v) = 0 \tag{1}$$

$$\rho u\cdot\nabla v + \rho\frac{\partial v}{\partial t} = -\nabla p + \nabla\cdot\left(\mu(\nabla v + \nabla v)^T - \frac{2}{3}\mu(\nabla\cdot v)I\right) + F \tag{2}$$

where, ρ is the density (kg/m^3), v is the velocity vector (m/s), p is the pressure (Pa), F is the body force vector (N/m^3), μ is the dynamic viscosity (Pa·s). It also solves the heat transfer through a fluid and governed by the following equation:

$$\rho C_p\left(\frac{\partial T}{\partial t} + (v\cdot\nabla)T\right) = \tau\cdot S - (\nabla\cdot q) - \frac{T}{\rho}\frac{\partial \rho}{\partial T}\Big|\, p\left(\frac{\partial p}{\partial t} + (v.\nabla)p\right) + Q \tag{3}$$

where C_p is the specific heat capacity at constant pressure (SI unit: J/(kg·K)), T is absolute temperature (SI unit: K), q is the heat flux by conduction (SI unit: W/m^2), τ is the viscous stress tensor (SI unit: Pa), S is the strain-rate tensor (SI unit: 1/s). The pressure work term:

$\frac{T}{\rho}\frac{\partial \rho}{\partial T}\,\big|\,p(\frac{\partial p}{\partial t} + (v\cdot\nabla)p\,)$ and the viscous heating term $\tau\cdot s$ are not included by default as they are commonly negligible. The interface also describes the heat transfer in solids:

$$\rho C_p\frac{\partial T}{\partial t} = -(\nabla\cdot q) - T\frac{\partial E}{\partial t} + \mathrm{Q}$$

where, E is the elastic contribution to entropy [SI unit: J/(m^3·K)]. As in the case of fluids, the pressure work term is $T\frac{\partial E}{\partial t}$.

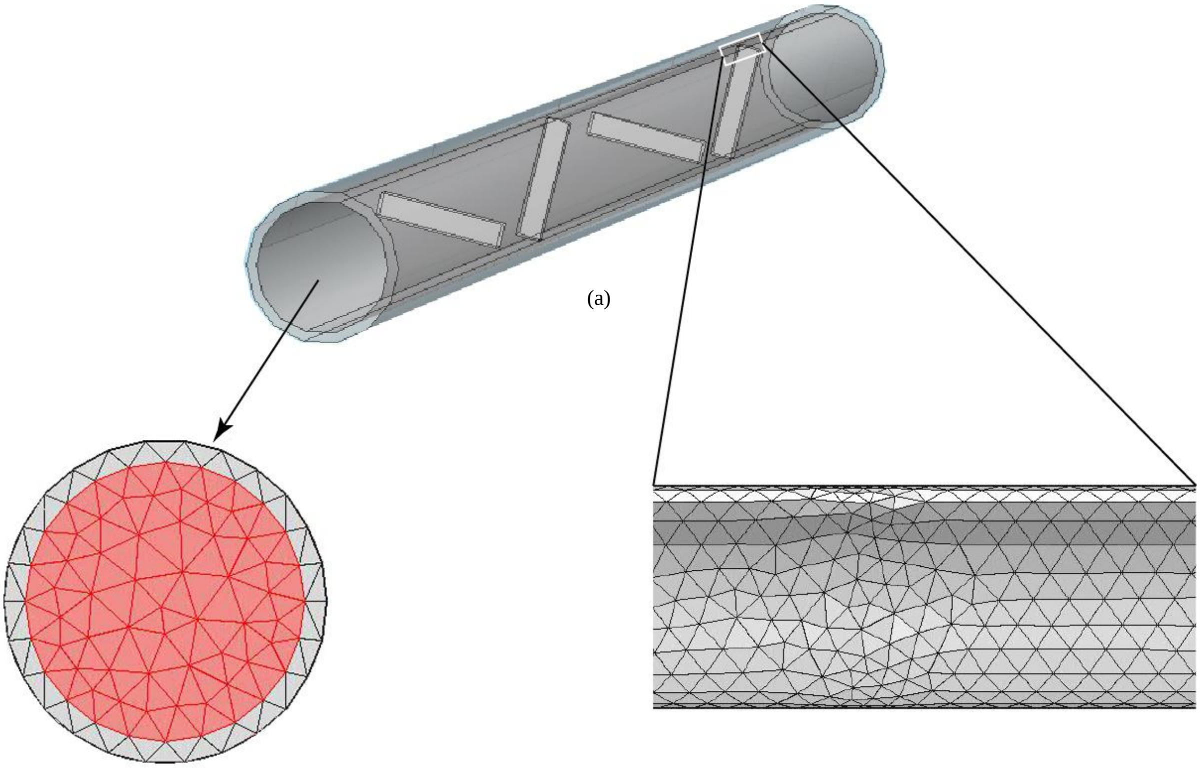

(a)

(b)

(c)

Fig.2.1: Computational domain with four inserts (a) computational domain, (b) mesh design for the inlet and (c) a part from wall of the tube.

2.2. Computational Model and Mesh Design:

In this study, at first we have designed a horizontal circular pipe without insert, two inserts, four inserts, six inserts, eight inserts and ten inserts are equally spaced from the leading edge. An example for four inserts, shown in Fig.2.1 (a). The tube has the total length of 800 mm, the inner and outer diameter of 26 mm and 30 mm respectively. Here, we set up the boundary conditions by selecting boundary layer. It is notable that, perfect meshing plays an important role in terms of accuracy of results. To achieve a satisfactory computational accuracy we continually change mesh design until the results obtained from two trial lead to very close to each other. As our domain length is short and computer processor capacity becomes an important factor for computing the study, we use coarse mesh Shown in Fig.2.1 (b, c) among the entire computational model for numerical simulation. Ash color shows mesh for tube and red color for water domain. Mesh element concentration becomes higher near the insert position have shown in Fig.2.1 (c). A comparison of mesh design among different insert combinations has shown below:

Table 2.1. Comparison of mesh design

Property name	No insert	Two inserts	Four inserts	Six inserts	Eight inserts	Ten inserts
Number of edge elements	374	454	534	606	690	758
Number of boundary elements	1908	2226	2546	2854	3194	3440
Number of elements	4112	5116	6232	7070	8225	8992

3. Numerical Result and Discussion

The main goal of our study is to observe the heat transfer phenomenon in a circular tube for non-isothermal laminar flow assuming time dependent and the flow time is considered for 8 seconds. The results of CFD carried on a flowing water through a plain tube of copper material with inserts and without inserts are shown in the next subsiding topics. For this analysis the tube thickness is neglected and the boundary conditions for the tube are being considered a uniform heat flux adjacent to the water domain wall. We assume that the initial velocity of the water U_{in}= 0.08 *m/s* for laminar flow, the inlet temperature of water is 293.15 K (assuming ambient temperature) and we generate heat source together with boundary heat source sub-feature of highly conductive layer with constant heat flux 32087 W/m^2. As we have only focused on improving the heat transfer rate by the flowing fluid thus we ignored the heat flowing through the solid tube. We also assume that the fluid as water and the tube as copper in our simulation. In this study, we run our simulation using COMSOL Multiphysics version 4.2a. The properties for copper and water are used in simulation that shown in Table-1 and Table-2 respectively.

Table 1. Parameters value for simulation (Copper).

Property name	Symbol	Value (unit)
Density	ρ	870 [kg/m^3]
Thermal conductivity	K	400 [$W/(m .k)$]
Heat capacity(at constant-.temperature)	C_p	385 [$J/(kg .k)$]
Relative permeability	μ_o	1
Relative permittivity	ε_o	1
Electrical conductivity	σ	5.998×10^7 [S/m]
Coefficient of thermal expansion	α	17×10^{-6} [$1/K$]
Young’s modulus	E	110×10^9 [N/m^2]
Poisson’s ratio	υ	0.35

Table 2. Parameters value for simulation (Water).

Property name	Symbol	Value (Unit)
Dynamic viscosity	μ	0.798×10^{-3} [$Pa.s$]
Ratio of specific heat	γ	1.0
Electrical conductivity	σ	5.5×10^{-6} [S/m]
Heat capacity(at const. temperature)	C_p	4.2 [$KJ/ (kg. K)$]
Density	ρ	1000 [kg/m^3]
Thermal conductivity	K	0.56 [$W / (m .K)$]

To understand the heat transfer phenomenon, we carried out the simulations by changing the number of inserts. The temperature distributions plot for water domain with transparent view has shown in Fig.3.1. The legends with each figure represent the temperature distribution of water at different positions of the computational domain. As higher heat flux is applied at the boundary layer, hence we observed large change in the temperature at the outlet. We can see the uniform temperature distribution for without insert combination [Fig.3.1. (a)] however after using inserts non-uniform temperature distribution is observed.

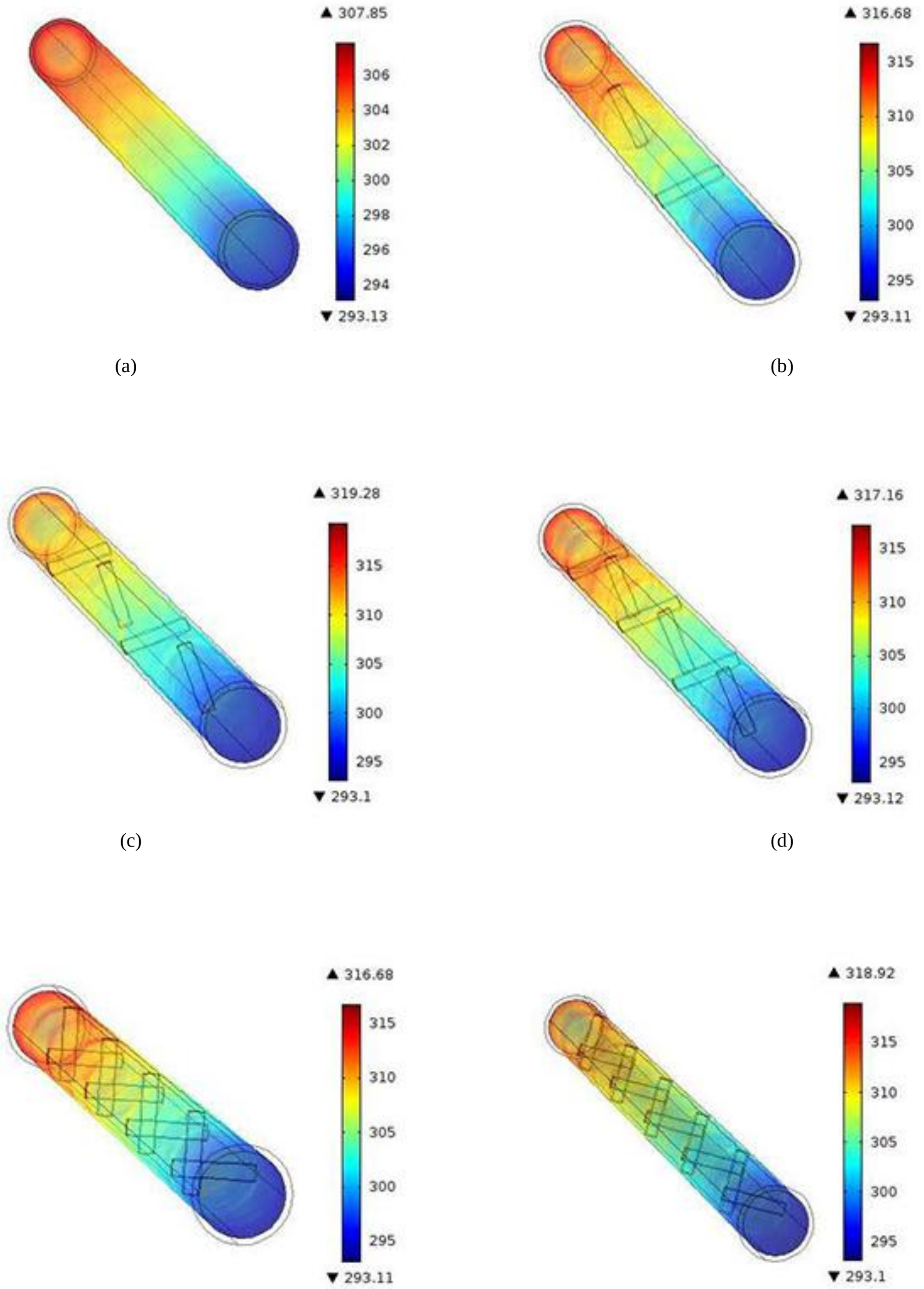

(a) (b)

(c) (d)

(e) (f)

Fig.3.1: Temperature distributions for different number of inserts (a) No insert; (b) two; (c) Four; (d) Six; (e) Eight; (f) Ten inserts.

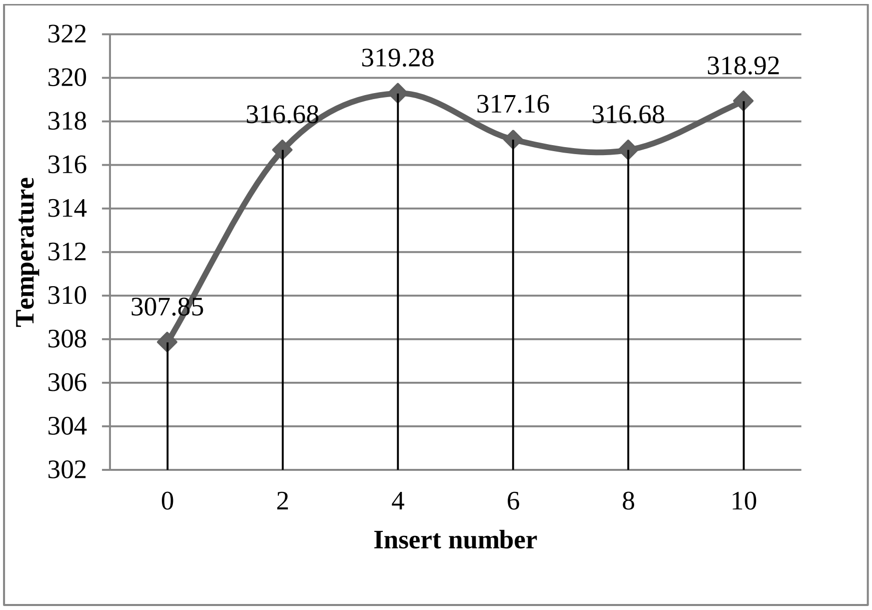

Fig.3.2: The comparison of the outlet temperature relationship for different inserts inside the computational domain.

From Fig.3.1 and 3.2, we have noticed that the outlet temperature increases to 307.85 *K* when there is no insert into the tube. When two inserts [Fig.3.1.(b)] are being fitted into the tube, we find the outlet temperature increases to 316.68 *K*. We get the highest outlet temperature 319.28 *K* for four inserts [Fig.3.1. (c)]. Then again, if we increase the insert number to six [Fig.3.1.(d)] and eight [Fig.3.1.(e)], we find the outlet temperatures are 317.16 *K* and 316.68 *K* respectively which is lower than the four inserts domain. But for ten inserts [Fig.3.1. (f)], we get the outlet temperature 318.92 *K*. Therefore, we noticed that there is an irregular variation of outlet temperature and cannot come to a certain decision to find out the reasons of such irregularities. Then, we changes the insert distance for six and eight inserts which are also simulated for the same physics used before.

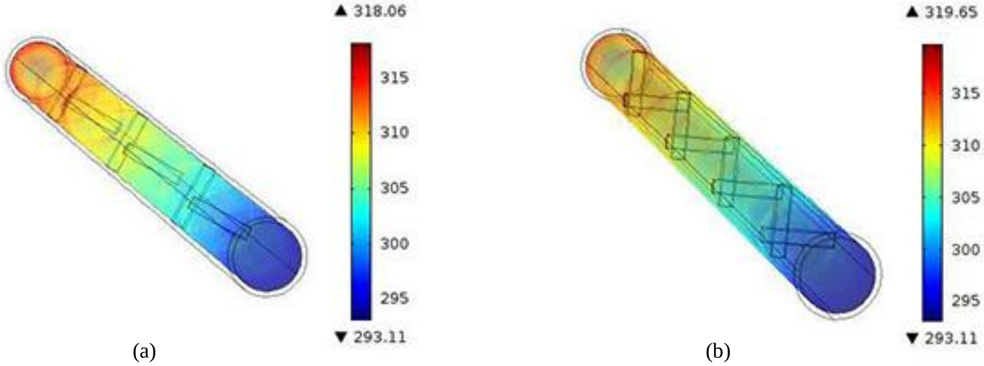

(a) (b)

Fig.3.3: Temperature distributions of water domain after changing insert distance (a) Six inserts; (b) Eight inserts.

In this case, the inserts does not arrange at equal distance. Here, we have considered three couples of inserts for six inserts domain and four couples of inserts for eight inserts domain. The distance among those couples are fitted equally. Then, we run our simulation for these domains and temperature distribution have shown in Fig.3.2.We get the outlet temperature 318.06 *K* for six inserts and 319.68 *K* for eight inserts after changing inserts distance which is more than previous designs. Therefore, there is an optimum condition for considering distance among the inserts. It means not only increasing the number of inserts will increase the heat transfer but the distance among the inserts also be considered.

4. Conclusion

A CFD Simulation study on heat transfer characteristics of fluid in a circular tube without insert and with inserts under constant boundary heat flux condition for non-isothermal laminar flow has been presented. The comparison of the outlet temperature for different inserts inside the computational domain has been shown. We found that the higher heat transfer rate is obtained after using inserts compare to without insert. The highest outlet temperature is found for the computational domain with four inserts. After changing inserts position, greater outlet temperature is obtained for six and eight inserts domain. Therefore, optimum distance among the inserts causes greater efficiency of the heat transfer rate. The optimum distance among the inserts should be considered for executing the design which makes it economic and easy to manufacture.

Acknowledgements

The second author gratefully acknowledges for the technical support to Prof. Dr. Benchawan Wiwatanapataphee, Department of Mathematics, Mahidol University, Bangkok-10400, Thailand and the Simulation Lab, Department of Mathematics, Chittagong University of Engineering and Technology, Chittagong-4349.

References

[1] E. Bergles, “Techniques to augment heat transfer,” in Handbook of Heat Transfer Applications, J. P. Hartnett, W. M. Rohsenow, and E. N. Ganic, Eds., chapter 1, McGraw-Hill, New York, NY, USA, 2nd edition, 1985.
[2] R. L. Webb, Principle of Enhanced Heat Transfer, John Wiley, New York, NY, USA, 1994.
[3] B. Salam, S. Biswas, S. Saha and M. M. K. Bhuiya, 2013, “Heat transfer enhancement in a tube using rectangular-cut twisted tape insert”, Procedia Engineering, Vol. 56, pp. 96-103.
[4] Murugesan P, Mayilsamy K and Suresh S. Turbulent heat transfer and pressure drop in tube fitted with square-cut twisted tape. Fluid Flow And Transport Phenomena, 2010; 18(4): 609-617.
[5] Eiamsa-ard S, Nivesrangsan P, Chokphoemphun S and Promvonge P. Influence of combined non-uniform wire coil and twisted tape inserts on thermal performance characteristics. International Communications in Heat and Mass Transfer, 2010a; 37: 850-856.
[6] Eiamsa-ard S, Thianpong C and Eiamsa-ard P. Turbulent heat transfer enhancement by counter/co-swirling flow in a tube fitted with twin twisted tapes. Experimental Thermal and Fluid Science, 2010b; 34:53-62.
[7] Eiamsa-ard S, Thianpong C, Eiamsa-ard P and Promvonge P. Convective heat transfer in a circular tube with short-length twisted tape insert. International Communications in Heat and Mass Transfer, 2009; 36: 365-371.
[8] Eiamsa-ard S, Thianpong C and Promvonge P. Experimental investigation of heat transfer and flow friction in a circular tube fitted with regularly spaced twisted tape elements. International Communications in Heat and Mass Transfer, 2006; 33: 1225-1233.
[9] Eiamsa-ard S, Wongcharee K, Eiamsa-ard P and Thianpong C. Heat transfer enhancement in a tube using delta-winglet twisted tape inserts. Applied Thermal Engineering, 2010c; 30: 310-318.
[10] J. N. Ready, “An introduction to the Finite Element Method”, Third Edition, McGraw-Hill Education Private Limited.
[11] www.comsol.com. Documentation of COMSOL Multiphysics.

Available online at www.sciencedirect.com

ScienceDirect

Procedia Engineering00 (2015) 000–000

Procedia Engineering

www.elsevier.com/locate/procedia

6th BSME International Conference on Thermal Engineering (ICTE 2014)

Effect of Corner Radius of a T- Junction Mini-Square Channel on Fluid Flow and Heat Transfer in the Developing Region: A Three Dimensional Numerical Simulation.

Abhik Majumder[a]*, Sambit Majumder[b]

[a]*National Institute of Technology, Agartala, 799055, India*
[b]*National Institute of Technology, Agartala, 799055, India*

Abstract

In recent years, there is a trend of miniaturization of devices like heat exchangers, microfluidic devices, MEMS and electronic chip devices. The study of fluid flow in these devices is of great significance nowadays. Due to small dimensions, the entrance design is a matter of concern and importance. In this work, the effect of variation of corner radius, on thermo- hydrodynamic characteristics of a three dimensional model of T-junction square mini-channel duct of 2 mm sides is studied under constant heat flux applied (H2 type) on the horizontal part. The length of horizontal section is 300 mm. The T junction is placed at the middle of 60 mm long vertical section. The numerical simulation was done in general purpose CFD package FLUENT. The simulation is performed for two Reynolds number, one in laminar flow range (Re 1000) and the other in turbulent flow range (Re 3200). It is observed that incorporation of fillets at T-junction changed the nature of the fluid flow and heat transfer locally. Variations in velocity and Nusselt number have been observed in both the laminar and turbulent flow regime. Within developing region local velocity is found to be increasing with increase in corner radii towards downstream of the channel in laminar and turbulent flow. Whereas the local Nusselt numbers are less as compared to base model for all heating conditions and corner radii, resulting in local wall temperature rise. Hence, such incorporation of corner radii may accelerate the uniform flow velocity growth. Vortices are observed to be diminishing near the junction with increase in corner radii.

Peer-review under responsibility of organizing committee of the 6th BSMEInternational Conference on Thermal Engineering (ICTE 2014).

*Keywords:*T junction; corner radius; heat transfer; fluid flow; local Nusselt number.

---

* Corresponding author. Tel.: +91-381-2346630; fax: +91-381-2346630.
*E-mail address:*abhikmajumder.me@nita.ac.in

Peer-review under responsibility of organizing committee of the 6th BSME International Conference on Thermal Engineering (ICTE 2014).

1. Introduction

Recent trend of miniaturization of devices and micro-fabrication technologies stimulated the research society during the last decades to study fluid flow and heat transfer in micro/mini-channels. Miniaturization has put upon considerable impact in the following applications: fuel cell technology [1], micro-electro-mechanical systems (MEMS) [2], microelectronics cooling [3], heat exchangers, medical and biomedical researches [4,5,6]. Among all these devices, micro/mini-channels were found to be most effective to remove high heat flux from miniature area. Besides it serves the purpose of transporting fluid within the small areas, connecting different chambers, chemical mixing and computer chips cooling. Hence, to design and fabricate such devices it is extremely necessary to understand the fundamental mechanisms, behavior of transport phenomena and energy transfer through these channels. Geometrical configurations play a vital role on the temperature, pressure and velocity distribution of the fluid flow through these channels.

Nomenclature

d_h	Hydraulic diameter (m)
h	Heat transfer coefficient (W/m-K)
q”	Constant heat flux (W/cm^2)
u	Main stream velocity (m/s)
x*	Non-dimensional axial distance (x/d_hRePr)
y*	Non-dimensional distance (y/0.002)
u*	Non-dimensional velocity (u_{local}/u)
Re	Reynolds number
Nu	Nusselt number
Pr	Prandtl number

Lee et al. [7] experimentally investigated the heat transfer effects in rectangular microchannels considering ten parallel microchannels (hydraulic diameter ranging from 318-903µm) using de-ionized water as the working fluid between Reynolds number from 300 to 3500 under constant wall temperature and wall heat flux. They reported, as the hydraulic diameter of channel decreased, the heat transfer coefficient increased for a constant flow rate.

Walker et al. [8] used two pipes connected perpendicularly with each other and investigated single phase flow phenomena inside the T-junction geometry. They observed kidney shaped contour lines at planes taken downstream the mixing pipe which resulted due to the wake structure produced by the side flow. A four fluid region at planes downstream the mixing junctions and a separation region having two vortices forming the recirculation were observed. A linear Nusselt number variation along the length of microchannels was observed in case of H2 boundary condition whereas exponential trend was observed in case of H1 and T boundary conditions in a rectangular microchannel [9]. A linear temperature profile with decreasing gradient along the longitudinal direction from inlet to outlet and a decrease in temperature was noted from top wall to bottom wall heat sinks as reported by Qu [10]. Recently Nimbalkar et al. [11] and Majumder et al. [12] investigated experimentally heat transfer phenomena in a T-junction and square minichannel respectively. In a three-dimensional numerical simulation of simultaneously developing convective flow in a square microchannel performed by Moharana et al. [13] reported, to enhance the Nusselt number in the channel, least substrate thickness should be incorporated for a constant thermal conductivity of the substrate material.

Recently Sakowitz et al. [14] used Large Eddy Simulation (LES) approach to analyze turbulent flow mechanism in two different models of T-junctions, one square cross-section and the other circular cross-section. Two different kind of recirculation zone downstream the duct was reported by them. In thermal mixing phenomena of two different streams at different temperature in a T-junction, numerical result quality strongly depends upon the selection of SGS model [15]

Failures of piping systems in nuclear power plants, particularly at T-junction area with an elbow on the upstream initiated Nematollahi et al. [16] to investigate and establish the most reliable geometry to serve the purpose. Two different types of geometries of pipe viz., S and E were simulated using water and sodium as the test fluid. Dimensionless distance (distance between junction and elbow) value of 2 for E-type and S-type geometries showed maximum risk of thermal fatigue whereas dimensionless distance value of 4 was concluded to be minimum distance for a T-junction for impinging jet which did not affect the downstream elbow. Benes et al. [17] performed a numerical simulation of laminar and turbulent flows of Newtonian and non-Newtonian fluids in a T-junction of square or circular cross-sections having two outlets. Highest pressure loss at the junction and small vortices were found which grew gradually downstream the channel.

It has been observed that, enough attention was not given in analysis of T-junction mini-channel, with change in the corner radii. In the present study a three dimensional numerical simulations of laminar and turbulent flow in square cross section T-junction mini-channel was performed. The numerical investigation was obtained using general purpose CFD package FLUENT 14. In this work the geometry of the computational domain incorporates corner radii of 0.2mm, 0.4mm and 0.6mm at the junction to investigate change in fluid flow and heat transfer. Then the results obtained with geometrical variations of corner radii were compared with the base model (with no corner radius).

2. Geometry and model

The three dimensional models and grids are generated in presolver GAMBIT. The base model T-Junction over which design modifications are done is shown in Fig.1(a). The cross sections of the ducts are square in shape with assumed hydraulic diameter (d_h) of 2mm. The length of the vertical duct is 60mm and that of horizontal duct is 300mm from the central vertical axis. The base model's design is modified by incorporating corner radius at the T-junction. The modification is done to improve the entrance type from abrupt entrance to smooth entrance. The corner radii are incorporated as 0.1, 0.2 and 0.3 times the hydraulic diameter of the base model. The modified model is shown in Fig. 1(b). The other dimensions viz. length of vertical and horizontal duct and the cross-sectional breadth and width are kept same. Thus, these models are then simulated. This helped us to study the entrance effects over the fluid flow and heat transfer results.

3. Procedure

Submap type hexahedral element scheme mesh volumes are generated in all the models as shown in Fig. 1(c, d). Grid independence test is carried out to find the best mesh spacing for the geometric model subjected to the constraint of computational resource. Three different meshes are generated over a model having 60000, 1.2 lacs and 1.7 lacs cells. The average local Nusselt number at the duct outlet (fully developed flow regime) varied by 12.9% from 60000 cells to 1.2 lacs cells whereas, it varied by 0.65% from 1.2 lacs cells to 1.7 lacs cells as shown in Fig. 2. Since no appreciable change is observed in the later comparison, hence, 1.2 lacs cells grid type is chosen for the rest of the simulations to reduce computational time and cost. FLUENT 14, CFD solver is used for the numerical simulation of the present study. Pressure based, absolute velocity formulation and steady state solver is considered. Energy equation is applied to incorporate heat transfer effect. SIMPLE scheme, pressure-velocity coupling is used as the iterative algorithm.

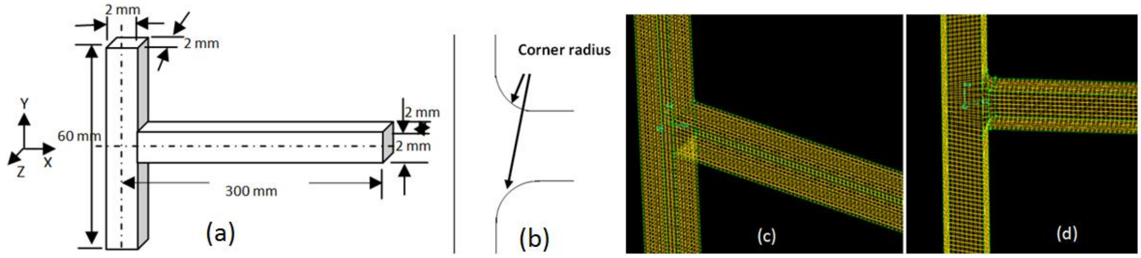

Fig. 1. (a) Schematic of the T-junction base model with sharp corner along with dimensions; (b) modified geometry of T-junction with corner radius; Generated grids in (c) base model; (d) corner radius model.

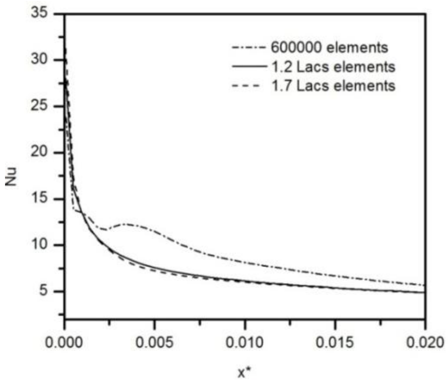

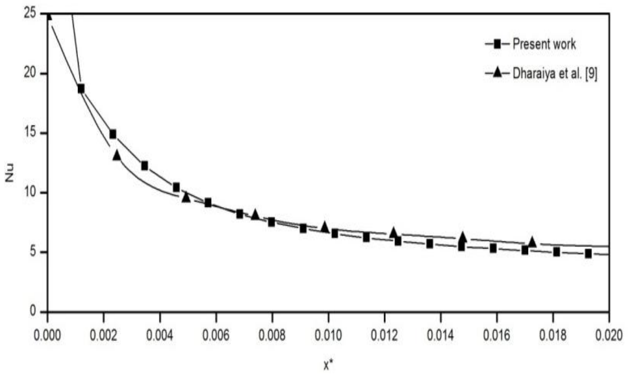

Fig. 2. Grid independency test plot.

Fig. 3. Comparison of Nusselt number of present study with Dharaiya et al. [9].

The simulation is performed initially for the base model incorporating H2 boundary condition (uniform heat flux on one wall). The Nusselt number variation along the non-dimensional axial length is then compared with the values reported by Dharaiya et al. [9] for the same heating condition as shown in Fig. 3. It is clear from the plot that change in Nusselt number of present numerical model in simultaneously developing region is in good agreement as reported by Dharaiya et al. [9]. Then the simulations are performed for each model by varying corner radius at the junction and applying different heating conditions.

The numerical simulations of 3D square cross section T-junction, along with its modified models are performed for the following cases of wall heating configurations- (a) uniform heat flux on one wall (b) uniform heat flux on two opposite walls and (c) uniform heat flux on two adjacent walls as shown in Fig.4.

Two different Reynold numbers are chosen for the flow simulation of all the cases, one in laminar flow range (Re = 1000) and another in turbulent flow range (Re = 3200). The velocity calculated corresponding to Re = 1000 is 0.2795m/s and 0.8944m/s for Re = 3200. Water and copper are considered as the working fluid and substrate material respectively. The properties for water like density, specific heat, thermal conductivity, viscosity and kinematic viscosity are considered as 998.2 (kg/m^3), 4182 (J/Kg-K), 0.6 (W/m-K), 0.001 (kg/m-s), 0.559e-06 (m^2/s) respectively. Properties for Copper like density, specific heat and thermal conductivity are considered as 8978 (kg/m^3), 381(J/Kg-K), 387.6 (W/m-K) respectively. A constant heat flux of 50 W/cm^2 is applied. Navier stokes equation coupled with Energy equation is solved by control volume method. Laminar viscous model was chosen for simulation of laminar flow whereas standard k-ε model was applied in turbulent flow simulation.

4. Results and Discussions

Various velocity profiles are taken at different positions in the horizontal channel for laminar flow which are shown in Fig. 5. Velocity is found to be increasing with increase in corner radius. At 0.0001 non-dimensional distance past the junction, magnitude of local velocity is greater in base model as compared to corner modified models at the centre of the channel. At x*=0.0001 and 0.0007, developing velocity profile is observed which is due to the recirculation of fluid. The vortices developed near the junction can be seen clearly in velocity contours and vectors shown in Fig. 6.

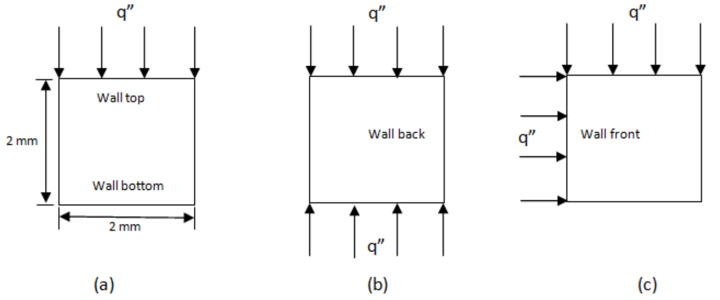

Fig. 4. Constant heat flux on (a) one wall; (b) two opposite walls; (c) two adjacent walls

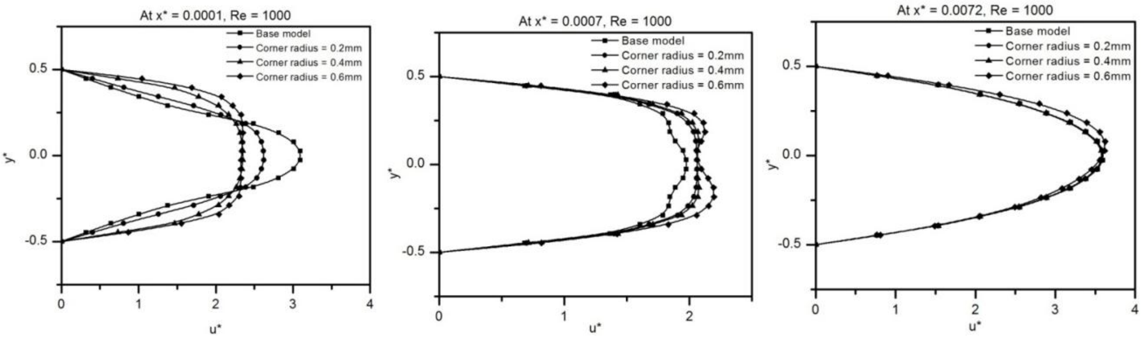

Fig. 5. Velocity profiles for laminar flow.

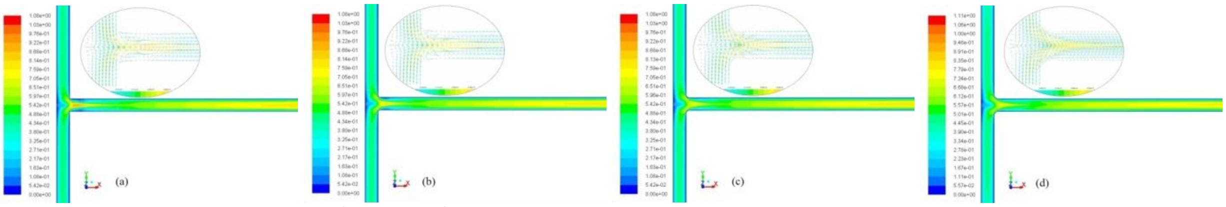

Fig. 6. Velocity contours and vectors for laminar flow (a) base model; (b) corner radius 0.2mm; (c) corner radius 0.4mm; (d) corner radius 0.6mm.

It is clear from the figures that vortices near the junction walls are found to be diminishing with increase in corner radius. Velocity profiles at different positions inside the channel and contour for turbulent flow are shown in Fig. 7 and Fig. 8 respectively. It is observed that the velocity profile of 0.6mm corner radius model is developing at faster rate. Similar phenomena of diminishing vortices are also found in turbulent flow. The incorporation of corner radius led to faster development of velocity profiles in both laminar and turbulent flow. Fig. 9 (a)(b)(c) show the variation of Nusselt number as a function of non-dimensional axial length for one wall, two opposite walls and two adjacent walls heating configuration for laminar flow (Re = 1000). These cases are plotted for first 100mm (x*=0.007) length of mini-channel (simultaneously developing region).

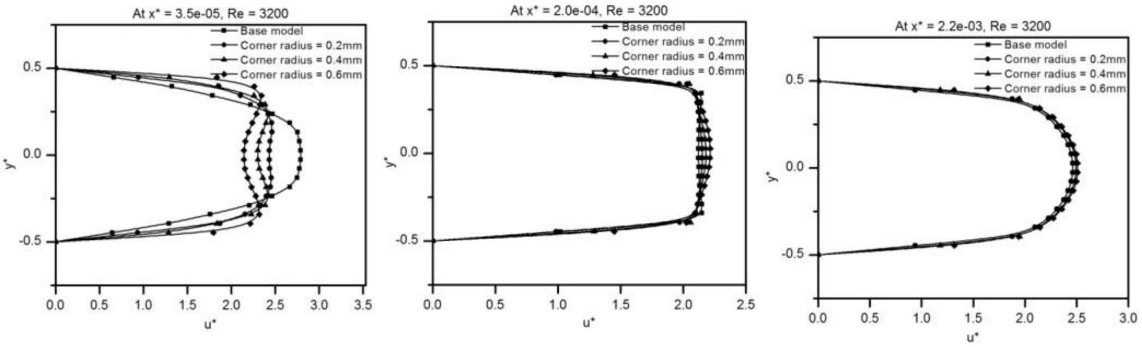

Fig. 7. Velocity profiles for turbulent flow.

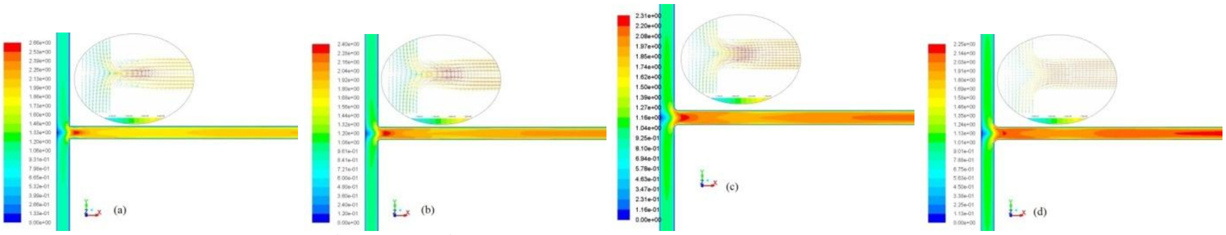

Fig. 8. Velocity contours and vectors for turbulent flow (a) base model; (b) corner radius 0.2mm; (c) corner radius 0.4mm; (d) corner radius 0.6mm.

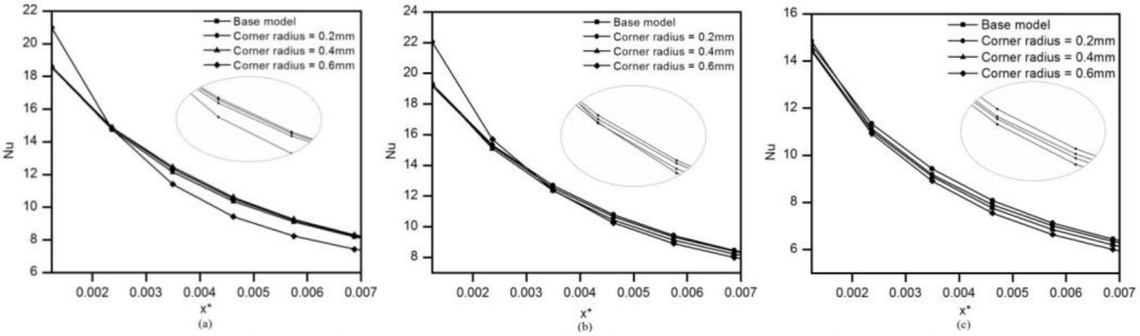

Fig. 9. Local Nusselt number as a function of non-dimensional length for different heating conditions for laminar flow (a) one wall heating; (b) two opposite walls heating; (c) two adjacent walls heating.

As expected, the graphs reveal high value of Nusselt number at the beginning and decrease along the length of mini-channel. It is clear from the graph that for one wall heating condition change in Nusselt number does not vary significantly from the base model. A similar trend is observed in case of two opposite walls and two adjacent walls heating conditions. It is found that change in Nusselt number as compared to base model is insignificant for 0.2mm corner radius model whereas a significant decrease in Nusselt number was found for 0.4mm and 0.6mm corner radius models. This is attributed to the lack of reverse flow resulted from disappearance of vortices. Fig. 10 (a)(b)(c) represent the Nusselt number variation in turbulent flow region (Re = 3200). The graphs show similar characteristics of Nusselt number variation along the length of minichannel, i.e., high value of Nusselt number initially and then decrease exponentially. In one wall heating condition, change in Nusselt number is insignificant in 0.2mm and 0.4mm corner radius models as compared to base model but significant rise in Nusselt number (about 5.5%) is observed in 0.6mm corner radius model which needs further study and verification in the intermediate corner radii to confirm the trend. In two opposite walls heating condition very less change in Nusselt number is observed in 0.2mm and 0.4mm corner radius. Similar trend is followed in two adjacent walls heating conditions. The Change in local Nusselt number is found varying slightly as compared to base model for all heating conditions and corner radii.

5. Conclusions

A three dimensional numerical simulation of laminar and turbulent flow in square cross section T-junction mini-channel is performed using general purpose CFD package FLUENT. Corner radii of 0.2mm, 0.4mm and 0.6mm are incorporated at the junction to investigate change in fluid flow and heat transfer as compared to base model. H2 boundary condition is applied in each case of three different heating conditions. Within developing region local velocity is found to be increasing with increase in corner radii towards downstream of the channel in laminar and turbulent flow. Whereas the local Nusselt numbers are less as compared to base model for all heating conditions and corner radii, resulting in local wall temperature rise. Hence, such incorporation of corner radii may accelerate the uniform flow velocity growth. Vortices are observed to be diminishing with increase in corner radii.

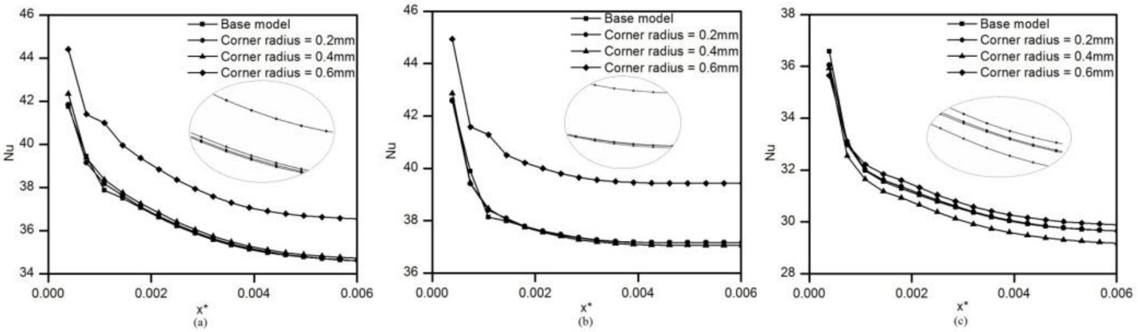

Fig. 10. Local Nusselt number as a function of non-dimensional length for different heating conditions for turbulent flow (a) one wall heating; (b) two opposite walls heating; (c) two adjacent walls heating.

Acknowledgements

Authors of the paper greatly acknowledge the support received from Department of Mechanical Engineering, National Institute of Technology, Agartala, Tripura, India.

References

[1] E. Kjeang, R. Michel, D.A. Harrington, N. Djilali, D. Sinton, A microfluidic fuel cell with flow through porous electrodes, J. Am. Chem. Soc. 130(12) (2008) 4000-4006.
[2] C.M. Ho, Y.C. Tai, Micro-electro mechanical systems (MEMS) and fluid flows, Ann. Rev. Fluid Mech. 30(1) (1998) 579-612.
[3] D.B. Tuckerman, R.F.W. Pease, High performance heat sinking for VLSI, IEEE Electron Device Lett. 2(8).
[4] C.S. Effenhauser, A. Manz, H.M. Widmer, Glass chips for high speed capillary electrophoresis separation with submicrometer plate heights, Anal. Chem. 65(9) (1993) 2637-2642.
[5] T. Bodnar, A. Sequeira, Numerical simulation of the coagulation dynamics of blood, Comp. and Math. Methods in Medicine. 4 (2008) 83-104.
[6] T. Bodnar, A. Sequeira, M. Prosi, On the shear thining and visco elastic effects of blood flow under various flow rates, App. Math. and Comp. 217 (2011) 5055-5067.
[7] P.S. Lee, S.V. Garimella, D. Liu, Investigation of heat transfer in rectangular microchannels, Int. J. Heat and Mass Transfer. 48 (2005) 1688-1704.
[8] C. Walker, M. Simiano, R. Zboray, H-M. Prasser, Investigations on mixing phenomena in single phase flow in a T-junction geometry, Nuclear Engg. Design. 239 (2009) 116-126.
[9] V.V. Dharaiya, S.G. Kandlikar, Numerical investigation of heat transfer in rectangular microchannels under H2 boundary condition during developing and fully developed laminar flow, J. Heat Transfer. 134 (2012) 020911-1.
[10] W. Qu, I. Mudawar, Analysis of three dimensional heat transfer in microchannel heat sinks, Int. J. Heat and Mass Transfer. 45 (2002) 3973-3985.
[11] V.S.N. Nimbalkar, A.W. Patwardhan, I. Banerjee, G. Padmakumar, G. Vaidyanathan, Thermal mixing in T-junctions, Chem. Engg. Sci. 65 (2010) 5901-5911.
[12] A. Majumder, B. Mehta, S. Khandekar, Local nusselt number enhancement during gas-Taylor bubble flow in a square mini-channel: An experimental study, Int. J. Thermal Sci. 66 (2013) 8-18.
[13] M.K. Moharana, P.K. Singh, S. Khandekar, Axial heat conduction in the context of developing flows in microchannels, Proc. of the ASME 2011, 9th Int. Conf. on Nanochannels, Microchannels and Minichannels, Alberta, Canada. (June 19-22, 2011).
[14] A. Sakowitz, M. Mihaescu, L. Fuchs, Turbulent flow mechanisms in mixing T-junctions by large eddy simulations, Int. J. Heat and Fluid Flow. 45(2014) 135-146.
[15] S. Kuhn, O. Braillard, B. Niceno, H-M. Prasser, Computational study of conjugate heat transfer in T-junctions, Nuclear Engg. Design. 240 (2010) 1548-1557.
[16] M. Nematollahi, B. Khonsha, Comparison of T-junction flow pattern of water and sodium for different geometries of power plant piping piping systems, Annals of Nuclear Energy. 39 (2012) 83-93.
[17] L. Benes, P. Louda, K. Kozel, R. Keslerova, J. Stigler, Numerical simulations of flow through channels with T-junction, App. Math. and Comp. 219 (2013) 7225-7235.

Available online at www.sciencedirect.com

ScienceDirect

Procedia Engineering00 (2015) 000–000

Procedia Engineering

www.elsevier.com/locate/procedia

6th BSME International Conference on Thermal Engineering (ICTE 2014)

Natural convection of fluid with viscous dissipation and variable viscosity from a heated vertical wavy surface

Nazma Parveen* and Md. Abdul Alim

Department of Mathematics, Bangladesh University of Engineering and Technology, Dhaka-1000, Bangladesh

Abstract

A numerical analysis used to simulate the effects of the viscous dissipation and variable viscosity on natural convection heat transfer boundary layer flow along a vertical wavy surface has been investigated. A simple coordinate transformation is employed to transform the wavy surface into a flat plate. The boundary layer equations and the boundary conditions are discretized and solved numerically using by the finite difference scheme known as the Keller-box method. Effects of the viscous dissipation and variable viscosity parameter on the skin friction coefficients, the local Nusselt number, the streamlines as well as the isotherms are presented and discussed in detail. The results of this investigation illustrate that the skin friction coefficient increases with an increase of the variable viscosity and viscous dissipation parameter, while the local Nusselt number at the heated surface decreases with increasing variable viscosity and viscous dissipation parameter.

Peer-review under responsibility of organizing committee of the 6th BSMEInternational Conference on Thermal Engineering (ICTE 2014).

Keywords: Viscous dissipation; variable viscosity; natural convection; uniform surface temperature; Keller-box method; wavy surface

1. Introduction

Viscous dissipation is of interest for many applications: significant temperature rises are observed in polymer processing flows such as injection molding or extrusion at high rates. The viscous dissipation effect plays an important role in natural convection in strong gravitational field processes on large scales, in geological process and in nuclear engineering in connection with the cooling of reactors. It is also necessary to study the heat transfer from an irregular surface because irregular surfaces are often present in many applications, such as radiator, heat

---

* Corresponding author. Tel.: 88-017-11265349
E-mail address: nazma@math.buet.ac.bd

Peer-review under responsibility of organizing committee of the 6th BSME International Conference on Thermal Engineering (ICTE 2014).

exchangers and heat transfer enhancement devices. The present study is to incorporate the idea that the effects of temperature dependent viscosity with natural convection boundary layer flow along a vertical wavy surface. However, it is known that this physical property (viscosity) may be change significantly with temperature. To predict accurately the flow behavior, it is necessary to take into account of viscosity.

The viscosity of the fluid to be proportional to a linear function of temperature, two semi-empirical formulae which was proposed by Charraudeau [1]. Larger scale surface non-uniformities are encountered, for example, in cavity wall insulating systems and grain storage containers. The only papers to date that study the effects of such non-uniformities on the vertical convective boundary layer flow of a Newtonian fluid are those of Yao [2], and Moulic and Yao [3]. The problem of free convection flow from a wavy vertical surface in presence of a transverse magnetic field was studied by Alam et al. [4]. Wang and Chen [5] investigated transient force and free convection along a vertical wavy surface in micropolar fluid. Hossain et al. [6] studied natural convection of fluid with temperature dependent viscosity from heated vertical wavy surface. Natural convection heat and mass transfer along a vertical wavy surface have been investigated by Jang et al. [7]. Molla et al. [8] have studied natural convection flow along a vertical wavy surface with uniform surface temperature in presence of heat generation/absorption. Viscous dissipation effects on MHD natural convection flow over a sphere in the presence of heat generation has been investigated by Alam et al [9]. Jha and Ajibade [10] studied the effect of viscous dissipation on natural convection flow between vertical parallel plates with time-periodic boundary conditions. Parveen and Alim [11] investigated fr**ee** convection flow along a vertical wavy surface with the effects of viscous dissipation on magnetic field.

The above literatures survey it is found that viscous dissipation effect on natural convection flow variation of viscosity with temperature along a vertical wavy surface has not been well investigated. In the present study is detailed numerically investigation of the temperature dependent viscosity on natural convection flow with viscous dissipation along a vertical wavy surface. The developed equations are made dimensionless by using suitable transformations. The non-dimensional equations are then transformed into non-linear equations by introducing a non-similarity transformation. The resulting non-linear equations together with their corresponding boundary conditions based on convection are solved numerically by using the finite difference method along with Newton’s linearization approximation [12]. Graphs and table are presented to show the important features of the solution.

Nomenclature

C_{fx}	local skin friction coefficient
C_p	specific heat at constant pressure (Jk/gK)
f	dimensionless stream function
g	acceleration due to gravity (m/s^2)
Nu_x	local Nusselt number
P	pressure of the fluid (N/m^2)
T	temperature of the fluid in the boundary layer (K)
T_w	temperature at the surface (K)
T_∞	temperature of the ambient fluid (K)
u, v	dimensionless velocity components along the (x, y) axes (m/s)
x, y	axis in the direction along and normal to the tangent of the surface

Greek symbols

α	amplitude-to-length ratio of the wavy surface
β	volumetric coefficient of thermal expansion (1/K)
θ	dimensionless temperature function
ψ	stream function (m^2/s)
μ	viscosity of the fluid (kg/ms)
ν	kinematic viscosity (m^2/s)
ρ	density of the fluid (kg/m^3)
$\sigma(x)$	surface profile function defined in equation (1)

Subscripts

w	wall conditions
∞	ambient conditions
Superscripts	
′	differentiation with respect to η

2. Formulation of the problem

The boundary layer analysis outlined below allows $\bar{\sigma}(X)$ being arbitrary, but our detailed numerical work assumed that the surface exhibits sinusoidal deformations. The wavy surface may be described by

$$Y_w = \bar{\sigma}(X) = \alpha \sin\left(\frac{n\pi X}{L}\right) \tag{1}$$

where L is the characteristic length associated with the wavy surface.
The geometry of the wavy surface and the two-dimensional cartesian coordinate system are shown in Fig. 1.

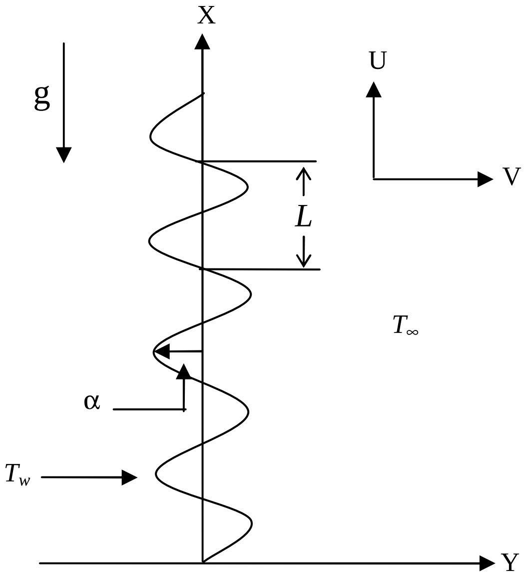

Fig. 1. Physical model and coordinate system

Under the usual Boussinesq approximation, the flow governed by the following dimensionless form of the governing equations:

$$\frac{\partial u}{\partial x} + \frac{\partial v}{\partial y} = 0 \tag{2}$$

$$u\frac{\partial u}{\partial x} + v\frac{\partial u}{\partial y} = -\frac{\partial p}{\partial x} + Gr^{1/4}\sigma_x\frac{\partial p}{\partial y} + \left(1+\sigma_x^2\right)(1+\varepsilon\theta)\frac{\partial^2 u}{\partial y^2} + \varepsilon\left(1+\sigma_x^2\right)\frac{\partial\theta}{\partial y}\frac{\partial u}{\partial y} + \theta \tag{3}$$

$$\sigma_x\left(u\frac{\partial u}{\partial x} + v\frac{\partial u}{\partial y}\right) = -Gr^{1/4}\frac{\partial p}{\partial y} + \sigma_x\left(1+\sigma_x^2\right)(1+\varepsilon\theta)\frac{\partial^2 u}{\partial y^2} + \varepsilon\sigma_x\left(1+\sigma_x^2\right)\frac{\partial\theta}{\partial y}\frac{\partial u}{\partial y} - \sigma_{xx}u^2 \tag{4}$$

$$u\frac{\partial\theta}{\partial x}+v\frac{\partial\theta}{\partial y}=\frac{1}{\Pr}\left(1+\sigma_x^2\right)\frac{\partial^2\theta}{\partial y^2}+vd\left(\frac{\partial u}{\partial y}\right)^2 \tag{5}$$

It is worth noting that the σ_x and σ_{xx} indicate the first and second differentiations of σ with respect to x, therefore, $\sigma_x = d\bar{\sigma}/dX = d\sigma/dx$ and $\sigma_{xx} = d\sigma_x / dx$.

where $\Pr=\frac{C_p\mu_\infty}{k}$ is the Prandtl number, $\varepsilon=\varepsilon^*(T_w-T_\infty)$ is the viscosity variation parameter and $vd=\frac{v^2 Gr}{L^2C_p(T_w-T_\infty)}$ is the viscous dissipation parameter.

There are very few forms of viscosity variation available in the literature. Among them we have considered that one which is appropriate for liquid introduced by Hossain et al. [6] as follows:

$$\mu=\mu_\infty[1+\varepsilon^*(T-T_\infty)] \tag{6}$$

where μ_∞ is the viscosity of the ambient fluid and ε^* is a constant evaluated at the film temperature of the flow $T_f=1/2(T_w+T_\infty)$.
Following Yao [2], here introduce the following non-dimensional variables

$$x=\frac{X}{L},\ y=\frac{Y-\bar{\sigma}}{L}Gr^{\frac{1}{4}},\ u=\frac{\rho L}{\mu_\infty}Gr^{-1/2}U,\quad v=\frac{\rho L}{\mu_\infty}Gr^{-1/4}\left(V-\sigma_x U\right)$$

$$\theta=\frac{T-T_\infty}{T_w-T_\infty},\sigma_x=\frac{d\bar{\sigma}}{dX}=\frac{d\sigma}{dx},Gr=\frac{g\beta(T_w-T_\infty)}{v^2}L^3,\ p=\frac{L^2}{\rho v^2}Gr^{-1}P$$

Eq. (4) indicates that the pressure gradient along the y-direction is $O(Gr^{-1/4})$, which implies that lowest order pressure gradient along x-direction can be determined from the inviscid flow solution. For the present problem this pressure gradient ($\partial p/\partial x=0$) is zero. Eq. (4) further shows that $Gr^{1/4}\partial p/\partial y$ is O(1) and is determined by the left-hand side of this equation. Thus, the elimination of $\partial p/\partial y$ from Eqs. (3) and (4) leads to

$$u\frac{\partial u}{\partial x}+v\frac{\partial u}{\partial y}=\left(1+\sigma_x^2\right)(1+\varepsilon\theta)\frac{\partial^2 u}{\partial y^2}-\frac{\sigma_x\sigma_{xx}}{1+\sigma_x^2}u^2+\varepsilon\left(1+\sigma_x^2\right)\frac{\partial u}{\partial y}\frac{\partial\theta}{\partial y}+\frac{1}{1+\sigma_x^2}\theta \tag{7}$$

The corresponding boundary conditions for the present problem are

$$\left.\begin{array}{ll}u=v=0,\quad \theta=1 & at\quad y=0\\ u=\theta=0,\quad p=0 & as\quad y\to\infty\end{array}\right\} \tag{8}$$

Now introduce the following transformations to reduce the governing equations to a convenient form:

$$\psi=x^{3/4}f(x,\eta),\quad \eta=yx^{-1/4},\quad \theta=\theta(x,\eta) \tag{9}$$

where η is the pseudo similarity variable, θ is the dimensionless temperature and ψ is the stream function.

Introducing the transformations given in Eq. (9) into Eqs. (7) and (5) the momentum and energy equations are transformed the following forms:

$$\left(1+\sigma_x^2\right)(1+\varepsilon\theta)\,f''' + \frac{3}{4}ff'' - \left(\frac{1}{2}+\frac{x\sigma_x\sigma_{xx}}{1+\sigma_x^2}\right)f'^2 + \frac{1}{1+\sigma_x^2}\theta + \varepsilon\left(1+\sigma_x^2\right)\theta' f'' = x\left(f'\frac{\partial f'}{\partial x} - f''\frac{\partial f}{\partial x}\right) \tag{10}$$

$$\frac{1}{\Pr}\left(1+\sigma_x^2\right)\theta'' + \frac{3}{4}f\theta' + vdxf''^2 = x\left(f'\frac{\partial \theta}{\partial x} - \theta'\frac{\partial f}{\partial x}\right) \tag{11}$$

The boundary condition (8) now takes the following form:

$$\left.\begin{array}{ll} f(x,o) = f'(x,o) = 0, & \theta(x,o) = 1 \\ f'(x,\infty) = 0, & \theta(x,\infty) = 0 \end{array}\right\} \tag{12}$$

The rate of heat transfer in terms of the local Nusselt number, Nu_x and the local skin friction coefficient, C_{fx} take the following forms:

$$Nu_x (Gr/x)^{-1/4} = -\sqrt{1+\sigma_x^2}\,\theta'(x,o) \tag{13}$$

$$C_{fx}(Gr/x)^{1/4}/2 = (1+\varepsilon)\sqrt{1+\sigma_x^2}\; f''(x,o) \tag{14}$$

3. Numerical approach

The nonlinear system of partial differential equations that govern the flow are solved numerically with the help of implicit finite difference method. The set of Eqs. (10)–(11) are written in terms of a system of first order equations, which are then expressed in finite difference form by approximating the functions and their derivatives in terms of the central differences in both coordinate directions. Denoting the mesh points in the x and η-plane by x_i and η_j where i = 1, 2 ,…., M and j = 1, 2,…,N, central difference approximations are made, such that those equations involving x explicitly are centered at $(x_{i-1/2}, \eta_{j-1/2})$ and the remainder at $(x_i, \eta_{j-1/2})$, where $\eta_{j-1/2} = 1/2(\eta_j + \eta_{j-1})$ etc. The above central difference approximations reduce the system of first order differential equations to a set of non-linear difference equations for the unknown at x_i in terms of their values at x_{i-1}. The resulting set of non-linear difference equations are solved by using the Newton's quasi-linearization method. The Jacobian matrix has a block-tridiagonal structure and the difference equations are efficiently solved using a block-matrix version of the Thomas algorithm. During the program test, the convergent criteria for the relative errors between two iterations are less 10^{-5}. A uniform grid of 201 points is used in x- direction with $\Delta x = 0.05$, while a non-uniform grid of 76 points lying between $\eta = 0.0$ and 10.00 is chosen.

4. Results and discussion

Solutions of the present problem are obtained in terms of the skin friction coefficient, Nusselt number, the streamlines as well as the isotherms for different values of the viscous dissipation parameter vd(= 0.0, 1.0, 4.0, 8.0), variable viscosity variation parameter ε (= 5, 10, 15 and 20), the amplitude-to-length ratio of the wavy surface α = 0.3 and Prandtl number Pr = 1.73 which correspond to the water at 100^0C.

The influence of viscous dissipation parameter on the produced skin friction coefficient C_{fx} and reduced local rate of heat transfer Nu_x at different position of x are demonstrated through in Figs. 2(a) and 2(b) respectively while α = 0.3, ε = 5.0 and Pr =1.73. For increasing values of vd the skin friction coefficient increases along the upward direction of the surface. It is observed that skin friction coefficient increases by approximately 64% for the increasing value of vd from 0.0 to 8.0. The opposite result observed for heat transfer rate.

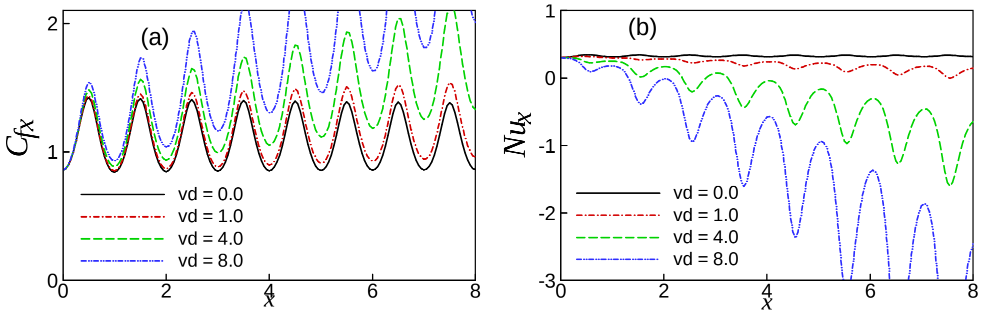

Fig. 2. Effect of *vd* on (a) skin friction coefficient C_{fx} and (b) rate of heat transfer Nu_x against *x*.

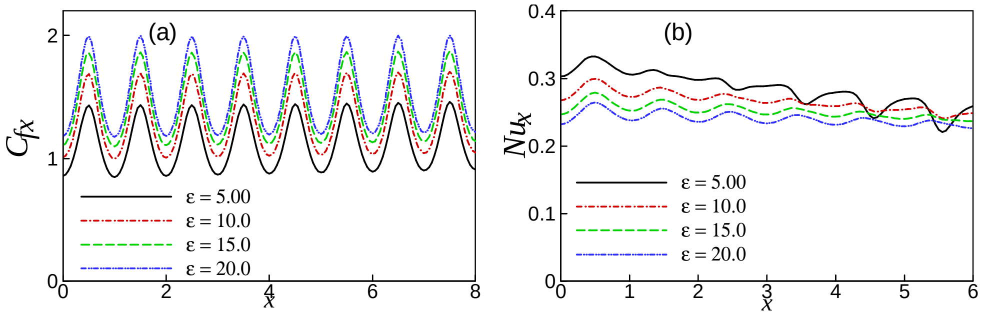

Fig. 3. Effect of *ε* on (a) skin friction coefficient C_{fx} and (b) rate of heat transfer Nu_x against *x*.

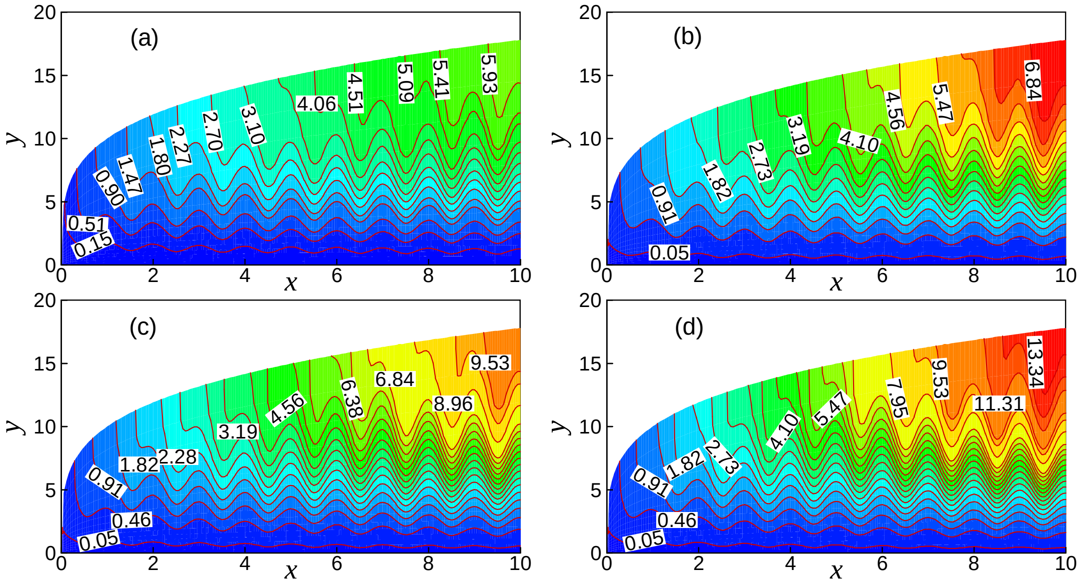

Fig. 4. Streamlines for (a) *vd* = 0.0 (b) *vd* = 1.0 (c) *vd* = 4.0 and (d) *vd* = 8.0 while Pr = 1.73, *ε* = 5.0 and α = 0.3.

Numerical values of the skin friction coefficient and the rate of heat transfer in terms of the local Nusselt number are depicted graphically in Fig. 3 against the axial distance of *x* in the interval [0, 8] for the effect of temperature dependent viscosity keeping all other controlling parameters α = 0.3, *vd* = 0.5 and Pr = 1.73. Fig. 3(a) indicates that increasing values of the viscosity parameter leads to enhance in the results of skin friction coefficient C_{fx} and the local skin friction coefficient increases by approximately 26% as *ε* changes from 5.0 to 20.0. The rate of heat transfer decreases by approximately 21% due to the increased value of ε which is evident from Fig. 3(b). When the ε increases, the temperature of the surface rises. For balancing the temperature difference between surface and fluid the local Nusselt number Nu_x decreases.

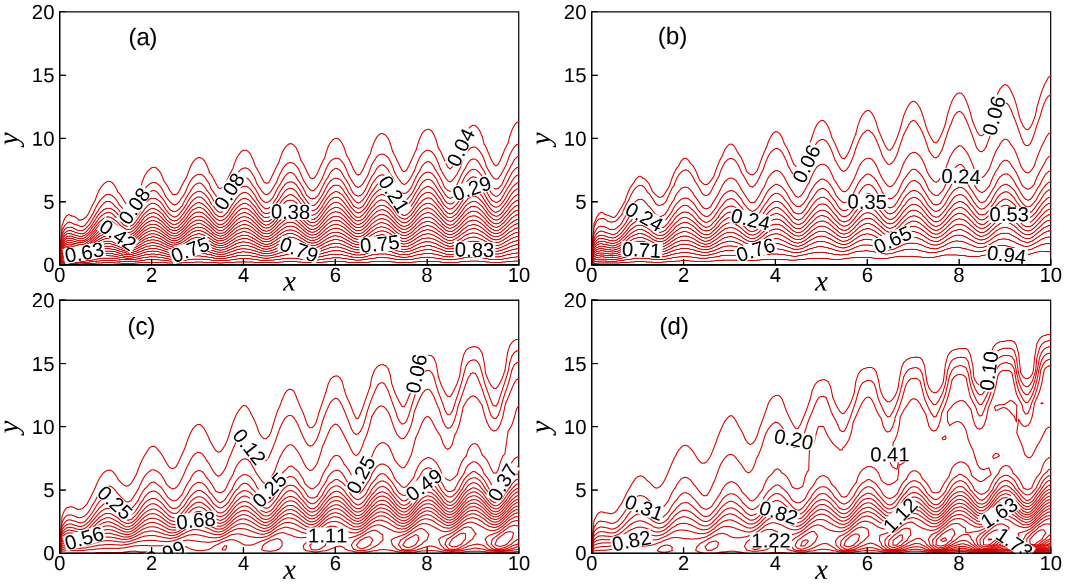

Fig. 5. Isotherms for (a) (a) vd = 0.0 (b) vd = 1.0 (c) vd = 4.0 and (d) vd = 8.0 while Pr = 1.73, ε = 5.0 and α = 0.3.

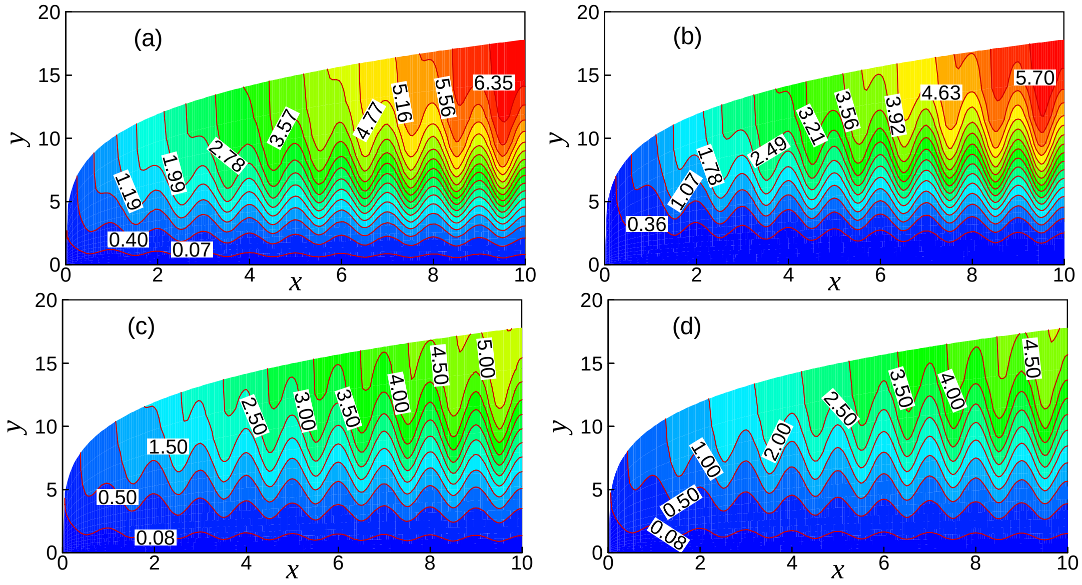

Fig. 6. Streamlines for (a) ε = 5.0 (b) ε = 10.0 (c) ε = 15.0 and (d) ε = 20.0 while α = 0.3, vd = 0.5 and Pr = 1.73.

Figs. 4 and 5 show the effect of vd on the formation of streamlines and isotherms respectively for α = 0.3, ε = 5.0 and Pr =1.73. It is observed that without effect of viscous dissipation parameter (vd = 0.0) the value of stream function, that is, ψ_{max} is 5.93. The maximum values of stream function, that is, ψ_{max} are 6.84 for vd = 1.0, 9.53 for vd = 4.0 and 13.34 for vd = 8.0 respectively. Finally, it is concluded that with the effect of the vd, the flow flux in the boundary layer increases due to increase the buoyancy force. From Fig. 5, it is noted that for the effect of vd, the temperature enhances within the boundary layer and hence the thermal boundary layer grows thicker.

The effect of variation of the surface roughness on the streamlines and isotherms for the values of ε are depicted by the Figs. 6 and 7 respectively while $\alpha = 0.3$, $vd = 0.5$ and $\Pr = 1.73$. Fig. 6 depicts that the maximum values of ψ decreases while the values of ε increases. The maximum values of ψ, that is ψ_{max} are 6.35, 5.70, 5.00 and 4.50 for ε = 5.0, 10, 15 and 20 respectively. It is concluded from Fig. 7 that with the effect of ε the temperature of the fluid increases within the boundary layer. The thermal boundary layer becomes thicker.

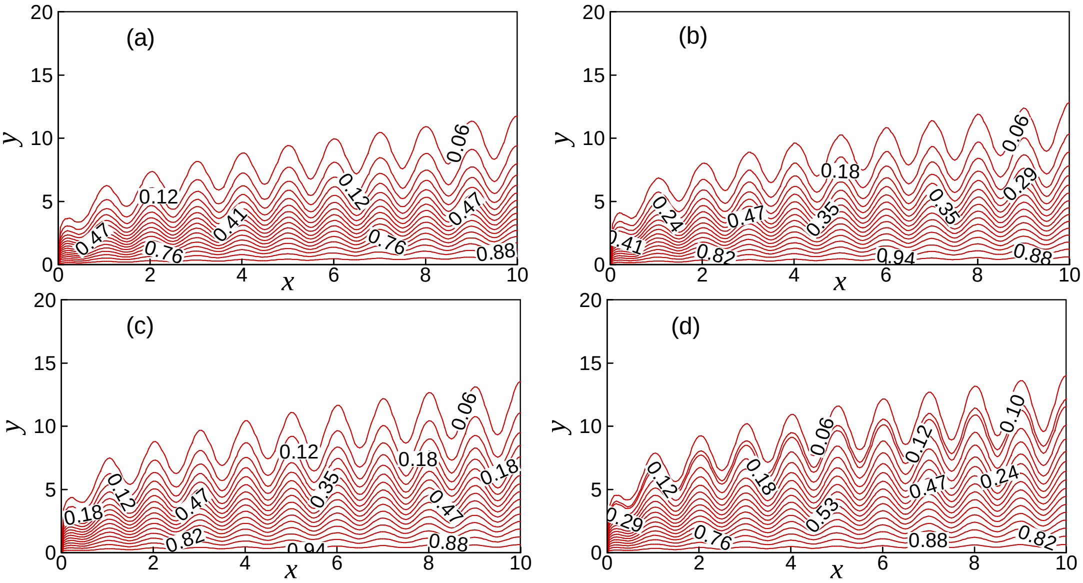

Fig. 7. Isotherms for (a) ε = 5.0 (b) ε = 10.0 (c) ε = 15.0 and (d) ε = 20.0 while $\alpha = 0.3$, $vd = 0.5$ and $\Pr = 1.73$.

Conclusion

The effect of viscous dissipation and temperature dependent viscosity on natural convection flow along a vertical wavy surface has been studied numerically. It is noted that the local skin friction coefficient increases for increasing values of viscous dissipation parameter. But the local rate of heat transfer reduced. For increasing values of viscous dissipation parameter the velocity and thermal boundary layer become thicker. The local skin friction coefficient enhanced for increasing values of temperature dependent viscosity. But with the increase of variable viscosity the local rate of heat transfer decreases. The velocity and the thickness of the momentum boundary layer decrease. Fluid temperature increases and the thermal boundary layer grow thicker due to increase value of variable viscosity.

References

[1] J. Charraudeau, Influence de gradients de properties physiques en convection force application au cas du tube, Int. J. Heat Mass Transfer, 18 (1975) 87-95.

[2] L. S. Yao, Natural convection along a vertical wavy surface, ASME J. Heat Transfer, 105 (1983) 465–468.

[3] S. G. Moulic and L. S. Yao, Natural convection along a wavy surface with uniform heat flux, ASME J. Heat Transfer, 111 (1989) 1106–1108.

[4] K. C. A. Alam, M. A. Hossain and D. A. S. Rees, Magnetohydrodynamic free convection along a vertical wavy surface, Int. J. Appl. Mech. Engrg, 1 (1997) 555–566.

[5] C. C. Wang and C. K. Chen, Transient force and free convection along a vertical wavy surface in micropolar fluid, Int. J. Heat Mass Transfer, 44 (2001) 3241–3251.

[6] M.A. Hossain, S. Kabir and D.A.S. Rees, Natural convection of fluid with temperature dependent viscosity from heated vertical wavy surface, ZAMP, 53 (2002) 48–52.

[7] J. H. Jang, W. M. Yan and H. C. Liu, Natural convection heat and mass transfer along a vertical wavy surface, Int. J. Heat Mass Transfer, 46 (2003) 1075–1083.

[8] M. M. Molla, M. A. Hossain and L. S. Yao, Natural convection flow along a vertical wavy surface with uniform surface temperature in presence of heat generation/absorption, Int. J. Therm. Sci., 43 (2004) 157-163.

[9] M.M. Alam, M.A. Alim and M.M.K. Chowdhury, Viscous dissipation effects on MHD natural convection flow over a sphere in the presence of heat generation, Nonlinear Analysis: Modelling and Control, 12 (2007) 447-459.

[10] B. K. Jha and A.O. Ajibade, Effect of viscous dissipation on natural convection flow between vertical parallel plates with time-periodic boundary conditions, J. Thermophysics and Aeromechanics, 18 (2011) 561-571.

[11] N. Parveen and M. A. Alim, Free convection flow along a vertical wavy surface with the effects of viscous dissipation on magnetic field, Int. J. Energy Technology, 6 (2014) 1–10.

[12] H. B. Keller, Numerical methods in boundary layer theory, Ann. Rev. Fluid Mech., 10 (1978) 417-433.

Available online at www.sciencedirect.com

ScienceDirect

Procedia Engineering 00 (2015) 000–000

Procedia Engineering

www.elsevier.com/locate/procedia

6th BSME International Conference on Thermal Engineering (ICTE 2014)

Effect of magnetic field on natural convection in a *C*-shaped cavity filled with ferrofluid

Satyajit Mojumder*, Sourav Saha, Sumon Saha, M.A.H. Mamun

Department of Mechanical Engineering , Bangladesh University of Engineering and Technology,Dhaka-1000.

Abstract

In this paper, natural convection heat transfer has been analyzed for a *C*-shaped cavity filled with ferrofluid. Cobalt-kerosene ferrofluid is selected here for different solid volume fractions ($\varphi = 0 \sim 0.15$). Galerkin weighted residual method is applied to obtain the numerical solution. Simulations are carried out for a wide range of Rayleigh ($Ra = 10^3 \sim 10^7$) and Hartmann ($Ha = 0 \sim 100$) numbers for both the ferrofluid and the plain fluid. From this work, it is found that higher Rayleigh number enhances the heat transfer rate significantly, whereas presence of magnetic field tries to retard convection. Moreover, addition of 15% solid volume fraction of nanoparticle can augment the heat transfer rate up to 52.65% at moderate Rayleigh number compared to the base fluid. By an optimization of these parameters, effective heat transfer control equipment can be developed. Results are interpreted on the basis of streamline and isotherm patterns, and average Nusselt number of the heated wall and average fluid temperature of the cavity.

Peer-review under responsibility of organizing committee of the 6th BSME International Conference on Thermal Engineering (ICTE 2014).

*Keywords:*Ferrofluid; *C*-shaped cavity; Magnetic field; Natural convection.

1. Introduction

Nanofluid has been given enoromus importance for enhancement of heat transfer due to its wide application fields. It has application in solar thermal collector, desalination, cavity problem [1-4] and so on. It has been reported that nano-sized (0 ~ 100 nm) of metal, metal oxide and carbonaceous particle such as carbon nanotube (cnt) have

---

* Corresponding author. Tel.:+880-1737-434034
E-mail address: sjit018@gmail.com

Peer-review under responsibility of organizing committee of the 6th BSME International Conference on Thermal Engineering (ICTE 2014).

higher thermal conductivity which enhance the effective thermal conductivity of the mixuture of the base fluid with it. Different types of nanofluid such as alumina-water, *Cu*-water, TiO_2-water are very common and widely used due to their low cost. On the other hand, cnt, diamond, silver, gold nanoparticles give better heat transfer when mixed with different base fluids such as water, glycol, mineral oil, etc. Among different nanofluids, ferrofluid is actually quite old. Though it has a great potential for better heat transfer, it has been overlooked in the recent years. Carbon nanotube based nanofluids are stirring the scientific world at the moment [5-7]. In most of the cases of ferrofluids, the nano particles are ferrous particles. Besides, some other materials like nickel and cobalt are also used. Moshen and Mofid [8] recently analyzed free convection of nickel ferrofluid in a square cavity which was heated from the below and subjected to a magnetic field. They concluded that larger solid volume fraction of nanoparticles in the base fluid provided better heat transfer. Basically, ferrofluid can be very much effecive when it is applied in a cavity under magnetic field because the nanoparticle of the ferrofluid has magnetic susceptibility. Recently, some studies show that ferrofluid is a very good alterantive to conventional nanofluids [9-10].

Shape of the cavity is an important factor which basically depends on the actual physical problem. Different shapes of cavity have been analyzed for nanofluid in presence of magnetic field extensively. Among them square, rectangular, circular and trapezoidal cavities are very common [11-12]. Bakier [13] analyzed the *C*-shaped cavity filled with nanofluid, whose sides are open and side walls are discretely heated and reported that heater length had significant effect on the heat transfer.

The objective of this paper is to investigate the effect of implementation of a ferrofluid in a *C*-shaped cavity subjected to magnetic field and has one of its side walls isothermally heated. Special attention is given to analyze the effect of Rayleigh and Hartmann numbers on the characteristics of convection heat transfer inside the cavity.

2. **Problem formulation**

2.1. *Physical modelling*

The details of the *C*-shaped cavity is shown in Fig. 1. The top and the bottom walls along with some portions of the outer-right vertical walls are kept adiabatic. Left side wall is maintained at a high temperature (T_h) and the notched portion of the right side is maintained at a low temperature T_c ($< T_h$). The entire cavity is filled with cobalt-kerosene ferrofluid. The Cartesian co-ordinate system of the problem is well defined and the gravity is acting in the negative direction of the *y*-axis. The cavity has an equal height and width of *L*. Aspect ratio of the notch (*a/b*) is kept unity and $a/2L = c/L = 0.25$. A magnetic field with strength B_o is applied on the right side of the cavity along the negative horizontal direction. The radiation effect and viscous dissipation are neglected for the simplification of the problem.

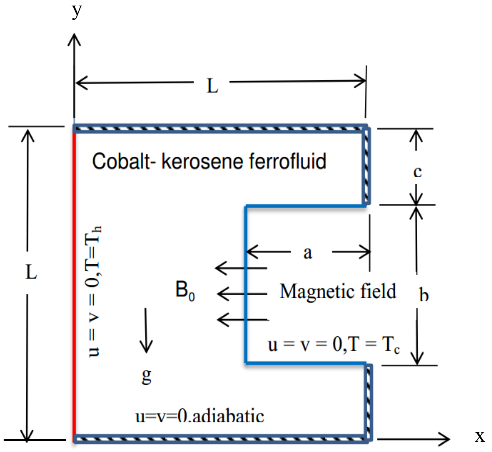

Fig. 1. Schematic diagram of a *C*-shaped cavity filled with cobalt-kerosene ferrofluid.

2.2. *Mathematical formulation*

The two-dimensional steady state continuity, momentum and energy equations are applied to model this problem for flow and thermal fields. The working fluid is assumed to be incompressible Newtonian with constant properties and thermal equlibrium between the ferromagnetic particles and the base fluid are assumed. Boussinesq approximation is applied for the density variation of the fluid. From the above stated assumptions, the non-dimensional governing equations take the form as

$$\frac{\partial(U\delta)}{\partial X}+\frac{\partial(V\delta)}{\partial Y}=\frac{\partial}{\partial X}\left(\Gamma_\delta\frac{\partial\delta}{\partial X}\right)+\frac{\partial}{\partial Y}\left(\Gamma_\delta\frac{\partial\delta}{\partial Y}\right)+S_\delta. \tag{1}$$

Here non-dimensional dependent variables are designated by δ and corresponding diffusion and source term are defined by Γ_δ and S_δ, respectively and those are summarized in Table 1.

Table 1. A summary of the terms of the non-dimensional governing equations (1).

Equations	δ	Γ_δ	S_δ
Continuity	1	0	0
U-momentum	U	$\mu_{ff}/\rho_{ff}\alpha_f$	$-\partial P/\partial X$
V-momentum	V	$\mu_{ff}/\rho_{ff}\alpha_f$	$-\partial P/\partial Y + (\rho\beta)_{ff}RaPr\Theta / (\rho_{ff}\beta_f) - Ha^2PrV$
Thermal energy	Θ	α_{ff}/α_f	0

Scales which are adopted to obtain the above non-dimensional governing equation are presented below

$$X=\frac{x}{L},\ Y=\frac{y}{L},U=\frac{uL}{\alpha_f},\ V=\frac{vL}{\alpha_f},\ P=\frac{\left(p+\rho_f gy\right)L^2}{\rho_{ff}\ \alpha_f^{\ 2}},\ \ \Theta=\frac{\left(T-T_c\right)}{\left(T_h-T_c\right)}. \tag{2}$$

In the aforementioned equations, *U*, *V*, *P* and *Θ* are non-dimensional velocities, pressure and temperature respectively. Here subscripts '*ff*' and '*f*' stand for the properties of the ferrofluid and the base fluid respectively.

The non-dimensional governing parameters Rayleigh number (*Ra*), Prandtl number (*Pr)* and Hartmann number (*Ha)* can be defined as

$$Ra=\frac{g\beta_f L^3\left(T_h-T_c\right)}{\alpha_f\nu_f},Pr=\frac{\nu_f}{\alpha_f},Ha=B_oL\sqrt{\frac{\sigma_{ff}}{\rho_{ff}\nu_f}}, \tag{3}$$

where σ_{ff} indicates the electrical conductivity of the ferrofluid.

The density of ferrofluid which is assumed to be constant can be expressed as,

$$\rho_{ff}=\left(1-\varphi\right)\rho_f+\varphi\rho_s. \tag{4}$$

Here property of solid ferromagnetic particles (cobalt) is represented by subscript 's'. In the above equation, solid volume fraction (φ) has significant effect on thermal diffusivity of ferrofluid which is quite different from the base fluid and can be modeled as,

$$\alpha_{ff}=\frac{k_{ff}}{\left(\rho c_p\right)_{ff}}, \tag{5}$$

where heat capacitance of ferrofluid $(\rho c_p)_{ff}$ can be found by,

$$\left(\rho c_p\right)_{ff}=\left(1-\varphi\right)\left(\rho c_p\right)_f+\varphi\left(\rho c_p\right)_s. \tag{6}$$

In addition, the thermal expansion coefficient (β_{ff}) of the ferrofluid can be obtained as

$$\left(\rho\beta\right)_{ff}=\left(1-\varphi\right)\left(\rho\beta\right)_f+\varphi\left(\rho\beta\right)_s. \tag{7}$$

Moreover, dynamic viscosity of the ferrofluid (μ_{ff}) and can be expressed as,

$$\mu_{ff}=\frac{\mu_f}{\left(1-\varphi\right)^{2.5}}. \tag{8}$$

Effective thermal conductivity of the ferrofluid can be described as,

$$\frac{k_{ff}}{k_f} = \frac{k_s + 2k_f - 2\varphi\left(k_f - k_s\right)}{k_s + 2k_f + \varphi\left(k_f - k_s\right)}, \tag{9}$$

The thermophysical properties of the base fluid (kerosene) and the ferromagnetic particle (cobalt) are given in Table 2.

Table 2. Thermophysical properties of kerosene and cobalt [8].

	c_p ($\mathrm{Jkg^{-1}K^{-1}}$)	ρ ($\mathrm{kgm^{-3}}$)	k ($\mathrm{Wm^{-1}K^{-1}}$)	β ($\mathrm{K^{-1}}$)	μ (PaS)
Fluid **:** Kerosene	2090	780	0.149	9.9×10^{-4}	0.00164
Solid **:** Cobalt	420	8900	100	1.3×10^{-5}	-

Boundary conditions in the dimensionless form for the present problems are given in Table 3.

Table 3. Nondimensional boundary conditions of the present problem.

All walls	$X = 0$ $0 \leq Y \leq 1$	$0 \leq X \leq 1$ $Y = 0, 1$	$X=1$ $0 \leq Y \leq 0.25,\ 0.75 \leq Y \leq 1$	$0.5 \leq X \leq 1$ $Y = 0.25, 0.75$	$X = 0.5$ $0.25 \leq Y \leq 0.75$
$U = V = 0$	$\Theta = 1$	$\partial\Theta/\partial Y = 0$	$\partial\Theta/\partial X = 0$	$\Theta = 0$	$\Theta = 0$

Average Nusselt number is evaluated for the vertical heated wall and calculated from the following expression

$$Nu = -\frac{k_{ff}}{k_f}\int_0^1 \frac{\partial\Theta}{\partial X}\,dY. \tag{10}$$

Average fluid temperature inside the cavity can also be found by the following expression

$$\Theta_{av} = \frac{1}{A}\int \Theta dA, \tag{11}$$

Where A is the non-dimensional area which can be evaluated by $A = 1 - ab/L^2$.

Flow field of the present problem is visualized through streamline which is obtained from stream function. Stream function is defined from velocity components *U* and *V*. Relation between the stream function and velocity components for a two-dimensional flow is given by,

$$U = \frac{\partial\Psi}{\partial Y},\ V = -\frac{\partial\Psi}{\partial X}. \tag{12}$$

3. **Numerical procedure and grid independency test**

The entire domain of *C*-shaped cavity is discritized into triangular mesh elements of different size. Galerkin weighted residual method of finite element analysis is applied to obtain the numerical solution. Non-dimensional governing equations are transformed into a set of algebric equations and iteration technique is employed to find the converged solution. The convergence criterion is set to 10^{-5}, so that $|\gamma^{m+1}-\gamma^{m}| \leq 10^{-5}$ where γ is the general dependent variable. A grid sensitivtiy test is performed to ensure the numerical accuracy of the computation. The details of the grid test is shown in Table 4. It can be found that with the increment of number of the elements, the average Nusselt number is decreased and average fluid temperature is increased simultanously. After reaching the grid size having element number 4526, the average Nusselt number and average fluid temperature becomes less sensitive to the number of elements. So for the present problem, grid having element number 4526 is taken as the optimum grid and all the simulations are carried out at this specified grid.

Table 4. Grid sensitivity test for $Ra = 10^5$, $Ha = 25$ with base fluid ($\varphi = 0$).

Number of elements	136	544	2176	4526	8704
Average Nusselt number (Nu)	3.9209	3.6475	3.5818	3.5689	3.5699
Average fluid temperature (Θ_{av})	0.4025	0.4027	0.4027	0.4027	0.4027

4. **Code validation**

A code validation is performed for checking the reliability of the present code. The present code is compared with the results of Ghasemi *et al.* [14] on the basis of average Nusselt number for two different Hartmann numbers at $Ra = 10^5$. The details of the code validation is presented in Fig. 2. From the figure, it is found that the present code is in very close agreement with the published result. Thus the numerical accuracy of the present work is ensured.

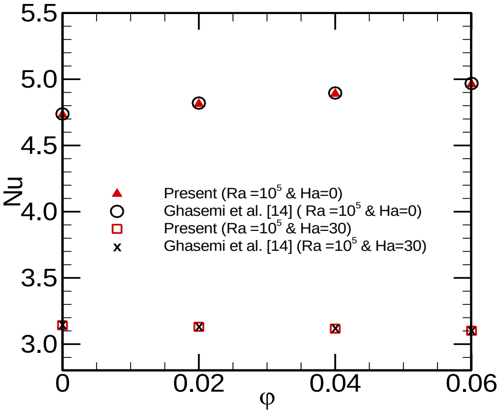

Fig. 2. Comparison of average Nusselt number as a function of solid volume fraction for $Ha = 0$ and 30 at $Ra = 10^5$ with Ghasemi *et al.* [14].

5. **Results and Discussions**

Goal of this investigation is to find out the effect of Rayleigh and Hartmann numbers on natural convection inside a *C*-shaped cavity containing cobalt-kerosene ferrofluid. Consequently, Rayleigh and Hartmann numbers are varied to compare heat transfer performance between plain fluid and cobalt-kerosene ferrofluid in terms of streamline and isotherm contours, average Nusselt number and average temperature of the fluid. Influence of Rayleigh number is observed by varying its value from 10^3 to 10^7 and Hartmann number is varied from 0 to 100 for the present analysis. To intensify the comparison, 15% solid volume fraction of ferromagnetic particles ($\varphi = 0.15$) is selected as representative of ferrofluid.

5.1. Effect of Rayleigh number

Fig. 3 depicts influence of Rayleigh number on streamline and isotherm contours and compares between flow scenarios for ferrofluid ($\varphi = 0.15$) and plain fluid ($\varphi = 0$). The analysis shown here is presented for $Ha = 25$, while varying Rayleigh numbers ($Ra = 10^5$, 10^6 and 10^7). Figs. 3(a), (b) and (c) show streamline patterns for $Ra = 10^5$, 10^6 and 10^7 respectively. A large vortex is observed inside the cavity with clockwise rotation for both ferrofluid and plain fluid. The vortex has its center near the middle of the enclosure and adjacent to the left wall. The vortex seems stretched in the narrower regions of the cavity. This particular shape of the vortex is due to the result of thermal buoyant force generated by the heated vertical left wall. Fluid inside the cavity gets heat from the left wall and the density of the fluid becomes lower adjacent to the heated wall. As a result, fluid close to the heated left wall becomes lighter at first and then moves in the upward direction along the wall. Eventually, the heat is transferred to the longest corner of the cavity. On the other hand, fluid near the cold wall has higher density comparatively. Due to its higher density, fluid near the cold wall moves downward creating a clockwise current inside the cavity. This tendency of moving downward is higher near the vertical portion of the cold wall than the horizontal portions of it. As the Rayleigh number is increased, strength of the vortex becomes higher and at $Ha = 25$, $Ra = 10^7$ and $\varphi = 0$, it has a value of Ψ_{min} = -28.9862. Introducing ferrofluid (φ = 0.15) the strength of the central vortex reduce to Ψ_{min} = -27.4823. Moreover, the vortex tends to elongate in the horizontal corner direction. This is due to higher temperature difference between the side walls as indicated by high Rayleigh number. By the introduction of ferrofluid, a slight shift in the position of streamlines can be attained without any significant improvement in the strength of the flow. However, more streamlines with higher value of stream function are observed near the middle of the cavity. This occurs because ferrofluid has improved thermal properties, especially higher thermal conductivity compared to plain fluid. From Figs. 3(d), (e) and (f), a comparison between isotherm contours for ferrofluid and plain fluid can be made at $Ra = 10^5$, 10^6 and 10^7 respectively for Ha = 25. Near the hot and the cold walls, the isotherms are nearly parallel to each other. This pattern indicates the development of thermal boundary layers near the hot and the cold walls. Isotherms near the middle of the enclosure are distorted showing evidence of increased convection. The pattern of isotherm contours is the same for both ferrofluid and plain fluid. However, at $Ra = 10^5$ and 10^6, there is a clear difference in the formation of isotherm contours between ferrofluid and plain fluid.

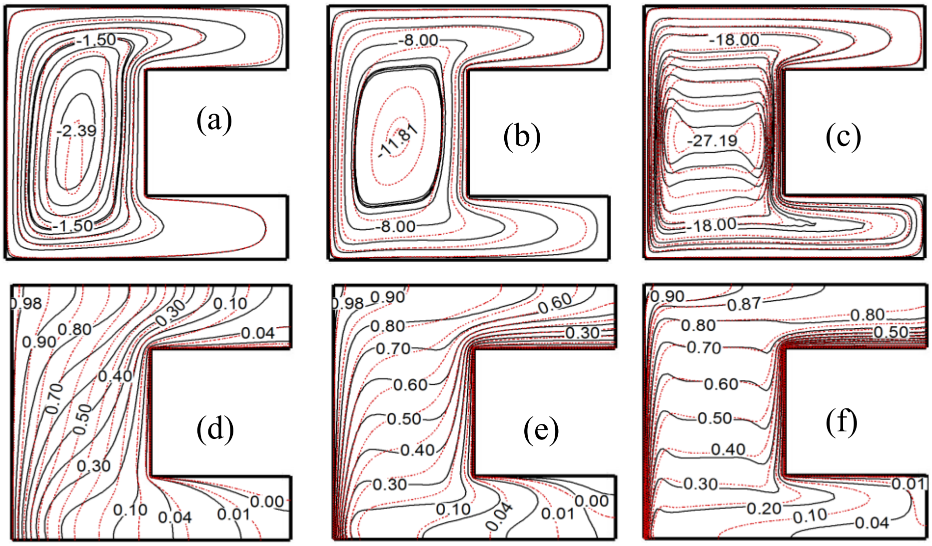

Fig. 3. Comparison of streamline and isotherm contours for (a), (d) $Ra = 10^5$, (b), (e) $Ra = 10^6$; (c), (f) $Ra = 10^7$ at Ha = 25. Figures in the top row are for streamline, whereas those in the bottom row represent isotherm contours. The solid line in each figure represents the data for plain fluid (φ = 0), whereas the dashed line represents ferrofluid with φ = 0.15.

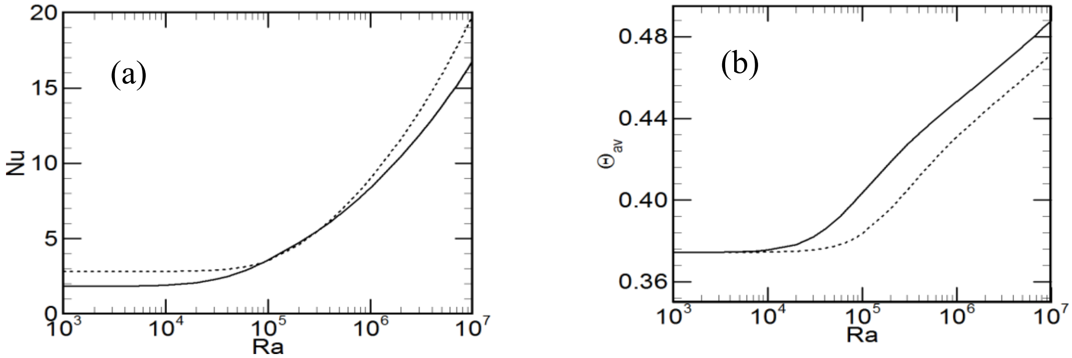

Fig. 4. Variation of (a) average Nusselt number of the heated wall and (b) average temperature of fluid inside the cavity as a function of Ra for Ha = 25. The solid line indicates results for the plain fluid and the dashed line for the ferrofluid.

For ferrofluid, the isotherm contours are less distorted in general and more isotherms with higher values are seen at the middle of the enclosure. This occurs because of the improved thermal conductivity of ferrofluid which ensures increased heat transfer. With higher value of Rayleigh number, the isotherm patterns are greatly distorted at the middle causing better convection. There is no remarkable difference in the isotherms between ferrofluid and plain fluid at Ra = 10^7 because convection becomes strong for both ferrofluid and plain fluid. At Ra = 10^7, isotherms become almost horizontal at the middle of the cavity because of very steep temperature difference between the walls.

Figs. 4(a) and (b) show the influence of Rayleigh number on average Nusselt number at the heated wall and average temperature of the fluid for Ha = 25. From Fig. 4(a), it can be observed that with increasing Rayleigh number, average Nusselt number increases for both ferrofluid and plain fluid. Rate of this increment is low in the range of $10^3 \leq Ra \leq 10^5$. When $Ra > 10^5$, average Nusselt number increases at an elevated rate with Ra. Ferrofluid always gives better heat transfer compared to plain fluid except in the region of Ra = 10^5. In this region, both ferrofluid and plain fluid show equal performance. Fig. 4(b) shows that, average temperature of the ferrofluid inside the cavity increases with increasing Rayleigh number. Rate of increment of average temperature is low up to Ra = 10^4 and after that average temperature increases very rapidly. Throughout the entire range of Rayleigh number, average temperature of plain fluid is higher than that of the ferrofluid. Both of these outcomes suggest that use of ferrofluid in place of plain fluid might result in better heat transfer.

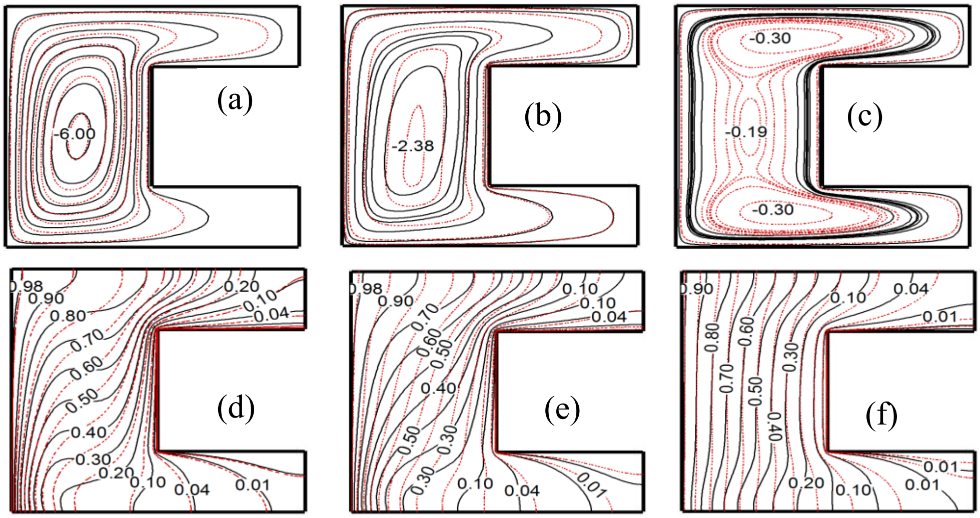

Fig. 5. Comparison of streamline and isotherm contours for (a), (d) Ha = 10; (b), (e) Ha = 25; (c), (f) Ha = 100 at Ra = 10^5. Figures in the top row are for streamline, whereas those in the bottom row represent isotherm contours. The solid line in each figure represents the data for plain fluid whereas the dashed line represents ferrofluid.

5.2. Effect of Hartmann number

Effect of Hartmann number on the streamline and the isotherm contours is presented in Fig. 5. Here, Hartmann number is varied from 0 to 100 at Ra = 10^5. As representative, comparison between ferrofluid and plain fluid in terms of streamlines and isotherms is shown for Ha = 10, 25 and 100. For Ha = 10 and 25, a clockwise rotating vortex is observed inside the cavity. At Ha = 100, this vortex splits into two weak vortices at the top and the bottom of the cavity. The most noticeable change in the streamline pattern is the reduction of stream function value with higher Hartmann numbers. Increasing Hartmann number induces stronger magnetic field, which produces Lorentz force acting on the flow domain. This force reduces the strength of the flow current inside the cavity. Since ferrofluid contains magnetic particle in it, it has higher magnetic susceptibility than plain fluid. Consequently, high Hartmann number influences ferrofluid more intensely than plain fluid. At Ha = 100, weakening of convective current introduces the two weaker vortices at the top and the bottom of the cavity as mentioned earlier. Figs. 5(d),

(e) and (f) show isotherm contours for *Ha* = 10, 25 and 100 respectively at *Ra* = 10^5. For both ferrofluid and plain fluid at *Ha* = 10 and 25, isotherms are parallel to each other near the heated and the cold walls, while those are distorted in the center region of the cavity. This pattern evolves due to the development of boundary layers near the heated and the cold walls as well as strong convection in the middle of the cavity. Analysis of isotherm contours reveals one interesting point at higher Hartmann number (*Ha* = 100). When *Ha* = 100, isotherms for both plain fluid and ferrofluid have similar distribution and are almost vertical. This particular pattern suggests very weak convection where conduction effect is more dominant.

Figs. 6(a) and (b) depict variation in average Nusselt number at the heated wall and average temperature of the fluid with Hartmann numbers at *Ra* = 10^5. Fig. 6(a) shows that value of average Nusselt number at the heated wall decreases with increasing Hartmann numbers. It agrees with the previous observation where it was found that Hartmann number has an adverse effect on the flow strength inside the cavity. Average Nusselt number decreases very rapidly up to *Ha* = 20 for both plain fluid and ferrofluid. At higher value of Hartmann number ($Ha \geq 40$), value of *Nu* becomes more or less constant for ferrofluid, whereas it is decreasing for the plain fluid. Average Nusselt number is always greater for ferrofluid than plain fluid except within the region of $20 \leq Ha \leq 30$, where the values of *Nu* for both ferrofluid and plain fluid are almost same. Fig. 6(b) exhibits the change in average temperature of the fluid with Hartmann number at *Ra* = 10^5. One can notice from the figure that average temperature is always greater for plain fluid. Increasing Hartmann number causes a reduction in the value of average temperature of the fluid inside the cavity. This reduction occurs at an elevated rate up to low Hartmann number ($Ha \leq 22$) for ferrofluid and comparatively moderate Hartmann number ($Ha \leq 40$) for plain fluid. At higher Hartmann number ($Ha > 40$), average temperature of the fluid is almost constant for ferrofluid.

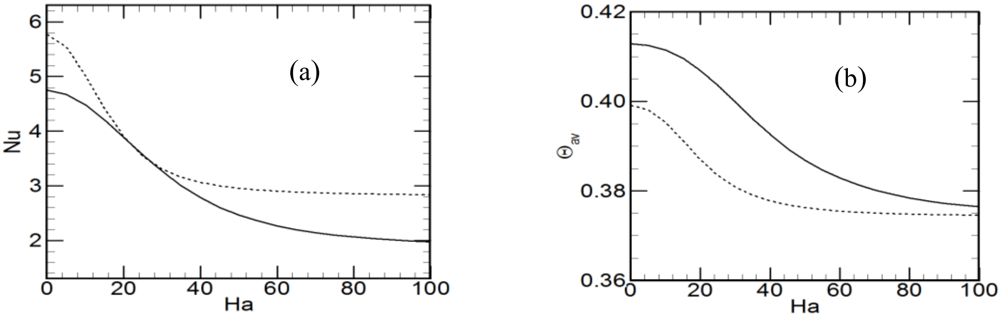

Fig. 6. Variation of (a) average Nusselt number of the heated wall and (b) average temperature of fluid inside the cavity as a function of *Ha* for *Ra* = 10^5. The solid line indicates results for the plain fluid and the dashed line for the ferrofluid.

6. **Conclusion**

Problem of steady, laminar natural convection inside a *C*-shaped cavity at varying Rayleigh and Hartmann numbers is investigated thoroughly in this paper for two types of fluid (plain fluid containing no ferromagnetic particle and ferrofluid containing up to 15% solid volume fraction of ferromagnetic particles). It is found that ferrofluid produces higher heat transfer rate at low and high value of Rayleigh numbers. At moderate Rayleigh number, ferrofluid has no significant improvement in heat transfer over plain fluid. Increment in Rayleigh number increases heat transfer rate for both ferrofluid and plain fluid. Rate of increase in average Nusselt number is higher at high value of Rayleigh numbers. On the other hand, increasing Hartmann numbers has the opposite effect than that of increasing Rayleigh numbers. Higher Hartmann number weakens convection for both ferrofluid and plain fluid. However, ferrofluid provides higher value of *Nu* than plain fluid even under strong magnetic field (very high *Ha*).

Acknowledgements

The authors would like to thank Department of Mechanical Engineering, Bangladesh University of Engineering and Technology (BUET) for the support provided during this research work.

References

[1] J. M. Wu, J. Zhao, A review of nanofluid heat transfer and critical heat flux enhancement-Research gap to engineering application, Prog. Nucl. Energ. 66 (2013) 13-24.

[2] A. M. Hussein, K.V. Sharma, R. A. Bakar, K. Kadirgama, A review of forced convection heat transfer enhancement and hydrodynamic characteristics of a nanofluid, Renew. Sust. Energy Rev. 29 (2014) 734-743.

[3] L. SyamSundar, M. K. Singh, I. Bidkin, A. C. M. Sousa, Experimental investigations in heat transfer and friction factor of magnetic Ni nanofluid flowing in a tube, Int. J. Heat Mass Transfer 70 (2014) 224-234.

[4] Z. H. Liu, Y. Y. Li, A new frontier of nanofluid research – Application of nanofluids in heat pipes, Int. J. Heat Mass Transfer 55 (2012) 6786-6797.

[5] M. Ashouri, B. Ebrahimi, M. B. Shafii, M. H. Saidi, M. S. Saidi, Correlation for Nusselt number in pure magnetic convection ferrofluid flow in a square cavity by a numerical investigation, J. Magn. Magn. Mater. 322 (2010) 3607-3613.

[6] T. C. Jue, Analysis of combined thermal and magnetic convection ferrofluid flow in a cavity, Int. Commun. Heat Mass Transfer 33 (2006) 846-852.

[7] H. Aminfar, M. Mohammadpourfard, S. A. Zonouzi, Numerical study of the ferrofluid flow and heat transfer through a rectangular duct in the presence of a non-uniform transverse magnetic field, J. Magn. Magn. Mater. 327 (2013) 31-42.

[8] S. Mohsen, G. B. Mofid, Free convection of ferrofluid in a cavity heated from below in the presence of an external magnetic field, Powder Technol. 256 (2014) 490-498.

[9] G. H. R. Kefayati, Natural convection of ferrofluid in a linearly heated cavity utilizing LBM, J. Mol. Liq. 191 (2014) 1-9.

[10] M. Goharkhah, M. Ashjaee, Effect of an alternating nonuniform magnetic field on ferrofluid flow and heat transfer in a channel, J. Magn. Magn. Mater. 362 (2014) 80-89.

[11] F. Selimefendigil, H. F. Öztop, Effect of a rotating cylinder in forced convection of ferrofluid over a backward facing step, Int. J. Heat Mass Transfer, 71 (2014) 142-148.

[12] S. M. Snyder, T. Cader, B. A. Finlayson, Finite element model of magnetoconvection of a ferrofluid, J. Magn. Magn. Mater. 262 (2003) 269-279.

[13] M. A. Y. Bakier, Flow in open C-shaped cavities: How far does the change in boundaries affect nanofluid?, Engineering Science and Technology, an International Journal, Available online 3 June 2014, ISSN 2215-0986, http://dx.doi.org/10.1016/j.jestch.2014.04.007.

[14] B. Ghasemi, S. M. Aminossadati, A. Raisi, Magnetic field effect on natural convection in a nanofluid-filled square enclosure, Int. J. Therm. Sci. 50 (2011) 1748 -1756.

Available online at www.sciencedirect.com

ScienceDirect

Procedia Engineering 00 (2015) 000–000

Procedia Engineering

www.elsevier.com/locate/procedia

6th BSME International Conference on Thermal Engineering (ICTE 2014)

Soret and Dufour effects in an MHD flow over a porous rotating disk using HAM

Navid Freidoonimehr[a,]*, Mohammad Mehdi Rashidi[b,c], Mohammad Shakhaoath Khan[d], Mohammad Ferdows[e]

[a]*Young Researchers & Elite Club, Hamedan Branch, Islamic Azad University, Hamedan, Iran*
[b]*Mechanical Engineering Department, Engineering Faculty of Bu-Ali Sina University, Hamedan, Iran*
[c]*Mechanical Engineering Department, University of Michigan-Shanghai Jiao Tong University Joint Institute, Shanghai Jiao Tong University, Shanghai, Peoples Republic of China*
[d]*Department of Chemical Engineering, University of Newcastle, NSW 2308, AUSTRALIA*
[e]*Department of Mathematics, University of Dhaka, Dhaka-1000, Bangladesh*

Abstract

The main concern of the present article is to study the steady MHD flow past a porous rotating disk using a semi numerical/analytical method named Homotopy analysis method (HAM). The von-Karman transformations are employed to transform the governing equations into system of nonlinear ordinary differential equations (ODEs). The results of the present study are compared with numerical quadrature solutions employing a shooting technique with excellent correlation in an especial case. The effects of flow physical parameters such as magnetic interaction parameter, suction parameter, Prandtl number, Schmidt number, Soret and Dufour number on the fluid velocity, temperature and concentration distributions are presented graphically and discussed in details. Results show that the effect of increasing Soret number or decreasing Dufour number tends to decrease the temperature distribution while enhances the concentration distribution.

Keywords: Heat and mass transfer; MHD flow; Rotating disk; HAM; Soret effect; Dufour effect

---

* Corresponding author. Tel.: +98-918-311-4160; fax: +98-813-825-4393.
E-mail address: nfreidoonimehr@yahoo.com

1. Introduction

Rotating disk flows have received much attention in several industrial and engineering processes. They have feasible applications in many industries, such as rotating machinery, lubrication, oceanography and computer storage devices. Von karman [1] was probably the first one who studied the fluid flow due to an infinite rotating disk. He introduced his famous appropriate transformations, caused to ordinary differential equations which are reduced form of governing partial differential equations.

In several studies, the Dufour and Soret effects on heat and mass transfer were assumed to be negligible according to the effects described by Fourier’s and Fick’s laws [2]. These effects are important when density differences exist in the flow regime [3]. When heat and mass transfer happen simultaneously in a moving fluid, the energy flux can be generated by temperature gradients as well as composition gradients. The energy flux which is caused by a composition gradient is named the Dufour or diffusion-thermo effect and also the mass fluxes can also be developed by temperature gradients which is called the Soret or thermal-diffusion effect [4]. In this matter, several works have been carried out. Das *et al* [5] displayed the effect of mass transfer on free convective flow and heat transfer of a viscous incompressible electrically conducting fluid past a vertical porous plate through a porous medium. Rashidi *et al* [6] presented the analytical solution for the steady MHD convective and slip flow due to a rotating disk in the presence of the Viscous dissipation and Ohmic heating. Hayat *et al* [7] illustrated the thermal-diffusion and diffusion-thermo effects on the 2D MHD axisymmetric flow of a second grade fluid in the presence of Joule heating and first order chemical reaction. Osalusi *et al* [4] studied the Soret and Dufour effects on combined heat and mass transfer of a steady hydro-magnetic convective and slip flow due to a rotating disk in the presence of viscous dissipation and Ohmic heating numerically by shooting method. Pal and Talukdar [8] investigated the effects of thermal radiation and first-order chemical reaction on unsteady MHD convective flow past a semi-infinite vertical flat plate in the presence of transverse magnetic field under oscillatory suction and heat source in slip-flow regime.

Some of strongly nonlinear equations used to describe physical systems in the form of mathematical modelling do not have exact solutions. The numerical or analytical methods can be applied to solve these nonlinear equations. Despite all the benefits, there are many disadvantages for the numerical methods in comparison with the analytical methods. Thus in this article, we apply one of the analytic methods named Homotopy analysis method (HAM) to solve the system of nonlinear differential equations. The HAM was firstly introduced by Liao [9-11] to offer a general analytic method for nonlinear problems. The HAM was used to solve many kinds of nonlinear problems in fluid dynamics and heat transfer in recent years [12-15].

The objective of this paper is to study the steady MHD flow over a porous rotating disk in the presence of the Soret and Dufour effects analytically via HAM. The effects of various involved parameters such as magnetic interaction parameter, suction parameter, Prandtl number, Soret number, Dufour number, and Schmidt number on the fluid velocity, temperature and concentration distributions are analysed.

2. Mathematical formulation

We assume the steady, axially symmetric, incompressible flow of an electrically conducting fluid with heat and mass transfer flow past a rotating porous disk. Consider the fluid is infinite in extent in the positive *z*-direction. The fluid is assumed to be Newtonian. The external uniform magnetic field B_0 which is considered unchanged by taking small magnetic Reynolds number is imposed in the direction normal to the surface of the disk. The induced magnetic field due to the motion of the electrically-conducting fluid is negligible. The uniform suction is also applied at the surface of the disk. The flow description and geometrical coordinates are shown in Fig. 1. The equations, respectively, of continuity, momentum, energy and species diffusion in laminar incompressible flow are given by:

$$\frac{\partial u}{\partial r}+\frac{u}{r}+\frac{\partial w}{\partial z}=0, \tag{1}$$

$$u\frac{\partial u}{\partial r}+w\frac{\partial u}{\partial z}-\frac{v^2}{r}+\frac{1}{\rho}\frac{\partial P}{\partial r}=\nu\left(\frac{\partial^2 u}{\partial r^2}+\frac{1}{r}\frac{\partial u}{\partial r}-\frac{u}{r^2}+\frac{\partial^2 u}{\partial z^2}\right)-\frac{\sigma B_0^2}{\rho}u, \tag{2}$$

$$u\frac{\partial v}{\partial r}+w\frac{\partial v}{\partial z}+\frac{uv}{r}=\nu\left(\frac{\partial^2 v}{\partial r^2}+\frac{1}{r}\frac{\partial v}{\partial r}-\frac{v}{r^2}+\frac{\partial^2 v}{\partial z^2}\right)-\frac{\sigma B_0^2}{\rho}v, \tag{3}$$

$$u\frac{\partial w}{\partial r}+w\frac{\partial w}{\partial z}+\frac{1}{\rho}\frac{\partial P}{\partial z}=\nu\left(\frac{\partial^2 w}{\partial r^2}+\frac{1}{r}\frac{\partial w}{\partial r}+\frac{\partial^2 w}{\partial z^2}\right), \tag{4}$$

$$u\frac{\partial T}{\partial r}+w\frac{\partial T}{\partial z}=\frac{k}{\rho c_p}\left(\frac{\partial^2 T}{\partial r^2}+\frac{1}{r}\frac{\partial T}{\partial r}+\frac{\partial^2 T}{\partial z^2}\right)+\frac{DK_T}{C_s c_p}\left(\frac{\partial^2 C}{\partial r^2}+\frac{1}{r}\frac{\partial C}{\partial r}+\frac{\partial^2 C}{\partial z^2}\right), \tag{5}$$

$$u\frac{\partial C}{\partial r}+w\frac{\partial C}{\partial z}=D\left(\frac{\partial^2 C}{\partial r^2}+\frac{1}{r}\frac{\partial C}{\partial r}+\frac{\partial^2 C}{\partial z^2}\right)+\frac{DK_T}{T_m}\left(\frac{\partial^2 T}{\partial r^2}+\frac{1}{r}\frac{\partial T}{\partial r}+\frac{\partial^2 T}{\partial z^2}\right), \tag{6}$$

Using the cylindrical polar coordinates (r, ϕ, z), the disk rotates with constant angular velocity (Ω) and is placed at $z=0$, where z is the vertical axis in the cylindrical coordinate system with r and ϕ as the radial and tangential axes. The components of the flow velocity (u, v, w) are in the directions of increasing (r, ϕ, z) respectively. The P is pressure, ρ is the density of the fluid, T and C are the fluid temperature and concentration. ν is the kinematic viscosity of the ambient fluid, σ is the electrical conductivity, k is the thermal conductivity, c_p is the specific heat at constant pressure, D is the molecular diffusion coefficient, K_T is the thermal diffusion ratio, C_s is the concentration susceptibility, and T_m is the mean fluid temperature. The appropriate boundary conditions subjected to uniform suction w_0 through the disk are introduced as:

$$u=0,\quad v=\Omega r,\quad w=w_0,\quad T=T_w,\quad C=C_w\quad \text{at}\quad z=0, \tag{7}$$

$$u\to 0,\quad v\to 0,\quad P\to P_\infty,\quad T\to T_\infty,\quad C\to C_\infty\quad \text{at}\quad z\to\infty, \tag{8}$$

We consider the temperature differences within the flow are such that the term T^4 can be expressed as a linear function of temperature. This is accomplished by expanding it in a Taylor series about T_∞ as follows [16]:

$$T^4=T_\infty^4+4T_\infty^3(T-T_\infty)+6T_\infty^2(T-T_\infty)^2+\cdots \tag{9}$$

By neglecting second and higher-order terms in the above equation beyond the first degree in ($T-T_\infty$), we obtain

$$T^4\cong 4T_\infty^3 T-3T_\infty^4, \tag{10}$$

Thus, according to Eqns. (9)-(10), Eq. (5) reduces to

$$u\frac{\partial T}{\partial r}+w\frac{\partial T}{\partial z}=\frac{k}{\rho c_p}\left(\frac{\partial^2 T}{\partial r^2}+\frac{1}{r}\frac{\partial T}{\partial r}+\frac{\partial^2 T}{\partial z^2}\right)+\frac{DK_T}{C_s c_p}\left(\frac{\partial^2 C}{\partial r^2}+\frac{1}{r}\frac{\partial C}{\partial r}+\frac{\partial^2 C}{\partial z^2}\right), \tag{11}$$

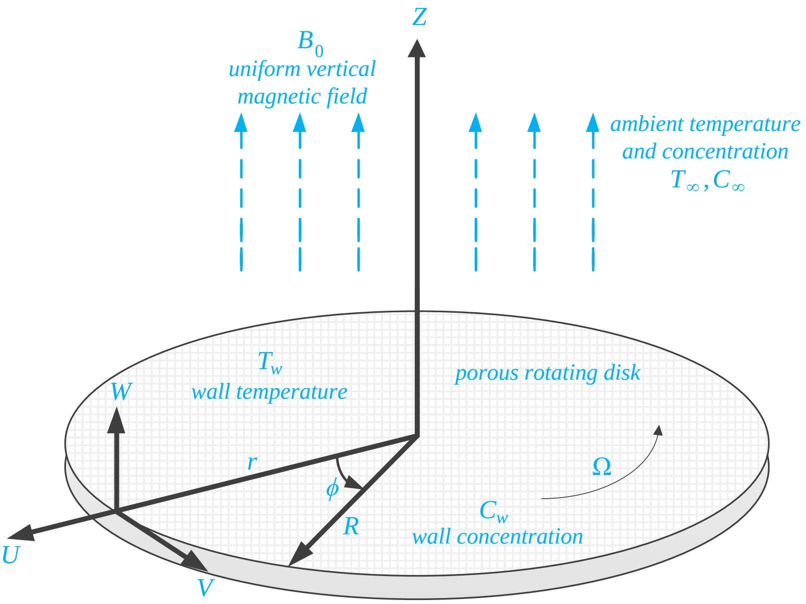

Fig. 1. Configuration of the flow and geometrical coordinates.

In order to obtain the non-dimensional form of the Eqns. (1)-(4), (6) and (11), the following dimensionless variables are introduced as Eqns. (12)-(13).

$$\bar{R} = \frac{r}{L}, \qquad \bar{Z} = \frac{z}{L}, \qquad \bar{U} = \frac{u}{\Omega L}, \qquad \bar{V} = \frac{v}{\Omega L}, \qquad \bar{W} = \frac{w}{\Omega L},$$
$$\bar{P} = \frac{p - p_\infty}{\rho \Omega^2 L^2}, \quad \bar{\nu} = \frac{\nu}{\Omega L^2}, \quad \bar{T} = \frac{T - T_w}{T_\infty - T_w}, \quad \bar{C} = \frac{C - C_w}{C_\infty - C_w}, \tag{12}$$

$$\bar{U} = \bar{R} F(\eta), \quad \bar{V} = \bar{R} G(\eta), \quad \bar{W} = (\bar{\nu})^{1/2} H(\eta), \quad \bar{T} = \theta(\eta), \quad \bar{C} = \varphi(\eta), \tag{13}$$

Substituting the dimensionless variables Eqns. (12)-(13) into the Eqns. (1)-(4), (6) and (11), and by introducing a dimensionless normal distance from the disk, $\eta = \bar{Z}(\bar{\nu})^{-1/2}$ along with the von-Karman transformations (12)-(13) and substituting them into the non-dimensional form of the Eqns. (1)-(4), (6) and (11), the nonlinear ordinary differential equations are obtained

$$H' + 2F = 0, \tag{14}$$
$$F'' - HF' - F^2 + G^2 - MF = 0, \tag{15}$$
$$G'' - HG' - 2FG - MG = 0, \tag{16}$$
$$\frac{1}{Pr}\theta'' - H\theta' + Du\,\varphi'' = 0, \tag{17}$$
$$\frac{1}{Sc}\varphi'' - H\varphi' + Sr\,\theta'' = 0, \tag{18}$$

where $M = \sigma B_0^2 / \Omega \rho$ is the magnetic interaction parameter, $Pr = \nu \rho c_p / k$ is the Prandtl number, $Sc = \nu / D$ is the Schmidt number, $Sr = D (T_\infty - T_w) K_T / \nu T_m (C_\infty - C_w)$ is the Soret number, $Du = D (C_\infty - C_w) K_T / C_s c_p \nu (T_\infty - T_w)$ is the Dufour number, and *F*, *G*, *H*, θ, and φ are non-dimensionless functions of modified dimensionless vertical coordinate η. The transformed boundary conditions are given as

$$\begin{array}{lllll} F(0)=0, & G(0)=1, & H(0)=W_s, & \theta(0)=1, & \varphi(0)=1, \\ F(\eta)\to 0, & G(\eta)\to 0, & \theta(\eta)\to 0, & \varphi(\eta)\to 0, & \text{as} \quad \eta\to\infty, \end{array} \tag{19}$$

where $Ws = w_0 / (\nu\,\Omega)^{1/2}$ is the suction/injection parameter and $Ws < 0$ shows a uniform suction at the disk surface.

3. HAM solution

We choose the suitable initial approximations, according to the boundary conditions (19) and the rule of solution expression

$$H(0)=W_s, \quad F(0)=0, \quad G(0)=e^{-\eta}, \quad \theta(0)=e^{-\eta}, \quad \varphi(0)=e^{-\eta}, \tag{20}$$

The auxiliary linear operators $\mathcal{L}_1(H),\ \mathcal{L}_2(F),\ \mathcal{L}_3(G),\ \mathcal{L}_4(\theta)$ and $\mathcal{L}_5(\varphi)$ are:

$$\begin{array}{lll} \mathcal{L}(H)=\dfrac{\partial H}{\partial\eta}, & \mathcal{L}(F)=\dfrac{\partial^2 F}{\partial\eta^2}+\dfrac{\partial F}{\partial\eta}, & \mathcal{L}(G)=\dfrac{\partial^2 G}{\partial\eta^2}+\dfrac{\partial G}{\partial\eta}, \\ \mathcal{L}(\theta)=\dfrac{\partial^2\theta}{\partial\eta^2}+\dfrac{\partial\theta}{\partial\eta}, & \mathcal{L}(\varphi)=\dfrac{\partial^2\varphi}{\partial\eta^2}+\dfrac{\partial\varphi}{\partial\eta}, & \end{array} \tag{21}$$

with the following properties

$$\begin{array}{lll} \mathcal{L}_1(c_1)=0, & \mathcal{L}_2(c_2 e^{-\eta}+c_3)=0, & \mathcal{L}_3(c_4 e^{-\eta}+c_5)=0, \\ \mathcal{L}_4(c_6 e^{-\eta}+c_7)=0, & \mathcal{L}_5(c_8 e^{-\eta}+c_9)=0, & \end{array} \tag{22}$$

where $c_i,\ i=1-9$, are the arbitrary constants. The nonlinear operators, due to the Eqns. (14)-(18), are introduced as

$$\mathcal{N}_1\left[\hat{H}(\eta;p),\ \hat{F}(\eta;p)\right]=\frac{\partial\hat{H}(\eta;p)}{\partial\eta}+2\hat{F}(\eta;p), \tag{23}$$

$$\begin{aligned} \mathcal{N}_2\left[\hat{H}(\eta;p),\ \hat{F}(\eta;p),\ \hat{G}(\eta;p)\right]=&\frac{\partial^2\hat{F}(\eta;p)}{\partial\eta^2}-\hat{H}(\eta;p)\frac{\partial\hat{F}(\eta;p)}{\partial\eta} \\ &-\hat{F}(\eta;p)^2+\hat{G}(\eta;p)^2-M\ \hat{F}(\eta;p), \end{aligned} \tag{24}$$

$$\begin{aligned} \mathcal{N}_3\left[\hat{H}(\eta;p),\ \hat{F}(\eta;p),\ \hat{G}(\eta;p)\right]=&\frac{\partial^2\hat{G}(\eta;p)}{\partial\eta^2}-\hat{H}(\eta;p)\frac{\partial\hat{G}(\eta;p)}{\partial\eta} \\ &-2\hat{G}(\eta;p)\hat{F}(\eta;p)-M\ \hat{G}(\eta;p), \end{aligned} \tag{25}$$

$$\mathcal{N}_4\left[\hat{H}(\eta;p),\hat{\theta}(\eta;p),\hat{\varphi}(\eta;p)\right]=\frac{1}{Pr}\frac{\partial^2\hat{\theta}(\eta;p)}{\partial\eta^2}-\hat{H}(\eta;p)\frac{\partial\hat{\theta}(\eta;p)}{\partial\eta}+Du\,\frac{\partial^2\hat{\varphi}(\eta;p)}{\partial\eta^2}, \tag{26}$$

$$\mathcal{N}_5\left[\hat{H}(\eta;p),\hat{\theta}(\eta;p),\hat{\varphi}(\eta;p)\right]=\frac{1}{Sc}\frac{\partial^2\hat{\varphi}(\eta;p)}{\partial\eta^2}-\hat{H}(\eta;p)\frac{\partial\hat{\varphi}(\eta;p)}{\partial\eta}+Sr\,\frac{\partial^2\hat{\theta}(\eta;p)}{\partial\eta^2}, \tag{27}$$

The zero-th order deformation equations are formed as

$$(1-p)\,\mathcal{L}_1\left[\hat{H}(\eta;p)-H_0(\eta)\right]=p\,\hbar\,\mathcal{H}_H(\eta)\,\mathcal{N}_1\left[\hat{H}(\eta;p),\hat{F}(\eta;p)\right], \tag{28}$$

$$(1-p)\,\mathcal{L}_2\left[\hat{F}(\eta;p)-F_0(\eta)\right]=p\,\hbar\,\mathcal{H}_F(\eta)\,\mathcal{N}_2\left[\hat{H}(\eta;p),\hat{F}(\eta;p),\hat{G}(\eta;p)\right], \tag{29}$$

$$(1-p)\,\mathcal{L}_3\left[\hat{G}(\eta;p)-G_0(\eta)\right]=p\,\hbar\,\mathcal{H}_G(\eta)\,\mathcal{N}_3\left[\hat{H}(\eta;p),\hat{F}(\eta;p),\hat{G}(\eta;p)\right], \tag{30}$$

$$(1-p)\,\mathcal{L}_4\left[\hat{\theta}(\eta;p)-\theta_0(\eta)\right]=p\,\hbar\,\mathcal{H}_\theta(\eta)\,\mathcal{N}_4\left[\hat{H}(\eta;p),\hat{\theta}(\eta;p),\hat{\varphi}(\eta;p)\right], \tag{31}$$

$$(1-p)\,\mathcal{L}_5\left[\hat{\varphi}(\eta;p)-\varphi_0(\eta)\right]=p\,\hbar\,\mathcal{H}_\varphi(\eta)\,\mathcal{N}_5\left[\hat{H}(\eta;p),\hat{\theta}(\eta;p),\hat{\varphi}(\eta;p)\right], \tag{32}$$

where $\mathcal{H}_H(\eta),\mathcal{H}_F(\eta),\mathcal{H}_G(\eta),\mathcal{H}_\theta(\eta)$, and $\mathcal{H}_\varphi(\eta)$ are the auxiliary functions, which are selected as

$$\mathcal{H}_H(\eta)=\mathcal{H}_F(\eta)=\mathcal{H}_G(\eta)=\mathcal{H}_\theta(\eta)=\mathcal{H}_\varphi(\eta)=1, \tag{33}$$

Subject to the boundary conditions

$$\begin{gathered}\hat{H}(0;p)=W_s,\;\; \hat{F}(0;p)=0,\quad \hat{G}(0;p)=1,\quad \hat{\theta}(0;p)=1,\quad \hat{\varphi}(0;p)=1,\\ \hat{F}(0;\infty)=0,\quad \hat{G}(0;\infty)=0,\quad \hat{\theta}(0;\infty)=0,\quad \hat{\varphi}(0;\infty)=0,\end{gathered} \tag{34}$$

Finally by the Taylor's theorem, we obtain

$$\hat{H}(\eta;p)=H_0(\eta)+\sum_{m=1}^{\infty}H_m(\eta)\,p^m, \tag{35}$$

$$\hat{F}(\eta;p)=F_0(\eta)+\sum_{m=1}^{\infty}F_m(\eta)\,p^m, \tag{36}$$

$$\hat{G}(\eta;p)=G_0(\eta)+\sum_{m=1}^{\infty}G_m(\eta)\,p^m, \tag{37}$$

$$\hat{\theta}(\eta;p)=\theta_0(\eta)+\sum_{m=1}^{\infty}\theta_m(\eta)p^m, \tag{38}$$

$$\hat{\varphi}(\eta;p)=\varphi_0(\eta)+\sum_{m=1}^{\infty}\varphi_m(\eta)p^m, \tag{39}$$

where

$$H_m(\eta) = \frac{1}{m!}\frac{\partial^m \hat{H}(\eta;p)}{\partial p^m}\bigg|_{p=0}, \qquad F_m(\eta) = \frac{1}{m!}\frac{\partial^m \hat{F}(\eta;p)}{\partial p^m}\bigg|_{p=0},$$

$$G_m(\eta) = \frac{1}{m!}\frac{\partial^m \hat{G}(\eta;p)}{\partial p^m}\bigg|_{p=0}, \qquad \theta_m(\eta) = \frac{1}{m!}\frac{\partial^m \hat{\theta}(\eta;p)}{\partial p^m}\bigg|_{p=0}, \tag{40}$$

$$\varphi_m(\eta) = \frac{1}{m!}\frac{\partial^m \hat{\varphi}(\eta;p)}{\partial p^m}\bigg|_{p=0},$$

The convergence of the series (35)-(39) strongly depend on the auxiliary parameter $(\hbar)$ [9]. Consider $\hbar$ is chosen such that the series of Eqns. (35)-(39) are convergent at p = 1 we have

$$H(\eta) = H_0(\eta) + \sum_{m=1}^{\infty} H_m(\eta), \tag{41}$$

$$F(\eta) = F_0(\eta) + \sum_{m=1}^{\infty} F_m(\eta), \tag{42}$$

$$G(\eta) = G_0(\eta) + \sum_{m=1}^{\infty} G_m(\eta), \tag{43}$$

$$\theta(\eta) = \theta_0(\eta) + \sum_{m=1}^{\infty} \theta_m(\eta), \tag{44}$$

$$\varphi(\eta) = \varphi_0(\eta) + \sum_{m=1}^{\infty} \varphi_m(\eta), \tag{45}$$

According to have *m*th-order deformation equations, by differentiating Eqns. (28)-(32) *m* times with respect to *p*, divide by *m*! in *p* = 0. The results become:

$$\mathcal{L}_1\left[H_m(\eta) - \chi_m \ H_{m-1}(\eta)\right] = \hbar \mathcal{H}_H(\eta) R_{1,m}(\eta), \tag{46}$$

$$\mathcal{L}_2\left[F_m(\eta) - \chi_m \ F_{m-1}(\eta)\right] = \hbar \mathcal{H}_F(\eta) R_{2,m}(\eta), \tag{47}$$

$$\mathcal{L}_3\left[G_m(\eta) - \chi_m \ G_{m-1}(\eta)\right] = \hbar \mathcal{H}_G(\eta) R_{3,m}(\eta), \tag{48}$$

$$\mathcal{L}_4\left[\theta_m(\eta) - \chi_m \ \theta_{m-1}(\eta)\right] = \hbar \mathcal{H}_\theta(\eta) R_{4,m}(\eta), \tag{49}$$

$$\mathcal{L}_5\left[\varphi_m(\eta) - \chi_m \ \varphi_{m-1}(\eta)\right] = \hbar \mathcal{H}_\varphi(\eta) R_{5,m}(\eta), \tag{50}$$

where

$$R_{1,m}(\eta) = \frac{\partial H_{m-1}(\eta)}{\partial \eta} + 2F_{m-1}(\eta), \tag{51}$$

$$R_{2,m}(\eta)=\frac{\partial^2 F_{m-1}(\eta)}{\partial\eta^2}-\sum_{n=0}^{m-1}\left(H_n(\eta)\frac{\partial F_{m-1-n}(\eta)}{\partial\eta}+F_n(\eta)F_{m-1-n}(\eta)-G_n(\eta)G_{m-1-n}(\eta)\right)$$
$$-M\,F_{m-1}(\eta), \tag{52}$$

$$R_{3,m}(\eta)=\frac{\partial^2 G_{m-1}(\eta)}{\partial\eta^2}-\sum_{n=0}^{m-1}\left(H_n(\eta)\frac{\partial G_{m-1-n}(\eta)}{\partial\eta}+2F_n(\eta)G_{m-1-n}(\eta)\right)-M\,G_{m-1}(\eta), \tag{53}$$

$$R_{4,m}(\eta)=\frac{1}{Pr}\frac{\partial^2\theta_{m-1}(\eta)}{\partial\eta^2}-\sum_{n=0}^{m-1}\left(H_n(\eta)\frac{\partial\theta_{m-1-n}(\eta)}{\partial\eta}\right)+Du\,\frac{\partial^2\varphi_{m-1}(\eta)}{\partial\eta^2}, \tag{54}$$

$$R_{5,m}(\eta)=\frac{1}{Sc}\frac{\partial^2\varphi_{m-1}(\eta)}{\partial\eta^2}-\sum_{n=0}^{m-1}\left(H_n(\eta)\frac{\partial\varphi_{m-1-n}(\eta)}{\partial\eta}\right)+Sr\,\frac{\partial^2\theta_{m-1}(\eta)}{\partial\eta^2}, \tag{55}$$

and

$$\chi_m=\begin{cases}0 & m\le 1\\ 1 & m>1\end{cases}, \tag{56}$$

with respect to the following boundary conditions

$$\begin{aligned}&H_m(0)=W_s,\quad F_m(0)=0,\quad G_m(0)=1,\quad \theta_m(0)=1,\quad \varphi_m(0)=1,\\ &F_m(\infty)=0,\quad G_m(\infty)=0,\quad \theta_m(\infty)=0,\quad \varphi_m(\infty)=0,\end{aligned} \tag{57}$$

The symbolic software *MATHEMATICA* is used to solve the system of linear equations, Eqns. (46)-(50) with the boundary conditions (57), one after the other in the order of $m=1,2,3,\ldots$.

The convergence of the series of Eqns. (35)-(39) forcefully depends on the auxiliary parameter, as mentioned by Liao [9]. It is essential to select a proper value of auxiliary parameter to control and speed the convergence of the approximation series by the help of the so-called $\hbar-$ curve. Obviously, the valid regions of $\hbar$ correspond to the line segments nearly parallel to the horizontal axis. The $\hbar-$curves of $F'(0)$, $G'(0)$, $H''(0)$, $\theta'(0)$ and $\varphi'(0)$ obtained by the 20th order approximation are shown in Fig. 2.

4. Results and Discussion

The nonlinear ordinary differential equations (14)-(18) subject to the boundary conditions (19) have been solved via HAM for some values of the magnetic interaction parameter (*M*), Prandtl number (*Pr*), Schmidt number (*Sc*), Soret number (*Sr*), Dufour number (*Du*), and suction parameter (W_s). The values of the flow physical parameters are mentioned in each of the graphs and tables. Table 1 illustrates a comparison between the presented results and those reported by Turkyilmazoglu [17] and Kelson and Desseaux [18] for $F'(0)$ and $G'(0)$ as well as different values of magnetic interaction parameter and suction parameter. An excellent agreement can be observed between them. The diluting chemical species of most common interest have Schmidt number between 0.1 and 10.0. Thus, we took the Schmidt number 0.22, 0.64, 0.78, and 1 which represents the Schmidt number of Helium, Ammonia, Carbon monoxide, and Carbon dioxide, respectively.

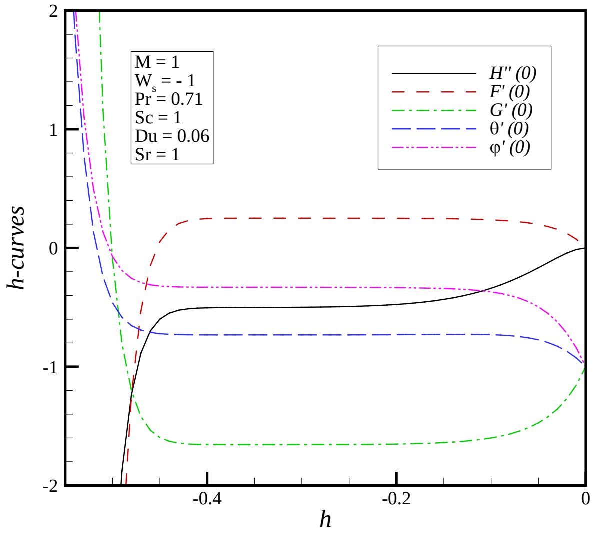

Fig. 2. The $\hbar$ – curves obtained by 20th order approximation of the HAM solution.

Table 1. Numerical values of the radial skin friction coefficient $F'(0)$.

M	W_s	Ref. [17]	Ref. [18]	Present
0	0	-	0.510233	0.510186
	-1	-	0.389569	0.389559
	-2	-	0.242421	0.242416
1	0	0.309258	-	0.309237
	-1	0.251044	-	0.251039
	-2	0.188719	-	0.188718

Table 2. Numerical values of the tangential skin friction coefficient $-G'(0)$.

M	W_s	Ref. [17]	Ref. [18]	Present
0	0	-	0.61592	0.61589
	-1	-	1.17522	1.17523
	-2	-	2.03853	2.03853
1	0	1.06905	-	1.06907
	-1	1.65708	-	1.65709
	-2	2.43136	-	2.43137

The effect of magnetic interaction parameter on the velocity components in radial, tangential and axial directions, temperature distribution as well as concentration profile is presented in Fig. 3. Infliction of the vertical magnetic field to the electrically conducting fluid causes a drag-like force named the Lorentz force. This force has the tendency to slow down the flow around the disk at the expense of increasing its temperature and concentration. Thus, as the magnetic field becomes stronger, the velocity profiles in radial, tangential and axial directions decrease and the thermal boundary layer and concentration field increase. It is important to note that as the vertical magnetic field increases, the great resistance on the fluid particles apply, which cause to generate heat in the fluid.

The effect of the suction parameter on all velocity components as well as temperature distribution and concentration profile is illustrated in Fig. 4. When suction is applied at the disk surface, the radial, tangential and axial velocity profiles decrease. This phenomenon occurs due to this fact that applying suction leads to draw the amount of fluid particles into the wall and consequently the velocity boundary layers decrease. In addition, the radial velocity component becomes very small for large values of the suction parameter. The usual decay of temperature and concentration profiles occurs for the larger values of the suction parameter.

Fig. 5 demonstrates the effect of Prandtl number on the temperature distribution as well as the effect of Schmidt number on the concentration profile. The thermal boundary-layer thickness gets decreased with increasing the Prandtl number. It physically means that the flow with large Prandtl number prevents spreading the heat in the fluid. The results also present that as the Schmidt number increases, the concentration boundary layer thickness decreases. In other word, the molecular diffusion decreases, as the Schmidt number increases.

Fig. 6 indicates the simultaneous effects of the Soret and Dufour number on the temperature distribution as well as concentration profile. The Soret effect is a mass flux due to a temperature gradient and the Dufour effect is enthalpy flux due to a concentration gradient and appears in the energy equation. It should be mentioned that Dufour and Soret numbers are arbitrary constants provided that their product remains constant [6, 7, 19]. Moreover, $Du = 0$ and $Sr = 0$ correspond to the condition when the thermal diffusion and diffusion thermo effects are smaller order of magnitude than the effects described by Fourier’s and Fick’s laws [7, 20]. The thermal boundary layer increases by increasing Dufour number or simultaneously decreasing Soret number. As the Dufour number increases or Soret number decreases, the rate of mass transfer (concentration boundary layer thickness) decreases at the disk.

5. Conclusion

In the current study, a mathematical formulation has been derived for an MHD fluid flow due to a porous rotating disk. HAM is used to solve the system of ordinary differential equations. The present semi numerical/analytical simulations agree closely with the previous studies for some especial cases. HAM has been shown to be a very strong and efficient technique in finding analytical solutions for nonlinear differential equations. The effects of the five key thermo-physical parameters governing the flow i.e. magnetic interaction parameter, Prandtl number, Schmidt number, Soret number, Dufour number, and suction parameter on the all dimensionless velocity components as well as temperature distribution and concentration profile have been depicted graphically and interpreted in details. The main results of the present analysis are listed below:

a) HAM is shown to demonstrate excellent potential, convergence and accuracy for simulating flow over rotating disk problems.
b) As the magnetic field becomes stronger, the velocity profiles in radial, tangential and axial directions decrease and the thermal boundary layer and concentration field increase.
c) When suction is applied at the disk surface, the radial, tangential and axial velocity profiles decrease. The usual decay of temperature and concentration profiles occurs for the larger values of the suction parameter.
d) The thermal boundary-layer thickness gets decreased with increasing the Prandtl number. The results also present that as the Schmidt number increases, the concentration boundary layer thickness decreases.
e) The thermal boundary layer increases by increasing Dufour number or simultaneously decreasing Soret number. As the Dufour number increases or Soret number decreases, the rate of mass transfer (concentration boundary layer thickness) decreases at the disk.

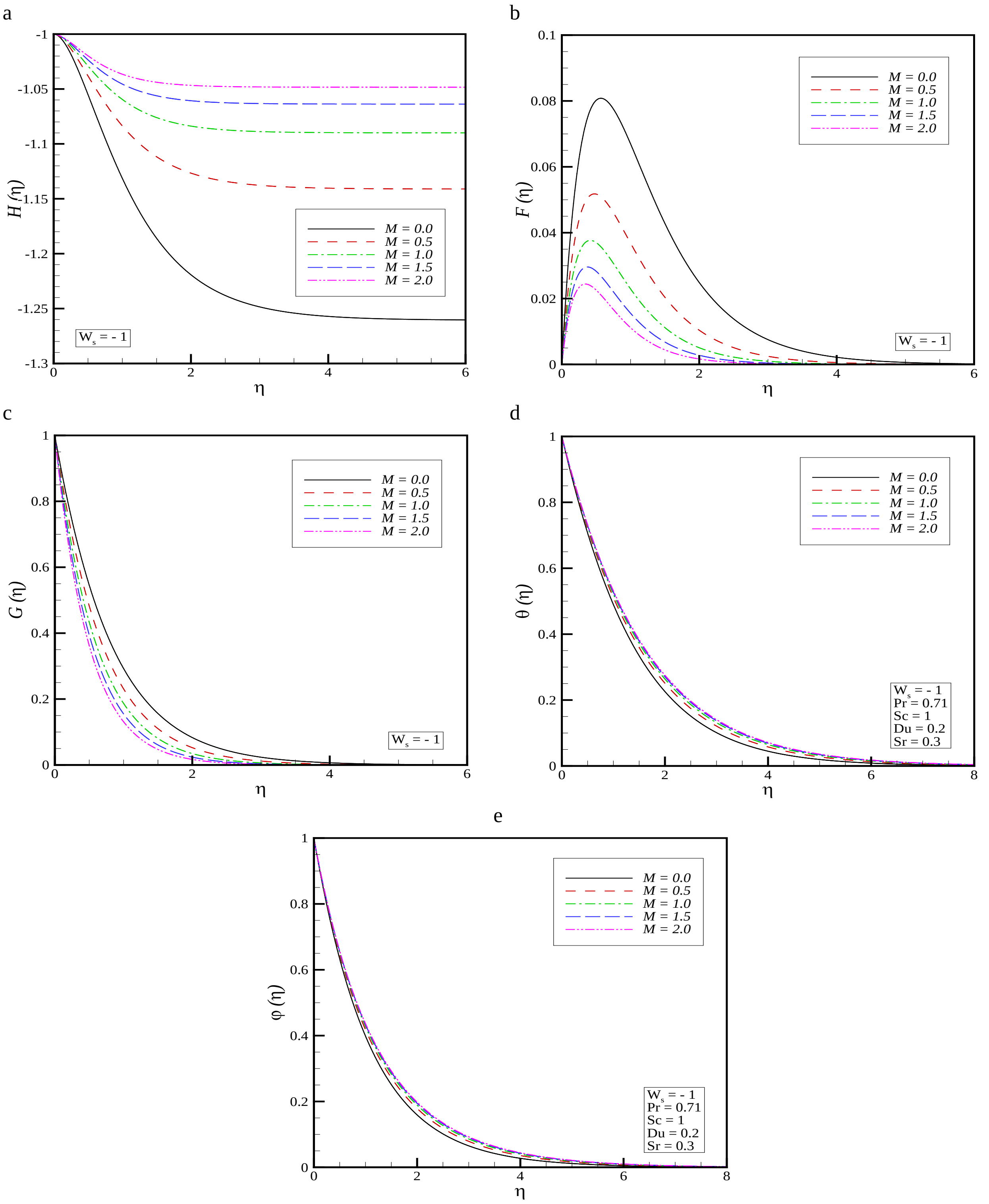

Fig. 3. Effect of magnetic interaction parameter on a) axial, b) radial and c) tangential velocity profiles, d) temperature distribution and e) concentration profile.

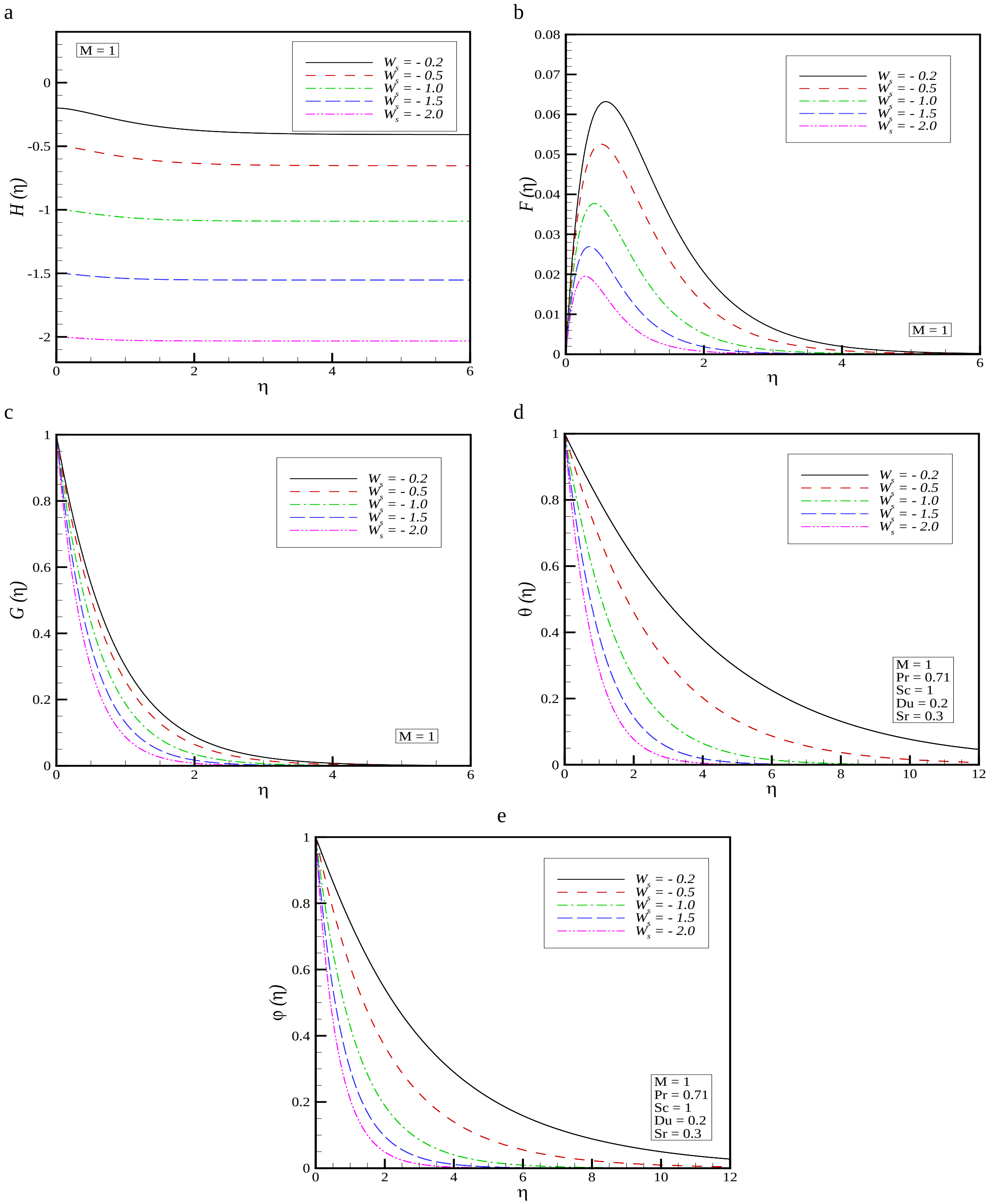

Fig. 4. Effect of suction parameter on a) axial, b) radial and c) tangential velocity profiles, d) temperature distribution and e) concentration profile.

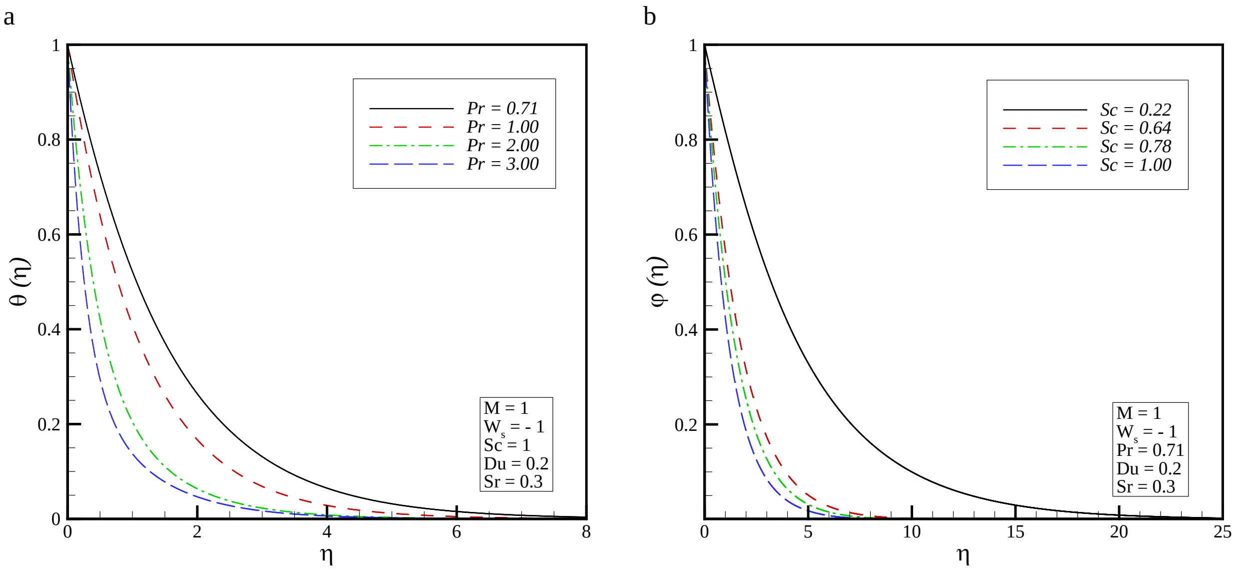

Fig. 5. a) Effect of Prandtl number on the temperature distribution and b) Effect of Schmidt number on the concentration profile.

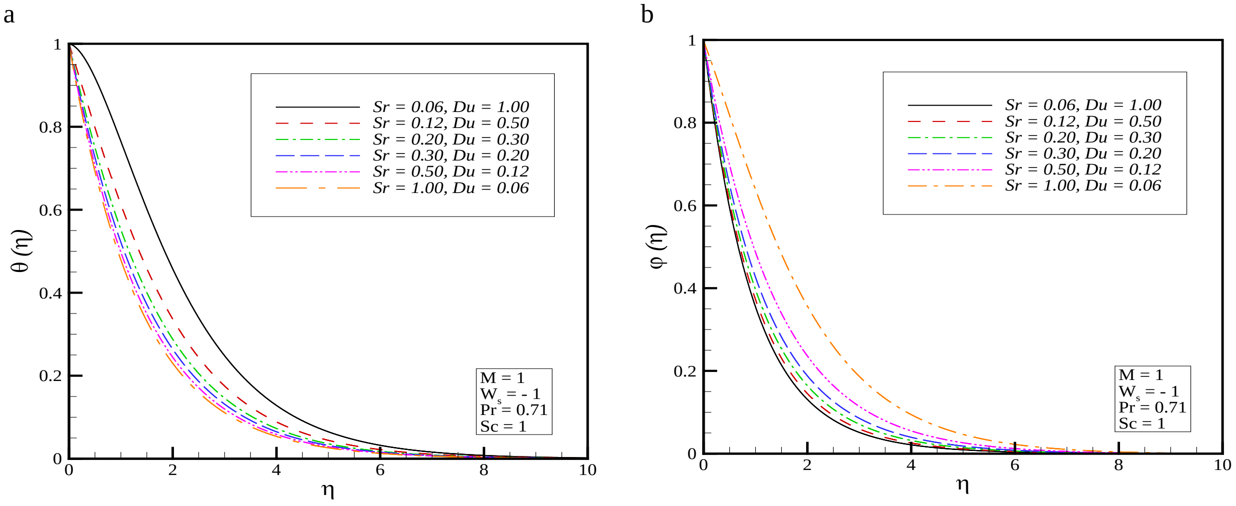

Fig. 6. Effects of Soret and Dufour numbers on a) temperature distribution and b) concentration profile.

References

[1] T. V. Kármán, Über laminare und turbulente Reibung, ZAMM - Journal of Applied Mathematics and Mechanics / Zeitschrift für Angewandte Mathematik und Mechanik 1 (1921) 233-252.

[2] T. Hayat, F. A. Hendi, Thermal-diffusion and diffusion-thermo effects on MHD three-dimensional axisymmetric flow with Hall andion-slip currents, Journal of American Science 8 (2012) 284-294.

[3] S. P. Anjali Devi, R. Uma Devi, Soret and Dufour effects on MHD slip flow with thermal radiation over a porous rotating infinite disk, Communications in Nonlinear Science and Numerical Simulation 16 (2011) 1917-1930.

[4] E. Osalusi, J. Side, R. Harris, Thermal-diffusion and diffusion-thermo effects on combined heat and mass transfer of a steady MHD convective and slip flow due to a rotating disk with viscous dissipation and Ohmic heating, International Communications in Heat and Mass

Transfer 35 (2008) 908-915.
[5] S. S. Das, A. Satapathy, J. K. Das, J. P. Panda, Mass transfer effects on MHD flow and heat transfer past a vertical porous plate through a porous medium under oscillatory suction and heat source, International Journal of Heat and Mass Transfer 52 (2009) 5962-5969.
[6] M. M. Rashidi, T. Hayat, E. Erfani, S. A. Mohimanian Pour, A. A. Hendi, Simultaneous effects of partial slip and thermal-diffusion and diffusion-thermo on steady MHD convective flow due to a rotating disk, Communications in Nonlinear Science and Numerical Simulation 16 (2011) 4303-4317.
[7] T. Hayat, M. Nawaz, S. Asghar, S. Mesloub, Thermal-diffusion and diffusion-thermo effects on axisymmetric flow of a second grade fluid, International Journal of Heat and Mass Transfer 54 (2011) 3031-3041.
[8] D. Pal, B. Talukdar, Influence of fluctuating thermal and mass diffusion on unsteady MHD buoyancy-driven convection past a vertical surface with chemical reaction and Soret effects, Communications in Nonlinear Science and Numerical Simulation 17 (2012) 1597-1614.
[9] S. J. Liao, Beyond perturbation: introduction to the homotopy analysis method, Chapman & Hall/CRC, 2004.
[10] S. J. Liao, On the homotopy analysis method for nonlinear problems, Applied Mathematics and Computation 147 (2004) 499-513.
[11] S. J. Liao, An explicit, totally analytic approximation of Blasius viscous flow problems, International Journal of Non-Linear Mechanics 34 (1999) 759-778.
[12] M. M. Rashidi, M. Ali, N. Freidoonimehr, F. Nazari, Parametric analysis and optimization of entropy generation in unsteady MHD flow over a stretching rotating disk using artificial neural network and particle swarm optimization algorithm, Energy 55 (2013) 497-510.
[13] M. M. Rashidi, M. Ali, N. Freidoonimehr, B. Rostami, M. A. Hossain, Mixed Convective Heat Transfer for MHD Viscoelastic Fluid Flow over a Porous Wedge with Thermal Radiation, Advances in Mechanical Engineering 2014 (2014) 10.
[14] M. M. Rashidi, N. Freidoonimehr, A. Hosseini, O. A. Bég, T. K. Hung, Homotopy simulation of nanofluid dynamics from a non-linearly stretching isothermal permeable sheet with transpiration, Meccanica 49 (2014) 469-482.
[15] M. M. Rashidi, B. Rostami, N. Freidoonimehr, S. Abbasbandy, Free convective heat and mass transfer for MHD fluid flow over a permeable vertical stretching sheet in the presence of the radiation and buoyancy effects, Ain Shams Engineering Journal.
[16] D. Pal, Combined effects of non-uniform heat source/sink and thermal radiation on heat transfer over an unsteady stretching permeable surface, Communications in Nonlinear Science and Numerical Simulation 16 (2011) 1890-1904.
[17] M. Turkyilmazoglu, Purely analytic solutions of magnetohydrodynamic swirling boundary layer flow over a porous rotating disk, Computers & Fluids 39 (2010) 793-799.
[18] N. Kelson, A. Desseaux, Note on porous rotating disk flow, Australian & New Zealand Industrial and Applied Mathematics Journal 42 (2000) 837-855.
[19] A. Postelnicu, Influence of a magnetic field on heat and mass transfer by natural convection from vertical surfaces in porous media considering Soret and Dufour effects, International Journal of Heat and Mass Transfer 47 (2004) 1467-1472.
[20] N. G. Kafoussias, E. W. Williams, Thermal-diffusion and diffusion-thermo effects on mixed free-forced convective and mass transfer boundary layer flow with temperature dependent viscosity, International Journal of Engineering Science 33 (1995) 1369-1384.

Available online at www.sciencedirect.com

ScienceDirect

Procedia Engineering 00 (2015) 000–000

Procedia Engineering

www.elsevier.com/locate/procedia

6th BSME International Conference on Thermal Engineering (ICTE 2014)

Effect of fin and insert on the performance characteristics of Open Loop Pulsating Heat Pipe (OLPHP)

M Lutfor Rahman[a] , Fariha Mir[a*], Sumaiya Nawrin[a], R A Sultan[a], and Mohammad Ali[b]

aDepartment of Mechanical Engineering, MIST, Mirpur, Dhaka, Bangladesh
bDepartment of Mechanical Engg., BUET, Dhaka, Bangladesh

Abstract

The pulsating heat pipe, a serpentine tube of capillary dimension with many turns, has great impact on today's successful thermal management. It is an ascending technology to satisfy present requirement of increasing thermal performance. Focusing on this, an experiment has been done on the open loop pulsating heat pipes (OLPHP) to observe their performance characteristics by using two types of working fluid by varying inclination angles. The experiment is performed on 2.5 mm inner diameter and 3 mm outer diameter OLPHP with an insert of copper wire of 1 mm diameter and fins are added on the condensation section. This investigation is done using methanol and ethanol with 50% filling ratio in OLPHP with 8 loops. In this experiment the effects on the performance of using fins with insert with two different fluids (methanol and ethanol) and the variation of inclination angles are investigated. The results show that the performance characteristics in all the circumstances are better for setup with fin and insert than the normal setup. As higher thermal resistance indicates better performance, so we can say that setup with methanol performs better than ethanol. This performance is best at 45˚ inclination angle. It can be seen that, higher the inclination angle, better the performance and this performance is best at 45˚ inclination angle for this experiment.

Peer-review under responsibility of organizing committee of the 6th BSME International Conference on Thermal Engineering (ICTE 2014).

Keywords: Open loop closed end pulsating heat pipe; evaporation; condensation; inclination angle; thermal conductance.

---

* Corresponding author. Tel.: +8801718179437;
E-mail address: mir.fariha@gmail.com

Peer-review under responsibility of organizing committee of the 6th BSME International Conference on Thermal Engineering (ICTE 2014).

Nomenclature

R	thermal resistance, °C/W	T	temperature along the heat pipe, °C
ΔT	temperature drop along the device, °C	Q	heat input, W
L	length of heat pipe, cm	D	diameter of heat pipe, mm
IA	Inclination angle, °	FR	filling ratio, %

Subscripts

th	thermal	*e*	evaporator section
a	adiabatic section	*c*	condenser section

1. Introduction

Recently there are advances in electronics design and manufacturing which are of small in size and shape. These have resulted in increases in heat flux density and increase in power requirements. The insatiable urge for 'Going Nano' does come with associated interdisciplinary technological problems. In recent years thermal management has become major issue for microelectronics. As these devices are small in shape and size they have less area for cooling system, to manage these type of problem i.e. thermal management of microelectronic devices there is a requirement of miniaturization of heat exchangers [1].

Pulsating heat pipe (PHPs) is a novel passive 2-phase thermal control device first introduced by Akachi et al. [2]. PHPs consist of a capillary tube bent into several turns to form parallel passages. Reduced diameter is used here which are directly influenced by the selected working fluid. According to Zhang and Faghri [3] the vapour plugs generated by the evaporation of liquid push the liquid slugs toward the condensation section and this motion causes flow oscillations that guide device operation. Considering the sections of a PHP, it presents evaporation and a condensation section with an adiabatic section in the middle. There are two possible configurations for PHPs, being as an open loop and as a closed loop. In the open loop configuration, both ends of the tube is pinched off and welded. In the open loop PHP it is believed that a counter-current liquid-vapour flow occurs to promote proper device operations said by Riehl and R.R [4]. The pulsating action (plug/slug) is the motion force for the PHP, which is directly influenced by the inner tube diameter. The factors that influence the plug/slug formation in reduced diameters must be observed for this application, such as the correct working fluid selection, surface tension and shear stress effects, etc. Without this pumping action, the device will operate as a solid bar conducting heat from one end to another. Characterization of thermal performance in multi-loop PHPs has been reported in few experimental investigations done by Cai [5], Charoensawan et al. [6], Khandekar [7,8] and Meena et al [9]. Earlier, sensible heat transfer was thought of as the main reason of it which was shown by Groll [10], Nisho et al. [11] and Shafi et al. [12].

The present investigation is done on an open loop closed end bendy heat pipe which is shown in fig-1. Formation and transportation of bubbles is the main theme of heat transfer. Heating of the fluid in the evaporator section forms bubbles which moves to the condenser section, where it is cooled. Then it comes back to the evaporator section again to receive heat. The condenser section is placed above the evaporator section to allow the liquid's downward flow due to gravity.

In this investigation, the effect of use of fin in the condensation section and a copper insert inside the OLPHP is investigated. Fins in the condensation section helps increase the heat transfer rate while insert helps to break the bubbles and thus decrease the effect of internal friction. Insert in PHP is a new concept. In this study, using two types of working fluid same and changing the inclination angles, the efficiency of an OLPHP is investigated and compared with the basic OLPHP.

2. Design and construction

The three basic components of a heat pipe are the container, working fluid and the wick or capillary structure. The function of the container is to isolate the working fluid from the outside environment. It has to therefore be leak-proof, maintain the pressure differential across its walls, and enable transfer of heat to take place from and into the working fluid. Prime requirements of working fluid are compatibility with wick structure, thermal stability, high latent heat and thermal conductivity, low viscosity etc. The prime purpose of the wick is to generate capillary pressure to transport the working fluid from the condenser to the evaporator. The schematic diagram of the OLPHP used in this experiment is shown in fig.1.

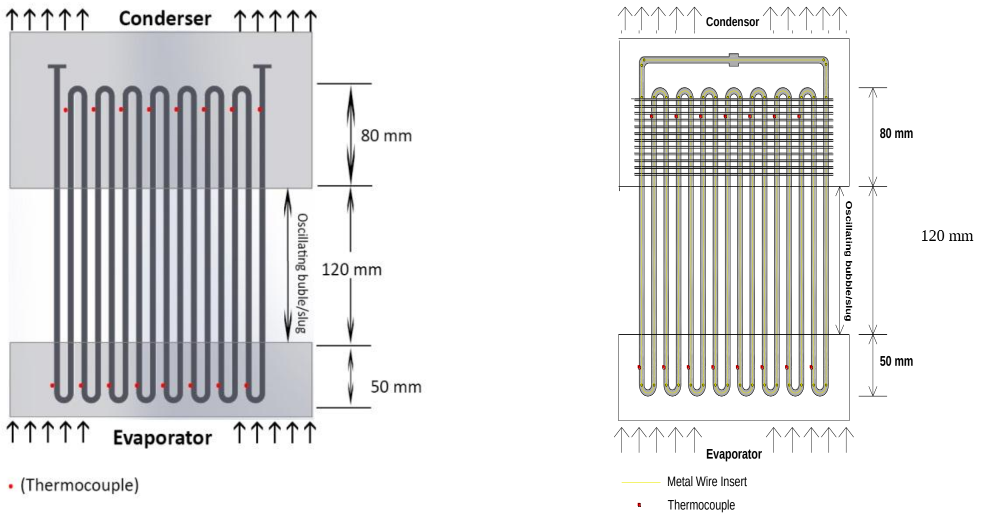

(a) (b)

Fig.1: Schematic diagram of OLPHP: (a) basic structure; (b) with fin and insert

2.1. PHP design

The cooling device performance depends on its structure, shape, material and length. Thermal performance of any device vastly depends on a parameter known as thermal resistance. Thermal resistance can be defined as:

$$R_{th}= \frac{\Delta T}{Q} \qquad (1)$$

More accurately, the thermal resistance equation can be written as:

$$R_{th} = \frac{(\overline{T}e - \overline{T}c)}{Q} \qquad (2)$$

where, $\overline{T}_e$ and $\overline{T}_e$ are the average evaporator and condenser surface temperatures, defined as,

$$\overline{T_i} = \frac{(Ti,1 + Ti,2 + Ti,3)}{3} \qquad i= e \text{ or } c \qquad (3)$$

Q is heat input power to the PHP, which is transported from evaporator to condenser.

The overall thermal resistance of a pulsating heat pipe composed of several components from evaporator to condenser. Best evaporation resistance is achieved due to the liquid film evaporation enhancement in the channel angles and best bubble rise in that case. For the same reason, a similar range for the heat transfer coefficient in the condensation region can be applied. Liquid vapor thermal resistance along the PHP is influenced by number of turns, inclination angle, filling ratio, area of PHP etc. Generally PHPs should introduce small contact resistances. Usually in power electronics, contact thermal resistances appear between the power module and the cooling device, heat sink or heat exchanger due to the surface roughness

3. Experimental setup and procedure

3.1. Experimental setup

The experimental setup is shown in Fig.2. It consists of a bendy heat pipe (Di: 2.5mm, Do: 3mm, L: 250cm, material: copper), creating a total of 8 loops. The heat pipe is divided into 3 regions- the evaporator (5 cm), adiabatic section (12 cm) and the condenser (8 cm).9 thermocouples (Type LM-35); range: (-40°C to +120°C) are attached to the wall of heat pipe; 3 for each sections. These are compatible with the digital thermometer used in temperature measurement. The evaporator section is inside a wooden box, separated from outside using mica tape, asbestos etc. The evaporative section is heated using Nichrome wire (diameter = 0.25 mm, resistivity: 1.0×10^{-6} Ω-m, specific heat: 450 $\mathrm{Jkg^{-1}K^{-1}}$) coiled around the loops, which is heated by a power supply unit (AC, 220V, 50Hz) via a variac (3F, 300V,60 Hz). For cooling the working fluid, forced convection is applied by a using an ID fan. The whole apparatus is set on a wooden stand which has facility of angular movement of the PHP. A servo motor (Modulation: Analog, Speed: 0.20 sec/60°, Weight: 55.0 g; Dimensions: Length: 40.6 mm, Width: 19.8 mm, Height: 42.9 mm; Motor Type: Coreless, Gear Type: Metal, Rotation/Support: Dual Bearings, Rotational Range:180°, Pulse Cycle:20 ms, Pulse Width:1000-2000 µs) is attached to allow automatic angular movements. For data collection Arduino Mega (Microcontroller: ATmega1280, Operating Voltage: 5V, Input Voltage (recommended): 7-12V, Analog Input Pins: 16) is used.

Fig.2: Experimental setup

3.2. Experimental procedure

- The experiment is carried out for basic open loop pulsating heat pipe and open loop pulsating heat pipe with insert and fins in condenser section.
- The experiment is performed for methanol and ethanol as working fluids and three different angular orientations of the heat pipe.
- Filling ratio for all the cases is 50% (injecting by syringe) and vertical (0°) position of the PHP is considered as the base of the other inclination angles.
- Heat inputs were varied using the variac and provided to the system. The reading of the temperatures of different sections was measured by thermocouples.
- The experimental data are stored in the computer directly using Arduino software.
- Data were recorded after every 2seconds. 200 sets of data were recorded for every requirement.
- Then the position is changed to 30°and 45˚ positions and keeping the filling ratio the same, above procedure is repeated.
- The condensation section is cooled using an ID cooling fan.

4. Results and discussion

The experiments being carried out for methanol with three different angular orientations of the heat pipe provide a similar trend of thermal characteristics. In this research, the value of thermal resistance is considered as an indication of efficiency, i.e. higher value of R_{th} refers to higher difference of temperature between evaporator and condenser section and eventually indicates a higher efficiency of the system.

4.1._Effect of fin and insert

4.1.1. Characteristics of temperature distribution

The curves presented in Fig.3, which shows the temperature vs. time characteristics curve for 0˚ inclination of the OLPHP without fin and insert and OLPHP with fin and insert exhibits a similar pattern for all the experimental conditions. For fin and insert, the temperature rises quite uniformly and the rate of temperature rise is higher than original structure. The temperature difference between the evaporator and the condensation section is greater for structure with fin and insert than for the basic structure. Fig.3 shows the comparison between the variations in the setup for condensation and evaporation section temperatures for methanol and Fig.4 shows the same for ethanol. This is same for all the temperature data; i.e. for evaporator, condenser and adiabatic section. But, certainly, the rate of increase is higher for evaporator section than for condenser section. Slowing down of the temperature increase in the condenser section can be attributed to the fact that, at some point of time, it becomes close to the room temperature. Therefore further cooling is then not needed..

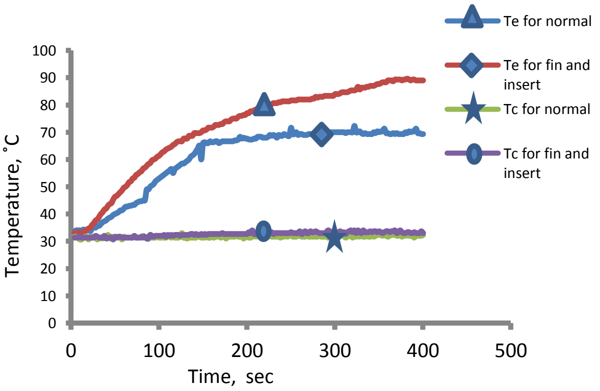

Fig.3: Variation of temperature with time (for methanol)

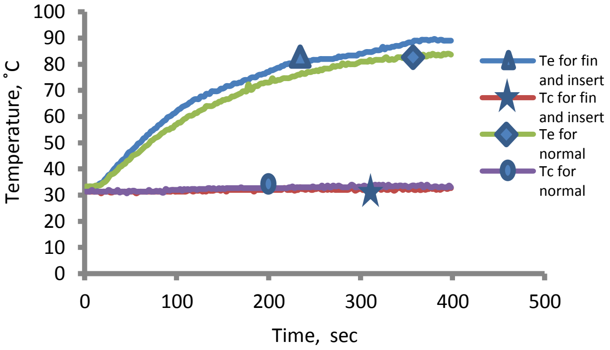

Fig.4: Variation of temperature with time (for ethanol)

4.1.2. Effect of inclination

The effect of heat flux in vertical orientation has been experimentally noted down by Tong et al. [13] and Khandekar et al. [14]. In vertical mode the vapor bubbles which take up heat in the evaporator grow in size. Their own buoyancy helps them to rise up in the tube section. Simultaneously other bubbles, which are above in the tube, are also helped by their respective buoyant forces. Comparative analysis of inclination using temperature vs. time curves for 0˚, 30˚ and 45° inclinations respectively for structures with fin and insert with methanol as working fluid is shown in Fig.5 for evaporator section and condenser section while the same kind is shown for ethanol in Fig.6. For all the experimental cases, the curves at first increase rapidly with heat input and then the rate of increase becomes slow to some extent. Temperature distribution along the heat pipes can be summarized to be in somewhat exponential pattern for evaporator section. This strongly suggests that gravity does play a role in the PHP. At 45° inclination, open loop PHP performs better than other position. Effect of gravity, pressure differential in the system, temperature may have influence in this fact. If we compare the results of ethanol and methanol then we can see that ethanol performs better than methanol.

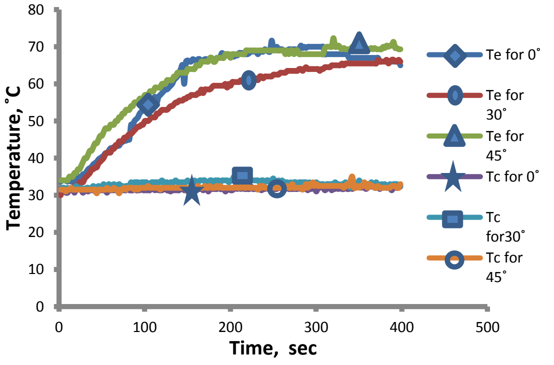

Fig.5: Variation of temperature with time & to inclination (for methanol)

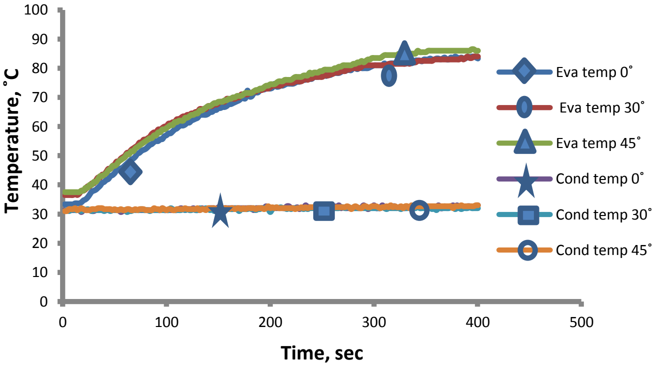

Fig.6: Variation of temperature with time & to inclination (for ethanol)

4.1.3. Variation of thermal resistance

Thermal resistance is considered in this paper as an indicator of heat pipe effectiveness. It indicates how much resistance does heat experiences in the system; so that the condenser region temperature cannot rise very high, and the system thus seems to be effective in cooling purpose. The curves of thermal resistance are of similar pattern for all the cases. They are maximum at minimum heat input and minimum at maximum heat input; i.e. thermal resistance has an inverse relationship with heat input. These curves follow an exponential pattern, and a typical graph is shown in Fig.7, which is taken from the data set of 0°, 30° and 45° inclination of the basic structure with methanol. But, the fall of thermal resistance is not of the same rate for all cases, it varies up to some extent. The thermal resistance, R_{th} falls slowly in the inclined mode. In the range of 0° to 30° the slopes are quite similar but in the case of 45° it is more effective. In the case of OLPHP with fin and insert this curve is steeper for 45˚ degree inclination and after a certain range of heat input it becomes nearly constant for all the cases. Fig.8 shows the same graph for structure with fin and insert with methanol as working fluid. Here we can see that the curve for 45˚ is steeper than other two angles and also steeper than the basic structure's 45˚ curve. Again for ethanol, we can see that the curves are quite similar but here too 45˚ inclination shows the best result. So, we can say that with highly heated appliances, heat pipe efficiency will fall down. But yet, this fall can be controlled with proper designing, which includes appropriate working fluid, filling ratio and inclination angle.

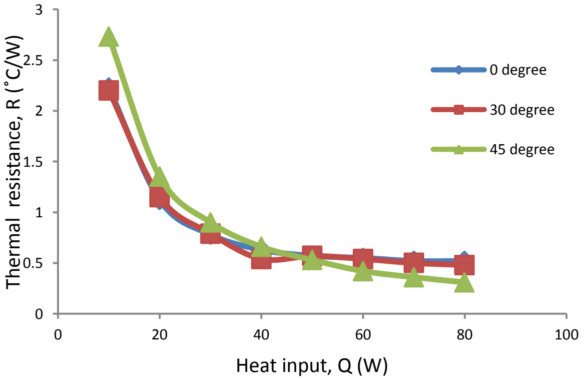

Fig.7: Variation of thermal resistance with heat input (without fin and insert for methanol)

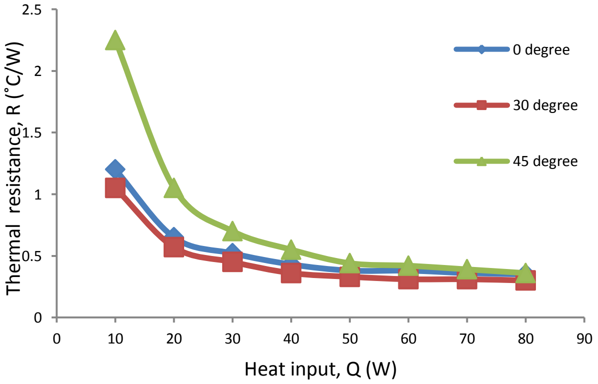

Fig.8: Variation of thermal resistance with heat input (with fin and insert for methanol)

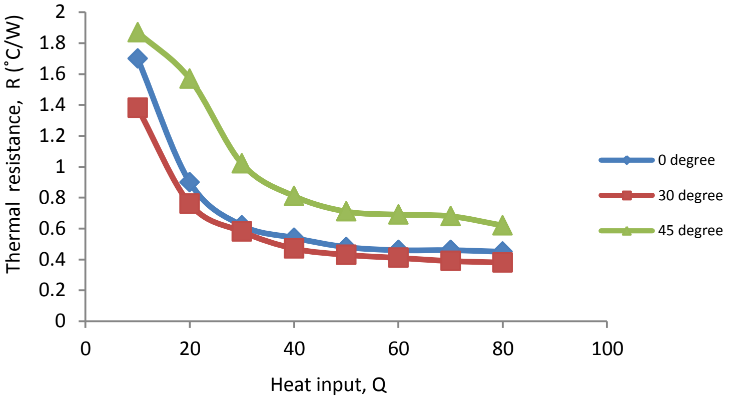

Fig.9: Variation of thermal resistance with heat input (with fin and insert for ethanol)

5. Conclusion

Pulsating heat pipe is gaining more and more popularity due to their simple design, cost effectiveness and excellent thermal performance. The work compiled here significantly increases the understanding of the phenomena, effect of working fluids and inclination angles that govern the thermal performance of pulsating heat pipes.
The following conclusions can be drawn from this experiment:

- Methanol is found to be the better working fluid compared to ethanol. Though ethanol has higher boiling point than methanol but methanol has higher specific gravity than ethanol. So here the specific gravity might have dominated the boiling point.
- It is suggested that the PHP should be operated at 45 degree orientation for its better thermal performance. The results helps us to conclude that the higher the inclination angle, the better the performance.
- The thermal resistance decreases with the increase of the heating power. The thermal resistance decreases more slowly after 40W but the rate of decrease is higher for Q less than 40W.
- The effect of pressure, bubble formation and phase transfer is very important in design of heat pipes. Different heat input to these devices give rise to different flow patterns inside the tubes.
- The use of insert helped to break the bubbles into smaller portions. This in turn is responsible for various heat transfer characteristics

The study strongly indicates that design of these devices should aim at thermo-mechanical boundary conditions which resulting convective flow boiling conditions in the evaporator leading to higher local heat transfer co-efficient. The inclination operating angle changes the internal flow patterns thereby resulting in different performance levels. Most satisfactory pattern of design may vary up to some extent from case to case. Many unsolved issues related to working fluids, design and inclination angle still exist, but continued exploration should be able to overcome these challenges. Many practical and sophisticated mathematical models of the PHPs are expected to be proposed for theoretical analysis.

Acknowledgements

The authors express their earnest gratitude to the Department of Mechanical Engineering, MIST and Department of Mechanical Engineering, BUET for providing necessary support for the accomplishment of this research.

References

[1] Moore.G, Cramming More components onto Integerated Circuits, Electronics, 1965 38(8).
[2] Akachi, H., Polášek F., Štulc P., “Pulsating Heat Pipes”, Proceedings of the 5th International Heat Pipe Symposium, 1996, pp.208-217, Melbourne Australia.

[3] Zhang, Y., Faghri, A., “Heat Transfer in a Pulsating Heat pipe with an Open End”, International Journal of Heat and Mass Transfer, Vol. 45, 2002, pp. 755-764.

[4] Riehl, R. R., “Evaluation of the Thermal-Hydro- Dynamics Behavior of an Open Loop Pulsating Heat Pipe”, National Institute for Space Research (INPE) Report, 2003, 35p.

[5] Cai, Q., Chung-lung Chen, Julie F. Asfia, “Operating Characteristic Investigations in Pulsating Heat Pipe”, journal of heat transfer, vol. 128, 2006, pp.1329-1334.

[6] Charoensawan, P., Khandekar, S., Groll, M. and Terdtoon, P. “Closed loop pulsating heat pipes”, part-A; Parametric experimental investigations”, Applied Thermal engineering, Vol.23, No.6, 2001, pp. 2009-2020.

[7] Khandekar, S., “Multiple Quasi- Steady States in a Closed Loop Pulsating Heat Pipe”, NTUS-IITK 2nd joint workshop in mechanical, Aerospace and Industrial Engineering, April 5-6, 2008, IIT, Kanpur, India.

[8] Khandekar, S., “Thermo Hydrodynamics of Pulsating Heat Pipes”, Ph.D Dissertation, University of Stuttgart, Germany, 2004.

[9] Meena, P., Rittidech, S., Tammasaeng, P, “Effect of inner Diameter and inclination angles on operation limit of closed-loop Oscillating heat pipes with check valves”, American journal of Applied Sciences, Vol. 1, No.2, 2008, pp. 100-103.

[10] Groll, M., Khandekar, S., 2002. Pulsating heat pipes: a challenge and still unsolved problem in heat pipe science, Applied Thermal Engineering 23 (4), p. 17–28.

[11] Nishio, S., Nagata, S., Baba, S. and Shirakashi R., 2002. “Thermal performance of SEMOS heat pipes,” Proceedings of 12th International Heat Transfer Conference, Grenoble, France, pp. 477–482.

[12] Shafii, M., Faghri, A. and Zhang, Y., 2001. Thermal Modeling of Unlooped and Looped Pulsating Heat Pipes, ASME Journal on Heat Transfer 23, p. 1159–1172.

[13] Tong, B., Wong, T. and Ooi, K., 2001. Closed-Loop Pulsating Heat Pipe, Applied Thermal Engineering 21(18), p. 1845–1862.

[14] Khandekar, S., Groll, M., Charoensawan, P. and Terdtoon, P., 2002. “Pulsating heat pipes: thermo-fluidic characteristics and comparative study with single phase thermosyphon, ” Proceedings of the 12th International Heat Transfer Conference. Grenoble, France, p.459–464.

Available online at www.sciencedirect.com

ScienceDirect

Procedia Engineering00 (2015) 000–000

Procedia Engineering

www.elsevier.com/locate/procedia

6th BSME International Conference on Thermal Engineering (ICTE 2014)

Experimental investigation on heat transfer characteristics of an Open Loop Pulsating Heat Pipe(OLPHP) with fin

Md Lutfor Rahman[a], Pijush Kanti Saha[a,*], Fariha Mir[a], Asfia Tanjim Totini[a], Sumaiya Nawrin[a] and Mohammad Ali[b]

[a]Department of Mechanical Engineering, MIST, Mirpur, Dhaka, Bangladesh
[b]Department of Mechanical Engineering, BUET, Dhaka, Bangladesh

---

Abstract

This paper presents an experimental investigation of an open loop pulsating heat pipe of 2 mm inner diameter and 2.5 mm outer diameter with fin in condenser section to study the heat transfer performance. The setup is an open loop closed end pulsating heat pipe creating a total of 8 loops with total length of 25 cm. The performance characterization will be done for methanol as working fluid with 50% filling ratio. The evaporator section is 5 cm in length and the condensation section is of 8 cm with an adiabatic section of 12 cm. The evaporator section is heated by electrical input using Ni-Chrome wire and the condenser section is cooled by fan. The effects of fin in PHP for open loop will be analyzed for heat transfer characteristics and the results are compared with that of without fin keeping constant the other parameters. The results explore the possibility of using the open loop pulsating heat pipe as an integrated structure to achieve higher thermal conductance to the host substrate. Effect of gravity, pressure differential in the system, temperature, heat input etc. may have influence in this fact due to which 45° inclined position of finned structure shows the best performance.

Peer-review under responsibility of organizing committee of the 6th BSME International Conference on Thermal Engineering (ICTE 2014).

Keywords: Open loop closed end pulsating heat pipe; evaporation; condensation; inclination angle; thermal conductance.

---

* Corresponding author. Tel.: 01678754801; fax: +0-000-000-0000 .
E-mail address: partha.saha717@gmail.com

Peer-review under responsibility of organizing committee of the 6th BSME International Conference on Thermal Engineering (ICTE 2014).

NOMENCLATURE

R	thermal resistance, °C/W
T	temperature along the heat pipe, °C
∆T	temperature drop along the device, °C
L	length of heat pipe, cm
IA	Inclination angle, °
Q	heat input, W
D	diameter of heat pipe, mm
FR	filling ratio, %
L	Characteristics length
OD	Outer diameter of tube
ID	Inner diameter of tube

Subscripts:

Th	thermal
a	adiabatic section
e	evaporator section
c	condenser section

1. Introduction

Thermal management of modern electronics is the challenge of the day in the wake of component miniaturization and attracted the attention of researchers to develop efficient cooling systems. Due to huge amounts of heat generation in industrial grounds, there had been always a great demand for having robust and promising cooling devices in technological fields. Currently, thermal management of electronics has become an encouraging issue for researchers since proper treatment of high operating temperature and heat flux density of these miniature devices can improve their maintenance and performance. At first, Gaugler [1], suggested the idea of heat pipe. However, it was not well appreciated until Grover [2], Grover et al. [3] invented its remarkable properties and started developed the insisting ideas. To this end, the pulsating heat pipe, proposed and patented by Akachi [4], is a new member of the wickless heat pipes. Miyazaki and Arikawa [5] presented an experimental investigation on the oscillatory flow in the PHP, and they measured wave velocity, which agreed reasonably well with the prediction of Akachi et al. Miyazaki and Akachi [6] derived the wave equation of pressure oscillation in a PHP based on self-excited oscillation. The vapour plugs generated by the evaporation of the working fluid push the liquid slugs toward the condensation section and this motion causes flow oscillations that guide the device operation, Zhang [7] proposed by experimental data's. Lee et al. [8] work on flow Visualization of Oscillating Capillary Tube Heat Pipe. Due to its excellent features, such as high thermal performance, rapid response to high heat load, simple design and low cost, PHP has been considered as one of the promising technologies for electronic cooling, heat exchanger, cell cryopreservation, the spacecraft thermal control system, etc.

There are two possible configurations for PHPs, being as an open loop and as a closed loop. In our experiment we worked for the open loop PHP. Close loop PHP is having some extra space requirement, charging difficulty, construction difficulty but having good fluid circulation between the evaporation and condensation and in case of open loop PHP it required less space, easier charging, easier construction and a counter-current liquid/vapor flow occurs in order to promote the proper device operation. In the open loop configuration, one end of the tube is pinched off and welded, while the other end may present a service valve for evacuation and charging. The evaporation section is in contact with Ni-Cr wire which is coiled around two mica sheets to deliver the desired heat load. The heat loads are administered by an AC power supply. A total of 6 thermocouples are located at each section. The thermocouples are connected to a digital temperature controller (0°C to 800°C) to monitor wall temperatures. The temperatures are recorded at every 5 minutes. All experimental tests are performed on a heat load profile basis, where the perspective is to evaluate the behavior of OLPHP related to the orientation and applied power. On the open loop configuration, the liquid circulation is not possible. In this case, it is believed that a counter-current liquid/vapor flow occurs in order to promote the proper device operation. There are some important requirements as follows [9-14]: good thermal stability, moderate vapors pressure on the operating temperature range, high latent heat, high thermal conductivity, high surface tension, acceptable freezing or pour point, low liquid and vapors viscosity etc. With the increase in heat load, the oscillations become more intensive and it can be detected by slight temperature decreasing. This behavior was detected by Khandekar et al. [15] during flow observation through transparent tubes in their experiment. On this open loop configuration, the liquid circulation is not possible. In this case, it is believed that a counter-current liquid/vapor flow occurs in order to promote the proper device operation which is proved by Riehl et al. [16].

The present investigation is done on a two phase thermo-mechanical device which is open and shown in fig-1.The whole device is divided into three parts known as evaporator section, adiabatic section and condenser section. The evaporator section is placed in lower portion and the condenser section is placed in upper portion so that liquid may go downward due to gravity. The formation of vapor bubbles on a micro heater inside micro machined channels is observed as a result of heat absorption by the evaporator and heat release by the condenser. After heat release it moves back to evaporator. The liquid and vapor slugs are transported because of the pressure pulsation caused inside the system which causes heat transfer. In earlier, it was thought that sensible heat transfer is the main reason of it [7-9] but later this concept had changed as described by Khandekar et al. [10]. Several investigations have been done on multi-turn PHP [11-13].

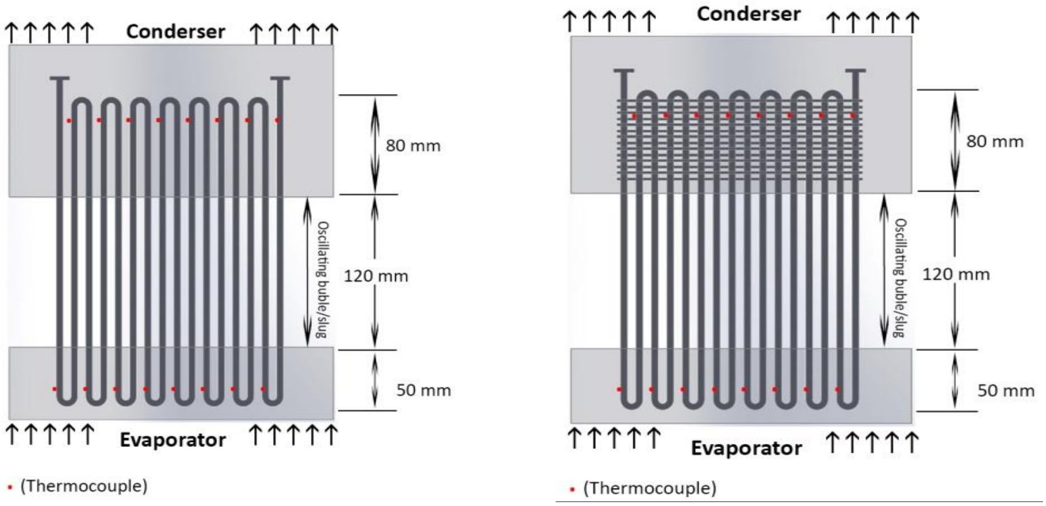

(a) Without Fin OLPHP (b) Finned OLPHP

Fig.1. Schematic of OLPHP

Therefore, better understanding on this behavior is still a motivation for further investigations. The purposes of this investigation are to study the heat transfer characteristics of an OLPHP and evaluate several issues related to its performance.

2. Experimental method

2.1. Experimental setup

The experimental setup is shown in Fig.2. The setup consists of a meandering heat pipe (ID: 2 mm, OD: 2.5 mm, L: 25 cm, material: copper), creating a total of 8 turns. The heat pipe is divided into 3 regions- the evaporator section (5 cm), adiabatic section (12 cm) and the condenser section (8 cm). Copper wire of 2 mm is used in condenser section at equal distance as fin in finned OLPHP. Thermocouples of 16 in number (LM-35 sensors, Local Sensor Accuracy (Max) (+/- C): 0.5, range: -55°C to +150°C) are glued to the wall of heat pipe in evaporator section and condensation section; 8 for each sections. Evaporator section is insulated inside a box of wood frame, separated from outside using mica sheets with Nichrome wire (diameter = 0.25 mm, resistivity: 1.0×10^{-6} Ω-m, specific heat: 450 $\mathrm{Jkg^{-1}K^{-1}}$) wounded inside, which is heated by a power supply unit (AC, 220V, 50Hz) via a variac (3F, 300V, 60 Hz). Methanol is used as working fluid at the amount of FR 50% (by volume) for each setup. For cooling the working fluid, forced convection is used by a DC fan. The whole apparatus is set on a wooden test stand (wood frame) with provision of angular movement of the PHP using servo motor (Modulation: Analog, Speed: 0.20 sec/60°, Weight: 1.94oz (55.0 g), Dimensions: Length:1.60 in (40.6 mm),Width:0.78 in (19.8 mm), Height:1.69 in (42.9 mm), Motor Type: Coreless, Gear Type: Metal, Rotation/Support: Dual Bearings, Rotational Range:180°, Pulse Cycle:20 ms, Pulse Width:1000-2000 µs). For data collection Arduino Mega (Microcontroller: ATmega1280, Operating Voltage: 5V, Input Voltage (recommended): 7-12V, Analog Input Pins: 16) is used. For avoiding complicacy, working fluids are incorporated in the heat pipe manually. The other accessories of the setup are adapter circuit, selector switches etc.

Fan

LM 35 sensor

Pulsating heat pipe

Bread board
Variac

Arduino Mega

Fig.2: Experimental setup

2.2. Experimental procedure

- After the construction of the whole setup the experiment is carried out.
- The experiment is performed for Finned and un-finned condenser sections with 50% filling ratio of Methanol as working fluid and three different angular orientation of heat pipe.
- First the heat pipe is filled 50% by working fluid Methanol (injecting by syringe) keeping the PHP in vertical (0°) position for both finned and un-finned condenser OLPHP.
- Different heat inputs were provided to the system and temperatures reading of different sections were measured by thermocouples using Arduino Mega.
- Then the position is changed to 30°, 45° positions and keeping the filling ratio the same, above procedures repeated later on for both finned and un-finned condenser.
- For cooling the condenser a cooling fan is used. It is connected to an adapter circuit.

3. Results and discussion

The experiment has been carried out for methanol and for 3 different angular orientations of finned and un-finned heat pipe where fin is used in condenser section. In this research, the value of thermal resistance is considered as an indication of efficiency, i.e. higher value of R_{th} refers to higher difference of temperature between evaporator and condenser section and eventually indicates a higher efficiency of the system.

Result is compared between finned and un-finned structure on basis of different characteristics.

3.1. Characteristics of temperature distribution with time

The Temperature vs. time curves shows a similar pattern for all the experimental conditions. So a typical curve is presented in Fig.3 and Fig.4, which is taken at 0° inclination for 50 W heat input with methanol as working fluid. In fact, for all the experimental cases, the curves at first increase rapidly with time and then the rate of increase become slow to some extent. This is same for all the temperature data; i.e. for evaporator and condenser section. But, certainly, the rate of increase is different for different regions. After reaching the boiling point, the temperature increase in evaporator slows down due to the heat required in phase transfer. Temperature increase rate being slow in the condenser section can be attributed to the fact that, at some point of time, it becomes close to the room temperature .So no further need of cooling is then necessary. From both Fig.3 and Fig.4 it is clear that till first 150 seconds there is a higher increase rate of evaporator temperature but after 100 seconds the rate decreases.

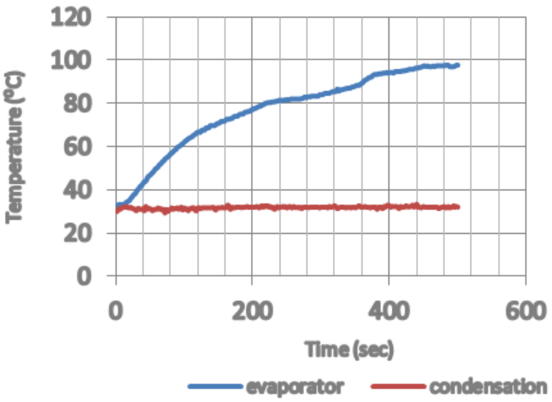

Fig.3: Variation of temperature with time for open loop Finned structure at 0 degree inclination & 50W heat input

Fig.4: Variation of temperature with time for open loop normal structure at 0 degree inclination & 50W heat input

3.2. Variation of thermal resistance

Thermal resistance is defined as the ratio of difference in average temperature of evaporator section (T_e) and average temperature of condenser section (T_c) for any instance to the heat input at that time. It can be represented at

$$R_{th} = (\text{Evaporator section, } T_e - \text{Condenser section, } T_c) / \text{Heat input, } Q.$$

It indicates how much resistance does heat experiences in the system; so that the condenser region temperature cannot rise very high, and the system thus seems to be effective in cooling purpose. The curves of thermal resistance are of similar pattern for all the cases. They are maximum at minimum heat input and minimum at maximum heat input; i.e. thermal resistance has an inverse relationship with heat input. These curves follow an exponential pattern, and atypical graph is shown in Fig.5, which is taken from the data set of 0° inclination (vertical position).But, the fall of thermal resistance is not of the same rate for all cases; it varies up to some extent. In finned structure, R_{th} is higher than normal structure at each case of heat input. It seems that finned structure is having higher condensing capability than the normal OPHP, because from the equation lower the condenser section temperature higher the thermal resistance. That means the structure having higher thermal resistance is having higher condensing capability.

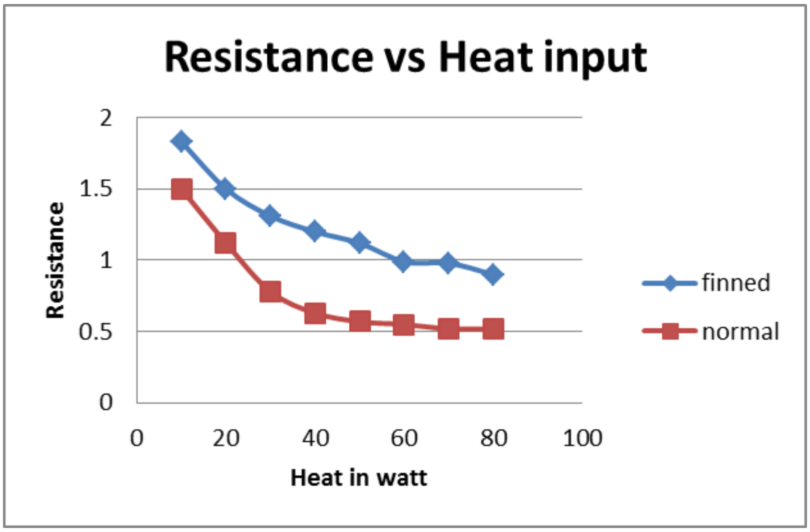

Fig.5: Variation of thermal resistance with heat input at 0 degree inclination

3.3 Effect of inclination

In vertical mode (0° inclination) the vapor bubbles which take up heat in the evaporator grow in size. Their own buoyancy helps them to rise up in the tube section. Simultaneously other bubbles, which are above in the tube, are also helped by their respective buoyant forces. These rising bubbles in the tube also carry the liquid slugs trapped in between them. In this mode of operation there is a natural tendency for the liquid slugs to travel downwards, helped by gravity force, toward the evaporator. In horizontal mode (90° inclination angle) of operation, there was hardly any macro movement of bubble. This strongly suggests that gravity does play a role in the PHP. Since gravity force is ineffective, all the movement of bubbles and slugs has to be necessarily done by the pressure forces. These forces are created due to temperature difference, which exists between evaporator and condenser. Fig.6 shows the effect of inclination for both finned and normal structure and it indicates finned structure at 45˚ inclination as best condition as R_{th} of this condition is higher than others. This is true for all heat inputs we have taken. In all cases, thermal resistances drop with increase in heat input initially with higher slope in the curves. But, as heat input increases, the slope of the curves are smaller, indicating the smaller rate of decrease in thermal resistances. Effect of gravity, pressure differential, temperature etc in the system may have influence in this fact due which 45˚ inclined position of finned structure shows best performance whereas 30˚ inclined position of normal structure shows worse performance.

Fig.6: Variation of resistance with heat input for finned and normal structure at different angle

4. Conclusions

Open loop pulsating heat pipes (OLPHP) have created a newer arena and promising possibilities as passive devices for heat transfer applications, especially suited for thermal management of electronics. Bubble formation, phase transfer and pressure are three important factors to be considered to design heat pipe. The design should give the emphasis on the desired thermo-mechanical boundary conditions resulting convective flow boiling conditions in the evaporator. These lead to higher local heat transfer co-efficient. Patterns and characteristics of flow vary with the change of heat input and operating angle. In our experiment 45˚ inclined position of finned structure shows best performance whereas 30˚ inclined position of normal structure shows worse performance. The overall effect leads to different heat transfer characteristics.

5. References

[1] Gaugler, R. S US patent 2350348, Appl. 21 Dec, 1972, Published 6 June 1944.

[2] Grover, G. M US patent 3229759, Filed 1963.

[3] Grover, G.M., Cotter, T.P. and Erickson, G.F., "Structures of very high thermal conductance", J. App. Phys., Vol. 35, pp.1190-1191,1964.

[4] Akachi, H., Polaassek, F., SStulc, P., "Pulsating heat pipes. Proceedings of the 5th International Heat Pipe Symposium", Melbourne, Australia, 1996,p. 208–217 (ISBN 0-08-042842-8).

[5] Miyazaki, Y., and Arikawa, M. "Oscillatory Flow in the Oscillating Heat Pipe", Proceedings of the 11th International Heat Pipe Conference, Japan Association for Heat Pipes, Tokyo, Japan, 1999, pp. 131–136

[6] Miyazaki, Y., and Akachi, H. "Self Excited Oscillation of Slug Flow in a Micro Channel", Proceedings of the 3rd International Conference onMultiphase Flow, Lyon, France, 1998.

[7] Zhang, Y., Faghri, A. "Heat Transfer in a Pulsating Heat pipe with an Open End", International Journal of Heat and Mass Transfer, Vol. 45, 2002, pp. 755-764.

[8] Lee,W. H., Jung,H. S., Kim, J. H., and Kim, J. S. "FlowVisualization of Oscillating Capillary Tube Heat Pipe", Proceedings of the 11th InternationalHeat Pipe Conference, Japan Association for Heat Pipes, Tokyo, Japan,1999, pp. 131–136

[9] Wallis, G. "One Dimensional Two-Phase Flow", McGraw Hill Inc., 1969 (ISBN 0-0706-794-28).

[10] Khandekar, S., Schneider, M., Groll, M., "Mathematical modeling of pulsating heat pipes", state-of-the-art and future challenges, 5th ASME/ISHMT Joint International Heat and Mass Transfer Conference, Kolkata, India, 2002, pp. 856– 862 (ISBN 0-07-047443-5).

[11] Groll, M., Khandekar, S., “Pulsating heat pipes: a challenge and still unsolved problem in heat pipe science”, Proceedings of the 3rd International Conference on Transport Phenomena in Multiphase Systems, Kielce, Poland, 2002, pp. 35–44 (ISBN 83-88906-03-8).
[12] Duminy, S., “Experimental investigation of pulsating heat pipes”, Diploma thesis, Institute of Nuclear Engineering and Energy Systems (IKE), University of Stuttgart, Germany, 1998.
[13] Khandekar, S., Schneider, M., Schaafer, P., Kulenovic, R., Groll, M., “Thermofluid dynamic study of flat plate pulsating heat pipes”, Microsc. Thermophys. Eng. 6 (4) (2002) pp. 303–318 (ISSN 1089-3954).
[14] Shafii, M.B., Faghri, A., Zhang, Y., “Thermal modeling of unlooped and looped pulsating heat pipes”, ASME J. Heat Transfer 123 (2001) pp. 1159.
[15] Khandekar, S., Dollinger, N., Groll, M., “Understanding Operational Regimes of Closed Loop Pulsating Heat Pipes”, An Experimental Study, Applied Thermal Engineering, Vol. 23, 2003, pp. 707-719.
[16] Riehl, R. R., “Evaluation of the Thermal-Hydro-Dynamics Behavior of an Open Loop Pulsating Heat Pipe”, National Institute for Space Research (INPE) Report, 2003, 35p.Pulsating Heat Pipe” Journal of Applied Fluid Mechanics, Vol. 5, No. 2, Issue 10, 2012, Accepted for Publication.

Available online at www.sciencedirect.com

ScienceDirect

Procedia Engineering00 (2015) 000–000

Procedia Engineering

www.elsevier.com/locate/procedia

6th BSME International Conference on Thermal Engineering (ICTE 2014)

Study of Thermal Conductivity and Mechanical Property of Insulating Firebrick Produced by Local Clay and Petroleum Coal Dust As Raw Materials

Md. Hamidur Rahman[a,*], Md.Tariqul Islam[a], Tamzid Ibn Minhaj[a], M.A.K. Azad[a], Md.Mehedi Hasan[a] and A.A.Md. Rezaul Haque[a]

[a]Department of Materials and Metallurgical Engineering
Bangladesh University of Engineering and Technology (BUET)
Dhaka, Bangladesh

Abstract

Thermal insulation is one of the major requirements for various industrial applications. In this study the evaluation of thermal conductivity and mechanical property of an insulating refractory was carried out at elevated temperature. As additive, coal dust and 4-5wt% water were mixed with local clay. After forming the bricks by conventional uniaxial pressing method, the samples were first air dried for 2 hours at ambient temperature of 30°C, then oven dried for 8-10 hours at 110°C and finally fired in furnace for 6 hours at 1050°C. The combustion of fully combustible coal incorporated extra porosity in the final products resulting in enhanced thermal insulation. As experimental variables, three different sets of coal particle size range (coarse: 100-500 µm, medium 20-100 µm, fine: less than 20µm) and four different coal percentages were used. The results thus obtained showed that increased fineness of coal dust for a fixed coal percentage improved crushing strength and porosity and decreased thermal conductivity. In contrast, for a fixed coal particle size range, crushing strength and thermal conductivity decrease and the percentage of porosity increases with the increase of coal percentage.

Peer-review under responsibility of organizing committee of the 6th BSMEInternational Conference on Thermal Engineering (ICTE 2014).

Keywords: Thermal Insulation; Fireclay; Coal dust; Insulating Refractory; Porosity; Thermal Conductivity.

1. Introduction

The industrial application of insulating fire bricks is increasing day by day. Thermal resistance and crushing strength

---

* Corresponding author. Tel.: +8801916930465;
*E-mail address:*mrhamid.buet@gmail.com

Peer-review under responsibility of organizing committee of the 6th BSME International Conference on Thermal Engineering (ICTE 2014).

are most important properties from their application point of view. Like all the other cases, the structure property relationship plays very vital role in achieving and modifying the desired properties in refractory bricks. For example, how much heat flux will flow through the section of refractory body will be determined by the conductivity of the individual phases present, the nature of their interfaces, their distribution etc. The main challenge in producing insulating fire brick is the desired balance between mechanical and thermal properties. For example, incorporation of increased amount of pores may improve thermal resistance but at the same time deteriorate strength. For that reason, optimization of the properties by varying manufacturing parameters can be very significant area of investigation. Among many methods available for manufacturing the insulating bricks, burnout process is most common. In this method, normally an easily combustible bio material is incorporated in the slurry which during firing burns out producing a pore similar to its size. Rice husk, saw dust, coal dust etc. have been tried as combustible additives. Different types of additives create their characteristic pores. For example, rice husk gives d-shaped or longitudinal pores, saw dust gives pores of irregular size and coal dust gives spherical size pores [1, 2].
In this present study, coal was first collected and ball milled, then a sieve analysis was carried out to segregate particles of different size range. Chemical analysis of locally collected clay was made and then several batches of specimens (bricks) were made varying the coal particle size and percentage of coal incorporated. The specimens were fired in a furnace after required periods of drying cycle.

Percentage of porosity for each sample was calculated from their apparent and true densities. Then cold crushing test was carried out in a universal testing machine. The thermal conductivity of each sample was obtained using Lee's apparatus. Then the experimental results were represented graphically.

2. Experimental

2.1 Raw materials processing & analysis

The raw materials used for the manufacturing of insulating refractory brick were clay and coal dust. The composition of clay was found out by wet analysis method. Result of analysis is given in table 1.

Table 1. Chemical analysis of clay.

Components	Percentage(wt.%)
Iron(III) oxide, Fe_2O_3	5.99
Alumina, Al_2O_3	27.01
Silica, SiO_2	63.81

Hard coal pieces was first ball milled to achieve fine coal powder. Then sieve analysis was carried out in a sieve anlyser to separate the powders of different sizes. The hard coal, sieve analyzer and coal powders collected in separate containers are shown in figure 1.

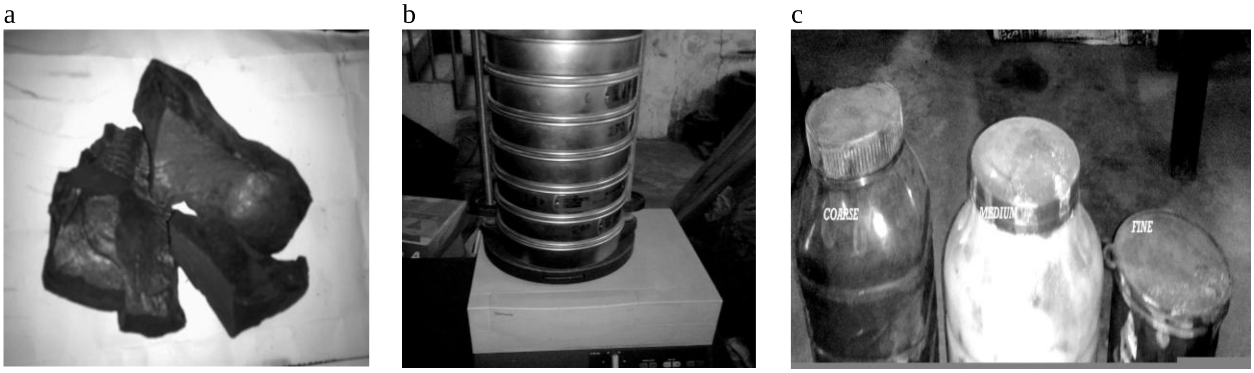

Fig. 1. (a) Hard coal pieces, (b) sieve analyzer , (c) Coarse, medium and fine coal powders collected after ball milling and sieve analysis.

Particles of three different ranges of particle sizes were collected under three different names. The type of powder and particle size range in micrometer (μm) is given in table 2.

Table 2. Particle size range of different types of coal powder

Type of coal powder	Particle size range(μm)
Coarse	100-500
Medium	20-100
Fine	Less than 20

The analysis of coal powder is then carried out. The analysis of coal is given in table 3 .

Table 3 Chemical analysis of coal.

Components	Percentage(wt.%)
Ash	5.04
Moisture	2.72
Volatile matter	28.61
Fixed carbon	63.63

2.2 Mould preparation

The function of mould is to give the shape and a dense packing to achieve the sufficient green strength for handling of the green bricks. Mould size, shape, consisting parts, material can be changed depending upon requirement. In present case, the mould was made of mild steel which consisted of three parts: (a) base part (b) ring shaped mould body and (c) ramming press or load. Different parts of mould and mould assembly is shown in figure 2.

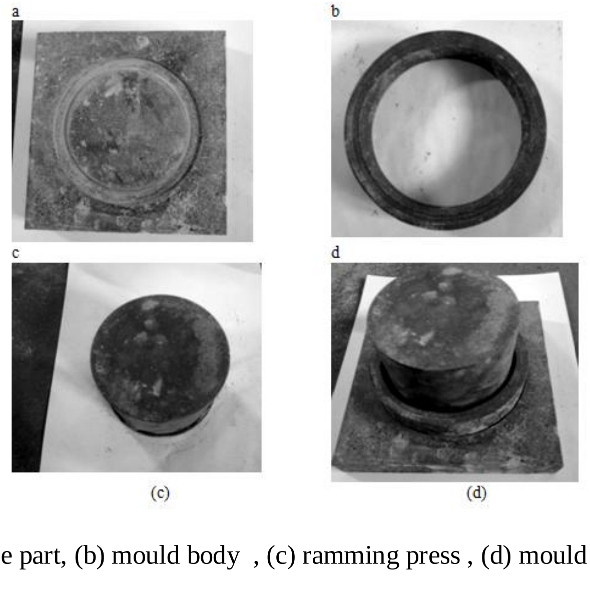

Fig. 2. (a) Base part, (b) mould body , (c) ramming press , (d) mould assembly .

2.3 Specimen preparation

Coal powder of particular size range was weighed and added to a mixing bowl. Clay was also weighed and then mixed thoroughly with coal powder in the bowl. However, water was added insufficiently each time, mixing it into the slurry by hand. Care was taken so that the water gets absorbed into the mixture instead of setting down the bowl. After preparing the slurry, the mould was filled and pressed hard so that the mixture reaches to all the corners and sides. Finally, the brick was ejected from the mould. Then, the green bricks were at first dried for several hours at the room temperature followed by oven drying at 110°C for 8-10 hours. After drying they were taken into the furnace and arranged separately to get sufficient amount of oxygen for proper burning of the combustible material (coal) in the brick. They were heated slowly up to 400°C and then rapidly to 1050°C. Total firing time was about 6 hours. The assembly of the bricks inside the box type muffle furnace used in this investigation is shown in fig.3.

Fig. 3. Circular bricks placed in oven.

2.4 Measurement of apparent and true density

At first the specimen was weighed and by measuring radius and thickness of the circular brick volume was calculated. Dividing the mass by volume, apparent density was measured. For measuring true density, the circular block was crushed first and then a known amount of this powder was taken into a pycnometer bottle full of water . The weight of water lost from pycnomoter gives the volume of the water which is equal to the volume of the powder. Dividing the previously known weight by this volume gives true density which excludes the presence of all types of pores (both internal and external) . From true and apparent density, percentage of porosity was calculated from the following formula,

$$\%\text{Porosity} = [1 - (\frac{Apparent \quad density}{True \quad density})] \times 100 \ \%$$

Using this method, apparent density and percent porosity were measured for all speciments. Then two graphs were plotted showing change of apparent density and percent porosity with increasing percentages of coal and varying coal particle size (Fig.7b).

2.5 Measurement of crushing strength

At first, a square shaped block was prepared from the circular brick. Then it was polished for getting accurate dimension of one inch by one inch. After preparing the block, it was set into the crushing machine and load was applied on the block. The block was broken at a certain load and this load was noted for measuring the crushing strength. Dividing the load by area (load bearing surface), Crushing strength was calculated.

Crushing strengths for all specimens were determined by this process and then a graph was plotted showing change of crushing strength with increasing percentage of coaland varying coal particle size(fig. 8b).

Fig. 4. The cold crushing test assembly of a universal testing machine.

2.6 Measurement of thermal conductivity

Lee's apparatus [3] was used for measuring the thermal conductivity of the specimens which is shown in figure 1. The apparatus consists of a hollow cylinder C with two tubes attached to it, known as steam chamber, two brass discs A & B with radial holes.

Weight of the disc A was measured first and the thickness and diameter of the specimen were measured. Then the specimen was polished for good contact with the brass discs and placed over the disc A. Disc B and hollow cylinder was placed over

the specimen S respectively. Steam was passed into the steam chamber. Two thermometers were set and waited for taking the steady temperature T_1 & T_2. At this steady state, the heat conducted through the refractory specimen (which is a bad conductor) will be eual to the heat radiated from the lower exposed portion of the metallic disc.Then to find the heat radiated from the lower disc, the steam supply was stopped and steam chamber with disc B was removed. Specimen S with disc A was placed upon by a concentric insulator disc and heated by burner for increasing the temperature up to (T_1 +10°C).Then the disc A was cooled and cooling time was noted for every 1°C decrease in temperature. By plotting cooling time and temperature values, a cooling curve was drawn. A tangent was drawn to the curve at or near temperature T_2 and dT/dt was calculated. The thermal conductivity was measured by using the following formula,

$$K = \left[ms \frac{\left(\frac{dT}{dt}\right)\left(\frac{d}{D}\right)}{(T_1 - T_2)} \right] cal.cm^{-1}.{}^{\circ}c^{-1}.\sec^{-1}$$

Where, m=Weight of Disc A;

S=Specific heat of A (specific heat of brass);

d=Thickness of A;

D=Cross sectional area of A;

T_1= steady temperature of disc B;

T_2= steady temperature of disc A.

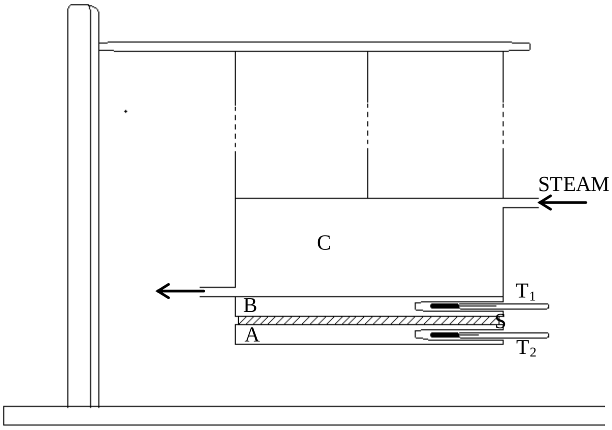

Fig. 5. Schemetic image of Lee’s apparatus.

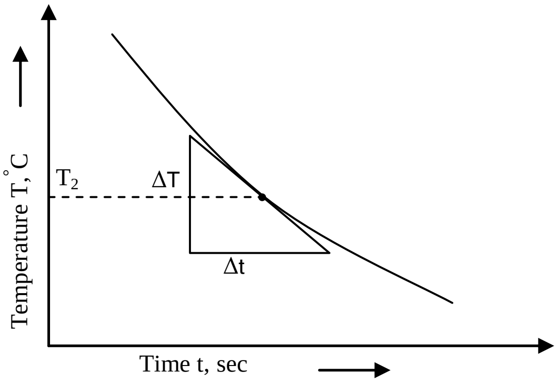

Fig. 6. Cooling Curve.

3. Results and discussions

As seen from figure 7(a), as the percentage of the coal increases, apparent density decreases. Density has been decreased from 1.48 to 1.1 for fine coal particle, from 1.56 to 1.20 for medium coal particle, from 1.62 to 1.3 for coarse coal particle with increasing the percentage of coal from 5% to 20 % which is shown in figure 7(a). From figure 7(b), we can see that porosity has been increased from 46.50% to 58.48% for fine coal, from 42.03% to 56.60% for medium coal, from 38.36% to 53.65% for coarse coal with increasing the coal amount from 5% to 20 %.

The coal is of lower density than clay. This coal almost burned out during firing leaving minute amount of ash and spherical pores created against pressure of carbon-di-oxide and vapour which are product of combustion. This means incorporation of higher coal percentages, increases the overall points which areoccupied by light weight coal rather than clay, in other words, increasing coal percentage decreases weight in a fixed volume. The apparent density calculates weight per unit volume. That’s why apparent density decreases with increasing coal percentage, whereas true density almost remains same. Porosity in a sense, is a measure of how low the value of apparent density is from true density. Percentage of porosity increases as apparent density decreases. For that reason increasing coal percentage increases percentage porosity.

From figure 7(a), it is obvious that apparent density values are little affected by particle size. Although specimens with finer particles possess higher surface area with the furnace environment once combustion is started (surface coal particles burnt out leaving smaller size pores) so effective combustion throughout the bulk volume is preferred here and possibility of remaining unburnt coal particles is reduced.

Figure 7(b) shows that size effect is more obvious in case of percentage porosity; for example, at 15 wt% coal it s around 58% for fine coal but 45% for specimens containing coarse coal particles. So, it can be concluded that as fineness increases, percentage of porosity also increases. This can be attributed to the favorable complete combustion condition existing in fine coal samples explained above.

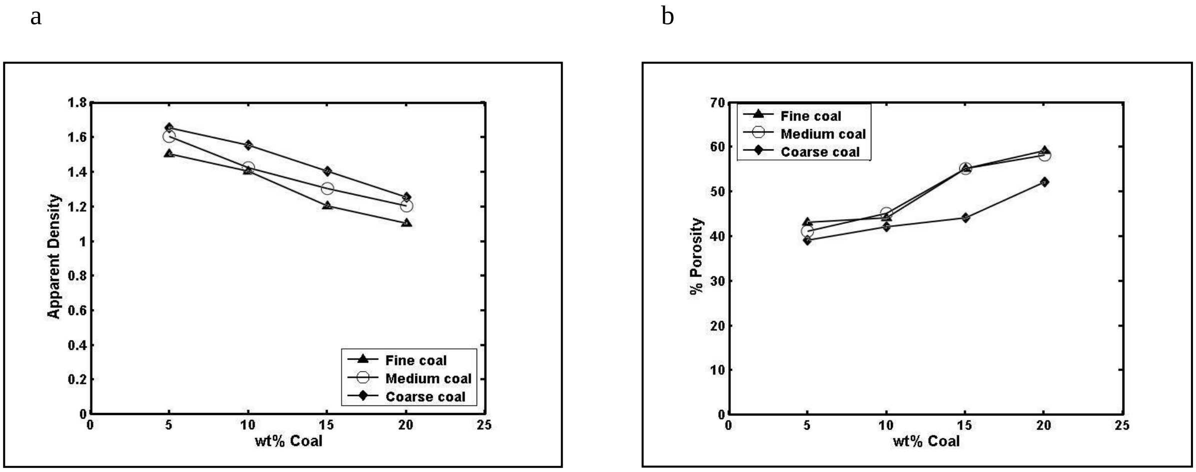

Fig.7. Relationship of (a) apparent density and (b) percentage of porosity of insulating fire bricks with coal weight percentage and particle size.

Figure 8(a) shows the effect of coal addition on thermal conductivity. It shows that thermal conductivity decreases from $4.1^{x}10^{-4}$cal$\cdot$cm$^{-1\cdot\circ}$C$^{-1\cdot}$sec^{-1}to $2.37^{x}10^{-4}$cal$\cdot$cm$^{-1\cdot\circ}$C$^{-1\cdot}$sec^{-1}for fine coal, from $4.18^{x}10^{-4}$cal$\cdot$cm$^{-1\cdot\circ}$C$^{-1\cdot}$sec^{-1}to $2.38^{x}10^{-4}$cal$\cdot$cm$^{-1\cdot\circ}$C$^{-1\cdot}$sec^{-1}for medium coal, from $4.24^{x}10^{-4}$cal$\cdot$cm$^{-1\cdot\circ}$C$^{-1\cdot}$sec^{-1}to $2.85^{x}10^{-4}$cal$\cdot$cm$^{-1\cdot\circ}$C$^{-1\cdot}$sec^{-1}for coarse coal with increase of coal amount from 5% to 20%. Thermal conductivity depends not only on the clay but also on the size, shape, and amount of the organic particles. With the increase of coal addition, the porosity increases. This porosity acts as a barrier to the flow of heat and as a result of which thermal conductivity decreases. From figure 7(a), it can be concluded that thermal conductivity of the brick using fine coal is relatively less than the medium and coarser coal of same composition. Fine coal gives smaller pore size. Which means heat flux needs to face a higher area of low conductivity in its way across the brick. That's may be the reason for slightly decreasing thermal conductivity with decreasing coal particle size.

From figure 8(b), we can see that cold crushing strength decreases from 22.79MPa to 5.5MPa for fine coal particle, from 20 MPa to 5MPa for medium coal, from 18.6MPa to 6.1Mpa for coarse coal with increase of coal content from 5% to 20%. Coal is a non plastic material. With the addition of coal, binding action decreases. Moreover during firing, this coal particles burn out and leaves the pores and decreases the density. This results in decrease of crushing strength. From figure 8(b), it can be seen that cold crushing strength of the brick using fine coal is relatively high than the medium and coarser coal of same composition. This can be attributed to the fact that, specimens with finer coal powders possess finer pores and consequently offers higher load carrying area during test.

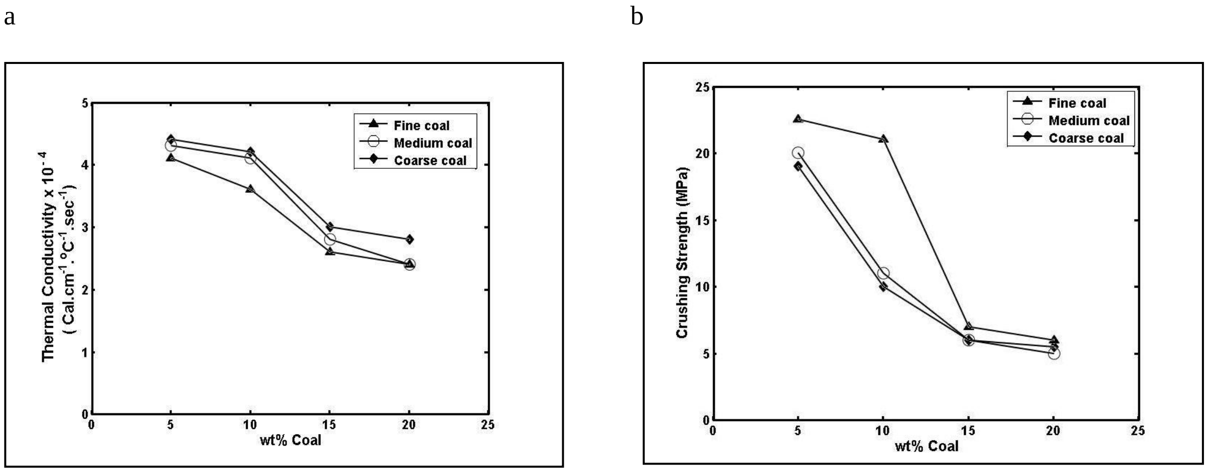

Fig.8. Relationship of (a) thermal conductivity and (b) crushing strength of insulating fire bricks with coal weight percentage and particle size.

Stress is calculated from force per unit area, so these specimens will undergo less stress for same applied load. Also any internal crack will face more obstacles in its way of propagation in specimens with finer coal powder. That’s why specimens of fine coal powder shows higher crushing strength than coarse ones.

4. Conclusion

The relationship between thermal and mechanical properties of insulating bricks with the particle size and percentage of coal was investigated. The investigation revealed that apparent density, thermal conductivity and cold crushing strength decreases and percentage porosity increases as the coal percentage increases in the specimens. On the other hand, apparent density and thermal conductivity decreases but percentage porosity and cold crushing strength increases as the fineness of the coal particles increases.

References

[1] A. Bhatia, B.E.,Overview of Refractory Materials, 2011.
[2] Law, N.M.P., Faizo,P. and Guite, P., Ceramic International 2, 1984 page- 59.
[3] J.D.Gilchrist, Fuels, Furnaces and Refractoroes, 1977, page-250.

Available online at www.sciencedirect.com

ScienceDirect

Procedia Engineering00 (2015) 000–000

Procedia Engineering

www.elsevier.com/locate/procedia

6th BSME International Conference on Thermal Engineering (ICTE 2014)

Effect of fin and insert on the performance characteristics of close loop pulsating heat pipe (CLPHP)

M Lutfor Rahman[1], Sumaiya Nawrin[1,]*, Rasel A Sultan[1], Fariha Mir[1], Mohammad Ali[2]

[1]Military Institute of Science and Technology, Mirpur Cantonment, Dhaka-1216, Bangladesh
[2]Bangladesh University of Engineering & Technology, Dhaka-1000, Bangladesh

---

Abstract

The pulsating heat pipe, a serpentine tube of capillary dimension with many turns, has great impact on today's successful thermal management. It is an ascending technology to satisfy present requirement of increasing thermal performance. Focusing on this, an experiment has been done on the close loop pulsating heat pipes (CLPHP) to observe their performance characteristics by using two working fluids with varying inclination angles of 0^0 (vertical), 30^0 and 45^0. The experiment is performed on 2.5 mm inner diameter and 3 mm outer diameter CLPHP with an insert of copper wire of 1 mm diameter and fins are added on the condensation section where the evaporation section is 50 mm, adiabatic section is 120 mm and condensation section is 80 mm.This investigation is done using ethanol and methanol with 50% filling ratio in CLPHP with 8 loops. Methanol shows better performance at 45^oinclination than ethanol due to their physiochemical properties at different conditions.In this experiment the effects on the performance of using fins with insert and the variation of inclination angles are investigated. The results show the better performance characteristics and enhancement of heat transfer in the present experimental set-up because of using fin and insert.

Keywords: Pulsating heat pipe; Thermal performance; Close loop pulsating heat pipe (CLPHP); Insert of Copper wire; fin on condensation section

---

* Corresponding author. Tel.: +880-1681-773966
*E-mail address:*sumaiya.nawrin@yahoo.com

NOMENCLATURE:		*Subscripts:*	
R	thermal resistance, °C/W	*th*	thermal
T	temperature along the heat pipe, °C	*a*	adiabatic section
ΔT	temperature drop along the device, °C	*e*	evaporator section
L	length of heat pipe, cm	*c*	condenser section
IA	Inclination angle, °		
Q	heat input, W		
D	diameter of heat pipe, mm		
FR	filling ratio, %		
L	Characteristics length		
OD	Outer diameter of tube		
ID	Inner diameter of tube		

1. Introduction

Conventional heat pipes are the most common effective procedure to harness or transport thermal energy. They act as a blessing for the enhancement of thermal management of a variety of applications such as heat exchangers, space applications, electronic cooling and economizers. But in today's concept, there is higher demand on net heat flux dissipation and by following Moore's law these demands are becoming more challenging day by day. Modern thermal management faces considerable changes in the wake of component miniaturization to cope with these higher demands and one of the remarkable result of these challenges is pulsating heat pipe which was first introduced by Akachi et al. [1-4].

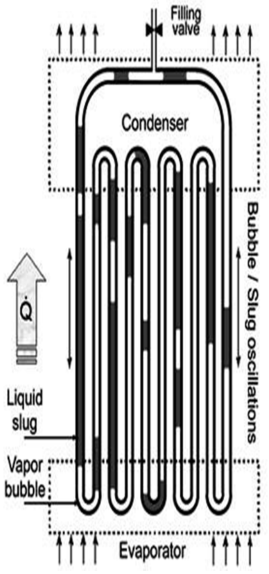

Fig.1. Close loop pulsating heat pipe

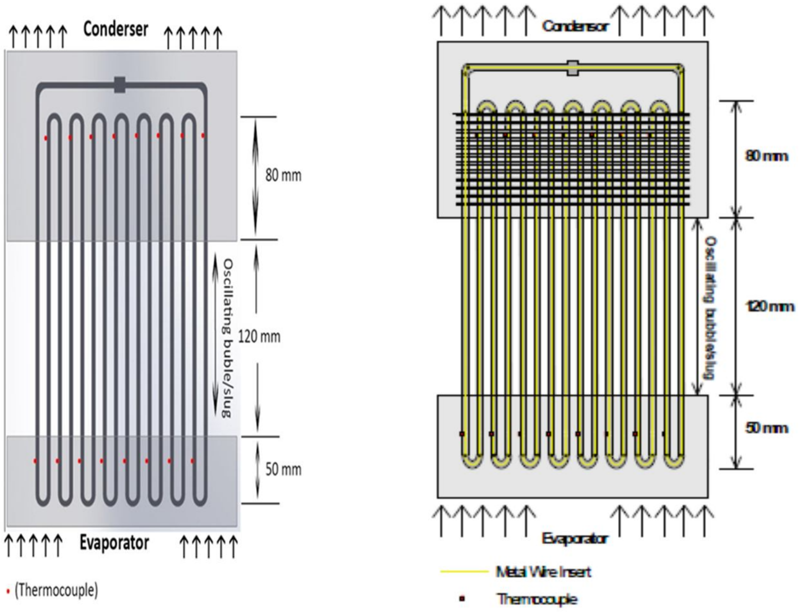

(a) Normal CLPHP (b) Finned-inserted CLPHP

Fig.2. Experimental setup

As a new and emerging technology, PHP has greater advantages over conventional heat pipes and it can be arranged in two ways known as CLPHP and OLPHP. This two phase thermal control device with arbitrary number of turns is filled with required quantity of working fluids which is a source of research, stated by S. Khandekar et al. [5] and M. Groll et al. [6].

The present investigation is done on a two phase thermo-mechanical device which is closed and shown in Fig.1.The whole device is divided into three parts known as evaporator, adiabatic and condenser section. The evaporator section is placed in lower portion and the condenser section is placed in upper portion so that liquid may go downward due to gravity. The formation of vapor bubbles on a micro heater inside micro machined channels is observed as a result of heat absorption by the evaporator and heat release by the condenser. After heat release it moves back to evaporator. The liquid and vapor slugs are transported because of the pressure pulsation caused inside the system which causes heat transfer. In earlier, it was thought that sensible heat transfer is the main reason of it, investigated by M. Groll et al. [6], S. Nishio et al. [7] and M. Shafii et al. [8] but later this concept had changed by S. Khandekar et al.[9]. Several investigation has been done on multi-turn PHP, suggested by Charoensawan et al. [10], Khandekar et al.[11] and Meena et al. [12].

Now the effect of fin and insert on CLPHP is investigated here with various inclination angles by filling the capillary tubes with methanol and ethanol. Fin is used here to increase heat transfer through convection process. To fulfill the strong demand for heat augmentation techniques of forced heat transfer, use of insert is also a new concept. So in present experiment the effect of fin and insert on PHP; as a heat increasing source how efficient is examined here.

2. Design and construction

The experimental setup is shown in Fig.2 and Fig.3. The setup consists of a meandering heat pipe (ID: 2.5mm, OD: 3mm, L: 25cm, material: copper), creating a total of 8 turns. The heat pipe is divided into 3 regions- the evaporator (5cm), adiabatic section (12cm) and the condenser (8cm).2mm copper wire in condenser section at equal distance is used as fin along with copper wire of 1 mm diameter as insert is used in finned with insert CLPHP. 6 thermocouples (LM-35 sensors, Local Sensor Accuracy (Max) (+/- C): 0.5, range: -55°C to +150°C) are glued to the wall of heat pipe in evaporator and condensation section; 3 for each sections.

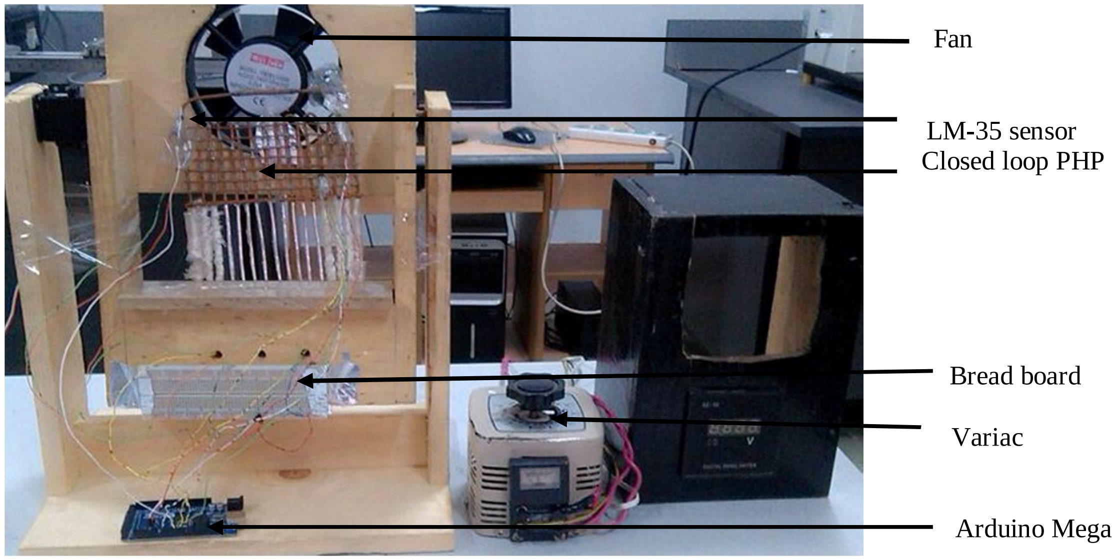

Fig.3. The prototype experimental set up

Evaporator section is insulated inside a box of wood frame, separated from outside using mica sheets with Nichrome wire (diameter = 0.25 mm, resistivity: 1.0 × 10−6 Ω-m, specific heat: 450Jkg^{-1}K^{-1}) wounded inside, which is heated by a power supply unit (AC, 220V, 50Hz) via a variac (3F, 300V,60 Hz). For cooling the working fluid, forced convection is used by a DC fan. The whole apparatus is set on a wooden test stand (wood frame) with provision of angular movement of the PHP using servo motor (Modulation: Analog, Speed: 0.20 sec/60°, Weight: 1.94 oz (55.0 g),Dimensions: Length:1.60 in (40.6 mm),Width:0.78 in (19.8 mm),Height:1.69 in (42.9 mm),Motor Type: Coreless, Gear Type: Metal, Rotation/Support: Dual Bearings, Rotational Range:180°, Pulse Cycle:20 ms, Pulse Width:1000-2000 µs). For data collection Arduino Mega (Microcontroller: ATmega1280, Operating Voltage: 5V, Input Voltage (recommended): 7-12V, Analog Input Pins: 16 is used. For avoiding complicacy, working fluids are incorporated in the heat pipe manually. The other accessories of the setup are adapter circuit, selector switches etc.

3. Experimental procedure

- After the construction of the whole setup the experiment is carried out.
- The experiment is performed for Finned (in condenser section) with insert and normal CLPHP with 50% filling ratio of Ethanol and Methanol as working fluid and three different angular orientation of heat pipe.
- First the heat pipe is filled 50% by working fluid Ethanol and Methanol (injecting by syringe) keeping the PHP in vertical (0°) position for both finned and un-finned condenser CLPHP.
- Different heat inputs were provided to the system and temperatures reading of different sections were measured by thermocouples using Arduino Mega.
- Then the position is changed to 30°, 45° positions and keeping the filling ratio the same, above procedures repeated later on for both finned and un-finned condenser.
- For cooling the condenser a cooling fan is used. It is connected to an adapter circuit.

4. Results and discussion

4.1. Effect of fin and insert on thermal resistance with different heat input

Thermal resistance is defined as the ratio of difference in average temperature of evaporator section (T_e) and average temperature of condenser section (T_c) for any instance to the heat input at that time. It can be represented as

$$R_{th}=(Te-Tc)/Q$$

The value of thermal resistance is considered as an indication of efficiency, i.e. higher value of R_{th} refers to higher difference of temperature between evaporator and condenser section and eventually indicates a higher efficiency of the system. The value (T_e- T_c) indicates how much resistance does heat experiences in the system; so that the condenser region temperature cannot rise very high and the system thus seems to be effective in cooling purpose. For both Methanol and Ethanol, the highest thermal resistance is obtained at lower heat input and gradually it decreases. Fig.4, Fig.5 and Fig.6 represent R_{th} for both finned-inserted and normal structure at different heat inputs. Graphical representation in Fig.4 and Fig.5 shows that in both cases of methanol and ethanol finned-inserted structure shows better performance as R_{th} is higher in finned-inserted structure than normal structure. It indicates finned-inserted structure experience higher resistance in the system; so that the condenser region temperature of finned-inserted structure cannot rise very high, and the system thus seems to be effective in cooling purpose.

Initially decreasing rate of R_{th} is large but gradually at higher heat input reduction rate ceases and this reduction rate can be controlled with proper designing, which includes appropriate working fluid, filling ratio and inclination angle.

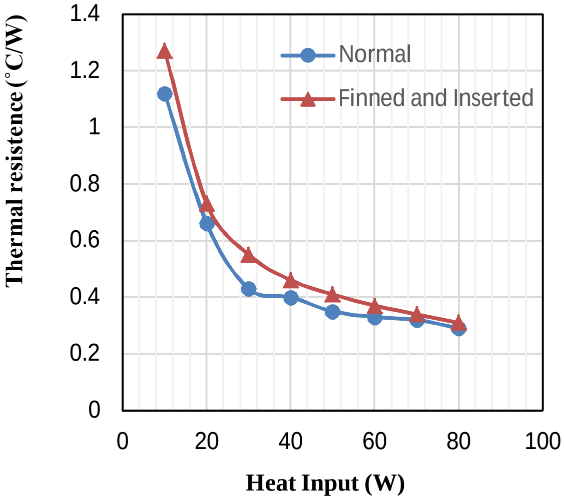

Fig.4.Variation of resistance with heat input at 0 degree inclination (Ethanol)

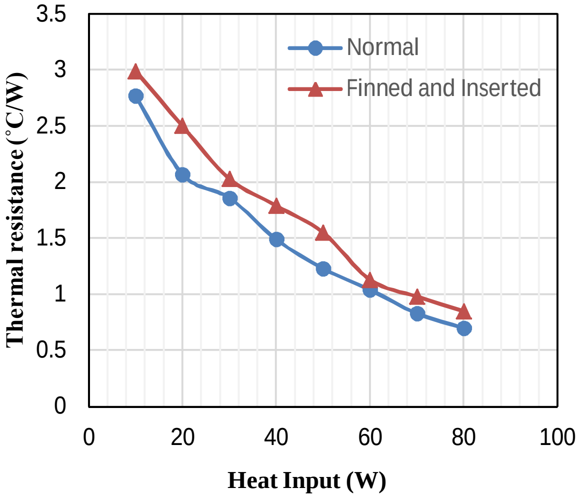

Fig.5.Variation of resistance with heat input at 0 degree inclination (Methanol)

Methanol shows higher thermal resistances than ethanol, which is shown in Fig.6. Because methanol has a higher specific heat value (Cp= 2.54 kJ/kg.k) than ethanol (Cp= 2.47 kJ/kg.k) (both at 20˚C). So heat is accumulated in methanol is higher in amount than ethanol; that allows it to keep the condenser region temperature (T_c) lower and resulting in better working efficiency compared with ethanol.

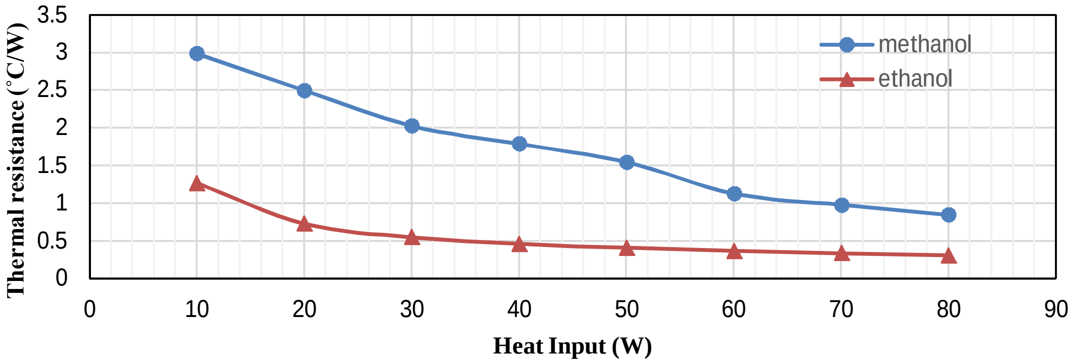

Fig.6.Variation of resistance with heat input for methanol and ethanol at 0 degree position (finned+ inserted)

4.2. Effect of fin and insert on evaporation and condenser temperature for methanol and ethanol

Both evaporation and condensation temperature increases with the increment of time, though temperature increase rate is much higher in evaporation section as forced convention keeps the temperature of condensation section lower. Lowering capacity of condensation temperature indicates better performing structure. Typical curves are presented in Fig.7, Fig.8, Fig.9 and Fig.10, which are taken at 0° inclination for 50 W heat input with methanol and ethanol as working fluid. By comparative analysis of experimental data, maximum temperature difference is found higher in finned-inserted structure for both fluids (for ethanol around 33˚C and for methanol around 38˚C) than normal structure (for ethanol around 31˚C and for methanol around 30˚C). Characteristic temperature difference in the heat pipe is decided from the transient temperatures after it reaches its startup time. Minimum heat input is required to start pulsating motion. Initially after applying a low heat input, liquid slugs cannot move in the tube and this results a temperature climb up in evaporating section. After a certain time (startup time), absorbed heat by the working fluid is adequate to commence low amplitude pulsating motions. Due to movement of working fluid, temperature of evaporating section becomes almost steady. Finally, evaporator's temperature

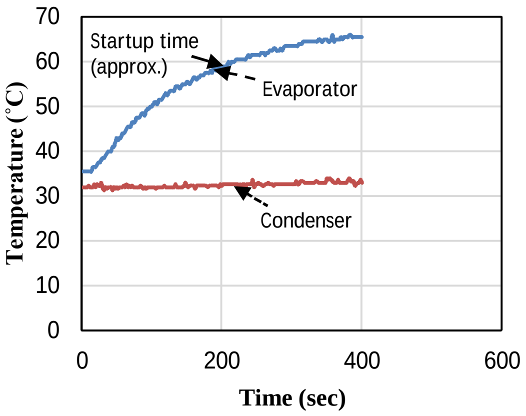

Fig.7. Variation of temperature with time of close loop finned and inserted structure at 0 degree for 50W input (Ethanol)

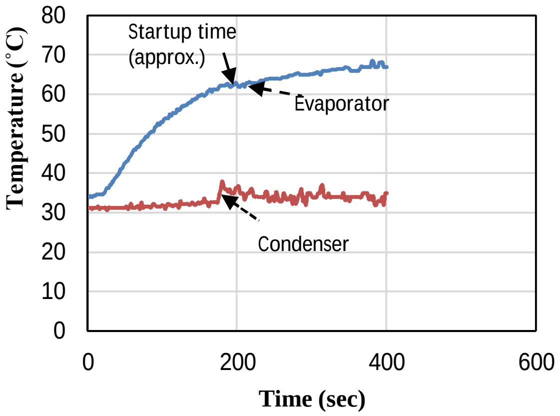

Fig.8. Variation of temperature with time of close loop without finned-inserted structure at 0 degree for 50W input (Ethanol)

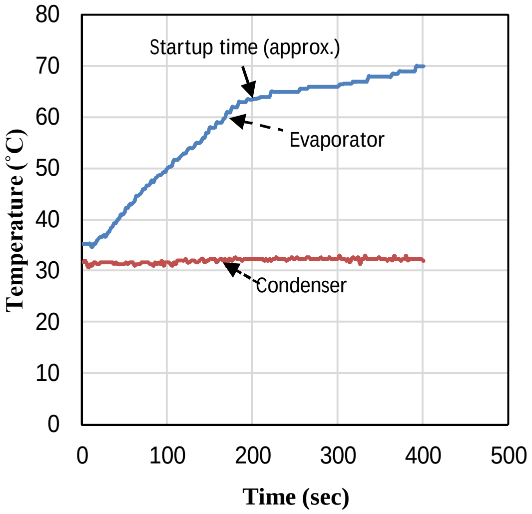

Fig.9.Variation of temperature with time of close loop finned and inserted structure at 0 degree for 50W input (Methanol)

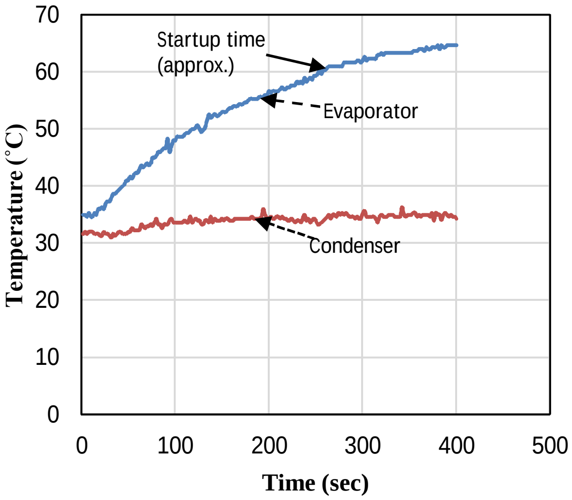

Fig.10.Variation of temperature with time of close loop without finned-inserted structure at 0 degree for 50W input (Methanol)

pulsates around a certain value [13]. As there is no scope of visual approach in our experiment (using copper pipe) from Figs. 7-10 it can be observed that the time when pulsating flow in the heat pipe starts in finned structure is approximately 200s (ethanol), 200s (methanol) but in un-finned structure it is approximately 220s (ethanol), 250s (methanol). For both working fluids finned-inserted structure shows better performance than normal structure. This is because of the combined effect of fin used in condenser section and copper wire used inside the structure. Fin provide extended surface in condenser section that increase heat transfer rate through convection and inserted wire ensures smaller bubble size than normal structure by breaking bubbles of original size into small bubble, these small bubbles can easily transfer heat than normal condition and as a result increase heat transfer. Between two fluids methanol performs better than ethanol in terms of heat transfer. This is an expected behavior due to their thermo physical properties. Also due to the difference of heat transfer rate in condenser section of two structures, amount of heat content in evaporator slightly changes (heat being trapped in evaporator in case of lower heat transfer rate) as a result evaporator temperature is slightly different (in case of finned structure it is slightly less than un-finned structure). This may be also due to unaccounted heat loss in evaporator though insulated.

4.3. Effect of fin and insert on thermal resistance with different orientation

Variation of orientation of structure has a large impact on the performance of CLPHP. Combined effect of gravity force and pressure force results in the variation of performance of CLPHP with inclination. Gravity force help then liquid slugs to travel downwards to the evaporator after carrying heat to the condenser section. Pressure forces are created due to temperature difference, which exists between evaporator and condenser. From experimental data (Fig.11 and Fig.12) it is found that, for both working fluids finned-inserted structure at 45˚ inclination shows best performance which is the combined effect of gravity and pressure forces. At this condition the value of R_{th} is higher for each heat input provided and so it indicates efficiency of heat transfer of this condition is higher than others.

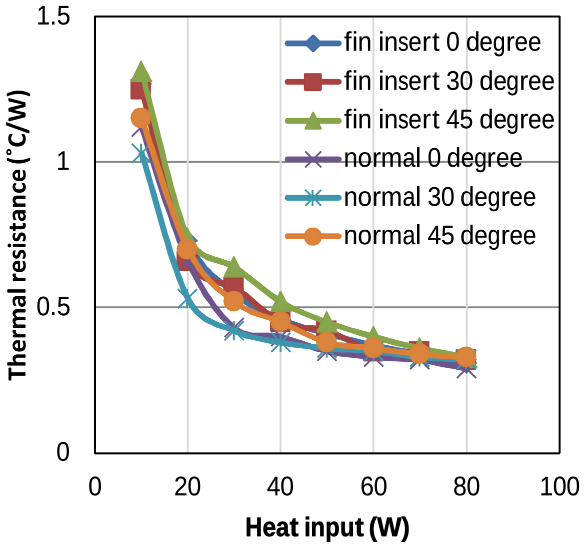

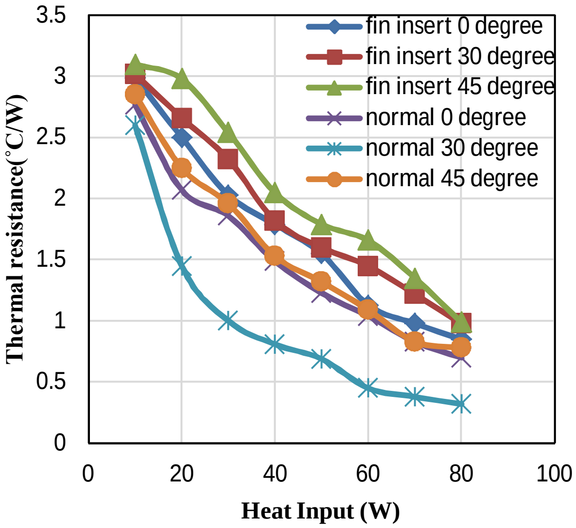

Fig.11. Variation of resistance with heat input for finned-inserted and normal structure at different angle (ethanol)

Fig.12. Variation of resistance with heat input for finned-inserted and normal structure at different angle (methanol)

5. Conclusions

From the investigation of this heat pipe at different heat input, inclination and fluid, the following findings are obtained. Methanol is better working fluid than ethanol at wide range of heat inputs in the basis of heat transfer. Both the working fluid shows nearly same thermal resistance but in every condition methanol has slightly higher R_{th} than ethanol that indicates better efficiency of performance of heat transfer, this is due to the effect of their thermo physical properties. Finned-inserted structure is better performed than normal structure. This is due to the combined effect of fin as extended surface in condenser section and copper insert as a medium to break bubble into small size to carry heat from evaporator to condenser section easily. Due to the gravity and pressure force, 45˚ inclined orientation shows better position to transfer heat than other orientations. Finally in this experiment, best performance is found with finned-inserted structure at 45˚ inclination carrying methanol as fluid. More satisfactory performance may be found with more variation of different parameters i.e. inclination, fluid, filling ratio, using fin and insert and their orientation etc.

Acknowledgements

The authors feel greatly honored to be able to express their earnest gratitude to the Department of Mechanical Engineering, MIST and BUET for the accomplishment of this research.

References

[1] H. Akachi, US Patent, Patent Number 4921041, 1990.
[2] H. Akachi, US Patent, Patent Number 5219020, 1993.
[3] H. Akachi, US Patent, Patent Number 5490558, 1996.
[4] H. Akachi, F. Polášek, P. Štulc, Pulsating heat pipes, in: Proceedings of the 5th International Heat PipeSymposium, Melbourne, Australia, 1996, pp. 208–217.
[5] S. Khandekar, N. Dollinger, M. Groll, Understanding operational regimes of pulsating heat pipes: an experimental study, Appl. Therm. Eng. 23 (6) (2003) 707–719 (ISSN 1359-4311).
[6] M. Groll, S. Khandekar, Pulsating heat pipes: a challenge and still unsolved problem in heat pipe science, Arch.Thermodyn. 23 (4) (2002) 17–28 (ISSN 1231-0956).
[7] S. Nishio, S. Nagata, S. Baba, R. Shirakashi, Thermal performance of SEMOS heat pipes, in: Proceedings of12thInternational Heat Transfer Conference, Grenoble, France, vol. 4, 2002, pp. 477–482 (ISBN 2-84299-307-1).
[8] M. Shafii, A. Faghri, Y. Zhang, Thermal modeling of unlooped and looped pulsating heat pipes, ASME J. Heat Transfer 123 (2001) 1159–1172.
[9] S. Khandekar, M. Groll, An insight into thermo-hydrodynamic coupling in pulsating heat pipes, Int. J. Therm. Sci.(Rev. Gn. Therm.) in press (ISSN: 1290-0729).
[10] Charoensawan, P., Khandekar, S., Groll, M. and Terdtoon, P. “Closed loop pulsating heat pipes”, part-A; Parametric experimental investigations”, Applied Thermal engineering, Vol.23 No.6, 2001, pp.2009-2020.
[11] Khandekar, S., “Multiple Quasi- Steady States in a Closed Loop Pulsating Heat Pipe”, NTUS-IITK 2nd joint workshop in mechanical, Aerospace and Industrial Engineering, April 5-6, 2008, IIT, Kanpur, India.
[12] Meena, P., Rittidech, S., Tammasaeng, P, “Effect of inner Diameter and inclination angles on operation limit of closed-loop Oscillating heat pipes with check valves”, American journal of Applied Sciences, vol. 1, No.2,2008,pp.100-103.
[13] Xu, J.L., and Zhang, X.M., 2005, “Start-up and Steady Thermal Oscillation of a Pulsating Heat Pipe,” Journal of Heat and Mass Transfer, 41(8), 685-694.

Available online at www.sciencedirect.com

ScienceDirect

Procedia Engineering00 (2015) 000–000

Procedia Engineering

www.elsevier.com/locate/procedia

6th BSME International Conference on Thermal Engineering (ICTE 2014)

An experimental investigation on the effect of fin in the performance of closed loop pulsating heat pipe (CLPHP)

M Lutfor Rahman[1], Rasel A Sultan[1,]*, T Islam[1], Noor M Hasan[1], Mohammad Ali[2]

[1]*Military Institute of Science and Technology, Mirpur Cantonment, Dhaka-1216, Bangladesh*
[2]*Bangladesh University of Engineering & Technology, Dhaka-1000, Bangladesh*

Abstract

Pulsating heat pipes (PHP) have created a newer arena and promising possibilities as passive devices for heat transfer applications, especially suited for thermal management of electronics. A closed loop pulsating heat pipe (CLPHP) made of copper with 2 mm ID and 2.5 mm OD with fin in the condenser section is used in the present work to evaluate the heat transfer performances where the evaporation section is 50 mm, adiabatic section is 120 mm and condensation section is 80 mm. The attempt is to analyze and compare the effects on the heat transfer performances of CLPHP with finned and un-finned condenser section with inclination angle of 0^0 (vertical), 30^0 and 45^0. Methanol is used as working fluid with 50% filling ratio in CLPHP with 8 loops during the experimentation. The experimental results indicate a strong influence of gravity and thermo physical properties of the working fluid on the performance of the CLPHP studied with different orientation and heat load. The results demonstrate the effect of fin used in condenser section, the input heat flux, inclination angle orientation and physiochemical properties of the working fluid on the thermal performance of the device. The finned CLPHP at 45□ inclination exhibits the considerable enhancement of heat transfer compared with that of CLPHP without fin.

Peer-review under responsibility of organizing committee of the 6th BSMEInternational Conference on Thermal Engineering (ICTE 2014).

Keywords: Electronic Cooling; Pulsating heat pipe (PHP); Close loop pulsating heat pipe (CLPHP); Thermal performance

---

Nomenclature

R	thermal resistance, °C/W	T	temperature along the heat pipe, °C
ΔT	temperature drop along the device, °C	Q	heat input, W

---

* Corresponding author. Tel.: +880-1675-706457;
E-mail address: raselahmed0411@yahoo.com

Peer-review under responsibility of organizing committee of the 6th BSME International Conference on Thermal Engineering (ICTE 2014).

L	length of heat pipe, cm	D	diameter of heat pipe, mm
OD	Outer diameter of tube	ID	Inner diameter of tube
FR	filling ratio, %	IA	Inclination angle, °
Subscripts			
th	thermal	*e*	evaporator section
a	adiabatic section	*c*	condenser section

1. Introduction

There are novel technologies which consist of small in size and shape electronic devices, because they are more efficient and compact in nature, due to this it has less area for cooling system, to manage these type of problem i.e. thermal management of microelectronic devices there is a requirement of miniaturization of heat exchangers [1]. Waste heat is generated in large quantities in various process industries, nuclear reactors etc. Efficient heat exchangers are required to harness the waste heat from various potential sections. A pulsating heat pipe or oscillating heat pipe has best potential to handle the above problems. It is relatively young member in the family of heat pipe. Although grouped as a subclass of the overall family of heat pipes, the subtle complexity of thermo-fluidic transport phenomena is quite unique justifying the need of a completely different research outlook. A Close loop pulsating heat pipe (CLPHP) is a type of meandering tube pulsating heat pipe (PHP) which consists of a metallic capillary tube wound in a serpentine manner and joined end to end as shown in Fig. 1. The empty capillary tube is partially filled with working fluids, which distributes itself naturally in the form of liquid-vapor slug and bubbles inside the capillary tube. One end of this tube (called evaporator section) is brought in thermal contact with a hot point to be cooled. The other end (called condenser section) is connected to the cold point where the heat can be dissipated. A portion of the tube between evaporator and condenser is called adiabatic section. The working fluid and its pressure are chosen in such a way that the saturation temperature is between the evaporator temperature T_e and condenser temperature T_c. The fluid is thus vaporized due heat absorption in the evaporator and its release in the condenser. The created vapor is transported to the condenser section and condenses there. The liquid is transported back to the evaporator section. There is no additional capillary weak structure inside the tube.

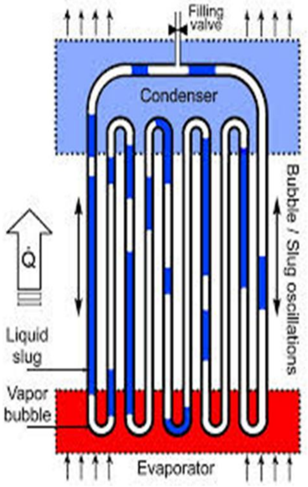

Fig.1. Close loop PHP

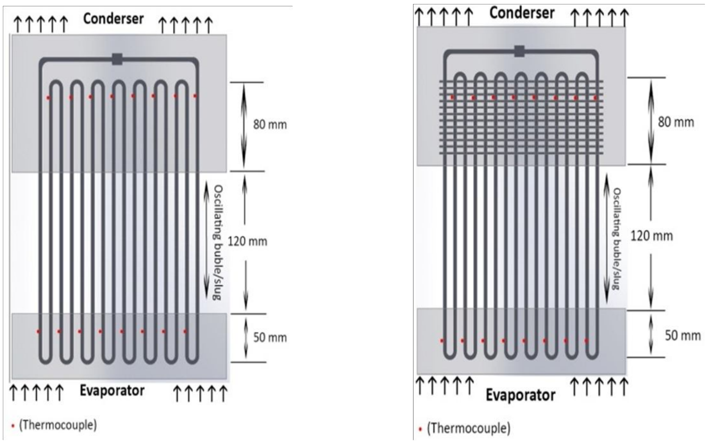

(a) Normal CLPHP (b) Finned CLPHP

Fig.2. Experimental setup

PHP was first proposed and patented by Akachi et al. [2] as a passive cooling device and gains the attention of many investigators. Although a plethora of heat pipe technology is established, the open literature available on PHPs is limited. The numerical studies on PHPs reported in the literature are limited to estimate the complex behavior of thermo-fluidic transport phenomena. More over the mathematical models proposed in the literature on PHPs needs experimental verification, as stated by Shafii [3], Zhang [4] and Rama Narasimha et al. [12]. Characterization of thermal performance in multi-loop PHPs has been investigated by Cai [5], Charoensawan [6], Khandekar [7, 8] and Meena et al. [9]. Results on thermal performance of single loop PHP are also investigated by Rama Narasimha et al. [10, 11]. Experimental results mainly focused on flow visualization studies and the measurement of temperature variation pattern. The effect of working fluid, heat input, tube material, orientation and fill ratio are identified by Nagvase S.Y. et al [13] as primary design parameters affecting the performance of PHP which requires detailed investigation. The present experiment is done with fin or extended surface in condenser section at different angle of inclination using working fluid Methanol with 50% filling ratio. A heat transfer analysis of an inclined two-phase closed thermo siphon was developed by Zuo et al. [14]. Fin is also used here which is a surface that extends from an object to increase the rate of heat transfer to the environment by increasing convection. The amount of conduction, convection, or radiation of an object determines the amount of heat it transfers. Effect of fin in case of conventional heat pipe is not examined before. Now present investigation is done to show the effect of fins which increase heat transfer coefficient on PHP.

2. Experimental method

2.1. Experimental setup

The experimental setup is shown in Fig. 2 and Fig. 3. The setup consists of a meandering heat pipe (ID: 2mm, OD: 2.5mm, L: 25cm, material: copper), creating a total of 8 turns. The heat pipe is divided into 3 regions- the evaporator (5cm), adiabatic section (12cm) and the condenser (8cm). The copper wire of 2mm is used in condenser section at equal distance as fin in finned CLPHP. 6 thermocouples (LM-35sensors, Local Sensor Accuracy (Max) (+/- C): 0.5, range: -55°C to +150°C) are glued to the wall of heat pipe in evaporator and condensation section; 3 for each sections. Evaporator section is insulated inside a box of wood frame, separated from outside using mica sheets with Nichrome wire (diameter = 0.25 mm, resistivity: 1.0×10^{-6} Ω-m, specific heat: 450 $\mathrm{Jkg^{-1}K^{-1}}$) wounded inside, which is heated by a power supply unit (AC, 220V, 50Hz) via a variac (3F, 300V, 60 Hz). Methanol is used as working fluid at the amount of FR 50% (by volume) for each setup.

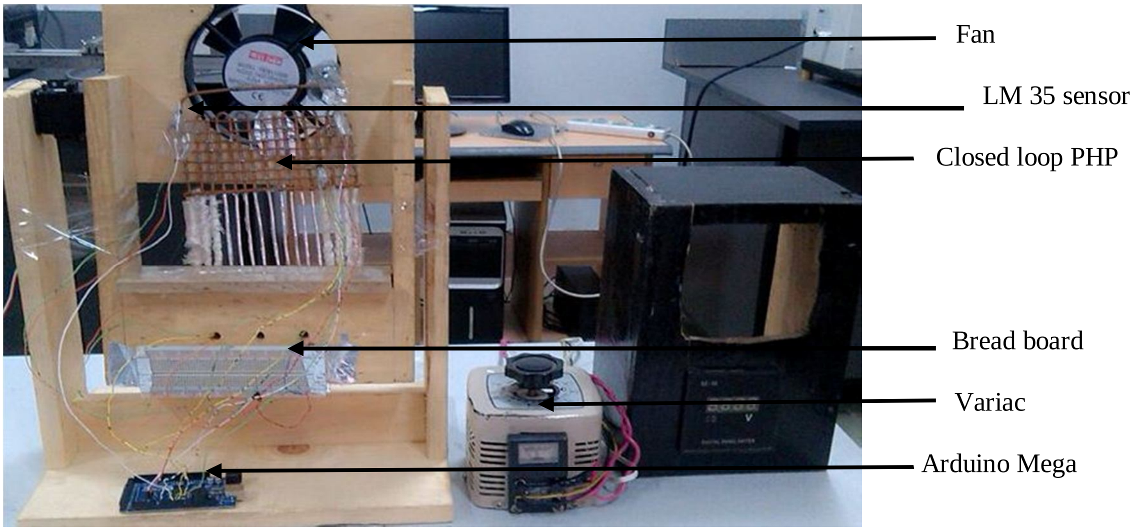

Fig.3. The prototype experimental set up

For cooling the working fluid, forced convection is used by a DC fan. The whole apparatus is set on a wooden test stand (wood frame) with provision of angular movement of the PHP using servo motor (Modulation: Analog, Speed: 0.20 sec/60°, Weight: 1.94oz (55.0 g), Dimensions: Length: 1.60 in (40.6 mm), Width: 0.78 in (19.8 mm), Height: 1.69 in (42.9 mm), Motor Type: Coreless, Gear Type: Metal, Rotation/Support: Dual Bearings, Rotational Range: 180°, Pulse Cycle: 20 ms, Pulse Width: 1000-2000 µs).For data collection Arduino Mega (Microcontroller: ATmega1280, Operating Voltage: 5V, Input Voltage (recommended): 7-12V, Analog Input Pins: 16) is used. For avoiding complicacy, working fluids are incorporated in the heat pipe manually. The other accessories of the setup are adapter circuit, selector switches etc.

2.2. Experimental procedure

- After the construction of the whole setup the experiment is carried out.
- The experiment is performed for Finned and un-finned condenser sections with 50% filling ratio of Methanol as working fluid and three different angular orientation of heat pipe.
- First the heat pipe is filled 50% by working fluid Methanol (injecting by syringe) keeping the PHP in vertical (0°) position for both finned and un-finned condenser CLPHP.
- Different heat inputs were provided to the system and temperatures reading of different sections were measured by thermocouples using Arduino Mega.
- Then the position is changed to 30°, 45° positions and keeping the filling ratio the same, above procedure is repeated later on for both finned and un-finned condenser.
- For cooling the condenser a cooling fan is used. It is connected to an adapter circuit.

3. Results and discussion

An experiment is carried out for methanol and three different angular orientations of finned and un-finned heat pipe where fin is used in condenser section. In this research, the value of thermal resistance is considered as an indication of efficiency, i.e. higher value of R_{th} refers to higher difference of temperature between evaporator and condenser section and eventually indicates a higher efficiency of the system. Result is compared between finned and un-finned structure on basis of different characteristics.

3.1. Characteristics of temperature distribution with time

The variation of temperature with time curves shows a similar pattern for all the experimental conditions. These typical curves are presented in Figs. 4 and 5, which are taken at 0° inclination for 50 W heat input with methanol as working fluid. In fact, for all the experimental cases, the curves at first increase rapidly with time and then the rate of increase become slow to some extent. This is same for all the temperature data; i.e. for evaporator and condenser section. But, certainly, the rate of increase is different for different regions. After reaching the boiling point, the temperature increase in evaporator slows down due to the heat required in phase transfer. Temperature increase rate being slow in the condenser section can be attributed to the fact that, at some point of time, it becomes close to the room temperature. So no further need of cooling is then necessary. From both Figs. 4 and 5 it is clear that till first 100 seconds there is a higher increase rate of evaporator temperature but after 100 seconds the rate decreases. In finned structure steady condition is achieved more early than un-finned structure in between 200 seconds. The reason is a minimum heat input is required to start pulsating motion. Initially after applying a low heat input, liquid slugs cannot move in the tube and this results a temperature climb up in evaporating section. After a certain time (startup time), absorbed heat by the working fluid is adequate to commence low amplitude pulsating motions. Due to movement of working fluid, temperature of evaporating section becomes almost steady. Finally, evaporator's temperature pulsates around a certain value [15]. As there is no scope of visual approach in our experiment (using copper pipe) from Figs. 4 and 5 it can be observed that the time when pulsating flow in the heat pipe starts in finned structure is approximately 180s but in un-finned structure it is approximately 220s. This indicates faster heat transfer rate in finned structure. Higher difference of temperature between evaporator and condenser section indicates higher efficiency of the system. In finned structure it is found around 35°C (max) whereas in un-finned structure it is around 30°C (max).

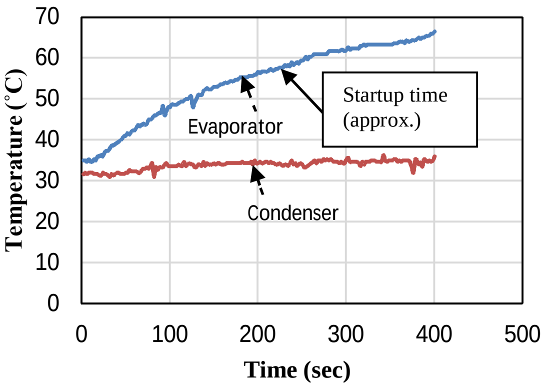

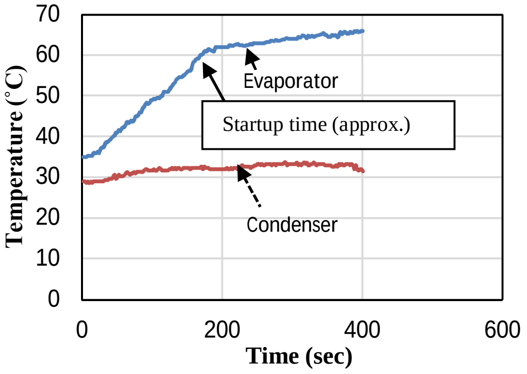

Fig.4. Variation of temperature with time of close loop without finned structure at 0 degree for 50W heat input

Fig.5. Variation of temperature with time of close loop finned structure at 0 degree for 50W heat input

Fin provide extended surface in condenser section that increase heat transfer rate through convection as a result keep the condenser region temperature low with better working efficiency. Also due to the difference of heat transfer rate in condenser section of two structures, amount of heat content in evaporator slightly changes (heat being trapped in evaporator in case of lower heat transfer rate) as a result evaporator temperature is slightly different (in case of finned structure it is slightly less than un-finned structure). This may be also due to unaccounted heat loss in evaporator though insulated.

3.2. Variation of thermal resistance

Thermal resistance is considered in this paper as an indicator of heat pipe effectiveness. It is defined as the ratio of difference in average temperature of evaporator section and average temperature of condenser section for any instance to the heat input at that time. The thermal resistance of PHP is given by

$$R_{th}=(T_e-T_c)/Q$$

The equation indicates how much resistance does heat experiences in the system; so that the condenser region temperature cannot rise very high, and the system thus seems to be effective in cooling purpose. The curves of thermal resistance are of similar pattern for all the cases. They are maximum at minimum heat input and minimum at maximum heat input; i.e. thermal resistance has an inverse relationship with heat input. These curves follow an exponential pattern, and a typical graph is shown in Fig. 6, which is taken from the data set of 0° inclination (vertical position). But, the fall of thermal resistance is not of the same rate for all cases, it varies up to some extent. In finned structure, Rth is higher than normal structure at each case of heat input. As we have already mentioned that higher resistance means higher efficiency, so we can state that finned structure exhibits better performance than normal structure. We can also state that with highly heated appliances, heat pipe efficiency will fall down. But yet, this fall can be controlled with proper designing, which includes appropriate working fluid, filling ratio and inclination angle.

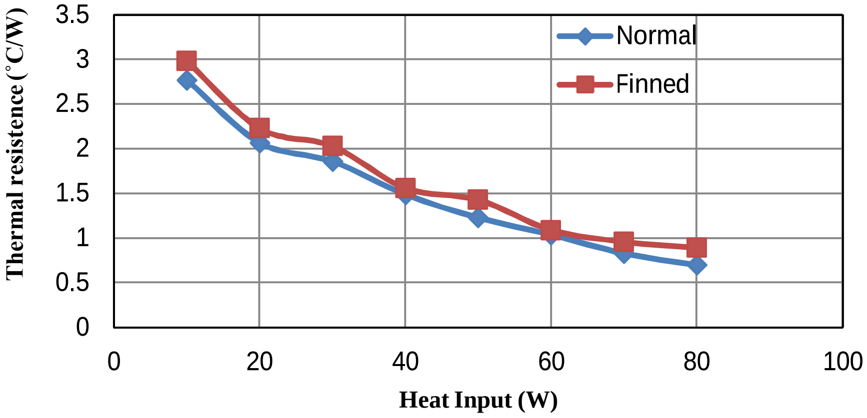

Fig.6. Variation of resistance with heat input at 0 degree inclination

3.3. Effect of inclination

The effect of heat flux in vertical orientation has been experimentally noted down by Tong et al. [15] and Khandekar et al. [16]. In vertical mode (0^o inclination) the vapor bubbles which take up heat in the evaporator grow in size. Their own buoyancy helps them to rise up in the tube section. Simultaneously other bubbles, which are above in the tube, are also helped by their respective buoyant forces. These rising bubbles in the tube also carry the liquid slugs trapped in between them. In this mode of operation there is a natural tendency for the liquid slugs to travel downwards, helped by gravity force, toward the evaporator. In horizontal mode (90° inclination angle) of operation, there was hardly any macro movement of bubble. This strongly suggests that gravity does play a role in the PHP. Since gravity force is ineffective, all the movement of bubbles and slugs has to be necessarily done by the pressure forces. These forces are created due to temperature difference, which exists between evaporator and condenser. Fig. 7 shows effect of inclination for both finned and normal structure and it indicates finned structure at 45˚inclination as best condition as R_{th} of this condition is higher than others. This is true for all heat inputs we have taken. In all cases of experiment, thermal resistances (R_{th}) drop with increase in heat input (Q) initially with higher slope in the curves.

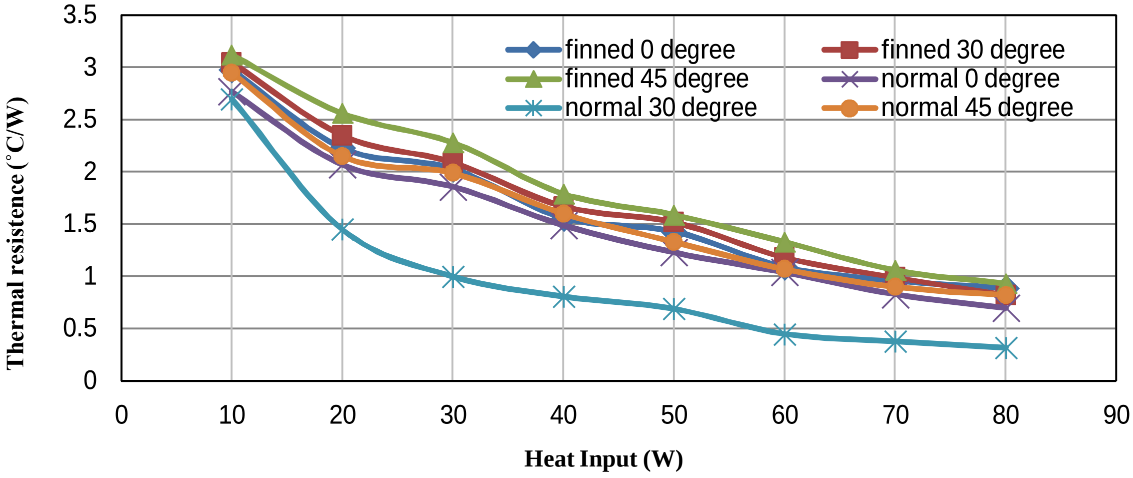

Fig.7. Variation of resistance with heat input for finned and normal structure at different angle

But, as heat input increases, the slope of the curves are smaller, indicating the smaller rate of decrease in thermal resistances. Effect of gravity, pressure differential in the system, temperature etc may have influence in this fact due which 45˚ inclined position of finned structure shows best performance whereas 30˚ inclined position of normal structure shows worse performance.

4. Conclusions

Closed loop pulsating heat pipes are complex heat transfer systems with strong thermo-hydrodynamic coupling governing the thermal performance. The effect of pressure, bubble formation and phase transfer is very important in design of heat pipes. Different heat input to these devices give rise to different flow patterns inside the tubes. This in turn is responsible for various heat transfer characteristics. The study strongly indicates that design of these devices should aim at thermo-mechanical boundary conditions which resulting convective flow boiling conditions in the evaporator leading to higher local heat transfer co-efficient. The inclination angle changes the internal flow patterns thereby resulting in different performance levels. In this research, best performance is obtained at 45° orientation. In all circumstances, finned structure provides better performance than normal structure in the experiment. A close comprehensive look is required for designing heat pipes, as their performance is a function of orientation, filling ratios, working fluid and use of fin. Most satisfactory pattern of design may vary up to some extent from case to case.

Acknowledgements

The authors feel greatly honored to be able to express their earnest gratitude to the Department of Mechanical Engineering, MIST and BUET for the accomplishment of this research.

References

[1] Moore.g, Cramming More components onto Integerated Circuits, Electronics, 1965 38(8).

[2] Akachi, H. “Structure Of Heat Pipe”, US patent, 4921041, 1990

[3] Shafii, B. M., Faghri, A., Zhang, Y., “Thermal modeling of unlooped pulsating heat pipes, Journal of Heat Transfer” Vol. 123, No. 6, 2001, pp. 1159-1172.

[4] Zhang, Y., Faghri, A., “Heat Transfer in a pulsating heat pipe with open end, International Journal of Heat Mass Transfer”, Vol. 45, No. 4, 2002, pp. 755-764.

[5] Cai, Q., Chung-lung Chen, Julie F. Asfia, “Operating Characteristic Investigations in Pulsating Heat Pipe”, journal of heat transfer, vol. 128, 2006, pp.1329-1334.

[6] Charoensawan, P., Khandekar, S., Groll, M. and Terdtoon, P. “Closed loop pulsating heat pipes”, part-A; Parametric experimental investigations”, Applied Thermal engineering, Vol.23 No.6, 2001, pp.2009-2020.

[7] Khandekar, S., “Multiple Quasi- Steady States in a Closed Loop Pulsating Heat Pipe”, NTUS-IITK 2nd joint workshop in mechanical, Aerospace and Industrial Engineering, April 5-6, 2008, IIT, Kanpur, India.

[8] Khandekar, S., “Thermo Hydrodynamics of Pulsating Heat Pipes”, Ph.D Dissertation, University of Stuttgart, Germany, 2004.

[9] Meena, P., Rittidech, S., Tammasaeng, P, “Effect of inner Diameter and inclination angles on operation limit of closed-loop Oscillating heat pipes with check valves”, American journal of Applied Sciences, vol. 1, No.2,2008,pp.100-103.

[10] Rama Narasimha, K., “Studies on Pulsating Heat pipes” Ph.D. Dissertation, Visveswaraya Technological University, India, 200

[11] Rama Narasimha, K., Rajagopal, M.S., Sridhara, S.N., “Influence of Heat Input, Working Fluid and Evacuation Level on the Performance of a Pulsating Heat Pipe” Journal of Applied Fluid Mechanics, Vol. 5, No. 2, Issue 10, 2012, Accepted for Publication.

[12] Rama Narasimha, K., Rajagopal, M.S., Sridhara, S.N., Seetharamu, K. N., “Parametric studies on Pulsating Heat Pipes”, International Journal for Numerical Methods for Heat and Fluid Flow, Vol. 20, Issue 4, 2010.pp. 392-415.

[13] Nagvase S.Y., Pachghare P.R., “Parameters affecting the function of closed loop pulsating heat pipe: A Review”, Research Journal of Engineering Sciences, Vol 2(1), 2013, pp. 35-39.

[14] Zuo, Z. J. and Gunnerson, F. S., 1995. Heat Transfer Analysis of a Inclined Two-Phase Closed Thermosyphon, Journal of Heat Transfer 117, p.1073-1075.

[15] Xu, J.L., and Zhang, X.M., 2005, “Start-up and Steady Thermal Oscillation of a Pulsating Heat Pipe,” Journal of Heat and Mass Transfer, 41(8), 685-694.

[16] Tong, B., Wong, T. and Ooi, K., 2001. Closed-Loop Pulsating Heat Pipe, Applied Thermal Engineering 21(18), p. 1845–1862.

[17] Khandekar, S., Groll, M., Charoensawan, P. and Terdtoon, P., 2002. “Pulsating heat pipes: thermo-fluidic characteristics and comparative study with single phase thermosyphon,” Proceedings of the 12th International Heat Transfer Conference. Grenoble, France, p.459–464.

Available online at www.sciencedirect.com

ScienceDirect

Procedia Engineering00 (2015) 000–000

Procedia Engineering

www.elsevier.com/locate/procedia

6th BSME International Conference on Thermal Engineering (ICTE 2014)

Effect of Waste Heat Recovery on Drying Characteristics of Sliced Ginger in a Natural Convection Dryer

Jnyana R. Pati[a] , Santosh K. Hotta[a,*] , P. Mahanta[b]

[a] *Centre for Energy, Indian Institute of Technology, Guwahati- 781039*
[b] *Department of Mechanical Engineering, Indian Institute of Technology, Guwahati- 781039*

Abstract

In the present work, quality drying characteristics of sliced ginger were studied utilizing the concept of waste heat recovery in a biomass operated natural convection dryer with sensible heat storage material (SHSM) and phase change material (PCM). Ginger slices (2 and 4 mm thickness) were dried from initial moisture content (MC) 88-90 % (w.b.) to final moisture content 11-12% (w.b.) with hot air maintained at temperature 60^0C, air velocity 0.2 m/sec, atmospheric average relative humidity 74% and ambient temperature 25^0C It was observed that the biomass consumption and melting time of PCM were significantly reduced due to the use of waste heat. The optimum drying time was found to be 5.5 h for 2 mm thick ginger slices. Color, texture and aroma were found better in treated sample.

Peer-review under responsibility of organizing committee of the 6th BSMEInternational Conference onThermal Engineering (ICTE 2014).

Keywords: Waste heat recovery; Natural convection dryer; Phase change material; Quality drying

---

1. Introduction

Ginger is one of the important tropical commercial spices and herbs used extensively in food and medicines [1]. It is used for extensively due to its fragrance and texture in the preparation of wide variety of dishes [2]. Ginger produced in North–East (NE) region of India is found to excellent in fragrance and texture. So it is considered as one of the major cash crop [3]. Ginger production from 7000 tonne during the year 1997-98 is now likely to increase to 702 MT making an impact in the world market [4, 5]. However, increase in production of ginger demands for high

---

* Corresponding author. Tel.: +91-995-763-0275; fax: +91-361-269-0762.
E-mail address: h.santosh@iitg.ernet.in

Peer-review under responsibility of organizing committee of the 6th BSME International Conference on Thermal Engineering (ICTE 2014).

cost in transportation and storage [6]. Most of the ginger growing areas are hot and humid rendering deterioration in quality of ginger during storage. For preservation, drying, canning and freezing have been found suitable. But, drying by hot air is considered to be simple and economical among these processes [7].

Open sun drying process can't be entertained due to the drawbacks like slowness of the process, the exposure of the product to the environment and the products get contaminated due to dust and insects. Hence an effective and quality drying technique is essential for drying of such good quality ginger all around the year which can be affordable and easily handled by the rural farmers. There are different drying techniques employed to dry different products. Each technique has its own advantage and limitation. So, choosing the right drying technique is crucial in the process of drying of these perishable products like ginger.

Drying is energy intensive process mainly in case of post harvesting [8] ,because the raw products with 80-90% moisture content have to bring down to equilibrium moisture content (EMC) by utilizing lot of heat energy. Drying through natural convection grain dryer is an important alternative for rural farmers [9]. Waste heat can be a source to be utilized in dryers to save energy as well as to reduce environmental impact. Many attempts have been made by the researchers to utilize waste heat in drying process. No extra cost of drying is required by utilizing exhaust gas of diesel engine for drying of paddy grains [10]. Waste heat of a pump used in irrigation purpose can be utilized to minimize post harvesting losses and effectively utilize the available energy resources for rural farmers [11]. Utilization of part of the exhaust heat of the flue gas through thermal coupling by a heat exchanger is the subject of present work. Present work involves utilization of waste heat of a natural convection dryer to improve its performance by reducing the energy consumption and time required for drying of ginger slices. Detailed description of the natural convection drier along with the process of experiments and the results for the optimized condition of drying are drawn and discussed in the present paper.

2. Materials and Methods

In present study, freshly harvested ginger (Zingiber officinale) was collected from the agricultural field. Rhizomes were washed properly in running water and sliced into almost uniform thickness of 2 mm. The slices were subsequently boiled in hot water at 90^0C for 15 minutes. The boiled samples were then spread upon a perforated container to drain the water from the samples for a period of 15 minutes. Similar method was followed for ginger samples with 4 mm thickness.

2.1 Pre drying treatment

2.1.1 Untreated samples

One kg from each of the boiled samples are measured in a strain gauge based weighing machine (Mettler-Telodo India Pvt. Ltd.) and soaked separately in water for 1 h followed by draining.

2.1.2 Treated samples

One kg from each of the boiled samples (2mm and 4mm thick ginger slices) are soaked in 2% (m/v) concentrated calcium hydroxide ($Ca(OH)_2$) solution for 1 h to avoid attack of insect and to provide better color and texture to the dried ginger rhizome [12]. The treated samples are then placed in a perforated container to let the water drain out. Initial moisture content of all the samples is measured by muffle furnace (Lab tech International Ltd).

2.2 Description of the natural convection drier

At the core of the dryer a conical furnace fabricated with MS sheet was placed centrally 22 cm above the bottom of the dryer. The furnace was placed over a base plate made of GI sheet with 1700 holes each of 5 mm in diameter to facilitate the supply of air for efficient combustion as well as for easy disposal of ash. The top of the furnace was connected to the exhaust pipe. As the flue gas coming out from the furnace carries lot of heat and rejects it to atmosphere, in this setup attempts have been made to recover the waste heat carried away by the flue gas. So a recuperator also known as direct transfer heat exchanger was introduced.

One end of the heat exchanger was connected to main exhaust pipe and circulated inside the wax tray and the other end was exposed to the atmosphere. At the out let of the heat exchanger pipe a DC exhaust fan of 700 rpm. was connected to create sufficient amount of pressure difference and to draw maximum amount of flue gas through the heat exchanger. Part of the flue gas coming out from biomass furnace at high temperature was bled and drawn into the heat exchanger. The tubular heat exchanger consists of copper tube of outer diameter 19.05 mm and wall thickness 1.06 mm. The flue gas which cannot be drawn to heat exchanger passed to the ambient. Wood chips were fed to the furnace through an inclined inlet connected to the body of the furnace. This pipe was termed as bio mass feeding pipe (BFP) as shown in Fig. 1(a). The conical furnace was surrounded by rectangular brick walls of dimension 145 cm x 117 cm x 115 cm and 13 cm thick. Eight rectangular vent holes of dimension 10cm x 9cm / 5 cm x 4 cm (3 nos. each on the left and right walls and 2 nos. on the rear wall) were constructed in equal spacing at the bottom of the dryer walls to facilitate supply of air inside the dryer as shown in Fig. 1(b). Vertical distance between the top surface of the furnace and the perforated tray is maintained to be 30 cm. In addition, a paraffin wax tray of 120 cm x 93 cm is fabricated for storage of phase changing material (PCM) to facilitate constant temperature drying. For faster melting of PCM the above mentioned heat exchanger of length 6 m., outer diameter 19.01 mm and wall thickness 1.06 mm was placed at the middle portion of the paraffin wax tray. Sensible heat storage materials (SHSM) of 5-7 cm diameters were used inside the drying chamber for storing the heat for a longer period time and to supply it continuously.

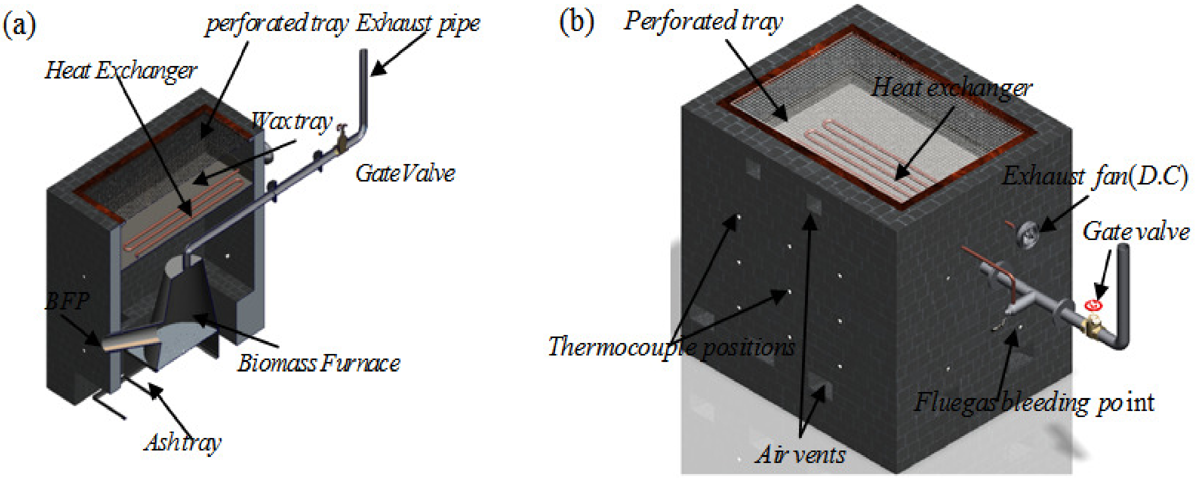

Fig.1. (a) Sectional view of the natural convection dryer; (b) Isometric view of the natural convection dryer

2.3 Instrumentation and procedure

In order to study variation of temperature profile in the dryer both T and K type thermocouples were fabricated, calibrated and placed at the desired locations. The dryer was divided into three horizontal sections, top (section-3), middle (section-2) and lower (section-1) sections which were 110 cm, 85.5 cm and 25.5 cm respectively from the base of the dryer. The temperature profile of the flue gas coming out from the biomass furnace was measured by two K type thermocouples attached before and after the bleeding point of the flue gas to the heat exchanger. Two K-type thermocouples were also attached at the inlet and exhaust of the heat exchanger. To study the uniformity in melting of Paraffin wax seven thermocouples were placed at different location uniformly on the paraffin wax tray. To find out the average temperature of the drying air below the perforated tray five thermocouples were used at different locations. The temperature profile at various locations was continuously monitored by a data acquisition system. Relative humidity was measured by a digital hygrometer. Weight of the ginger was recorded in each 30 min. interval by a strain gauge based digital weighing machine. The initial and final moisture content of the sample was found by using a muffle furnace.

Biomass was used as fuel in the developed dryer. Due to combustion of biomass (in present case it is wood-pongamia pinnata) huge amount of heat was released inside the furnace; as a result heat flew from the furnace to the surrounding air through the metallic wall by combined mode of heat transfer. The heated air inside the dryer rose up by natural convection and struck the wax tray which led to initiation of melting the paraffin wax ($C_{25}H_{52}$). On the other hand due to the difference in density of the flue gas inside the furnace it was forced to move through the exhaust pipe to the atmosphere. As soon as the combustion was initiated in the biomass furnace, exhaust fan running with 12 volt DC source located at the outlet of the heat exchanger (HE) was started and created a significance pressure drop to extract maximum amount of flue gas from the exhaust pipe of the biomass furnace. Flue gas entered through the heat exchanger inlet passed through the pipe and rejected its sensible heat to the stored PCM in the wax tray. Hence the waste heat was utilized by the dryer in the present study. Stored Paraffin wax in the wax tray changed from solid to liquid state when the temperature approached the melting point range i.e. 45-60^{o}C. The amount of flue gas circulated through the HE was varied by operating the exhaust valve placed on the exhaust pipe coming out from the biomass furnace. Biomass stopped fire when the wax completely changed from solid to liquid state. The paraffin wax which was in liquid state released its latent heat unless until it turns into solid state. Atmospheric air carried the latent heat released from the PCM in the plenum chamber and struck the perforated tray. Hence an almost stable isothermal drying condition was maintained below the perforated tray. As soon as the drying air temp approached to 60^{o}C both treated and untreated samples were placed on the drying tray. Heated air which struck the ginger slices increased the vapor pressure of the moisture present within the ginger which led to increase the migration of water vapor. Drying process was terminated when the moisture content of the sample reduced to 12% w.b. The same experiment was repeated for different percentage of opening of the exhaust valve to study the effect of heat exchanger on the air drying characteristics of sliced ginger.

3. Results and discussion

Experiments were repeated several times for a particular test to ensure correctness of the result. Experiments were carried out at IIT, Guwahati, Assam, India during winter season at an average relative humidity of 74% and average atmospheric temperature of 25^{0}C. Three sets of experiments were conducted by varying the percentage of opening i.e. at 100 %, 40 % and 30 % of the exhaust valve (EV). The mass flow rate of the flue gas through the HE pipe was found to be 0 kg/h, 3.85 kg/h, and 4.76 kg/h at 100 %, 40 % and 30 % opening of the exhaust valve respectively. Initial moisture content of the samples was found in between 88%-90% w.b and the drying process continued until the sample achieved desired moisture content i.e. ~12% w.b. The effect of slice thickness, pre treatment and drying characteristics were studied and explained below.

3.1 Effect of slice thickness of ginger on drying time

It was observed from the Fig. 2(a, b and c) that, decreased in slice thickness decreases the time required for drying. Moisture removal rate was found faster in case of thinner slices. From the nature of the curve it is observed that the moisture diffusion curve obeys drying mechanism, where there was a constant rate period and a falling rate period. Until unless the surface moisture does not migrate the moisture removal rate remained constant and when the dry patches appeared on the product moisture removal became slower, which was the falling rate period.

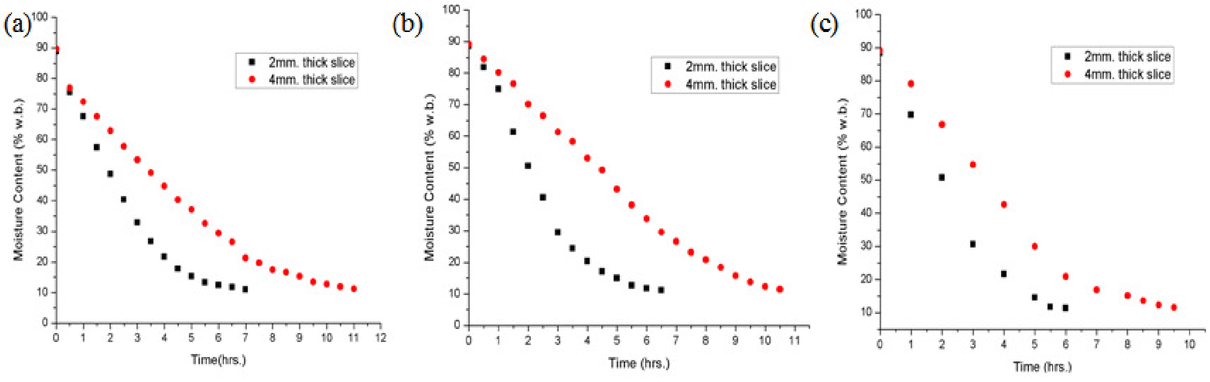

Fig . 2.(a) variation of MC at 100 % opening of EV ; (b) variation of MC at 40% opening of EV (c) variation of MC at 30% opening of EV

3.2 Effect of percentage of opening of exhaust valve on drying time

At 100 % opening of the exhaust valve flue gases coming out from the biomass furnace was allowed to move to the atmosphere without entering the HE (HE is not in function). As observed from the Fig. 3(a and b) with 100 % opening of the EV 2 mm thick slices dried faster than 4 mm thick slices and took 7 h and 11 h respectively. It was found that 2 mm thick slices at 30% opening dried faster than other percentages openings of exhaust valve. The same characteristics were also observed in case of 4 mm thick slices. At 30% opening of exhaust valve 2 mm thick slices obtain 11.31% moisture content (w.b.) with in 6 h after melting of paraffin wax, whereas 4 mm thick slices took 9.5 h to achieve the EMC. This happens because, at 30 % opening of exhaust valve more amounts of flue gas was passed through the HE. Hence much amount of heat was transferred to the paraffin wax as compared to other case. Implementation of HE was found fruitful by reducing drying time along with consumption of biomass effectively.

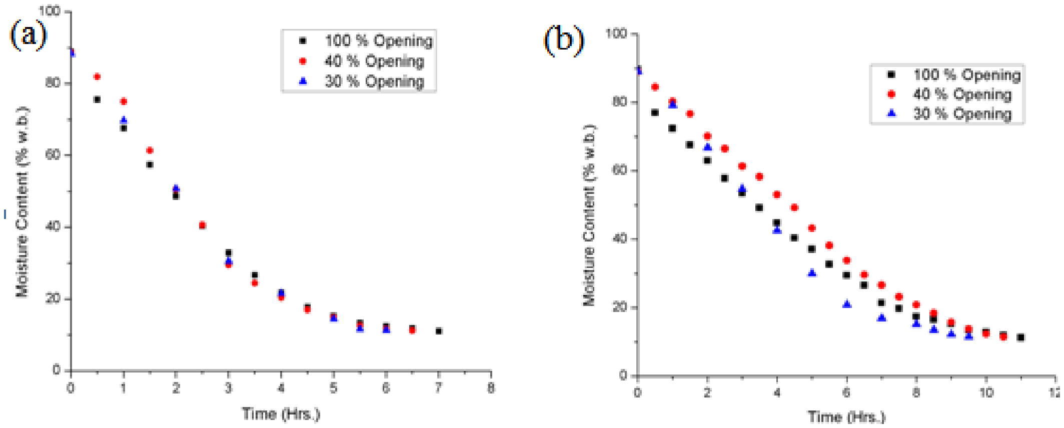

Fig. 3(a) variation of MC at different percentage of opening of EV for 2 mm thick ginger slice;(b) variation of MC at different percentage of opening of EV for 4 mm thick ginger slice.

3.3 Effect of pre-treatment on drying time

As observed from Fig. 4(a) at 100% opening, 2 mm thick treated slices took 6.5 h whereas the untreated slices took 7 h to achieve the EMC(~12 % w.b.). In case of 4 mm thick treated and untreated slices the EMC was achieved in 10.5 h and 11 h respectively. Same pattern of results were also observed from Fig. 4.(b & c) at 40 and 30 % of openings of exhaust valve and a conclusion was drawn that, the treated samples achieved the EMC faster than the untreated samples. The optimized result was found from Fig. 4.(c) for the case of treated ginger slices with 30 % opening of exhaust valve, which took 5.5 h to achieve 11.51% MC (w.b.). The color, texture and aroma of the treated samples found acceptable from the laboratory test. Experiments were conducted to study the effect of concentration of $Ca(OH)_2$ (m/v) on drying time by varying the percentage of concentration of $Ca(OH)_2$ form 2 to 6% (m/v), but no significance effect in drying time has been observed other than improved appearance of the dried sample.

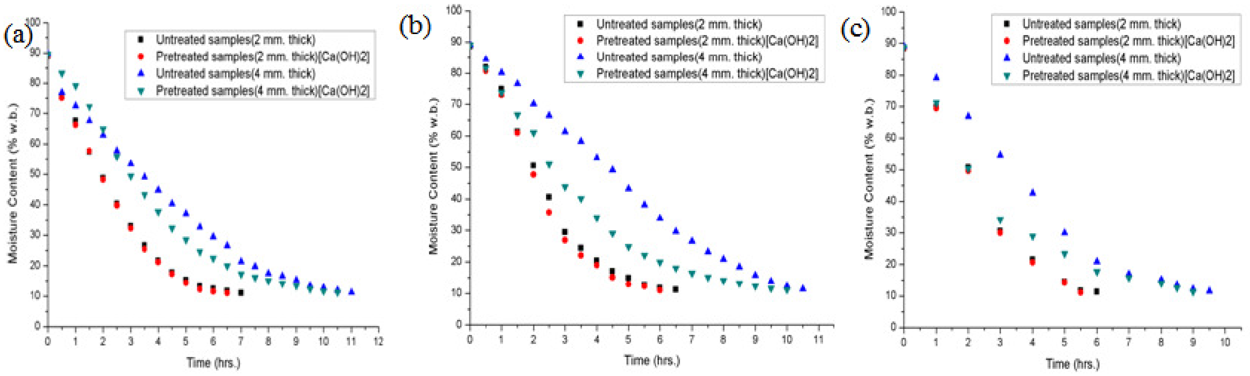

Fig.4.(a) variation of MC along with time for treated and untreated samples at 100 % opening of EV; (b) variation of MC along with time for treated and untreated samples at 40% opening of EV; (c) variation of MC along with time for treated and untreated samples at 30% opening of EV

3.4 Effect of waste heat on the temperature profile of the wax tray

For quality drying of any agricultural or herbal product it was essential to maintain the temperature of the drying air constant, but the drying temperature was different for different products. In the present setup to maintain the drying temperature constant, the temperature profile of the wax tray should remain constant. So during the experiment the temperature profile of the wax tray has been analyzed at the shown positions in Fig. 5.

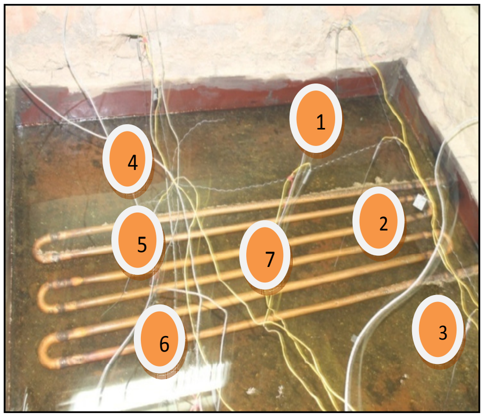

Fig. 5. Position of thermocouples on wax tray

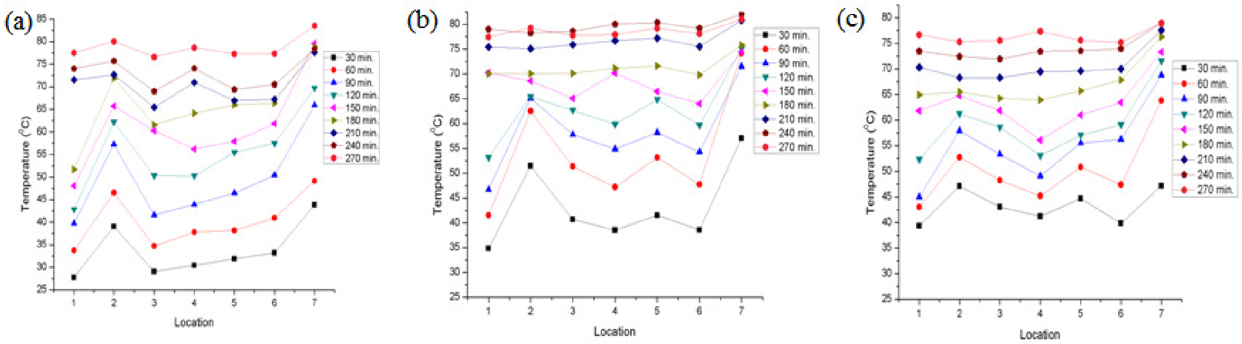

Fig. 6(a) temperature profile of the wax tray at 100 % opening of EV; (b) temperature profile of the wax tray at 40% opening of EV; (c) temperature profile of the wax tray at 30% opening of EV

It was observed from the Fig. 6(a, b and C) that the temperature profile of the wax tray remained almost constant for a longer period of time after complete melting of paraffin wax. Temperature at the various locations on the wax tray increased along with time and remained uniform throughout after a particular period of time. After an interval of 270 minute in case of 100 % opening of the EV, the temperature profile was found almost constant i.e. 80±3°C . It took 3.5 h to completely melt 30 kg. of paraffin wax with an expense of 4 kg. of biomass (Pongamia pinnata). As shown in Fig. 6(b), at 40 % opening of the EV, the temperature profile on the wax tray found to be uniform i.e. 75±3^{0}C after an interval of 210 minute where it had taken 2.5 h to completely melt 30 kg. of paraffin wax with an expense of 3kg of biomass. With 30 % opening no such changes are observed regarding time for completely melting of wax, in this case results were almost matching with 40% opening. In all the above mentioned cases the maximum temperature of the wax tray was maintained almost 80°C by controlling the feed rate of biomass. The drying air temperature was found to fall in the range of 60±3^{0}C. It is being observed that in the middle portion of the wax tray, the temperature was raising quickly. That is because of the position of the biomass furnace which liberates much amount of heat trough the top face by means of combined mode of heat transfer.

3.5 Physico-chemical properties of dried ginger

As per the report of analysis found from the office the drug testing laboratory (AYUSH), the dried treated ginger slices have the following characteristics. From organolaptic analysis the color, order and test found to be buff, aromatic and pungent respectively. From Physico-chemical analysis the following are the result drawn and tabulated below. By visual inspection the texture of the sample looks fine. As shown in Table. 1, all the constituents are within the acceptable limit and the organolaptic analysis supports the colour, order and test of the treated sample.

Table 1. Physico-chemical properties of dried ginger slices

Sl. No	Test	API(Ayurvedic Pharmacopeia of India) Limit	Result
1	Foreign matter	Not more than 1 %	0.98%
2	Total ash	Not more than 6 %	0.64 %
3	Acid insoluble ash	Not more than 1.5 %	0.08 %
4	Water soluble extractives	Not less than 10%	11.001-10.918 %
5	Alcohol soluble extractives	Not less than 3%	3.492-4 %

Conclusions

The optimum drying time for 2 mm untreated Ginger slices was found 6 h in 30 % opening of the EV. The best drying time of 4 mm thick untreated ginger was found to be 9.5 h in 30 % opening of EV. The best drying time was found to be 5.5 h and 9 h in 2 mm and 4 mm thick sliced ginger respectively due to the effect of treatment with $Ca(OH)_2$ in 30 % opening of the EV. The melting time of PCM, drying time of ginger and biomass consumption were completely dominated due to recovery of waste heat. Melting time of the paraffin wax was reduced by 1 h. This was because of capturing the waste heat from the flue gas and utilizing it inside the wax tray by recuperative heat exchanger whose average temperature was 150^0C. The effect of waste heat also reduced the biomass consumption from 4 kg to 3kg for melting the paraffin wax. Physico-chemical properties of ginger slices found to be acceptable after drying.

The main purpose of the present study was to determine effective application of this kind of setup in rural areas which will be beneficial for the farmers of ginger growing areas and will help them to store their product efficiently for a longer period of time. From the present study it has been concluded that the rate of drying will be faster if thinner slices of ginger were used for drying. The effect of treatment also provided a good effect on the color and texture of the product. The black patches that appeared in the untreated product can be omitted with the effect of treatment. Treated samples dried faster than the untreated samples.

Acknowledgements

The authors would like to thank the central work shop team of IIT Guwahati for their support. The authors would also like to acknowledge support from the technical experts of IIT Guwahati and Rural Technology Action Group-North East (RUTAG-NE) and AYUSH for their support and guidance The authors also thanks the Marie-Curie project FP7-PEOPLE-2012-IRSES, IComFluid for financial support.

REFERENCES

[1] Babu, K.N.; Samsudeen, K.; Minoo, D.; Geetha, S.P.; Ravindran, P.N.; Tissue Culture And Biotechnology Of Ginger. Ginger : The Genus Zingiber; Ravindran, P.N.; Babu, K. N.;CRC Press; United States of America, 2005; 181-210.
[2] Prasad, J.; Prasad, A.; Vijay, V. K. Studies on the Drying Characteristics of Zingiber Officinale Under Open Sun and Solar Biomass (Hybrid) Drying. International Journal of Green Energy 2006, 3 (1), 79-89.
[3] Loha, C.;Das, R.;Choudhury, B.;Chatterjee, P.K. Evaluation of Air Drying Characteristics of Sliced Ginger (Zingiber officinale) in a Forced Convective Cabinet Dryer and Thermal Conductivity Measurement. J Food Process Technol 2012, 3 (6), 2-5.
[4] Indian horticulture data base [2011], Ministry of Agriculture, Government of India, Chapter 1,P-6, www.nhb.gov.in
[5] Mani, B., Paikada, J., Verma, P. (2000): Different drying methods of ginger (Gingiber officinale): A Comparative study. Indian spice 1:3–15.
[6] Phoungchandang, S.;Nongsang, S.;Sanchai, P. The Development of Ginger Drying Using Tray Drying, Heat Pump–Dehumidified Drying, and Mixed-Mode Solar Drying, Drying Technology 2009, 27 (10),1123-1131.
[7] Westport.Van Arsdel W. B. and Copley M. J. (1964). Food Dehydration, Vol. 2, The AVI Publishing Company ,pp 196-197
[8] Mujumdar, A. S.;Law, C. L. Drying Technology: Trends and Applications in Postharvest Processing, Food Bioprocess Technology 2010, 3 (6),843–852.
[9] Mohapatra, S.S.; Mahanta, P. Experimental investigation of an indirect type of natural convection dryer for thin layer paddy drying, 2011; ISSN 2248-9347; pp. 47-54
[10] Akhter, Md. S.; Nabi, Md. N.; Afroz, Z. Recovery of waste heat from engine exhaust for utilization in a paddy dryer. In proceeding of International Conference on Mechanical Engineering (ICME) , Tehran , Iran, May 15-17, 2007; 29- 31.
[11] Basunia, M. A.;Abe, T. Performance study of a small engine waste heated bin dryer in deep bed drying of paddy. Agricultural Engineering International: CIGR Journal 2008, v. 10.
[12] Ravindran, P.N.; Babu, K. N. Ginger: The Genus Zingiber; CRC Press,United States of America, 2005; ISBN 0-415-32468-8.

Available online at www.sciencedirect.com

ScienceDirect

Procedia Engineering00 (2015) 000–000

Procedia Engineering

www.elsevier.com/locate/procedia

6th BSME International Conference on Thermal Engineering (ICTE 2014)

Effects of viscous dissipation on natural convection flow over a sphere with temperature dependent thermal conductivity in presence of heat generation

Md. Raihanul Haque[a], Md. M. Alam[a], Mohammad Mokaddes Ali[b], Rehayet Karim[c,]*

[a] Department of Mathematics, Dhaka University of Engineering and Technology, Gazipur-1700,Bangladesh
[b] Department of Mathematics, Mawlana Bhashani Science and Tech. University, Tangail-1902, Bangladesh
[c] *Department of Mathematics, Chittagong University of Engineering and Technology, Chittagong-4349, Bangladesh*

Abstract

In this paper, the steady two-dimensional laminar incompressible flow over a sphere in the presence of viscous dissipation and heat generation is considered. Thermal conductivity is assumed as a linear function of temperature. The governing equations are solved numerically by numerical solution strategy as per requirement and suitability. The obtained self similar equations are then solved numerically by an implicit, tri-diagonal, finite-difference method with Keller Box scheme. Favorable comparison with previously published work is performed. Computations are performed for a wide range of the governing flow parameters such as thermal conductivity variation parameter γ , heat generation parameter Q, Prandtl number Pr and Eckert number Ec. The computational findings for the dimensionless velocity, temperature profiles as well as for the skin-friction coefficient and heat transfer rate are presented in tabular form and graphically.

Keywords: Variable thermal conductivity; Heat generation; Eckert number

---

1. Introduction

The study of convective flow, heat transfer gets much interest of researchers for nature and industrial application.

---

* Corresponding author. Tel.: +88-0191-8225600; fax: +0-000-000-0000 .
*E-mail address:*duet_raihan@yahoo.com

Chen and Mucoglu [1,2] have studied mixed convection over a sphere with uniform surface temperature and uniform surface heat flux for very large Reynolds *Re* and Grashof numbers Gr , using the boundary layer approximations.

Nomenclature

a	Radius of the sphere
C_f	Skin friction coefficient
C_p	Specific heat at constant pressure
f	Dimensionless stream function
Gr	Grashof number
g	Acceleration due to gravity
k	Thermal conductivity
k_f	Thermal conductivity of the fluid
k_∞	Thermal conductivity of the ambient fluid
Ec	Eckert number
Nu	Local Nusselt number
Pr	Prandtl number
q_w	Heat flux at the surface
Q	Heat generation parameter
Q_0	Constant
r	Radial distance from the symmetric axis to the surface
T	Temperature of the fluid in the boundary layer
T_∞	Temperature of the ambient fluid
T_w	Temperature at the surface
u	Dimensionless velocity component along x direction
v	Dimensionless velocity component along y direction
U	Velocity component along the surface
V	Velocity component normal to the surface
X	Axis in the direction along the surface
Y	Axis in the direction normal to the surface

Greek Symbols

ξ	Dimensionless coordinate along to the surface
η	Dimensionless coordinate normal to the surface
ψ	Stream function
τ_w	Shearing stress
ρ	Density of the fluid
μ	Viscosity of the fluid
ν	Kinematics viscosity of the fluid
θ	Dimensionless temperature function
β	Coefficient of thermal expansion
β_0	Strength of magnetic field
γ	Thermal conductivity variation parameter
γ^*	Constant
σ_0	Electric conductivity

Viscous dissipation effects on natural convection flow along a sphere with radiation heat loss are examined by Alim *et al*. [3]. Viscous dissipation effects on natural convection flow along a sphere with heat generation is studied by Salina *et al*. [4]. Natural convection flow on a sphere through porous medium in presence of heat source/sink near a stagnation point was considered by Mukhopadhyay [5]. Magneto hydrodynamic natural convection flow on a sphere in presence of heat generation was investigated by Molla *et al.* [6]. Alam *et al*. [7] has been investigated the free convection from a vertical permeable circular cone with pressure work and non-uniform surface temperature. Viscous dissipation effects on MHD natural convection flow over a sphere in the presence of heat generation was introduced by Alam *et al.* [8]. Mixed convection boundary layer flow about a solid sphere with Newtonian heating was analyzed by Salleh *et al*. [9]. Rahman *et al*. [10] analyzed the effects of temperature dependent thermal conductivity on magnetohydrodynamic (MHD) free convection flow along a vertical flat plate with heat conduction. Combined effects of viscous dissipation and temperature dependent thermal conductivity on MHD free convection flow with conduction and joule heating along a vertical flat plate was studied by Nasrin and Alim [11]. Safiqul Islam *et al.* [12] investigated the effects of temperature dependent thermal conductivity on MHD free convection flow along a vertical flat plate with heat generation and joule heating. Effects of variable viscosity and thermal conductivity on unsteady MHD flow of non-Newtonian fluid over a stretching porous sheet was presented by Abdel Rahman [13]. Borah and Hazarika [14] studied the effects of variable viscosity & thermal conductivity on steady free convection flow along a semi-infinite vertical plate (in presence of uniform transverse magnetic field). He solved the governing boundary layer equations by taking series expansion of the stream function and temperature function. Uddin and Kumar [15] examined the effect of temperature dependent properties on MHD free convection flow and heat transfer near the lower stagnation point of a porous isothermal cylinder.

In all the aforementioned study the effects of viscous dissipation on natural convection flow over a sphere with temperature dependent thermal conductivity in presence of heat generation has not been considered yet. The governing partial differential equations are reduced to locally non-similar partial differential forms by adopting some appropriate transformations. The transformed boundary layer equations are solved numerically using implicit finite difference scheme together with Keller box technique. Numerical results have been obtained in terms of local skin friction, rate of heat transfer for a selection of relevant physical parameters are shown graphically.

2. Mathematical Formulation

The steady two-dimensional natural convection boundary layer flow of an incompressible viscous and electrically conducting fluid over a sphere of radius *a* has been considered. In this analysis T_w is assumed as the constant temperature at the surface of the sphere and T_∞ being the ambient temperature of the fluid. Whereas *T* is the temperature of the fluid in the boundary layer.

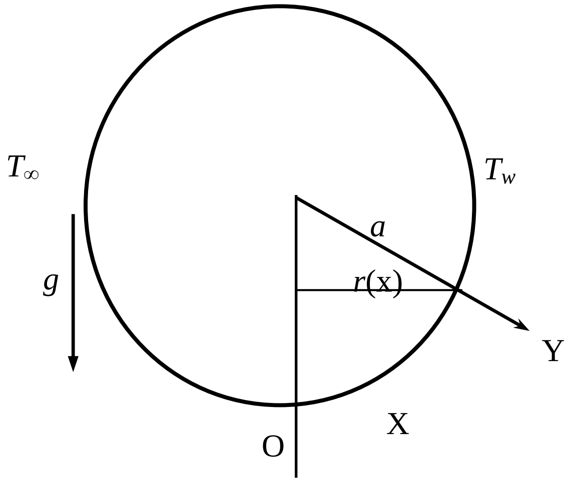

Fig. 1: Physical model and coordinate system

The conservation equations for the flow characterized with steady, laminar and two dimensional boundary layers, the continuity, momentum and energy equations can be written as:

$$\frac{\partial}{\partial X}\left(r\,U\right)+\frac{\partial}{\partial X}\left(r\,V\right)=0 \tag{1}$$

$$U\frac{\partial U}{\partial X}+V\frac{\partial U}{\partial Y}=\nu\frac{\partial^2 U}{\partial Y^2}+g\beta\left(T\text{-}T_\infty\right)sin\left(\frac{X}{a}\right) \tag{2}$$

$$U\frac{\partial T}{\partial X}+V\frac{\partial T}{\partial Y}=\frac{1}{\rho C_p}\frac{\partial}{\partial Y}\left(k_f\frac{\partial T}{\partial Y}\right)+\frac{\nu}{C_p}\left(\frac{\partial U}{\partial Y}\right)^2 \tag{3}$$

The boundary conditions for the governing equations are

$$\left.\begin{aligned}&U=V=0,\quad T=T_w\quad on\quad Y=0\\&U\to 0, T\to T_\infty\quad at\quad Y\to\infty\end{aligned}\right\} \tag{4}$$

$$r(x)=a\,sin\left(\frac{X}{a}\right) \tag{5}$$

where r is the radial distance from the symmetrical axis to the surface of the sphere, $k\left(T\right)$ is the thermal conductivity of the fluid depending on the fluid temperature T. Here we will consider the form of the temperature dependent thermal conductivity which is proposed by Charraudeau [16], as follows

$$k=k_\infty\left(1+\gamma^*(T-T_\infty)\right) \tag{6}$$

where k_∞ is the thermal conductivity of the ambient fluid and γ^* is constant which is defined as

$$\gamma^*=\frac{1}{k_f}\left(\frac{\partial k}{\partial T}\right)_f \tag{7}$$

The above equations are non-dimensional as usual manner by the following substitutions:

$$\xi=\frac{X}{a},\eta=Gr^{1/4}\frac{Y}{a},u=\frac{U}{u_0}=\frac{a}{\nu}Gr^{-1/2}\,\mathrm{U},\ v=\frac{a}{\nu}Gr^{-1/4}V,\theta=\frac{T-T_\infty}{T_w-T_\infty},\theta_w=\frac{T_w}{T_\infty} \tag{8}$$

Where, $u_0=\frac{\nu}{a}Gr^{1/2}$ is the characteristic velocity of the fluid.

Using the above transformations into equations (1) to (5), we have

$$\frac{\partial}{\partial\xi}\left(r\,u\right)+\frac{\partial}{\partial\eta}\left(r\,v\right)=0 \tag{9}$$

$$u\frac{\partial u}{\partial\xi}+v\frac{\partial u}{\partial\eta}=\frac{\partial^2 u}{\partial\eta^2}+\theta\,sin\,\xi \tag{10}$$

$$u\frac{\partial\theta}{\partial\xi}+v\frac{\partial\theta}{\partial\eta}=\frac{1}{Pr}\left(1+\gamma\theta\right)\frac{\partial^2\theta}{\partial\eta^2}+\frac{1}{Pr}\gamma\left(\frac{\partial\theta}{\partial\eta}\right)^2+Ec\left(\frac{\partial u}{\partial\eta}\right)^2 \qquad \text{since } \upsilon\rho=\mu \tag{11}$$

The reduced boundary conditions are

$$\begin{aligned} &u = v = 0,\ \theta = 1\ at\ \xi = 0 \\ &u = v = 0,\ \theta = 1\ at\ \eta = 0,\ \xi > 0 \\ &u \to 0,\ \theta \to 0\ as\ \eta \to \infty,\ \xi > 0 \end{aligned} \tag{12}$$

$$r(\xi) = a\ sin\ \xi \tag{13}$$

Here, $Gr = \dfrac{g\beta\left(T_w - T_\infty\right)a^3}{\nu^2}$ is the Grashof number and $\theta(\xi,\eta)$ is the non dimensional temperature function, viscous dissipation parameter $N = \dfrac{\nu^2 Gr}{\rho a^2 C_p\left(T_w - T_\infty\right)}$ is characterized by Eckert number $Ec = \dfrac{u_0^2}{C_p\left(T_w - T_\infty\right)}$, $Pr = \dfrac{\mu C_p}{k_\infty}$ is the Prandtl number, $\gamma = \dfrac{1}{k_f}\left(\dfrac{\partial k}{\partial T}\right)\left(T_w - T_\infty\right)$ is the thermal conductivity variation parameter. To solve equations (10) and (11) subject to the boundary conditions (12), we assume the following variables u and v where $\psi = \xi\ r(\xi)\ f(\xi,\eta)$ and $\psi(\xi,\eta)$ is the non-dimensional stream function which is related to the velocity components in the usual way as

$$u = \frac{1}{r}\frac{\partial \psi}{\partial \eta} \quad \text{and} \quad v = -\frac{1}{\mathrm{r}}\frac{\partial \psi}{\partial \xi} \tag{14}$$

Putting the above value in equation (10) and (11), we have

$$\frac{\partial^3 f}{\partial \eta^3} + \left(1 + \frac{\xi}{sin\ \xi}cos\ \xi\right) f\frac{\partial^2 f}{\partial \eta^2} - \left(\frac{\partial f}{\partial \eta}\right)^2 + \theta\frac{sin\ \xi}{\xi} = \xi\left(\frac{\partial f}{\partial \eta}\frac{\partial^2 f}{\partial \eta \partial \xi} - \frac{\partial f}{\partial \xi}\frac{\partial^2 f}{\partial \eta^2}\right) \tag{15}$$

$$\frac{1}{Pr}(1 + \gamma\theta)\frac{\partial^2 \theta}{\partial \eta^2} + \frac{1}{Pr}\gamma\left(\frac{\partial \theta}{\partial \eta}\right)^2 + \left(1 + \frac{\xi}{sin\ \xi}cos\ \xi\right) f\frac{\partial \theta}{\partial \eta} + Ec\xi^2\left(\frac{\partial^2 f}{\partial \eta^2}\right) = \xi\left(\frac{\partial f}{\partial \eta}\frac{\partial \theta}{\partial \xi} - \frac{\partial f}{\partial \xi}\frac{\partial \theta}{\partial \eta}\right) \tag{16}$$

The corresponding boundary conditions are

$$\left.\begin{aligned} &f = \frac{\partial f}{\partial \eta} = 0, \quad \theta = 1\ at\ \eta = 0 \\ &f = \frac{\partial f}{\partial \eta} = 0, \quad \theta = 1\ at\ \eta = 0, \xi > 0 \\ &\frac{\partial f}{\partial \eta} \to 0,\ \theta \to 0\ as\ \eta \to \infty, \xi > 0 \end{aligned}\right\} \tag{17}$$

It can be seen that near the lower stagnation point of the sphere i.e. $\xi \approx 0$ Equations (15) and (16) reduces to the following ordinary differential equations:

$$f''' + 2f\ f'' - \left(f'\right)^2 + \theta = 0 \tag{18}$$

$$\frac{1}{Pr}(1 + \gamma\ \theta)\theta'' + \frac{1}{Pr}\gamma\left(\theta'\right)^2 + 2\ f\theta' = 0 \tag{19}$$

Where primes denote the differentiation of the function with respect to η .

Subject to the boundary conditions

$$\left.\begin{array}{l} f(0) = f'(0) = 0, \theta(0) = 1 \\ f' \to 0, \theta \to 0 \text{ as } \eta \to \infty \end{array}\right\} \tag{20}$$

In practical application, the physical quantities of principal interest are the heat transfer and the skin- friction coefficient, which can be written in non- dimensional form as

$$Nu = \frac{aGr^{-1/4}}{k(T_w - T_\infty)} q_w \text{ and } C_f = \frac{Gr^{-3/4} a^2}{\mu\nu} \tau_w \tag{21}$$

Where $q_w = -k_f \left(\frac{\partial T}{\partial Y}\right)_{Y=0}$ and $\tau_w = \mu \left(\frac{\partial U}{\partial Y}\right)_{Y=0}$, k_f being the thermal conductivity of the fluid. Using the new variables (8) along with the boundary conditions (17), we have the simplified form of the heat transfer and the skin-friction coefficient as

$$Nu = -\theta'(\xi, 0) \text{ and } C_f = \xi f''(\xi, 0) \tag{22}$$

3. Result and discussion

In order to gain physical insight the velocity and temperature profiles as well as skin friction coefficient and rate of heat transfer have been discussed by assigning numerical values to the parameter encountered in the problem in which the numerical results are displayed with the graphical illustrations. Solutions are obtained for the fluid having Prandtl number *Pr* = 1.0, viscous dissipation parameter *N* which is characterized by Eckert number Ec (= 1.0, 1.5, 2.5, 3.5), thermal conductivity variation parameter γ (= 0.50, 1.50, 2.50, 3.50) and heat generation parameter *Q* (= 0.01, 0.15, 0.25, 0.35) against η at any position of ξ .

Figs. 2(a) and (b) display results for the velocity and temperature profiles, for different values of Eckert number Ec with thermal conductivity variation parameter γ = 0.50, heat generation parameter *Q*= 0.01 and Prandtl number *Pr* =1.0. From Fig. 2(a), it can be observed that the velocity goes significantly upward with the increase of the Eckert number Ec . From Fig. 2(b), it is seen that when the values of Eckert number Ec increases in the region $0 \le \eta \le 6.5$, the temperature distribution also increases. Figs. 3(a) and (b) show how variations in Ec affect the flow on skin-friction coefficient and the rate of heat transfer. It is observed that at ξ = 0.87266, the skin friction coefficient C_f increases by 10.03% and the Nusselt number Nu decreases by 77.74% as Ec increases from 1.0 to 3.5. Figs. 4(a) and (b) illustrate the velocity and temperature distribution against the variable η for different values of the thermal conductivity variation parameter γ while *Pr* =1.0, Ec = 1.0 and *Q* = 0.01. It is found that both the velocity and temperature distribution increases with the increasing values of the thermal conductivity variation parameter γ . It should be noted that at each value of the thermal conductivity variation parameter γ , the velocity profile has a local maximum value within the boundary layer. The maximum values of the velocity are 0.37182, 0.40869, 0.44253 at η = 1.11440 and final maximum value is 0.47266 at η = 1.17520 for γ = 0.50, 1.50, 2.50, 3.50 respectively. The velocity increases by 27.12% as γ increases from 0.50 to 3.50. It is obvious that the velocity boundary layer and the thermal boundary layer thickness enhance for large values of γ .

Figs. 5(a) and 5(b) deal with the effect of thermal conductivity variation parameter γ associated with the heat generation parameter *Q* = 0.01and Eckert number *Ec* =1.0 and Prandlt number *Pr* = 1.0. From Figs. 5(a) and 5(b) we observed that the skin friction co-efficient C_f increase sharply, on the contrary heat transfer rate decrease monotonically for selected value of γ . It is seen that skin friction co-efficient and heat transfer rate increases by 16.27% and decreases by 80.52% for distinct value of γ at ξ = 0.87266.The effect of heat generation parameter *Q*

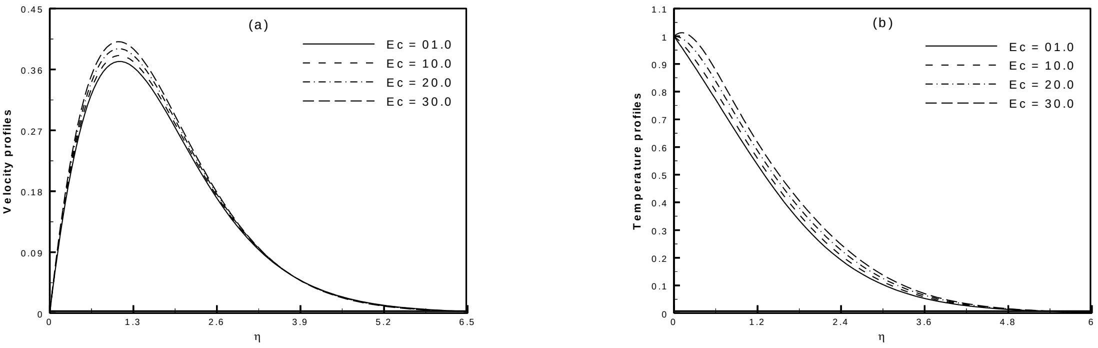

Fig. 2. (a)Velocity profiles and (b) temperature profiles for different values of *Ec* while γ = 0.50, *Q* = 0.01 and *Pr* =1.0.

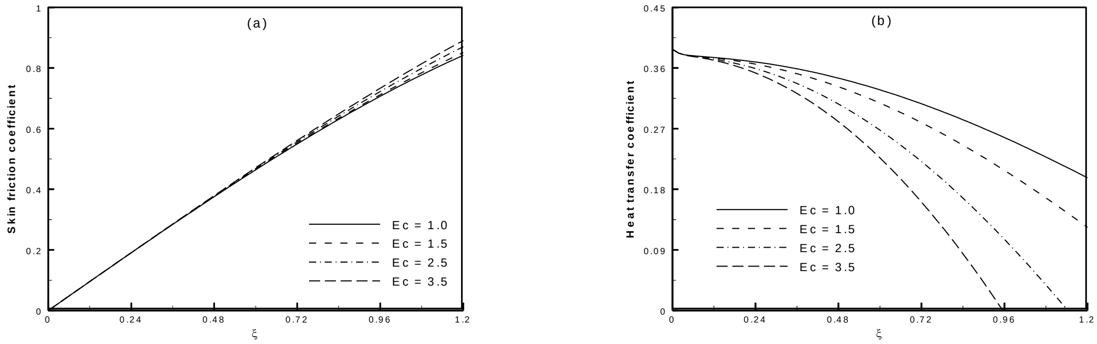

Fig. 3. (a) Skin friction coefficient and (b) rate of heat transfer for different values of *Ec* while γ = 0.50, *Q* = 0.01 and *Pr* =1.0.

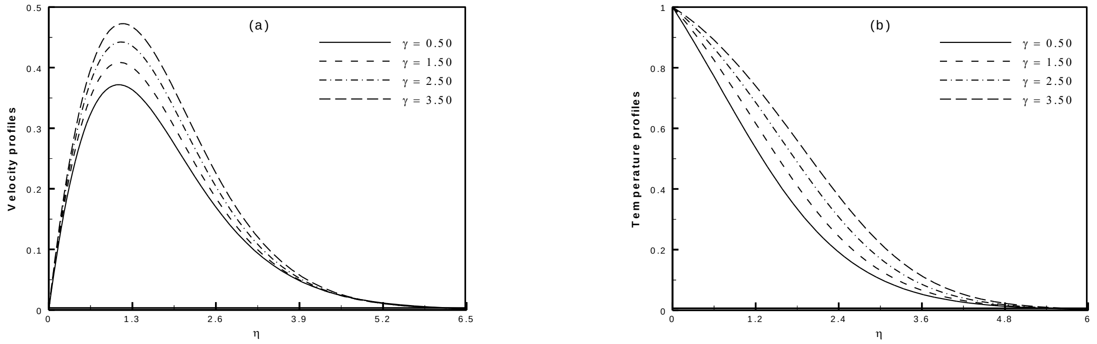

Fig. 4. (a)Velocity profiles and (b) temperature profiles for different values of γ while *Ec* = 1.0, *Q* = 0.01 and *Pr* =1.0.

on velocity and temperature profiles with γ = 0.50, *Ec* = 1.0 and *Pr* = 1.0 are exposed in Figs. 6(a) and 6(b). From Fig. 6(a), it can be stated that the velocity distribution increases as the values of heat generation parameter *Q* increase. It is obvious that when the heat is generated (Q > 0) the buoyancy force increases, which induces the flow rate to increase giving, rise to the increase in the velocity profiles. Again when the heat absorption (Q < 0) intensifies the velocity is found to decrease due the decrease in the buoyancy force. The maximum values of the velocity are 0.37182, 0.39892, 0.41964, 0.44168 for *Q* = 0.01, 0.15 0.25 and 0.35 respectively which occur at η = 1.11440. Here it is observed that the velocity increase by 18.78 % as *Q* increases from 0.01 to 0.35. From Fig. 6(b), it is seen that when the values of heat generation parameter *Q* increase, the temperature distributions also increase.

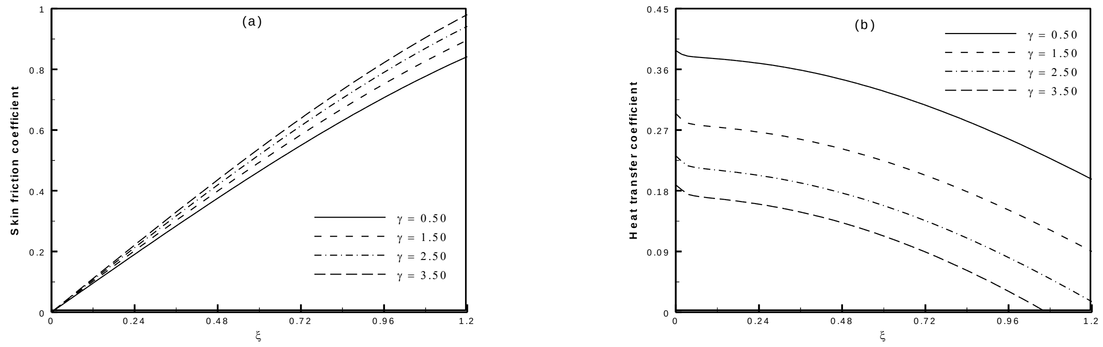

Fig. 5. (a) Skin friction coefficient and (b) rate of heat transfer for different values of of γ while *Ec* = 1.0, *Q* = 0.01 and *Pr* =1.0.

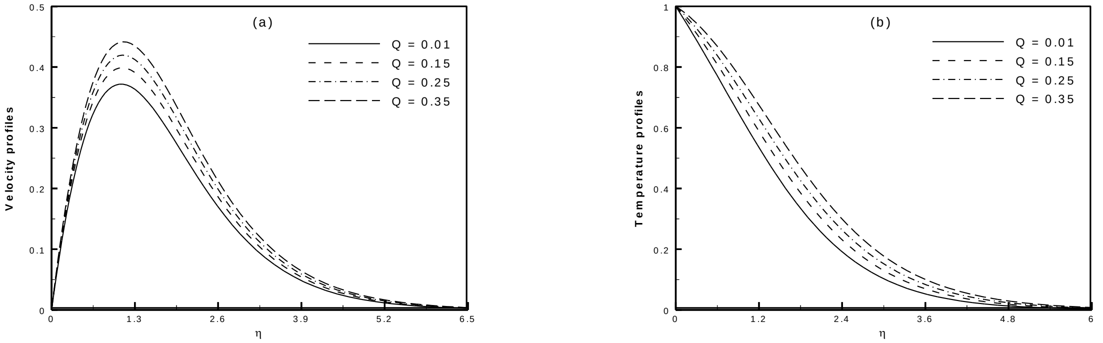

Fig. 6. (a)Velocity profiles and (b) temperature profiles for different values of *Q* while *Ec* = 1.0, γ = 0.50 and *Pr* =1.0.

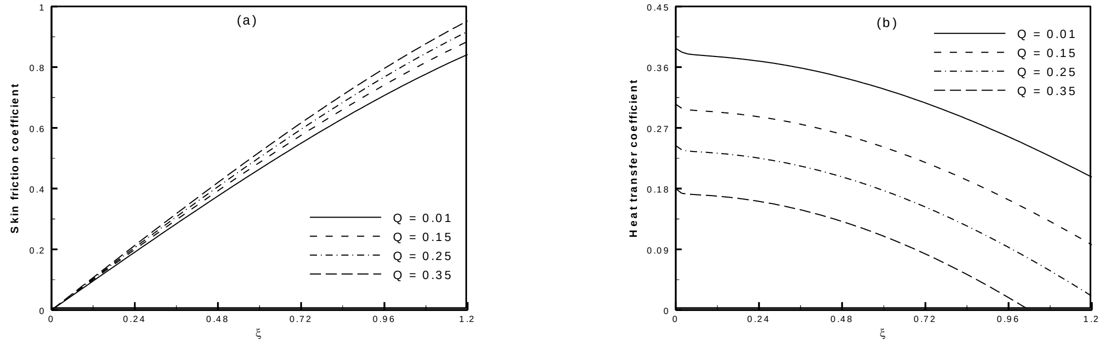

Fig.7. (a) Skin friction coefficient and (b) rate of heat transfer for different values of of *Q* while *Ec* = 1.0, γ = 0.50 and *Pr* =1.0.

The variation of the local skin friction coefficient and the local rate of heat transfer for different values of the heat generation parameter *Q* are depicted in Figs. 7(a) and 7(b) while γ = 0.50, *Ec* = 1.0 and Prandtl number *Pr* =1.0. From the Figs. 7(a) and 7(b), it exhibits that the increase of the heat generation parameter *Q* leads to an increase in the local skin-friction coefficient C_f and a decrease in the local Nusselt number *Nu* . Moreover, it is seen that at ξ = 0.87266 the skin friction coefficient C_f increases by 12.44% and the Nusselt number *Nu* decreases by 84.14% respectively, as *Q* increases from 0.01 to 0.35.

In order to verify the accuracy of the present work, the values of non dimensional heat transfer parameter *Nu* for

Ec = 0, γ = 0 and Q = 0 having prandlt number Pr = 0.7 at different position of ξ (in degree) are compared with those reported by Nazar *et al.*[17] and Molla *et al.* [6] as present in table 1. The results are found to be in good agreement.

Table 1: Rate of heat transfer against ξ for Prandlt number Pr = 0.70 with other controlling parameters Ec = 0.0, γ = 0.0 and Q =0.0.

ξ in degree	Nazar *et al.*[17]	Molla [6]	present
0	0.4576	0.4576	0.45762
10	0.4565	0.4564	0.45653
20	0.4533	0.4532	0.45336
30	0.4480	0.4479	0.44808
40	0.4405	0.4404	0.44067
50	0.4308	0.4307	0.43107
60	0.4181	0.4188	0.41920
70	0.4046	0.4045	0.40499
80	0.3879	0.3877	0.38828
90	0.3684	0.3683	0.36891

4. Conclusion

Natural convection heat transfer gained considerable attention because of its numerous applications in the areas of energy conservations cooling of electrical and electronic components, design of solar collectors, heat exchangers, pumps and flow meters and many others. An analysis has been carried out to study the effects of viscous dissipation on natural convection flow over a sphere with temperature dependent thermal conductivity in presence of heat generation. The following observations and conclusions can be drawn:

- The velocity and temperature within the boundary layer increases for increasing values of Eckert number Ec, thermal conductivity variation parameter γ , heat generation parameter Q.
- The local skin friction co-efficient C_f increases for the increasing values of Eckert number Ec, thermal conductivity variation parameter γ , heat generation parameter Q.
- The local Nusselt number Nu decreases for the increasing values of the Eckert number Ec, thermal conductivity variation parameter γ , heat generation parameter Q.
- The effect of increasing values of the thermal conductivity variation parameter γ is to increase the momentum boundary layer as well as the thermal boundary layer thickness.

References

[1] T. S. Chen and A. Mucoglu, Analysis of mixed forced and free convection about a sphere, International Journal of Heat Mass Transfer 20(1 977) 867–875.
[2] T. S. Chen and A. Mucoglu, Mixed convection about a sphere with uniform surface heat flux, Journal of Heat Transfer 100(1978) 542–544.
[3] M. A. Alim, M. M. Rahman, and S. Aktar, Viscous dissipation effects on natural convection flow along a sphere with radiation heat loss, BSME-ASME International Conference on Thermal Engineering(2008) Dhaka, Bangladesh.
[4] A. Salina, Mahmuda Binte Mostofa Ruma and N. Parveen, Viscous dissipation effects on natural convection flow along a sphere with heat generation, Global Journal of Science Frontier Research 10(2010) 7-14.
[5] S. Mukhopadhyay, Natural convection flow on a sphere through porous medium in presence of heat source/sink near a stagnation point, Mathematical Modelling and Analysis 13(2008) 513-520.
[6] M. M. Molla, M. A. Taher, , M. M. K Chowdhury, and M. A. Hossain, Magneto hydrodynamic Natural Convection Flow on a sphere in presence of heat generation, Nonlinear Analysis Modelling and Control 10(2005) 349-363.
[7] Md. M. Alam, M. A. Alim and Md. M. K. Chowdhury , Free convection from a vertical permeable circular cone with pressure work and non- uniform surface temperature, Nonlinear Analysis: Modelling and Control 12 (2007) 21-32.
[8] M. M. Alam, M. A. Alim and M. M. K. Chowdhury, Viscous dissipation effects on MHD natural convection flow over a sphere in the presence of heat generation, Nonlinear Analysis Modelling and Control 12(2007) 447–459.
[9] M. Z. Salleh, R. Nazar and I. Pop, Mixed convection boundary layer flow about a solid sphere with Newtonian heating, Architecture Mechanics 62(2010) 283–303.
[10] M. M. Rahman, A. A. Mamun, M. A. Azim and M. A. Alim, Effects of temperature dependent thermal conductivity on

magnetohydrodynamic (MHD) free convection flow along a vertical flat plate with heat conduction, Nonlinear Analysis: Modelling and Control 13(2008) 513–524.

[11] R. Nasrin and M. A. Alim, MHD free convection flow along a vertical flat plate with thermal conductivity and viscosity depending on temperature, Journal of Naval Architecture and Marine Engineering 6(2009) 72-83.

[12] A. K. M. Safiqul Islam, M. A. Alim and ATM. M. R. Sharker, Effects of temperature dependent thermal conductivity on MHD free convection flow along a vertical flat plate with heat generation and joule heating, The International Conference on Marine Technology(2010), BUET, Dhaka, Bangladesh.

[13] G. M. Abdel-Rahman, Effects of variable viscosity and thermal conductivity on unsteady MHD flow of non-Newtonian fluid over a stretching porous sheet, Thermal Science 17(2013) 1035-1047.

[14] G. Borah and G. C. Hazarika, Effects of variable viscosity & thermal conductivity on steady free convection flow along a semi-infinite vertical plate (in presence of uniform transverse magnetic field) ,Journal of Computer & Mathematical Science 6(2010) 732-739.

[15] Z. Uddin and M. Kumar, Effect of temperature dependent properties on MHD free convection flow and heat transfer near the lower stagnation point of a porous isothermal cylinder, Computer Modelling and New Technologies 13(2009) 15–20.

[16] J. Charruaudeau, Influence de gradients de properties physiques en convection force application au cas du tube, International Journal of Heat and Mass Transfer 18(1975) 87-95.

[17] R. Nazar, N. Amin, T. Grosan and I. Pop, Free convection boundary layer on an isothermal sphere in micropolar fluid , International communication in Heat and Mass Transfer 29(2002) 377-386.

Available online at www.sciencedirect.com

ScienceDirect

Procedia Engineering 00 (2015) 000–000

Procedia Engineering

www.elsevier.com/locate/procedia

6th BSME International Conference on Thermal Engineering (ICTE 2014)

Ground source heat pump system controlled by refrigerant average density

Koutaro Tsubaki[a]*, Yuichi Mitsutake[a]

[a]*Saga University, Honjo 1, Saga, 840-8502, Japan.*

Abstract

A ground source heat exists in a ground shallower than about 100 m in depth. The ground source heat was applied for heat pump for air conditioning and snow melting, etc. However it is not popular in South area of Japan. We focus on the ground source heat application in warm region, especially for air cooling. The ground temperature at isothermal layer, about under 5m depth, is constant at about 18 °C in Saga, Japan. This temperature is lower than the temperature required for air cooling. Then a heat pipe with ground source heat can be used instead of a heat pump with atmosphere heat source, usually used for air cooling. Heat pipe could operate with smaller energy consumption than heat pump. Nevertheless the cycle operated like heat pipe is not used for ground heat source application. The novel ground source heat application cycle, which could operate as heat pump and heat pipe, suit for an air cooling was investigated in this research. The cycle operation condition is controlled by the average density. The cycle simulation of this cycle is investigated. From the calculation results, heat transfer rate and exergy loss of cycle changed with refrigerant average density. And also the best density condition was changed with the heat source temperature. Heat pipe operation could operate as 1.32 times (R410A) and 1.34 times (R407C) higher the heat transfer rate per unit the total irreversible loss compared with heat pump operation (ΔP = 0.1 MPa). And heat pump operation (ΔP = 0.1 MPa) could increase a heat transfer rate 1.23 times (R410A) and 1.29 times (R407C) compared with heat pipe operation.

Peer-review under responsibility of organizing committee of the 6th BSME International Conference on Thermal Engineering (ICTE 2014).

Keywords: Ground source heat; Heat pump; Heat pipe; Air conditioning

---

1. Introduction

A ground source heat is heat energy existed in a ground shallower than about 100 m in depth. The ground source heat was applied for heat pump for air conditioning and snow melting, etc. The annular geothermal energy was 423,830 TJ during 2005-2009 [1]. There are many researches about ground source heat pump applied for a school building, an

Peer-review under responsibility of organizing committee of the 6th BSME International Conference on Thermal Engineering (ICTE 2014).

office building, etc. [2-5]. Most of the work has been performed on a usual heat pump cycle which used with an air source. We focus on a ground source heat application in warm region, especially for air cooling. Ground source heat application is not popular in warm region even in South area of Japan [6-8]. However ground source heat has a potential to reduce an air cooling energy consumption. The ground temperature at isothermal layer, about under 5m depth, is constant about 18 °C in Saga, South area of Japan. This temperature is lower than the temperature required for air cooling. Then a heat pipe with ground source heat can be used instead of a heat pump with atmosphere heat source. Heat pipe could operate with much smaller energy consumption than heat pump. It is better if the cycle could also operate as heat pump when high heat load was required. The cycle which can operate as both of heat pump and heat pipe is suitable for ground source heat application. The cycle can operate as heat pump mode using compressor, and it could operate as heat pipe mode using liquid pump, according to the heat source condition and heat load. It needs to control a refrigerant charge in the cycle to change operation modes, heat pump and heat pipe. Because refrigerant state has to be vapor state before compressor in heat pump operation and has to be liquid state before liquid pump in heat pipe operation. And the refrigeration state is due to a refrigeration change in the cycle. In usual heat pump, refrigerant charge is adjusted to make condenser outlet refrigerant as two phase, because heat transfer rate decrease if outlet state become liquid state. It needs to change the refrigerant charge to make condenser outlet refrigerant as liquid state. Moreover it is known that there was optimum refrigeration charge for each heat source conditions [9-12]. Refrigeration charge in normal cycle is fixed when it was charged. If the refrigerant charge could be control, the suitable cycle for ground source heat use could be actualized.

A novel cycle which controlled by the average density was investigated by cycle simulation in this research. A refrigerant average density could be used by dividing a refrigeration change by the volume. Heat pump operation is expected to increase a heat transfer rate, and heat pipe operation is expected to decrease an irreversible loss. Two types of refrigerants were used pseudo azeotropic mixture R410A and zeotropic mixture R407C. R410A is popular refrigerant used as room air conditioner, and R407C was used to clarify an effect of zeotropic mixture.

Nomenclature

c	Specific heat
h	Enthalpy
L	Exergy loss
m	Mass flow rate
Q	Heat transfer rate
T	Temperature
U	Heat exchanger heat conductance
x	Quality
ρ	Density

Subscripts

Con	Condenser
Eva	Evaporator
Exp	Expansion valve
in	Inlet
LMTD	Log mean temperature difference
out	Outlet
r	Refrigerant
s	Heat source
sl	Saturated liquid
sv	Saturated vapor
total	Total
0	Environment

2. Cycle Simulation

2.1. Cycle for ground heat source application

A schematic diagram of the cycle was shown in Fig. 1. The elements of the cycle are condenser, evaporator, compressor, expansion valve and liquid pump. A heat pump operation consist of a compressor, a condenser, an expansion valve, and an evaporator the short dot and solid line and in Fig. 1. In a heat pipe operation, the liquid pump is used instead of expansion valve and the compressor is not used as shown in the long dot line in Fig. 1. The state of refrigerant must be liquid phase before the liquid pump and vapor phase before the compressor. This is actualized by the average refrigerant density control.

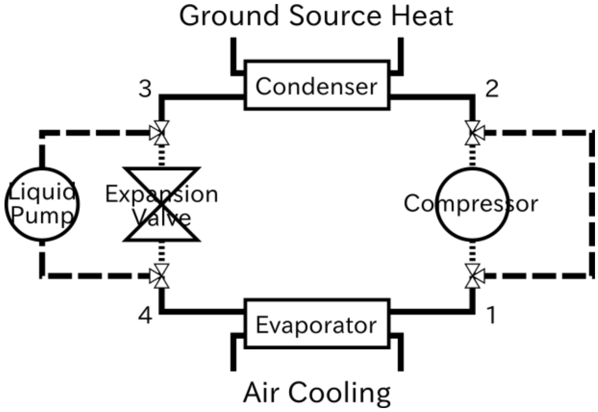

Fig. 1 Schematic diagram of the cycle

2.2. Governing equations

The system of governing equations was solved in a cycle simulation. The pressure difference between evaporator and condenser was set as calculation condition. The pressure difference at liquid pump consisted in heat pipe operation, the long dot line in Fig. 1, was set as 0 MPa. A heat transfer rate of evaporator and condenser were calculated by the refrigerant enthalpy change, the heat source temperature change, and logarithmic mean temperature difference for refrigerant and heat source, respectively. The evaporator process was assumed as isobaric. Average refrigerant density of evaporator was calculated by density and quality of refrigerant at inlet and outlet as shown in Eq. (1).

$$\rho_{Eva} = \frac{2(x_1 - x_4)}{\frac{x_1 - 1}{\rho_1} + \frac{x_1}{\rho_{sv}} - \frac{x_4 - 1}{\rho_{sl}} - \frac{x_4}{\rho_4}} \tag{1}$$

Average refrigerant density of condenser was calculated as same as evaporator. Total average refrigerant density was averaged by volume weighted equation as below.

$$\rho_{total} = \frac{\rho_{Con} V_{Con} + \rho_{Eva} V_{Eva}}{V_{Con} + V_{Eva}} \tag{2}$$

The process assumed as isentropic in compressor and isenthalpic in expansion valve.

Exergy loss of the condenser, the evaporator, the expansion valve, and whole cycle were calculated for a cycle estimation.

$$L_{Con} = T_0 \left\{ m_r (s_3 - s_2) + c_{s,Con} m_{s,Con} \log \frac{T_{s,Con,out}}{T_{s,Con,in}} \right\} \tag{3}$$

$$L_{Eva} = T_0 \left\{ m_r (s_1 - s_4) + c_{s,Eva} m_{s,Eva} \log \frac{T_{s,Eva,out}}{T_{s,Eva,in}} \right\} \tag{4}$$

$$L_{Exp} = T_0 m_r (s_4 - s_3) \tag{5}$$

$$L_{Total} = L_{Con} + L_{Eva} + L_{Exp} \tag{6}$$

2.3. Simulation procedure

The flow chart of the calculation procedure was shown in Fig. 2. Pseudo-azeotropic mixture R410A and zeotropic mixture R407C were used as refrigerant. The operation was assumed air cooling and changed cooling heat source temperature 24°C, 27°C, and 30°C. And the average refrigerant density in the cycle, heat exchanger performance of condenser and evaporator, the heat source temperature and flow rate, refrigerant flow rate, and pressure difference between condenser and evaporator were given as simulation parameters as shown in table 1. The pressure difference between condenser and evaporator was set as 0.0 MPa in heat pipe mode and less than 0.2 MPa in heat pump mode. The refrigerant state must be liquid before the liquid pump in heat pump mode. And it must be vapor before the compressor in heat pipe mode. In calculation procedure, enthalpy difference become less than 0.05 % and Difference of Thermal conductance become less than 0.01 %. Thermal properties were calculated by REFPROP ver. 9.

Table 1 Simulation parameters

Condenser		
Volume	V_{Con}	0.1 m^3
Thermal conductance	U_{Con}	0.15 kJ/K
Heat source mass flow rate	$m_{s,Con}$	0.07 kg/s
Heat source specific heat	$c_{s,Con}$	4.179 kJ/(kg K)
Heat source inlet temperature	$T_{Con,in}$	18 °C
Evaporator		
Volume	V_{Eva}	0.1 m^3
Thermal conductance	U_{Eva}	0.15 kJ/K
Heat source mass flow rate	$m_{s,Eva}$	0.07 kg/s
Heat source specific heat	$c_{s,Eva}$	4.179 kJ/(kg K)
Heat source inlet temperature	$T_{Eva,in}$	24, 27, 30 °C
Others		
Refrigerant mass flow rate	m_r	0.005 kg/s
Ambient temperature	T_0	30 °C
Pressure difference	ΔP	0.0 - 0.2 MPa

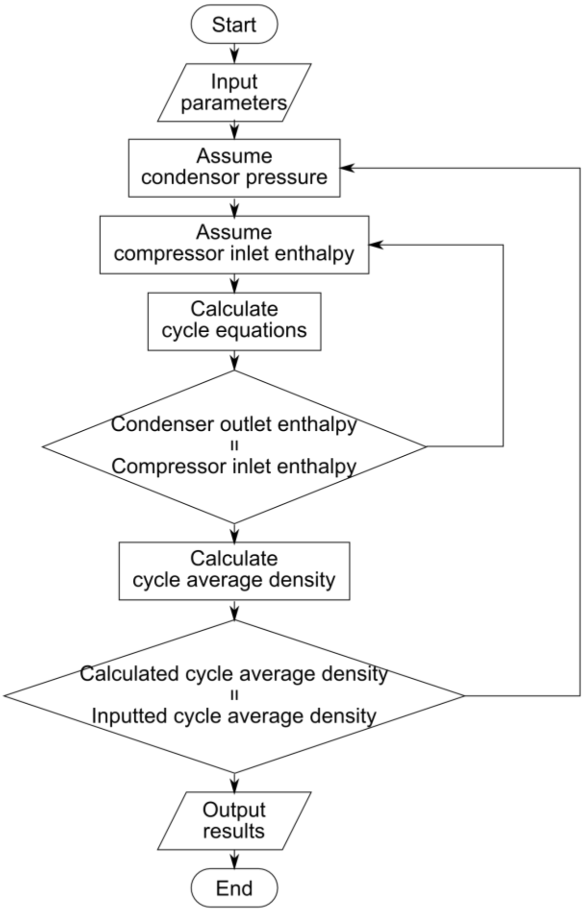

Fig. 2 Flow chart of the calculation procedure

3. Results and discussion

T-s diagrams at minimum, optimum and maximum density with each heat source temperature with the pressure difference 0.0 MPa were shown in Fig. 3 and Fig. 4. R410A and R407C were used as refrigerant respectively. The liquid pump inlet point 3 and outlet point 4 was plotted at same position, and point 1 and 2 was at same position also. The *T-s* diagrams with the pressure difference 0.1 MPa were shown in Fig. 5 and Fig. 6. An azeotropic mixture R407C has temperature glide in two phase region as shown in Fig. 4 and Fig. 6. In the *T-s* diagrams, the condenser pressure was increased with the average density increase. Due to the pressure increase, two phase temperature in the condenser also increase. Moreover high average density condition contained much liquid and entropy became small. Then the diagram shift to the upper left due to average density increase. The heat pipe operation with the pressure difference 0.0 MPa must took liquid phase at the liquid pump inlet. The state at liquid pump inlet became saturated liquid at the minimum density, as shown as red line in Fig. 3 and Fig. 4, and it became two phase in lower average density. And the heat pump operation must took vapor phase at the compressor inlet. The state of compressor inlet became saturated vapor at the maximum density, as shown as black line in Fig. 5 and Fig. 6, and it became two phase in higher average density. In the case higher than 217 kg/m^3, as shown as black line in Fig. 3, with the pressure difference 0.0 MPa and lower than 84 kg/m^3, as shown as red line in Fig. 5, with the pressure difference 0.1 MPa, the relation between refrigerant temperature and heat source temperature was inversed in a particular region. Then the calculation was not done in these conditions.

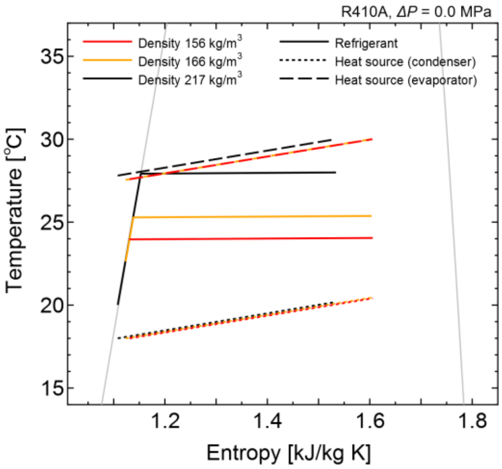

Fig. 3 *T-s* diagram
(R410A, ΔP = 0.0MPa, $T_{Eva,in}$ = 30°C)

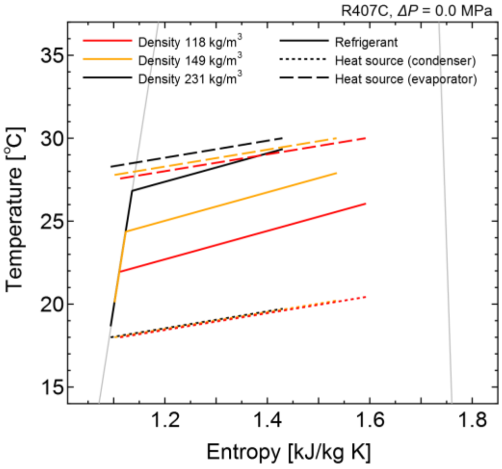

Fig. 4 *T-s* diagram
(R407C, ΔP = 0.0MPa, $T_{Eva,in}$ = 30°C)

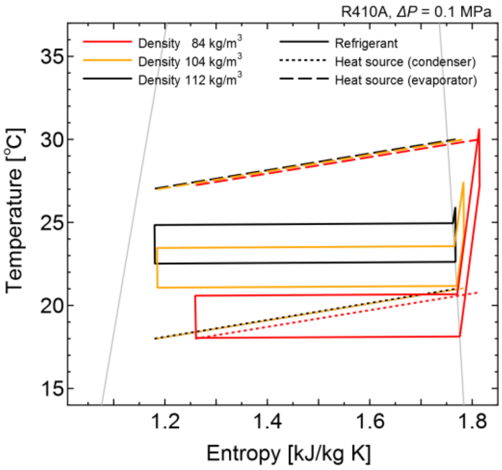

Fig. 5 *T-s* diagram
(R410A, ΔP = 0.1MPa, $T_{Eva,in}$ = 30°C)

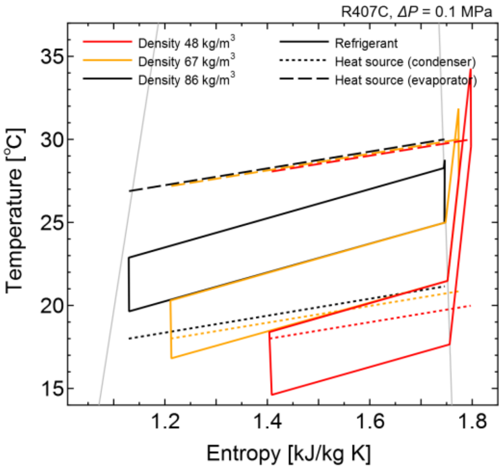

Fig. 6 *T-s* diagram
(R407C, ΔP = 0.1MPa, $T_{Eva,in}$ = 30°C)

The relations between the heat transfer rate and average density for various evaporator heat source inlet temperature were shown in Fig. 7 and Fig. 8. The heat transfer rate took high value in the case two phase state occupied area in heat exchanger was large. The temperature difference with heat source was decreased in superheat or subcool region because the refrigerant temperature substantially increased or decreased there. In the case the average density increased, the temperature difference between heat source and refrigerant in the evaporator increase, but that in the condenser decrease. The heat transfer rate was mainly effected by two phase area. Then the heat transfer rate increased with the average density increase in heat pipe operation and decreased in heat pump operation. The heat transfer rate took a peak with pseudo-azeotropic mixture R410A as shown in Fig. 7. An azeotropic mixture R407C has temperature glide even in two phase region. The maximum heat transfer rate were took at yellow line condition in Fig. 3 and Fig. 5, which the temperature difference of refrigerant in heat exchanger became close to that of heat source. The heat transfer rate with R407C did not take a peak with average density change as shown in Fig. 8 because the temperature glide of refrigerant is larger than heat source temperature difference. The optimum density was different in each heat source temperature condition. And average density range where the heat pipe mode and the heat pump mode could operate, did not overlap. To operate in the heat pipe and the heat pump mode, it is essential to control an average refrigerant density. The variation of the heat transfer rate and the heat transfer rate divided by the total irreversible loss with pressure difference was shown in Fig. 9 and Fig. 10. The temperature difference between refrigerant and heat source in heat exchangers increased with increasing the pressure difference, then the heat transfer rate increased. However the total irreversible loss increased more than the heat transfer rate increase. The cycle could operate as heat pipe with low power assumption and low irreversible loss when heat load was small. R407C took lower heat transfer

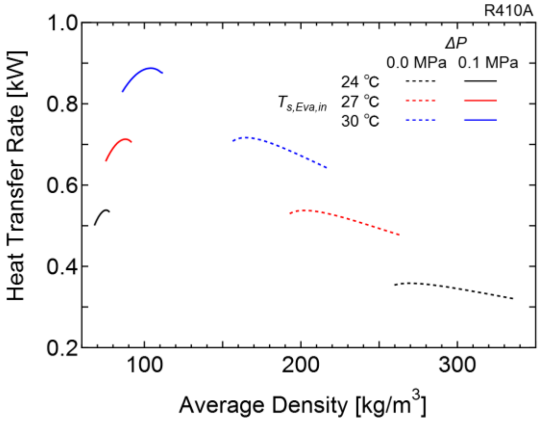

Fig. 7 Heat transfer rate with average density (R410A)

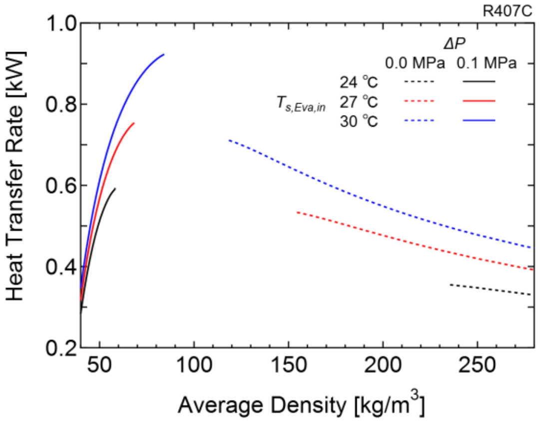

Fig. 8 Heat transfer rate with average density (R407C)

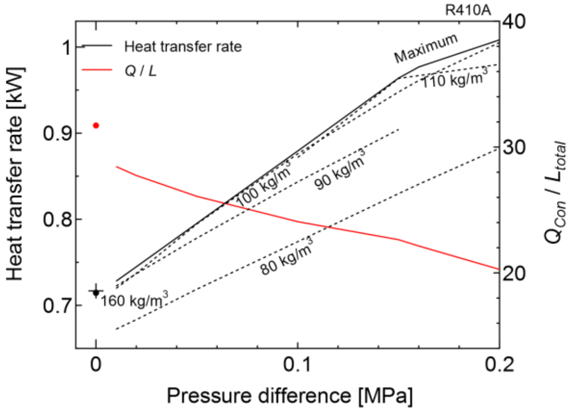

Fig. 9 Heat transfer rate with pressure difference (R410A, $T_{Eva,in}$ = 30°C)

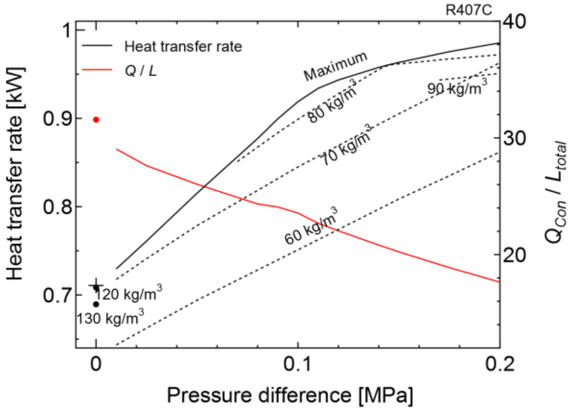

Fig. 10 Heat transfer rate with pressure difference (R407C, $T_{Eva,in}$ = 30°C)

rate for irreversible loss in heat pipe operation than R410A. It is because that the temperature glide of refrigerant did not match to heat source temperature change.

4. Conclusions

This paper analyzes the cycle which suit for ground source heat application by the cycle simulation. Heat pipe operation could operate as 1.32 times (R410A) and 1.34 times (R407C) higher the heat transfer rate per unit the total irreversible loss compared with heat pump operation (ΔP = 0.1 MPa). And heat pump operation (ΔP = 0.1 MPa) could increase a heat transfer rate 1.23 times (R410A) and 1.29 times (R407C) compared with heat pipe operation. The irreversible loss of the cycle using zeotropic mixture R407C would be smaller if the temperature glide fit to the heat source temperature change. The temperature change of heat source was too small in present case. By the cycle simulation we could find that the cycle could operate as heat pipe with low power assumption and low irreversible loss when heat load was small.

Acknowledgements

This investigation was supported by a Paloma environmental technology development foundation.

References

[1] J.W. Lund, D.H. Freeston, T.L. Boyd, Direct utilization of geothermal energy 2010 worldwide review, Geothermics; 40 (2010) 159-180.

[2] E. Kim, J. Lee, Y. Jeong, et al., Performance evaluation under the actual operating condition of a vertical ground source heat pump system in a school building, Energy and Buildings, 50 (2012) 1-6.

[3] C. Montagud, J. M. Corberan, F. Ruiz-Calvo, Experimental and modeling analysis of a ground source heat pump system, Applied Energy, vol. 109, pp. 328-336, (2013).

[4] J. Luo, J. Rohn, M. Bayer, et al., Heating and cooling performance analysis of a ground source heat pump system in Southern Germany, Geothermics, 53 (2015) 57-66.

[5] N. Zhu, P. Hu, L. Xu, et al., Recent research and applications of ground source heat pump integrated with thermal energy storage systems: A review, Applied Thermal Engineering, 71 (2014) 142-151.

[6] S. Kawazoe, N. Shirakura, Geothermal Power Generation and Direct Use in Japan, Proceedings World Geothermal Congress, (2005).

[7] V. R. Tarnawski, W. H. Leong, T. Momose, Y. Hamada, Analysis of ground source heat pumps with horizontal ground heat exchangers for northern Japan, Renewable Energy, 34 (2009) 127–134.

[8] K. Nagano, T. Katsura, S. Takeda, Development of a design and performance prediction tool for the ground source heat pump system, Applied Thermal Engineering, 26 (2006) 1578–1592.

[9] J.M. Corberan, , I.O. Martinez, J. Gonzalvez, Charge optimisation study of a reversible water-to-water propane heat pump, International Journal of Refrigeration, 31 (2008) 716-726.

[10] F. Poggi, H. Macchi-Tejeda, D. Leducq, A. Bontemps, Refrigerant charge in refrigerating systems and strategies of charge reduction, International Journal of Refrigeration, 31 (2008) 353-370.

[11] H. Cho, C. Ryu, Y. Kim, H. Y. Kim, Effects of refrigerant charge amount on the performance of a transcritical CO2heat pump, International Journal of Refrigeration, 28 (2005) 1266–1273.

[12] Y. Xuan, Y. Hong, Q. Li, Investigation on transient behaviors of flat plate heat pipes, Experimental Thermal and Fluid Science, 28 (2004) 249–255.

ELSEVIER

Available online at www.sciencedirect.com

ScienceDirect

Procedia Engineering 00 (2015) 000–000

Procedia Engineering

www.elsevier.com/locate/procedia

6th BSME International Conference on Thermal Engineering (ICTE 2014)

Thermal Diffusion Effect on Unsteady Viscous MHD Micropolar Fluid Flow through an Infinite Vertical Plate with Hall and Ion-slip Current

Nisat Nowroz Anika[a], Md. Mainul Hoque[b]*, Sheikh Imamul Hossain[c]
and Md. Mahmud Alam[c]

[a]Department of Mechanical Engineering, The University of Newcastle, Callaghan, NSW 2308, Australia
[b]Department of Chemical Engineering, The University of Newcastle, Callaghan, NSW 2308, Australia*
[c]Mathematics Discipline, Khulna University, Khulna-9208, Bangladesh

Abstract

An analysis is carried out to study the effect of Hall and Ion-slip current and heat transfer characteristics over an infinite vertical plate for micropolar fluid in the presence of magnetic field. The governing boundary layer equation first transformed into non-dimensional form and resulting non-linear system of partial differential equations are then solved numerically by using the robust implicit finite difference technique. Also the unconditional stability and convergence test has been carried out to establish the effect of shear stresses, couple stress, Nusselt number and Sherwood number on the flow field. Finally, the effects of various parameters are separately discussed and shown graphically.

Keywords: Micropolar fluid; Hall current; Ion-slip current ; Thermal diffusion.

---

* Corresponding author. Tel.: +61 406 618 193;
E-mail address: mohammadmainul.hoque@uon.edu.au

1. Introduction

Magneto-micropolar fluid flow with hall and ion slip currents is play an important role in the view of its wide applications in many engineering problems such as electric transformers and heating elements. Eringen [1] proposed the theory of micopolar fluid considering microrotation and microinertial effect. These flow characteristics cannot be described by the usual Navier-Stokes theory. Hence, the renowned Navier Stokes formula is not appropriate for modelling such type of problem. Since, the pioneering work by Eringen [1] has created a lot of interest. However, there are comprehensive works that have been carried out on viscous and incompressible fluid with the effect of Hall current by Chamhka [2], Seddeek [3], Takher et al. [4], Shateyi et al. [5,6], Salem and Abd El-aziz [7], Anika et al. [8,9], and among others.

Nomenclature

(x, y, z)	Cartesian Coordinates	(u, v, w)	Velocity components
ε	Suction velocity	M	Magnetic Parameter
β_e	Hall current	τ	Dimensionless time
P_r	Prandlt number	E_c	Eckert number
S_c	Schmidt number	$\mathbf{B}$	Magnetic field
Δ	Microrotation parameter	T_w	Temperature at the plate
λ	Spin gradient viscosity	T_∞	Temperature outside the boundary layer
Λ	Vortex viscosity	C_w	Concentration at the plate
G_r	Grashof number	C_∞	Concentration outside the boundary layer
G_r^*	Modified Grashof number	U	Dimensionless primary velocity
β_i	Ion-slip parameter	W	Dimensionless secondary velocity
S_o	Soret number	Ω	Dimensionless microrotation variable
θ	Dimensionless Temperature	Φ	Dimensionless Concentration variable

The momentum, heat, and mass transport on vertical plate have several practical engineering applications. The heat transfer problem associated with Hall and Ion slip current under different physical conditions has been analysed by several authors. Dash et al. [10] investigated MHD free convection and mass transfer flow over a continuously moving vertical plate under the action of strong magnetic field. The hall and ion slip current in the momentum equation are considered for high speed fluid flows and the level of concentration of foreign mass have been taken very high. Anika and Hoque [11] studied the one dimensional Magnetohydrodynamics flow behaviour through an infinite vertical plate. Hall and Ion slip current with strong magnetic field and constant suction are applied perpendicular to the plate. Recently, Haque et al. [12] studied MHD free convection and mass transfer flow past a semi-infinite vertical porous plate having variable suction with constant heat and mass fluxes. The diffusion thermo, thermal diffusion terms, viscous dissipation and Joule heating terms have been considered for high speed fluid. But the boundary layer micropolar fluid flow characteristic in presence of Hall and Ion slip with magnetic field still not well understood.

Hence our aim is to study the Unsteady One-dimensional Micropolar fluid flow behaviour through an infinite vertical plate with the influence of Hall and Ion-slip current having constant suction with constant heat and mass fluxes. The model has been solved by implicit finite difference technique. In general it is very complicated to evaluate the flow characteristic of this kind of problem. Therefore, it is necessary to investigate in detail the accuracy of primary velocity, secondary velocity, angular velocity, temperature and concentration across the boundary layer. The corresponding Shear stress in x and z direction, Couple stress, Nusselt number and Sherwood number have been shown graphically. In this study, all figures have not shown for brevity.

2. Mathematical Model of Flow

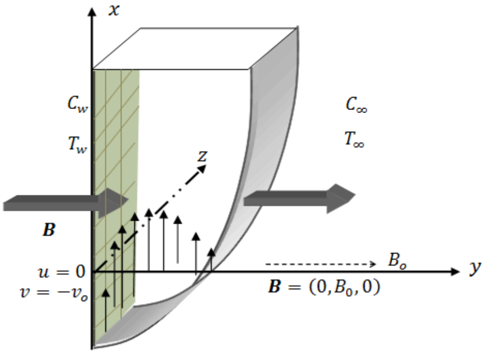

Fig.1: Boundary layer development on a vertical plate

An unsteady one dimensional free convection flow of ionized micropolar fluid along an infinite vertical plate $y = 0$ has been expedited in this work. The flow is permeated by a non-conducting vertical plate taken along x- axis in the upward direction and y- axis is normal to the plate. A uniform magnetic field of strength B_0 is assumed to be applied along the positive y-direction normal to the plate and that induced another magnetic field on the electrically conducting fluid. The flow configuration and coordinate system are shown in Fig.1. Consequently, electrically conducting fluid is affected Hall and Ion-slip current. A force (coriolis force named microrotational force) owing to the rotating of the particle and the interaction of magnetic and electric field induces a cross flow in the z-direction. The equation of conservation of charge $\Delta.J = 0$ gives $J_y =$ constant. Since the plate is of infinite extent and the fluid motion is unsteady so all the flow variables will depend only upon y and time t. Within the framework of the above stated assumption and using the dimensionless quantities, $Y = \frac{yU_0}{\vartheta}, U = \frac{u}{U_0}, W = \frac{w}{U_0}, \tau = \frac{tU_0{}^2}{\vartheta}, \theta = \frac{T-T_\infty}{T_w-T_\infty}$ in the equations relevant to the problem is governed by the following coupled non-dimensional partial differential equations under the electromagnetic Boussinesq approximations as:

$$\frac{\partial U}{\partial \tau} - \epsilon \frac{\partial U}{\partial Y} = (1+\Delta)\frac{\partial^2 U}{\partial Y^2} + \Delta \frac{\partial \Omega}{\partial Y} + G_r\theta + G_r^*\Phi \; - \frac{\mathrm{M}}{\left({\alpha_e}^2 + {\beta_e}^2\right)}(\alpha_e U + \beta_e W) \tag{1}$$

$$\frac{\partial W}{\partial \tau} - \epsilon \frac{\partial W}{\partial Y} = (1+\Delta)\frac{\partial^2 W}{\partial Y^2} + \frac{\mathrm{M}}{\left({\alpha_e}^2 + {\beta_e}^2\right)}(\beta_e U - \alpha_e W) \tag{2}$$

$$\frac{\partial \Omega}{\partial \tau} - \epsilon \frac{\partial \Omega}{\partial Y} = \Lambda \frac{\partial^2 \Omega}{\partial Y^2} - \lambda\left(2\Omega + \frac{\partial U}{\partial Y}\right) \tag{3}$$

$$\frac{\partial \theta}{\partial \tau} - \epsilon \frac{\partial \theta}{\partial Y} = \frac{1}{P_r}\frac{\partial^2 \theta}{\partial Y^2} + (1+\Delta)E_c\left[\left(\frac{\partial U}{\partial Y}\right)^2 + \left(\frac{\partial W}{\partial Y}\right)^2\right] + \mathrm{M}\frac{E_c}{\left({\alpha_e}^2 + {\beta_e}^2\right)}(U^2 + W^2) \tag{4}$$

$$\frac{\partial \Phi}{\partial \tau} - \epsilon \frac{\partial \Phi}{\partial Y} = \frac{1}{S_c}\frac{\partial^2 \Phi}{\partial Y^2} + S_0\frac{\partial^2 \theta}{\partial Y^2} \tag{5}$$

with the corresponding initial and boundary conditions

$$\tau > 0, \quad \begin{array}{ll} U = 0,\; W = 0,\; \Omega = -S\dfrac{\partial U}{\partial Y},\; \theta = 1,\; \Phi = 1 & \text{at } Y = 0 \\ U = 0,\; W = 0,\; \Omega = 0,\; \theta = 0,\; \Phi = 0 & \text{as } Y \to \infty \end{array} \tag{6}$$

where the symbols have their usual meaning and defined in nomenclature section.

3. Method of Solution

For simplicity the implicit finite difference method has been used to solve equations (1)-(5) subject to the initial and boundary conditions equation (6). In this case the region within the boundary layer is divided by some perpendicular lines of Y- axis, where Y- axis is normal to the medium as shown in Fig. 2. It is assumed that the maximum length of boundary layer is $Y_{\max}(=30)$ as corresponds to $Y \to \infty$ i.e. Y vary from **0** to 30. And the number of grid spacing in Y directions is $m(=200)$, hence the constant mesh size along Y axis becomes $\Delta Y = 0.15(0 \le Y \le 30)$ with the smaller time step $\Delta\tau = 0.001$.

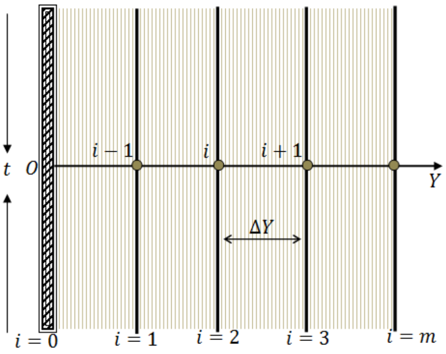

Fig 2. Implicit finite difference space grid.

Let $U_i^n, W_i^n, \Omega_i^n, \theta_i^n$ and Φ_i^n denote the values of U, W, Ω, θ and Φ at the end of a time-step respectively. Using the implicit finite difference approximation we have

$$\frac{U_i^{n+1} - U_i^n}{\Delta\tau} - \epsilon\frac{U_{i+1}^n - U_i^n}{\Delta Y} = (1+\Delta)\frac{U_{i+1}^n - 2U_i^n + U_{i-1}^n}{(\Delta Y)^2} + \Delta\frac{\Omega_{i+1}^n - \Omega_i^n}{\Delta Y} + G_r\theta_i^n + G_r^*\Phi_i^n - \frac{M}{\left({\alpha_e}^2 + {\beta_e}^2\right)}\left(\alpha_e U_i^n + \beta_e W_i^n\right) \quad (7)$$

$$\frac{W_i^{n+1} - W_i^n}{\Delta\tau} - \epsilon\frac{W_{i+1}^n - W_i^n}{\Delta Y} = (1+\Delta)\frac{W_{i+1}^n - 2W_i^n + W_{i-1}^n}{(\Delta Y)^2} + \frac{M}{\left({\alpha_e}^2 + {\beta_e}^2\right)}\left(\beta_e U_i^n - \alpha_e W_i^n\right) \quad (8)$$

$$\frac{\Omega_i^{n+1} - \Omega_i^n}{\Delta\tau} - \epsilon\frac{\Omega_{i+1}^n - \Omega_i^n}{\Delta Y} = \Lambda\frac{\Omega_{i+1}^n - 2\Omega_i^n + \Omega_{i-1}^n}{(\Delta Y)^2} - \lambda\left(2\Omega_i^n + \frac{U_{i+1}^n - U_i^n}{\Delta Y}\right) \quad (9)$$

$$\frac{\theta_i^{n+1} - \theta_i^n}{\Delta\tau} - \epsilon\frac{\theta_{i+1}^n - \theta_i^n}{\Delta Y} = \frac{1}{P_r}\frac{\theta_{i+1}^n - 2\theta_i^n + \theta_{i-1}^n}{(\Delta Y)^2} + (1+\Delta)E_c\left[\left(\frac{U_{i+1}^n - U_i^n}{\Delta Y}\right)^2 + \left(\frac{W_{i+1}^n - W_i^n}{\Delta Y}\right)^2\right] + \mathrm{M}\frac{E_c}{\left({\alpha_e}^2 + {\beta_e}^2\right)}\left({U_i^n}^2 + {W_i^n}^2\right) \quad (10)$$

$$\frac{\Phi_i^{n+1} - \Phi_i^n}{\Delta\tau} - \epsilon\frac{\Phi_{i+1}^n - \Phi_i^n}{\Delta Y} = \frac{1}{S_c}\frac{\Phi_{i+1}^n - 2\Phi_i^n + \Phi_{i-1}^n}{(\Delta Y)^2} + S_o\frac{\theta_{i+1}^n - 2\theta_i^n + \theta_{i-1}^n}{(\Delta Y)^2} \quad (12)$$

and the initial and boundary condition with finite difference scheme as

$$\begin{aligned} &U_0^n = 0, \quad W_0^n = 0, \quad \Omega_0^n = -S\frac{U_1^n - U_0^n}{\Delta Y}, \quad \theta_0^n = 1, \quad \Phi_0^n = 1, \quad \tau > 0 \\ &U_L^n = 0, \quad W_L^n = 0, \quad \Omega_L^n = 0, \quad \theta_L^n = 1, \quad \Phi_L^n = 1, \quad L \to \infty \end{aligned} \quad (13)$$

Here, i represent the grid points while n represents a value of time, $\tau = n\Delta\tau$, where, $n = 0,1,2,3,\ldots\ldots\ldots\ldots$ Also the numerical values of the shear stresses, couple stress, Nusselt number and Sherwood number are eventually by five point approximate formula for the derivatives. The continuity equation is ignored since $\Delta\tau$ does not appear in it. The general terms of the Fourier expansion for $U_i^n, W_i^n, \Omega_i^n, \theta_i^n$ and Φ_i^n at a time arbitrarily called $t = 0$ are all $e^{i\alpha Y}$ apart from a constant, where $i = \sqrt{-1}$. The stability conditions are not shown for brevity.

4. Results and Discussion

To investigate the physical conditions of the developed mathematical model the effects of dimensionless steady-state shear stresses (namely τ_x, τ_z), couple stress, Nusselt number and Sherwood number versus τ has been analysed in Figs. 3 to 15 respectively. Fig. 3 has shown the effects of magnetic parameters M on the several steady-state Shear stresses. It can be observed that the main flow decreased with the magnetic parameter M . But the Shear stress in z -direction (Fig. 4) gives the opposite effect with increase of magnetic parameter.

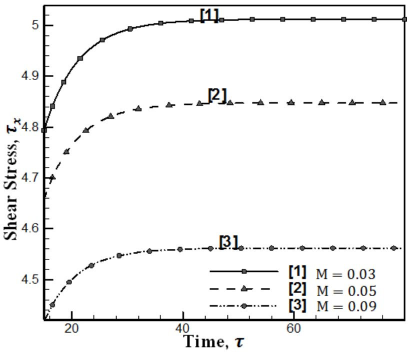

Fig. 3. Shear stress τ_x for different values of M .

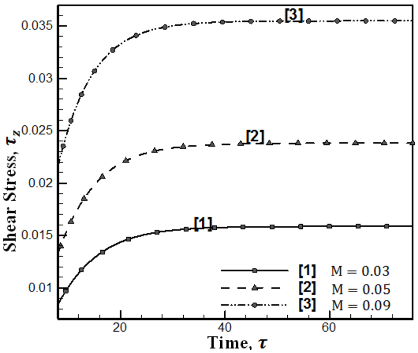

Fig. 4. Shear stress τ_z for different values of M .

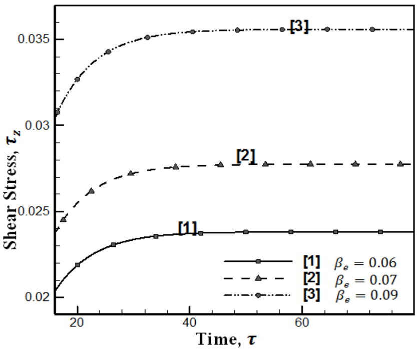

Fig. 5. Shear stress τ_z for different values of β_e .

Also from Fig. 5 it can be concluded that shear stress in the z -direction has increased with increase of Hall parameter β_e as compared to time τ , whereas the shear stress in x -direction has no visible effect (figure is not shown for brevity). Generally, it has been seen that an electrically conduction fluid is affected by Hall currents in the presence of transverse magnetic field. So the shear stress τ_z increases with increasing values of β_e , when $\beta_e \leq 1$. Fig.6 ascertain that the effect of P_r on Nusselt $(-N_u)$ number. The value of Nusselt $(-N_u)$ significantly increases with increase of P_r . Schmidt number S_c embodies the ratio of the momentum diffusivity to the mass (species) diffusivity. It physically relates the relative thickness of the hydrodynamic boundary layer and mass transfer (concentration) boundary layer. Fig. 7 has shown the effect of Sherwood $(-S_h)$ number for different values of S_c . The time development of couple stress for the different values Vortex viscosity λ has been presented in Fig.8. Shear viscosity causes a backward flow and then it rise to become linear. Therefore, the couple stress decrease as vortex viscosity λ increases with dimensionless time until they reach the steady-state condition as $\tau \to \infty$ .Local spinning motion of the fluid usually decreases in viscosity at higher shear rates. The effects of spin gradient viscosity Λ on couple stress have been plotted in Fig.9 with respect to τ . The steady state couple stress has a backward flow and increase steeply onwards as compared to τ . Again the couple stress increases with the increase of gradient viscosity Λ . Considerable effect of dimensionless Ion-slip parameter β_i on time development has been plotted in Fig.10. Because of considering very small magnetic parameter, the increase of β_i has negligible effects on those profiles.In order to get the physical insight of suction parameter ε , it has been seen from Figs. 11, 12 that shear stresses for both x and z direction has fallen for the rise of ε . So, boundary layer flow attains minimum velocity for large suction. And the Sherwood number $(-S_h)$

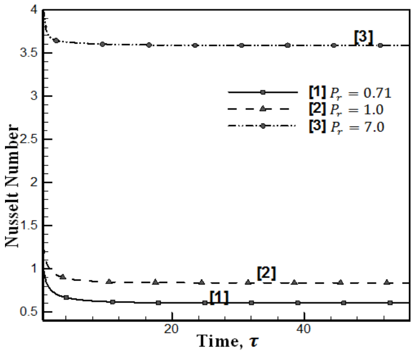

Fig. 6. Nusselt number for different values of P_r

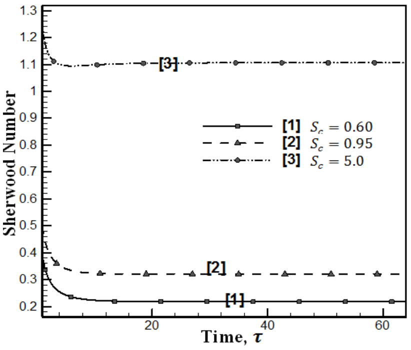

Fig. 7. Sherwood number for different values of S_c

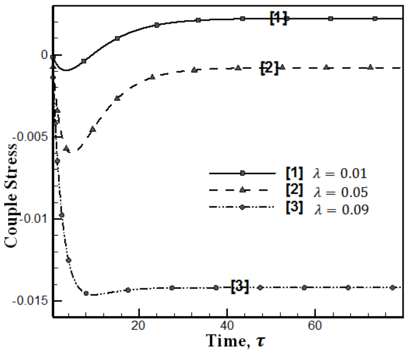

Fig. 8. Couple stress for different values of λ.

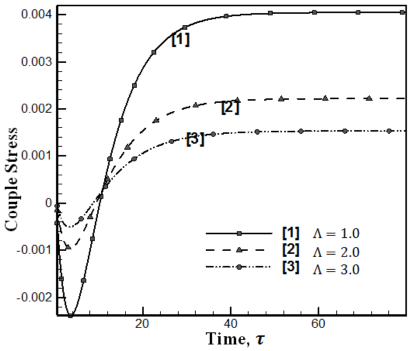

Fig. 9. Couple stress for different values of Λ.

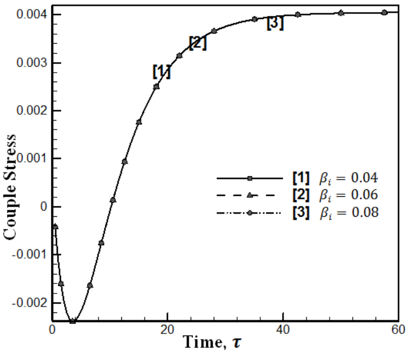

Fig.10. Couple stress for different values of dimensionless Ion-slip parameter β_i.

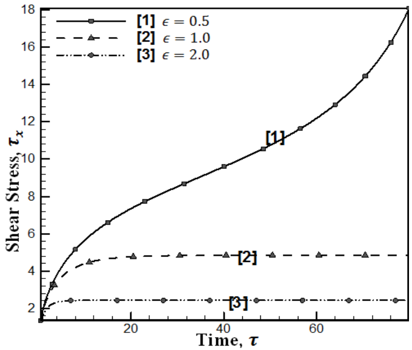

Fig.11. Shear stress τ_x for different values of dimensionless Suction parameter ϵ.

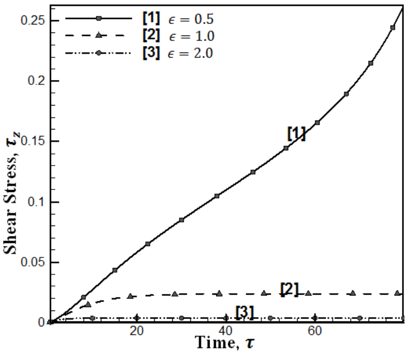

Fig.12. Shear stress τ_z for different values of dimensionless Suction parameter ϵ

has increases for low suction as illustrated in Fig.13. The effect of dimensionless Soret number S_o has been discussed in Figs.14 and 15. It is noticed that for increasing S_o, at low times, Couple stress decelerates for large S_o. And then onwards it was boosted from below for large time steps with the increase of S_o. The Sherwood number $(-S_h)$ decreases drastically for the increase of dimensionless Soret number S_o as illustrated in Fig.15.

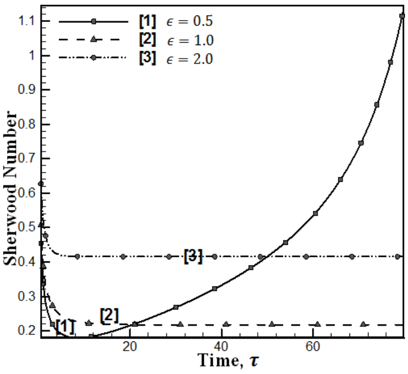

Fig.13. Sherwood number for different values of dimensionless Suction parameter ϵ

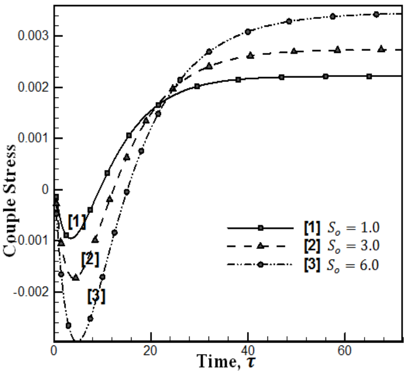

Fig.14. Couple stress for different values of dimensionless Soret number S_o.

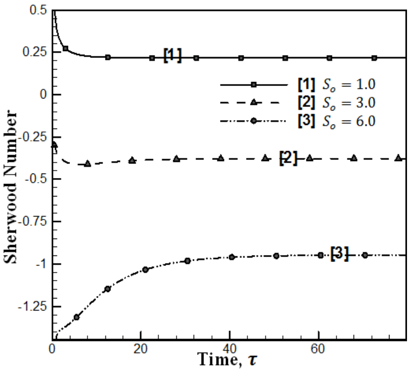

Fig.15. Sherwood number for different values of dimensionless Soret number S_o.

5. Conclusions

MHD mass transfer problem by free convection flow of an ionized incompressible viscous micropolar fluid across the infinite vertical plate under the action of Hall current and Ion-slip parameter has been taken into account. The physical properties are graphically discussed for different values of corresponding parameters. Some important findings of this study are given below:

1. The Shear stress in x-direction decreases with the increase of M and ε.
2. The Shear stress in $\boldsymbol{z}$-direction increases for of M and β_e while it decreases with the increase of ε.
3. The Couple stress increases with increase of Λ and decrease for λ and S_0.
4. The Sherwood number increases with the increase of S_c and ε and decrease for S_o.
5. The Nusselt number increases with increase of P_r.

References

[1] A. C. Eringen, Theory of micropolar fluids, Journal of Mathematics and Mechanic. 16 (1966) 1–18.

[2] A. J. Chamkha, MHD-free convection from a vertical plate embedded in a thermally stratified porous medium with hall effects, Applied Mathematical Modelling. 21(10) (1997) 603–609.

[3] M. A. Seddeek, Effects of hall and ion-slip currents on magneto-micropolar fluid and heat transfer over a non-isothermal stretching sheet with suction and blowing, Proceedings of the Royal Society A. 457 (2001) 3039–3050.

[4] H. S. Takhar, A. J. Chamkha, and G. Nath, MHD flow over a moving plate in a rotating fluid with magnetic field, hall currents and free stream velocity, International Journal of Engineering Science. 40 (13) (2002) 1511–1527.

[5] S. Shateyi, P. Sibanda, and S. S. Motsa, Magnetohydrodynamic flow past a vertical plate with radiative heat transfer, Journal of Heat Transfer. 129 (12) (2007) 1708–1713.

[6] S. Shateyi, S. S. Motsa, and P. Sibanda, The effects of thermal radiation, hall currents, soret, and dufour on MHD flow by mixed convection over a vertical surface in porous media, Mathematical Problems in Engineering. Article ID 627475 (2010) 1-20.

[7] A. M. Salem and M. Abd El-Aziz, Effect of hall currents and chemical reaction on hydromagnetic flow of a stretching vertical surface with internal heat generation/absorption, Applied Mathematical Modelling. 32 (7) (2008) 1236–1254.

[8] N. N. Anika, M. M. Hoque and M. M. Alam, Unsteady free convection flow with flow control parameter, Current Trends in Technology and Science. 2 (1) (2012) 193-201.

[9] N. N. Anika, M. M. Hoque and N Islam, Hall current effects on magnetohydrodynamics fluid over an infinite rotating vertical porous plate embedded in unsteady laminar flow, Annals of Pure and Appl. Mathematics. 3 (2) (2013) 189-200.

[10] K. Dash, M. M. Alam and M. Wahiduzzaman, MHD free convection and mass transfer flow from a vertical plate in the presence of hall and ion slip current, Advances in Mechanical Engineering. Article ID 851957 (2012) 1-20.

[11] N. N. Anika and M. M. Hoque, Thermal buoyancy force effects on developed flow considering hall and ion-slip current, Annals of Pure and Appl. Mathematics. 3 (2) (2013) 179-188.

[12] Z. Haque, M. M. Alam, M. Ferdows and A. Postelnicu, Micropolar fluid behaviour on steady MHD free convection and mass transfer flow with constant heat and mass fluxes, joule heating and viscous dissipation, J. King Saud Univ. Engineering Sciences, 24 (2) (2012) 71-84.

Available online at www.sciencedirect.com

ScienceDirect

Procedia Engineering00 (2015) 000–000

Procedia Engineering

www.elsevier.com/locate/procedia

6th BSME International Conference on Thermal Engineering (ICTE 2014)

Dean-Taylor Flow with Convective Heat Transfer through a Coiled Duct with Strong Curvature

Rabindra Nath Mondal[a]*, Raju Roy[b] and Md. Zohurul Islam[b]

[a] *Department of Mathematics, Jagannath University, Dhaka-1100, Bangladesh*
[b] *Department of Mathematics and Statistics, jessore University of Science and Technology*
Jessore-7408, Bangladesh.

Abstract

The present study addresses numerical prediction of Dean-Taylor flow through a coiled rectangular duct of curvature 0.5. Spectral method is used as a basic tool to solve the system of non-linear partial differential equation. The emerging parameters controlling the flow characteristics are the rotation parameter i.e. Tr, (incorporating Coriolis force), Grashof number (Gr), Prandtl number $(Pr = 7)$, aspect ratio $(a = 2)$, and pressure-driven parameter i.e. Dean number Dn (incorporating centrifugal force). The flow structures are examined for the effects of rotation parameter and pressure-driven parameter. We investigated unsteady flow characteristics for two cases of the duct rotation, *Case I:* Positive rotation and *Case II*: Negative rotation. For positive rotation, we investigate the unsteady flow for the Dean numbers Dn = 1000 and 2000 over the Taylor number $0 \le Tr \le 500$, and it is found that the chaotic flow turns into steady-state flow through periodic or multi-periodic flows, if Tr is increased in the positive direction. For negative rotation, however, unsteady flow characteristics are investigated over the Taylor number $-700 \le Tr \le -50$, and it is found that the unsteady flow undergoes through various flow instabilities, if Tr is increased in the negative direction. Contours of secondary flow patterns and temperature profiles are obtained at several values of Tr, and it is found that the unsteady flow consists of two-, three-, four-, five-, six-, seven- and eight-vortex solutions. Convective heat transfer is also investigated, and it is found that the chaotic flow enhances heat transfer more significantly than the steady-state or periodic solutions.

---

* Corresponding author. Cell Phone: +88-01710851580
E-mail address: rnmondal71@yahoo.com

1. Introduction

Flow and heat transfer through curved ducts and channels have attracted much attention because of their ample applications in fluids engineering. Due to engineering applications, such as in rotating systems, gas turbines, electric generators, heat exchangers, cooling systems and some separation processes, scientists have paid considerable attention to study the rotating curved duct flows. The readers are referred to Nandakumar and Masliyah [1], Ito [2] and Yanase *et al.* [3] for some outstanding reviews on curved duct flows.

The fluid flowing in a rotating curved duct is subjected to two forces: the *Coriolis force* due to rotation and the *centrifugal force* due to curvature. For isothermal flows of a constant property fluid, the Coriolis force tends to produce vortices while centrifugal force is purely hydrostatic. When a temperature induced variation of fluid density occurs for non-isothermal flows, both Coriolis and centrifugal type buoyancy forces can contribute to the generation of vortices. These two effects of rotation either enhance or counteract each other in a non-linear manner depending on the direction of wall heat flux and the flow domain. Therefore, the effect of system rotation is more subtle and complicated and yields new; richer features of flow and heat transfer in general, bifurcation and stability in particular, for non-isothermal flows. Selmi *et al.* [4] examined the combined effects of system rotation and curvature on the bifurcation structure of two-dimensional flows in a rotating curved duct with square cross section. Wang and Cheng [5], employing finite volume method, examined the flow characteristics and heat transfer in curved square ducts for positive rotation and found reverse secondary flow for the co-rotation cases. Selmi and Nandakumer [6] and Yamamoto *et al.* [7] performed studies on the flow in a rotating curved rectangular duct. When a temperature induced variation of fluid density occurs for non-isothermal flows, both Coriolis and centrifugal type buoyancy forces can contribute to the generation of vorticity (Mondal *et. al.*, [8]). These two effects of rotation either enhance or counteract each other in a non-linear manner depending on the direction of wall heat flux and the flow domain. Very recently, Mondal *et al.* [9] performed numerical investigation of the non-isothermal flows through a curved rectangular duct of large aspect ratio and obtained substantial results. However, there is no known study on the rotating curved rectangular channel flows in the presence of buoyancy force. The present paper is, therefore, an attempt to fill up this gap. Studying the effects of rotation on the flow unsteady characteristics, caused by the combined action of the centrifugal and coriolis force, is an important objective of the present study.

Nomenclature

Dn : Dean number
Tr : Taylor number
Gr : Grashof number
h : Half height of the cross section
d : Half width of the cross section
L : Radius of the curvature
P_r : Prandtl number
t : Time

T : Temperature
u : Velocity components in the $x-$direction
v : Velocity components in the $y-$direction
w : Velocity components in the $z-$direction
x : Horizontal axis
y : Vertical axis
z : Axis in the direction of the main flow
λ : Resistance coefficient

Greek letters

δ : Curvature of the duct
υ : Kinematic viscosity
ρ : Density

μ : Viscosity
κ : Thermal diffusivity
ψ : Sectional stream function

2. Mathematical Formulations

Consider a hydro-dynamically and thermally fully developed two-dimensional flow of viscous incompressible fluid through a rotating curved duct with rectangular cross section, whose height and wide are *2h* and *2l*, respectively. The coordinate system with the relevant notation is shown in Fig. 1, where x' and y' axes are taken to be in the horizontal and vertical directions respectively, and z' is the axial direction. The system rotates at a constant angular velocity Ω_T around the y' axis. It is assumed that the outer wall of the duct is heated while the inner wall cooled. The temperature of the outer wall is $T_0 + \Delta T$ and that of the inner wall is $T_0 - \Delta T$, where $\Delta T > 0$. The *x,* *y,* and *z* axes are taken to be in the horizontal, vertical, and axial directions respectively. It is assumed that the flow is uniform in the axial direction, which is driven by a constant pressure gradient *G* along the center-line of the duct as shown in Fig. 1. The variables are non-dimensionalized by using the representative length l and the representative velocity U_0.

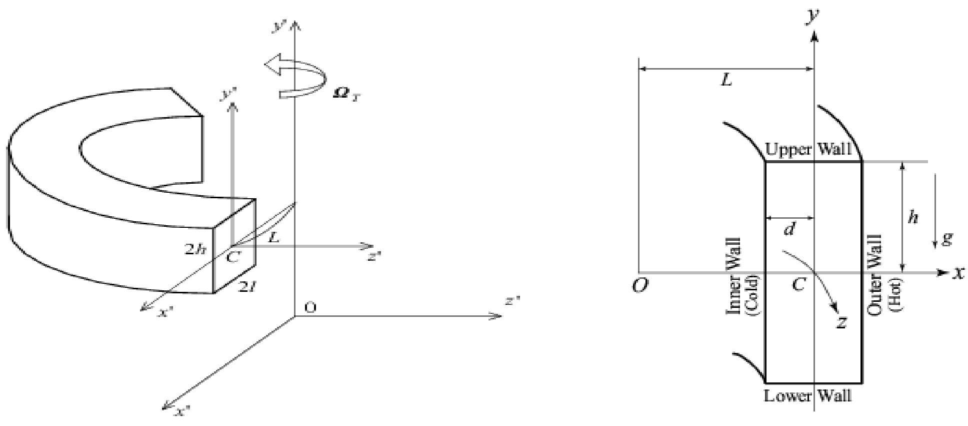

(a) (b)

Fig. 1. (a) Coordinate system of the rotating curved channel (b) Cross section of the curved channel.

The flow field is uniform in the z direction and so the sectional stream function ψ is introduced as

$$u=\frac{1}{1+\delta x}\frac{\partial\psi}{\partial y},\quad v=-\frac{1}{1+\delta x}\frac{\partial\psi}{\partial x}. \tag{1}$$

Now, a new coordinate variable y' is introduced in the y direction as $y=ay'$, where $a=h/d$ is the aspect ratio of the duct cross section. In the present case, $a=2$. From now on y denotes y' for the sake of simplicity. Then the basic equations for the axial velocity *w*, the stream function ψ and the temperature T are derived from the Navier-Stokes equations and the energy equation under the *Boussinesq approximation* as,

$$(1+\delta x)\frac{\partial w}{\partial t}+\frac{1}{a}\frac{\partial(w,\psi)}{\partial(x,y)}+\frac{\delta^2 w}{1+\delta x}-Dn=(1+\delta x)\Delta_2 w-\frac{1}{a}\frac{\delta}{(1+\delta x)}\frac{\partial\psi}{\partial y}w+\delta\frac{\partial w}{\partial x}-\delta Tr\frac{\partial\psi}{\partial y} \tag{2}$$

$$\begin{aligned}\left(\Delta_2-\frac{\delta}{1+\delta x}\frac{\partial}{\partial x}\right)\frac{\partial\psi}{\partial t}&=-\frac{1}{a}\frac{1}{(1+\delta x)}\frac{\partial(\Delta_2\psi,\psi)}{\partial(x,y)}+\frac{1}{a}\frac{\delta}{\left(1+\delta x\right)^2}\times\left[\frac{\partial\psi}{\partial y}\left(2\Delta_2\psi-\frac{3\delta}{1+\delta x}\frac{\partial\psi}{\partial x}+\frac{\partial^2\psi}{\partial x^2}\right)\right.\\&\left.-\frac{\partial\psi}{\partial x}\frac{\partial^2\psi}{\partial x\partial y}\right]+\frac{\delta}{\left(1+\delta x\right)^2}\times\left[3\delta\frac{\partial^2\psi}{\partial x^2}-\frac{3\delta^2}{1+\delta x}\frac{\partial\psi}{\partial x}\right]-\frac{2\delta}{1+\delta x}\frac{\partial}{\partial x}\Delta_2\psi+\frac{1}{a}w\frac{\partial w}{\partial y}+\Delta_2^2\psi\\&-Gr(1+\delta x)\frac{\partial T}{\partial x}-\frac{1}{2}Tr\frac{\partial w}{\partial y},\end{aligned} \tag{3}$$

$$\frac{\partial T}{\partial t}+\frac{1}{(1+\delta x)}\frac{\partial(T,\psi)}{\partial(x,y)}=\frac{1}{\Pr}\left(\Delta_2 T+\frac{\delta}{1+\delta x}\frac{\partial T}{\partial x}\right) \tag{4}$$

The non-dimensional parameters Dn , the Dean number, Tr , the Taylor number, *Gr*, the Grashof number and *Pr*, the Prandtl number, which appear in equations (2) to (4) are defined as:

$$Dn = \frac{Gl^3}{\mu\upsilon}\sqrt{\frac{2l}{L}}\ , \quad Tr = \frac{2\sqrt{2\delta}\Omega_T l^3}{\upsilon\delta}\ , \ Gr = \frac{\beta g \Delta T l^3}{\upsilon^2}, \quad \Pr = \frac{\upsilon}{\kappa} \tag{5}$$

In the present study, Dn and Tr are varied while Gr, a, δ and $\Pr$ are fixed as $Gr = 500$, $a = 2$, $\delta = 0.5$ and $\Pr = 0.71$ The rigid boundary conditions for w and ψ are used as

$$w(\pm 1, y) = w(x, \pm 1) = \psi(\pm 1, y) = \psi(x, \pm 1) = \frac{\partial \psi}{\partial x}(\pm 1, y) = \frac{\partial \psi}{\partial y}(x, \pm 1) = 0 \tag{6}$$

and the temperature T is assumed to be constant on the walls as

$$T(1, y) = 1, \quad T(-1, y) = -1, \ T(x, \ \pm 1) = x \tag{7}$$

3. Numerical Methods

In order to solve the Equations (2) to (4) numerically, the spectral method is used. By this method the expansion functions $\phi_n(x)$ and $\psi_n(x)$ are expressed as

$$\left.\begin{aligned} \phi_n(x) &= (1 - x^2)\, C_n(x), \\ \psi_n(x) &= (1 - x^2)^2 C_n(x) \end{aligned}\right\} \tag{8}$$

where $C_n(x) = \cos\left(n \cos^{-1}(x)\right)$ is the n^{th} order Chebyshev polynomial. $w(x, y, t)$, $\psi(x, y, t)$ and $T(x, y, t)$ are expanded in terms of the expansion functions $\phi_n(x)$ and $\psi_n(x)$ as

$$\left.\begin{aligned} w(x, y, t) &= \sum_{m=0}^{M} \sum_{n=0}^{N} w_{mn}(t)\, \varphi_m(x)\, \varphi_n(y) \\ \psi(x, y, t) &= \sum_{m=0}^{M} \sum_{n=0}^{N} \psi_{mn}(t)\, \psi_m(x)\, \psi_n(y). \\ T(x,, y, t) &= \sum_{m=0}^{M} \sum_{n=0}^{N} T_{mn}\, \varphi_m(x)\, \varphi_n(y) + x \end{aligned}\right\} \tag{9}$$

where M and N are the truncation numbers in the x and y directions respectively. Five types of grid sizes were used to check the dependence of grid size. The grid sizes are taken as 14×28, 16×32, 18×36, 20×40, 22×44, and it is found that $M = 16$ and $N = 32$ give sufficient accuracy of the numerical solutions, which are not shown here for brevity. In order to calculate the unsteady solutions, the Crank-Nicolson and Adams-Bashforth methods together with the function expansion (9) and the collocation methods are applied to Eqs. (2) to (4).

4. Resistance coefficient

We use the resistance coefficient λ as one of the representative quantities of the flow state. It is also called the *hydraulic resistance coefficient*, and is generally used in fluids engineering, defined as

$$\frac{P_1^* - P_2^*}{\Delta z^*} = \frac{\lambda}{dh^*} \frac{1}{2} \rho \left\langle w^* \right\rangle^2, \tag{10}$$

where quantities with an asterisk denote the dimensional ones, $\langle\,\rangle$ stands for the mean over the cross section of the rectangular duct. Since $\left(P_1^* - P_2^*\right) / \Delta z^* = G$, λ is related to the mean non-dimensional axial velocity $\langle w \rangle$ as

$$\lambda = \frac{16\sqrt{2\delta}Dn}{3\langle w \rangle^2}, \tag{11}$$

where $\langle w \rangle = \sqrt{2\delta}d / v \left\langle w^* \right\rangle$. In this paper, λ is used to calculate the unsteady solutions by numerical computations.

5. Results and Discussion

We take a curved rectangular duct of aspect ratio 2 and curvature $\delta = 0.1$ and rotate it around the centre of curvature with an angular velocity Ω_T in the positive direction for two cases of the duct rotation, *Case I*: *Dn* = 500 and *Case II*: *Dn* = 1000.

5.1 Case I: Dean Number, Dn=500

For positive rotation we perform time evolution of λ for $0 \le Tr \le 2000$ and $100 \le Dn \le 1000$. Figure 2(a) shows time evolution of λ for *Tr* = 100 and *Dn* = 500 at *Gr* = 500. It is found that the unsteady flow at Tr = 100 is a chaotic solution, which is well justified by drawing the phase spaces as shown in Fig. 2(b). Figure 2(c) shows typical contours of secondary flow patterns and temperature profiles for Tr = 100 and Dn = 500, where we find that the unsteady flow is a two and four-vortex solution. This is caused by the combined action of the Coriolis force and centrifugal force, which increased the number of secondary vortices (Wang and Cheng [5]). To draw the contours of secondary flow (ψ), axial flow (*w*) and temperature profiles (*T*), we use the increments $\Delta\psi = 0.6$, $\Delta w = 12$ and $\Delta T = 0.2$, respectively. In the figures of the secondary flows, solid lines ($\psi \ge 0$) show that the secondary flow is in the counter clockwise direction while the dotted lines $(\psi < 0)$ in the clockwise direction. Similarly in the figures of the temperature field, solid lines are those for $T \ge 0$ and dotted ones for *T*< 0.

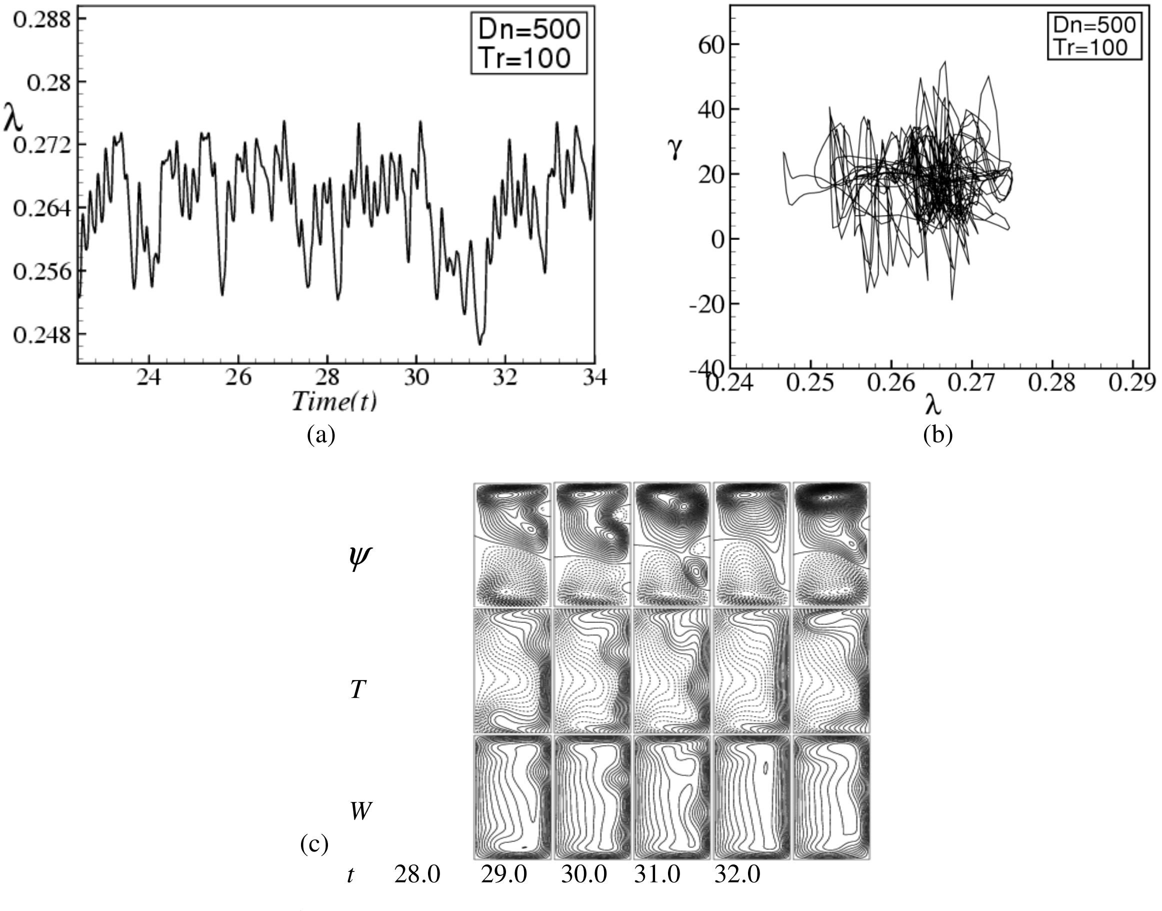

(a) (b)

(c)

Fig. 2. (a) Time evolution of λ for Dn = 500 and Tr = 100. (b) Phase space for Tr =100, (c) Contours of secondary flow patterns (top) temperature profiles (middle) and axial (bottom) for Tr = 100 at time $28.0 \le t \le 32.0$.

We performed time evolution of λ for *Tr* = 500 as shown in Fig. 3(a). It is found that the unsteady flow is a weak chaotic solution. In order to observe the chaotic oscillation more clearly, we draw the phase space of the time evolution result as shown in Fig. 3(b), and it is found that the flow oscillates in the irregular pattern, which confirms that the flow is chaotic. Typical contours of secondary flow patterns and temperature profiles are shown in Fig. 3(c), and we see that the unsteady flow is a two and four-vortex solution. Then we perform time evolution of λ for Tr = 555 as shown in Fig. 4(a). It is found that the unsteady flow at Tr = 555 is a multi-periodic solution, which is well justified by drawing the phase space as shown in Fig. 4(b). As seen in Fig. 4(b), the flow creates multiple orbits in its path, so that the unsteady flow at Tr = 555 is a multi-periodic solution. Typical contours of secondary flow patterns and temperature profiles for the corresponding flow parameters are shown in Fig. 4(c), where it is found that the multi-periodic oscillation at Tr = 555 is a two-vortex solution. Then we perform time evolution of λ for Tr = 557 as shown in Fig. 5(a). It is found that the unsteady flow at Tr = 557 is a multi-periodic solution, which is well justified by drawing the phase space as shown in Fig. 5(b). As seen in Fig. 5(b), the flow creates single orbits in its path, so that the unsteady flow at Tr = 557 is a periodic solution. Typical contours of secondary flow patterns and temperature profiles for the corresponding flow parameters are shown in Fig. 5(c), where it is found that the multi-periodic oscillation at Tr = 557 is a two-vortex solution. If the rotational speed increases more in the positive direction, for example Tr = 558 up to 2000, it is found that the flow becomes steady-state.

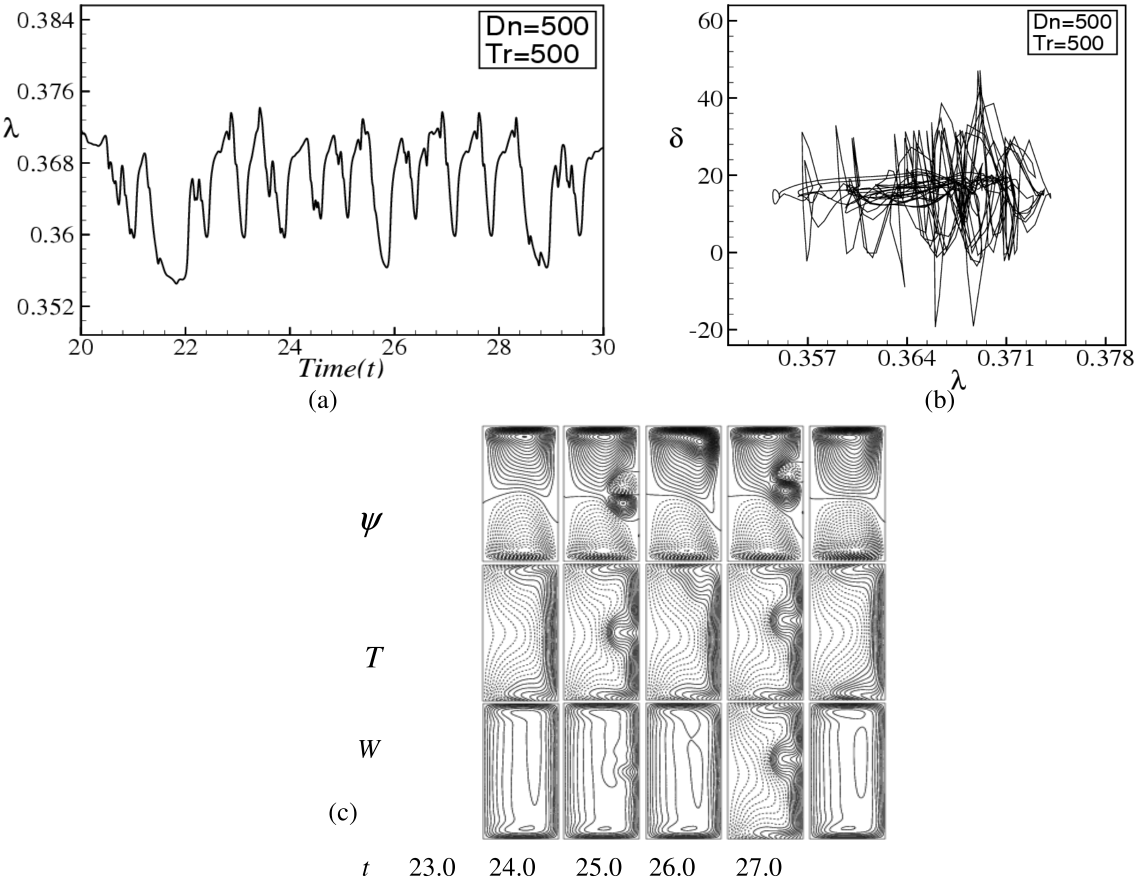

Fig. 3. (a) Time evolution of λ for Dn = 500 and Tr = 500. (b) Phase space for Tr =500, (c) Contours of secondary flow patterns (top) temperature profiles (middle) and axial (bottom) for Tr = 500 at time $23.0 \le t \le 27.0$

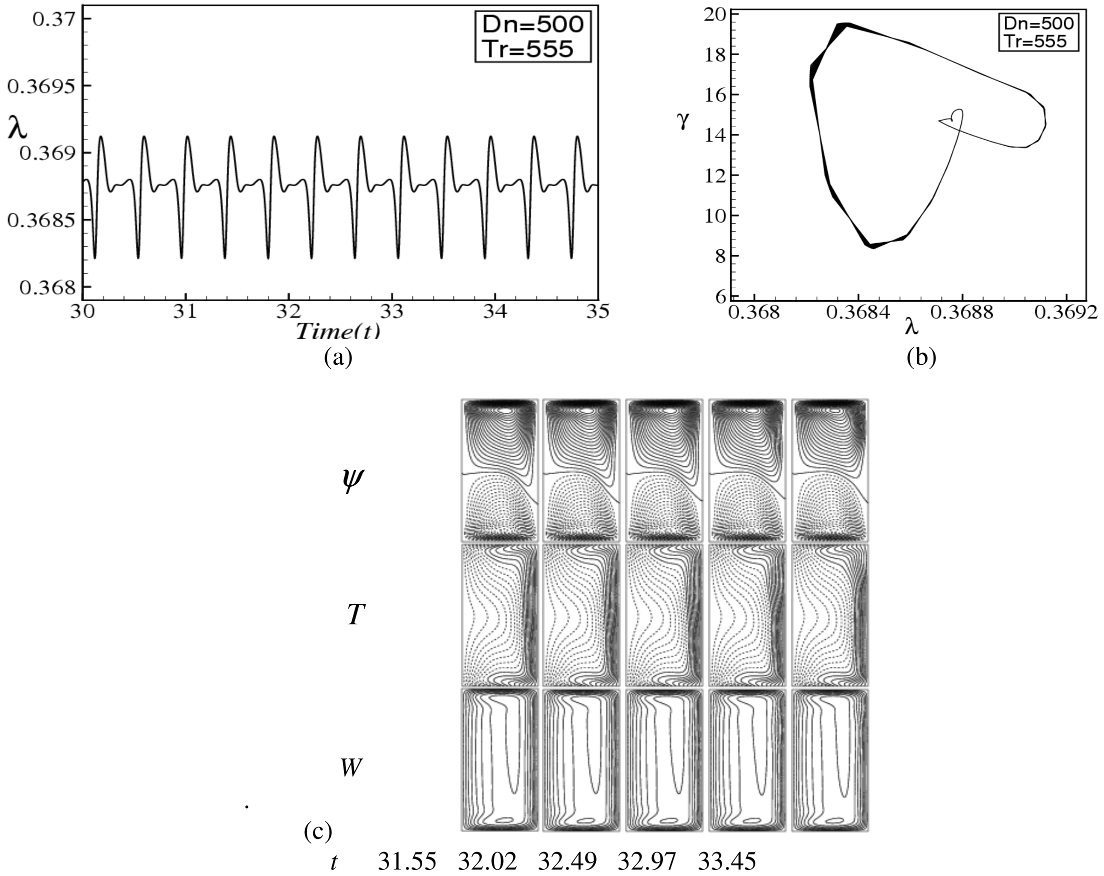

(a) (b) (c)

Fig. 4. (a) Time evolution of λ for Dn = 500 and Tr = 555. (b) Phase space for Tr = 555, (c) Contours of secondary flow patterns (top) temperature profiles (middle) and axial (bottom) for Tr = 555 at time $31.55 \le t \le 33.45$.

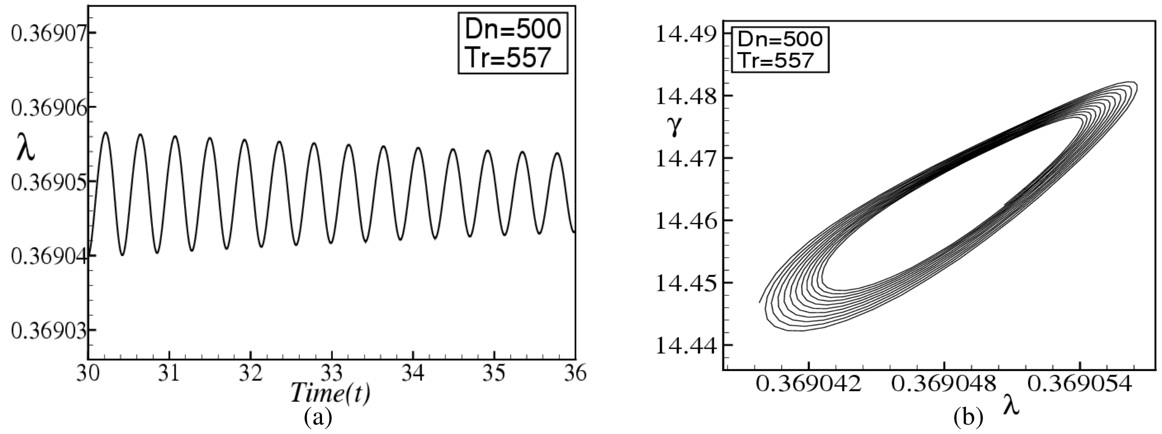

(a) (b)

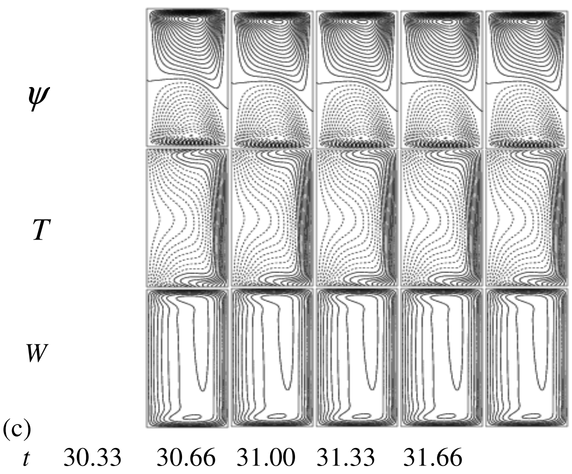

Fig. 5. (a) Time evolution of λ for Dn = 500 and Tr = 557. (b) Phase space for Tr = 557, (c) Contours of secondary flow patterns (top) temperature profiles (middle) and axial (bottom) for Tr = 557 at time $30.55 \le t \le 31.66$.

5.2 Case II: Dean Number, Dn=1000

We perform time evolution of λ for $0 \le Tr \le 2000$ and $Dn = 1000$ for $\delta = 0.5$. Figure 6(a) shows time evolution of λ for Dn = 1000 and Tr = 100 at Gr = 500. It is found that the unsteady flow at Tr = 100 is a strongly chaotic solution, which is well justified by drawing the phase spaces as shown in Fig. 6(b). Figure 6(c) shows typical contours of secondary flow patterns and temperature profiles for Tr = 100, where we find that the unsteady flow is a six-vortex solution. Then we perform time evolution of λ for Tr = 1500 and presented in Fig. 7(a). It is found that the unsteady flow is multi-periodic oscillation for Tr = 1500. The multi-periodic oscillation is well justified by depicting the phase space as shown in Fig. 8(b) for Tr = 1500. In Fig. 7(b) the multi-periodic orbits of the time evolution solutions are seen, which proves that the oscillation presented in Fig. 7(b) is multi-periodic. Typical contours of secondary flow patterns and temperature profiles are shown in Fig. 7(c) for Tr = 1500 and it is found that the multi-periodic solution is a four-vortex solution. If the rotational speed is increased more, for example Tr = 1560 or more, it is found that the flow becomes periodic first and then turns into steady-state. Figure 8(a) shows time evolution of λ for Tr = 1565 and Dn = 1000, and it is found that the flow is steady-state. Since the flow is steady-state, a single contour of secondary flow pattern and temperature profile is shown in Fig. 8(b) for Tr = 1665 and Dn = 1000, and it is found that the unsteady flow for Tr = 1565 and Dn = 1000 is an asymmetric two-vortex solution. In this study, it is found that combined action of the coriolis and centrifugal force help to increase the number of secondary vortices. It is also found that, as the flow becomes chaotic, the secondary flow increases and gets stronger and consequently heat is transferred substantially.

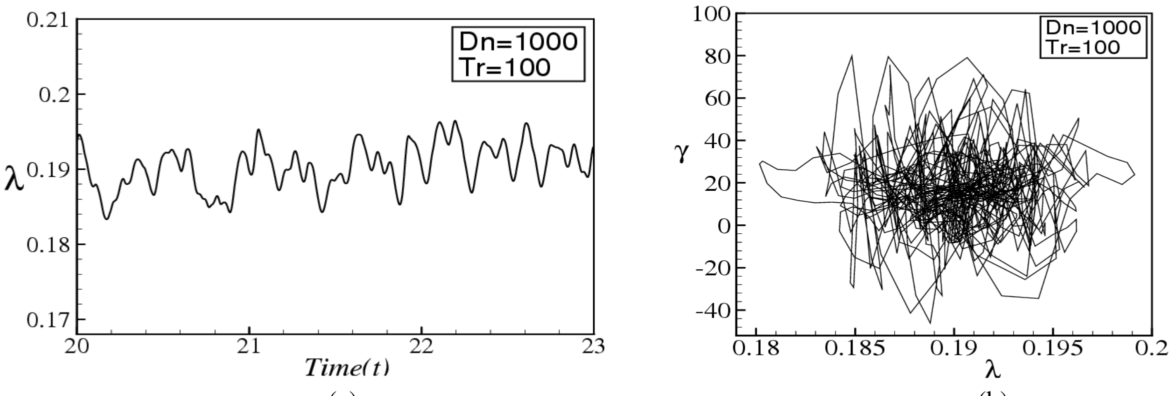

(a) (b)

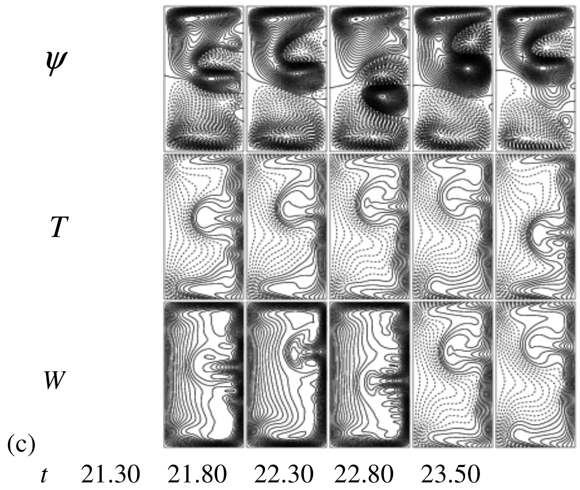

Figure 6: (a) Time evolution of λ for Tr = 100 and Dn = 1000 at Gr = 500. (b) Phase space for Tr = 100. (c) Contours of secondary flow patterns (top) temperature profiles (middle) and axial (bottom) for Tr = 100.

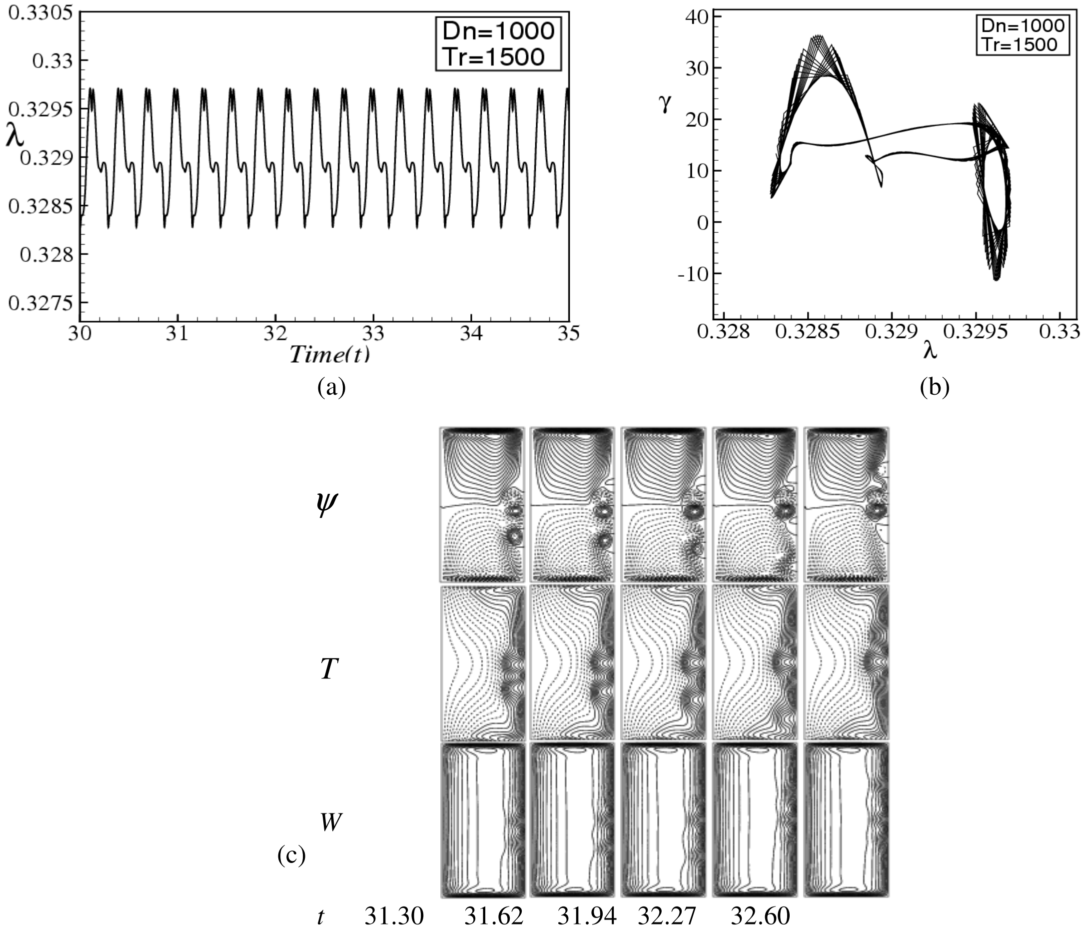

Fig. 7. (a) Time evolution of λ for Tr = 1500 and Dn = 1000 at Gr = 500. (b) Phase space for Tr = 1500. (c) Contours of secondary flow patterns (top) temperature profiles (middle) and axial (bottom) for Tr = 1500.

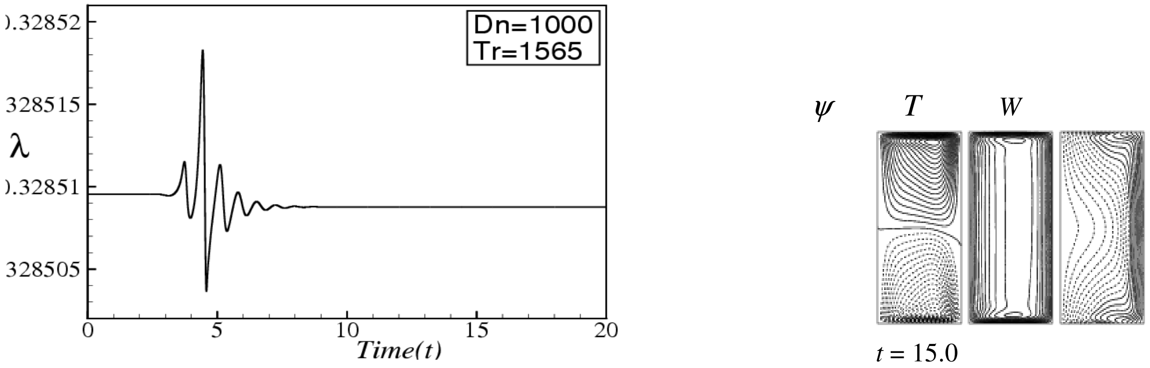

(a) (b)

Fig. 8. (a) Time evolution of λ for Dn = 1000 and Tr = 1565. (b) Contours of secondary flow patterns (left) temperature profiles (middle) and axial (right) for Tr = 1565 at time $t = 15.0$

6. Conclusion

A numerical study is presented for the flow characteristics through a rotating curved rectangular duct of aspect ratio 2 and curvature $\delta = 0.5$. Numerical calculations are carried out by using a spectral method, and covering a wide range of the Taylor number $0 \le Tr \le 2000$ for the Dean numbers, Dn = 500 and Dn = 1000 for the Grashof number $Gr = 500$. We investigated unsteady flow characteristics for the positive rotation of the duct by time evolution calculations, and it is found that the unsteady flow undergoes in the scenario '*Chaotic* ⟶ *multi-periodic* ⟶ *periodic* ⟶ *steady-state*', if *Tr* is increased in the positive direction. Phase spaces were found to be fruitful to justify the transition of unsteady flow characteristics. Typical contours of secondary flow patterns and temperature profiles are also obtained at several values of *Tr*, and it is found that there exist two-, four- and six- vortex solutions if the duct rotation involved in the positive direction. It is found that the temperature distribution is consistent with the secondary vortices, and convective heat transfer is enhanced as the secondary vortices increase. It is also found that chaotic flow enhances heat transfer more significantly than the periodic or steady-state solutions.

References

[1] Nandakumar, K. and Masliyah, J. H. (1986). Swirling Flow and Heat Transfer in Coiled and Twisted Pipes, *Adv. Transport Process.*, Vol. **4**, pp. 49-112.

[2] Ito, H (1987). Flow in curved pipes. *JSME International Journal*, **30**, 543–552.

[3] Yanase, S., Kaga, Y. and Daikai, R. (2002). Laminar flow through a curved rectangular duct over a wide range of the aspect ratio, *Fluid Dynamics Research*, Vol. **31,** pp. 151-183.

[4] Selmi, M. and Namdakumar, K. and Finlay W. H., 1994. A bifurcation study of viscous flow through a rotating curved duct, *J. Fluid Mech.* Vol. **262**, pp. 353-375.

[5] Wang, L. Q. and Cheng, K.C., 1996. Flow Transitions and combined Free and Forced Convective Heat Transfer in Rotating Curved Channels: the Case of Positive Rotation *Physics of Fluids*, Vol. **8**, pp.1553-1573.

[6] Selmi, M. and Namdakumar, K. (1999). Bifurcation Study of the Flow through Rotating Curved Ducts, *Physics of Fluids*, Vol. **11**, pp. 2030-2043.

[7] Yamamoto, K., Yanase, S. and Alam, M. M. (1999). Flow through a Rotating Curved Duct with Square Cross-section, *J. Phys. Soc*. Japan, Vol. **68**, pp. 1173-1184.

[8] Mondal, R. N., Alam M. M. and Yanase, S. (2007). Numerical prediction of non- isothermal flows through a rotating curved duct with square cross section, *Thommasat Int. J. Sci and Tech.*, Vol. **12**, No. 3, pp. 24-43.

[9] Mondal, R. N., Datta, A. K. and Uddin, M. S. (2012). A Bifurcation Study of Laminar Thermal Flow through a Rotating Curved Duct with Square Cross-section, *Int. J. Appl. Mech. and Engg.* Vol. **17** (2). (In Press).

Available online at www.sciencedirect.com

ScienceDirect

Procedia Engineering 00 (2015) 000–000

Procedia Engineering

www.elsevier.com/locate/procedia

6th BSME International Conference on Thermal Engineering (ICTE 2014)

Effects of geometric parameters on the flow characteristics for turbulent flow in a wavy finned-tube heat exchanger: CFD modeling

Arafat A. Bhuiyan[1,3,]*, M.Ruhul Amin[2] and A K M Sadrul Islam[3]

[1]*Faculty of Science, Engineering and Technology, Swinburne University of Technology, VIC-3122, Australia.*
[2]*Department of Mechanical Engineering, Montana State University, Bozeman, Montana,MT 59717-3800, USA*
[3]*Department of Mechanical Engineering, Islamic University of Technology (IUT), Gazipur-1704, Bangladesh.*

Abstract

In this study, the effects of thermal and hydraulic characteristics of wavy fin and tube heat exchanger are investigated. Simulation has been carried out by a commercial computational fluid dynamics code, ANSYS CFX12.0. The main objective of this study is to investigate the flow characteristics in turbulent flow. Results are predicted for the turbulent flow regime ($2100 \leq Re \leq 7000$) and compared with author's previous work for laminar ($400 \leq Re \leq 1200$) and transitional ($1300 \leq Re \leq 2000$) flow regime. Regarding turbulence, the k-ω model was used to predict the turbulent flow characteristics with 5% turbulence intensity. Predicted results were compared with the experimental data for the purpose of validation and the discrepancy is found within 10% in error range. Parametric study was conducted for different pitches and wavy angles. Flow characteristics obtained for the turbulent range is in line with the pattern observed in laminar and transitional ranges. This study demonstrates a clear understanding and relationship of among different flow ranges and the effects of different geometric parameters on the performance of heat exchanger.

Peer-review under responsibility of organizing committee of the 6th BSME International Conference on Thermal Engineering (ICTE 2014).

Keywords: Wavy fin tube heat exchanger, CFD modelling, Friction factor, Colburn factor, Efficiency index, Reynolds number.

---

1. Introduction

Finned-tube heat exchangers have been extensively used in several automotive applications for various purposes as a kind of compact heat exchanger. The performance of this type of heat exchanger is normally dominated by the thermal resistance [1-3]. The fin geometry has become as increasingly important factor in the design of a plate-and-

---

Corresponding author. Tel.: +88029291254-59; fax: +88029291260.
E-mail address: arafat@iut-dhaka.edu

Peer-review under responsibility of organizing committee of the 6th BSME International Conference on Thermal Engineering (ICTE 2014).

fin heat exchanger. Typical extended surfaces used for the plate-and-fin heat exchangers are: plain, wavy, offset strip, louvered, perforated and multi-louvered fin have been developed to minimize the thermal resistance [2, 3]. T The wavy fin extended surfaces are recognized by the wavy corrugations which boost the heat transfer performance in contrast to the plain plate surfaces. In last decades, several efforts have been devoted to investigate the fundamentals and performance related issues in different experimental works [1, 4-11]. Also few numerical attempts have been accomplished in 2D and 3D analysis [12-22]. But most of the earlier works are limited to laminar to transitional ranges. In this study, simulation results for wavy fin considering different tube arrangements for turbulent flow range will be investigated. This numerical study is a continuation of the author's previous work for laminar flow[16] and transitional flow [17] to show the thermal and hydraulic performance of different flow ranges. Overall, a comprehensive parametric study considering longitudinal (Ll) [23], transverse (Lt) [16-19, 23], fin pitch (Fp) [16-19] and wavy angle (Wa) [13, 17] has been carried out for staggered tube arrangement in a typical wavy heat exchanger using a commercial computational fluid dynamics code ANSYS CFX 12.0 [18, 24].

2. Model description and methodology

2.1. Physical and operating conditions of the heat exchanger

The computational domain and the coordinate system are shown in figure 1 for the two configurations such as wavy fin staggered configuration (left) and Wavy fin In-lined configuration (right). The dashed line in the figure designates the computational domain. Assuming symmetry condition on the mid plane between the two fins, the bottom and the top boundaries simulate the fin and the mid-plane respectively. The nomenclatures used for the present computation and the parametric study are shown in the middle of the figure 1. The detailed specifications of the selected heat exchanger is taken from the experimental work of Wang [1]. The boundary conditions of the present study are described in the author's previous work [14-19]. Based on the Reynolds number (Re), at upstream boundary, uniform flow with constant velocity and constant temperature are assumed; but at downstream, Neumann boundary condition is applied. At symmetric wall, no-slip boundary condition is used with constant wall temperature. In this study, turbulent flow is considered having Reynolds number in the range of $2100 \leq Re_H \leq 7000$. For parametric study, three different cases are considered as of previous [16-19] for different parameters and given in Table 1.

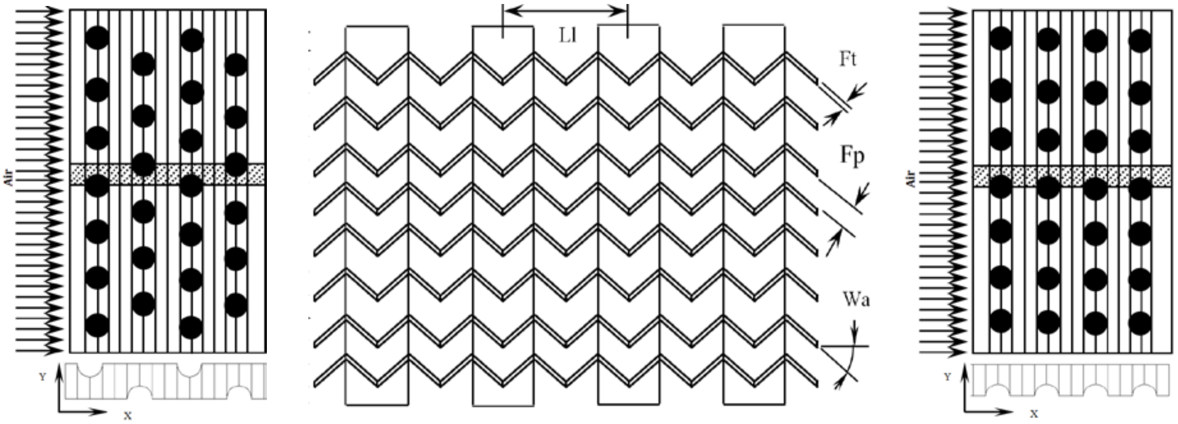

Figure 1: Computational domain and co-ordinate system: staggered arrangement (left), in-lined arrangement (right), nomenclatures (middle)

Table 1. Cases considered for parametric study in turbulent flow condition.

Parameter	Case-I	Case-II	Case-III
Longitudinal pitch (Ll)	19.050 mm	28.575 mm	38.100 mm
Transverse pitch (Lt)	25.400 mm	30.400 mm	35.400 mm
Fin pitch (Fp)	3.53 mm	2.53 mm	1.53 mm
Wavy angle (Wa)	8°	17°	35°

2.2. Numerical descriptions

The numerical simulations of the fin-tube heat exchanger were conducted for turbulent ($2100 \leq Re_H \leq 7000$) case. 3D Navier-Stokes equations [25] were considered for the simulation of flow and heat transfer and energy equation for steady incompressible fluid with constant properties. Details mathematical formulation is documented in author's previous work [14-18, 26]. Details of the used k-ω turbulent models are documented in literature [27-30]. Regarding convergence, a typical range of $1e^{-4}$ is set with minimum iteration of 1000. A comprehensive grid independency test is carried out and 549669 nodes with 1355049 elements are chosen for this study.

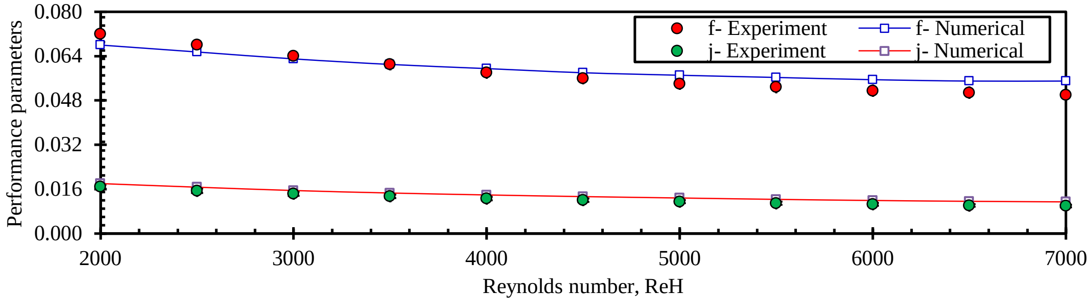

Figure 2: Comparison of numerical prediction with the experimental data [1] for (a). Friction factor (f) and (b). Colburn factor

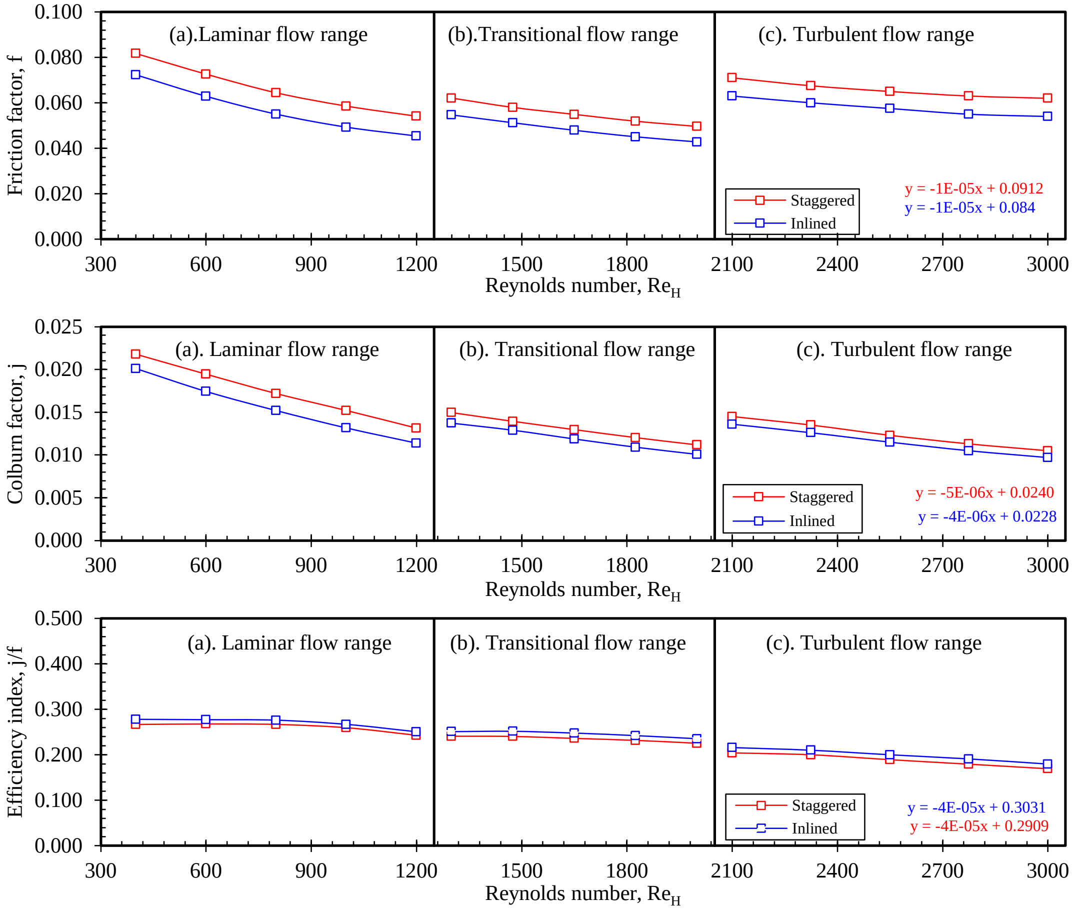

Figure 3: Flow characteristics for different tube arrangement in (c). Turbulent flow range (2100<Re<3000) compared with the published (a). laminar flow range (400<Re<1200) in [16] and (b). transitional flow range (1300<Re<2000) in [17]

3. Results and discussion

The main objective of this study is to predict the heat transfer and pressure drop performance in wavy fin and tube heat exchanger in turbulent flow regimes. In order to achieve the confidence in modeling, this CFD code was validated comparing the available experimental data from Wang [1] with the predicted friction factor and colburn factor in turbulent range for wavy staggered tube arrangement. Figure 2 shows the comparison of numerical prediction with the experimental data [1]. It is found that the numerical results fall within 10% of the experimental data. This numerical study is mainly concentrated in determination of flow characteristics in turbulent flow range and to compare the performance trend with the laminar and transitional flow range published in author’s previous work. Also the effects of different geometric parameters such as longitudinal pitch, transverse pitch, fin pitch and wavy angle have been explored. Though turbulent flow range covers Re up to 7000 in this study, but results are presented up-to 3000 comparing with others flow ranges in this paper. In [16] and [17], laminar and k-ω turbulent model were used for laminar and transitional flow. As of [26], k-ω turbulent model is employed for turbulent flow modeling.

Figure 3 represents the flow characteristics for different tube arrangements in turbulent flow range compared with the laminar and transitional flow ranges. There is a definite variation of staggered and in-lined tube arrangement presented here. The possible reasons and explanations of these variations are described in more details in [16-19]. Comparatively higher heat transfer and pressured drop is observed in all flow ranges in staggered case. Though f and j both are lower in in-lined arrangement but higher efficiency is found in in-lined case. Due to page limitations of the paper, the geometric variations are presented only for the staggered conditions but similar trend is observed for in-lined case.

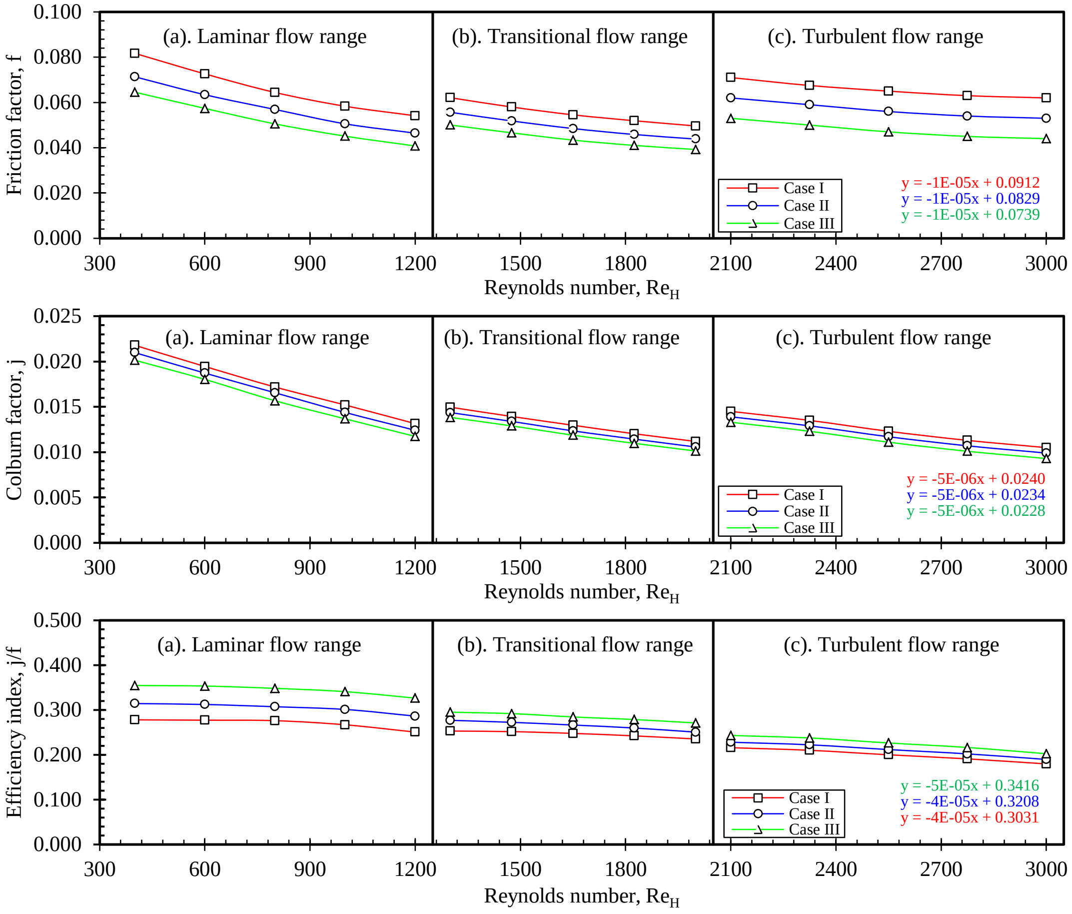

Figure 4: Flow characteristics for the variation of different longitudinal pitches (Ll) for staggered tube arrangement in (c). Turbulent flow range (2100<Re<3000) compared with the published (a). laminar flow range (400<Re<1200)[16] (b). transitional flow range (1300<Re<200)[17]

Flow characteristics for the variation of different longitudinal tube pitch (Ll) such as 19.05 mm, 28.575 mm and 38.10 mm in turbulent flow range are presented in figure 4. Also the comparisons with the laminar and transitional range are critically evaluated. It is found that with the increase of Ll, friction factor (f) and Colburn factor (j) decrease, but efficiency index increases. With the increase of Ll from 19.05 mm to 28.575 mm and 28.575 mm to 38.10 mm, f increases 19.54% and 15.84% while j increases 4.83% and 5.07% respectively in the turbulent range. But in laminar and transitional range, f increases 12.83% and 11.05% while j increases 4.20% and 4.55% respectively for the change of 19.05 mm to 28.575 mm. But for 28.575 mm to 38.10 mm pitch increase, f increase10.50% and 10.33%, while j changes 4.56% and 3.86% for laminar and transitional flow ranges respectively. Efficiency index increases 10% and 12% for the increase of Ll of 19.05mm to 28.575mm respectively. But it was seen previously that for laminar case this change was found as 9.74% and 6.67% while for transitional case, these change was observed as 7.3% and 7.2% respectively. While comparing the flow model, for laminar to transitional change, f increase 16.61% and 14.91% and 14.75% for the three longitudinal pitch cases respectively. But for the case of j, these changes are more significant. The change is around 25% in all cases. But for transitional to turbulent shift, f decrease 18.95%, 15.6% and 8.52 % for the selected case. But the change is nominal in these two flow changes.

Flow characteristics for the variation of different transverse pitches (Lt) for staggered tube arrangement in turbulent flow range (2100<Re<3000) compared with the published laminar flow range (400<Re<1200) [16] and transitional flow range (1300<Re<2000) [17] is presented in figure 5. For the increase of Lt from 25.4 mm to 30.4 mm, f increase 13.9%, 13.04% and 12.17% while j increase 5.1%, 5.8% and 5.63% for laminar, transitional and turbulent flow ranges respectively. For the increase of Lt from 30.4 mm to 35.4 mm, f increase 14.12%, 12.31% and

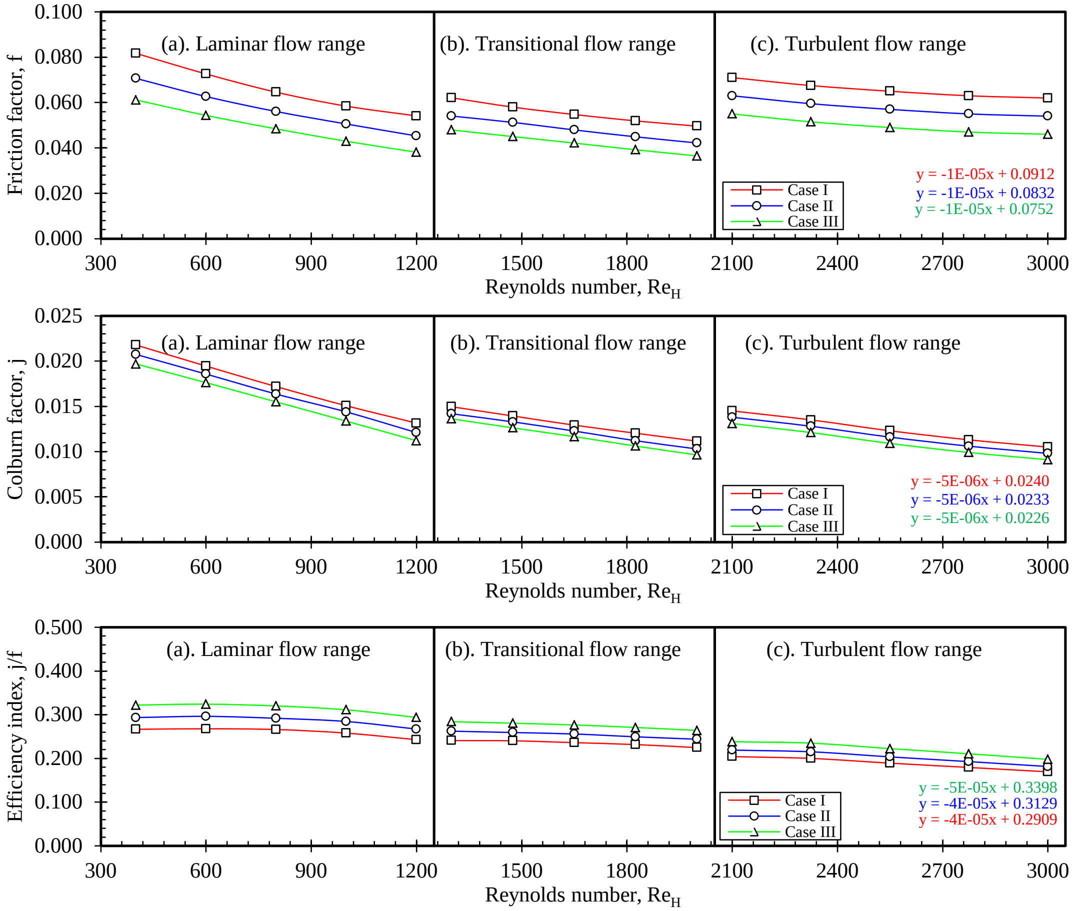

Figure 5: Flow characteristics for the variation of different transverse pitches (Lt) for staggered tube arrangement in (c). Turbulent flow range (2100<Re<3000) compared with the published (a). laminar flow range (400<Re<1200) [16] (b). transitional flow range (1300<Re<2000) [17]

13.86% while j increase 5.82%, 5.05% and 5.97% for laminar, transitional and turbulent flow ranges respectively. Though f and j increases with the increase of Lt, but j/f decrease. The decrease found as 10.12%, 8.28% and 7.39% for first set and 9.63%, 8.26% and 9.10% for the second set of Lt in the laminar, transitional and turbulent flow ranges respectively. While comparing the flow model, for laminar to transitional change, f increase 16.61%, 15.75% and 13.98 % for the three cases respectively. The value of j changes 24.97.5%, 25.47% and 24.86% respectively. While comparing laminar to transitional change, f decrease 18.86%, 20.04% and 17.93 % but the value of j changes 4.45%, 4.28% and 5.21% respectively.

Flow characteristics for the variation of different fin pitches (Fp) for staggered tube arrangement in turbulent flow range (2100<Re<3000) compared with the published laminar flow range (400<Re<1200) [16] and transitional flow range (1300<Re<2000) [17] is presented in figure 6. With the decrease of Fp, friction factor and Colburn factor both decreases but j/f increases. The behaviour is fully different with the characteristics found for Ll and Lt Cases. For the decrease of Fp from 3.53 mm to 2.53 mm, f decrease 17.07 %, 13.42 % and 12.17 % while j decrease 6.0 %, 6.59 % and 6.44 % for laminar, transitional and turbulent flow ranges respectively. For the decrease of Fp from 2.53 mm to 1.53 mm, f decrease16.50 %, 12.07 % and 13.86 % while j decrease 6.16%, 5.62% and 6.88% for laminar, transitional and turbulent flow ranges respectively. But j/f increase as 13.34 %, 7.85 % and 6.47 % for first set and 12.27%, 7.22% and 8.03% for second set in the laminar, transitional and turbulent flow ranges respectively. While comparing the flow model, for laminar to transitional change, f increase 16.55% and 12.87% and 8.20% for the three fin pitch cases respectively. The value of j changes 24.5%, 25.23% and 24.79% respectively. For transitional to turbulent shift, f decrease 18.86%, 20.57% and 18.05% for the three fin pitch cases respectively. The value of j changes 4.88%, 4.72 % and 5.99% respectively.

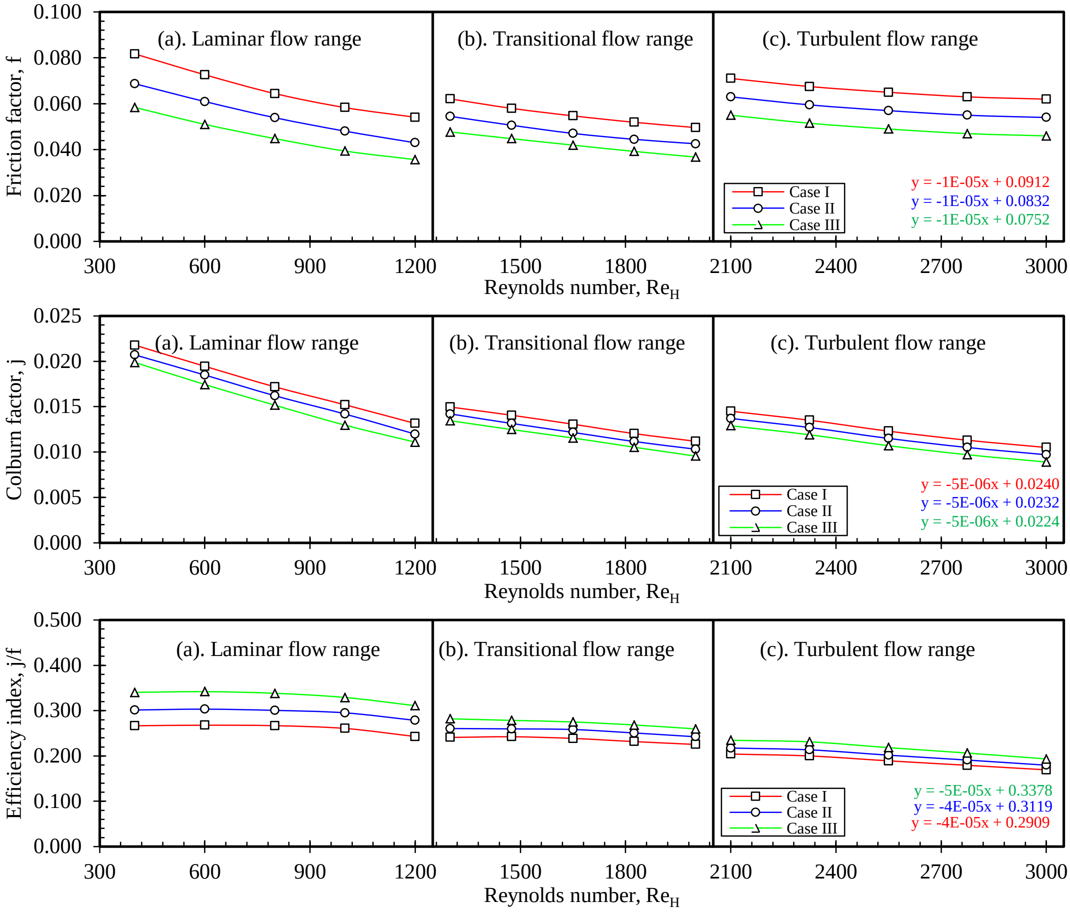

Figure 6: Flow characteristics for the variation of three different fin pitch (Fp) for staggered tube arrangement in (c). Turbulent flow range (2100<Re<3000) compared with the published (a). laminar flow range (400<Re<1200)[16], (b). transitional flow range (1300<Re<2000) [17].

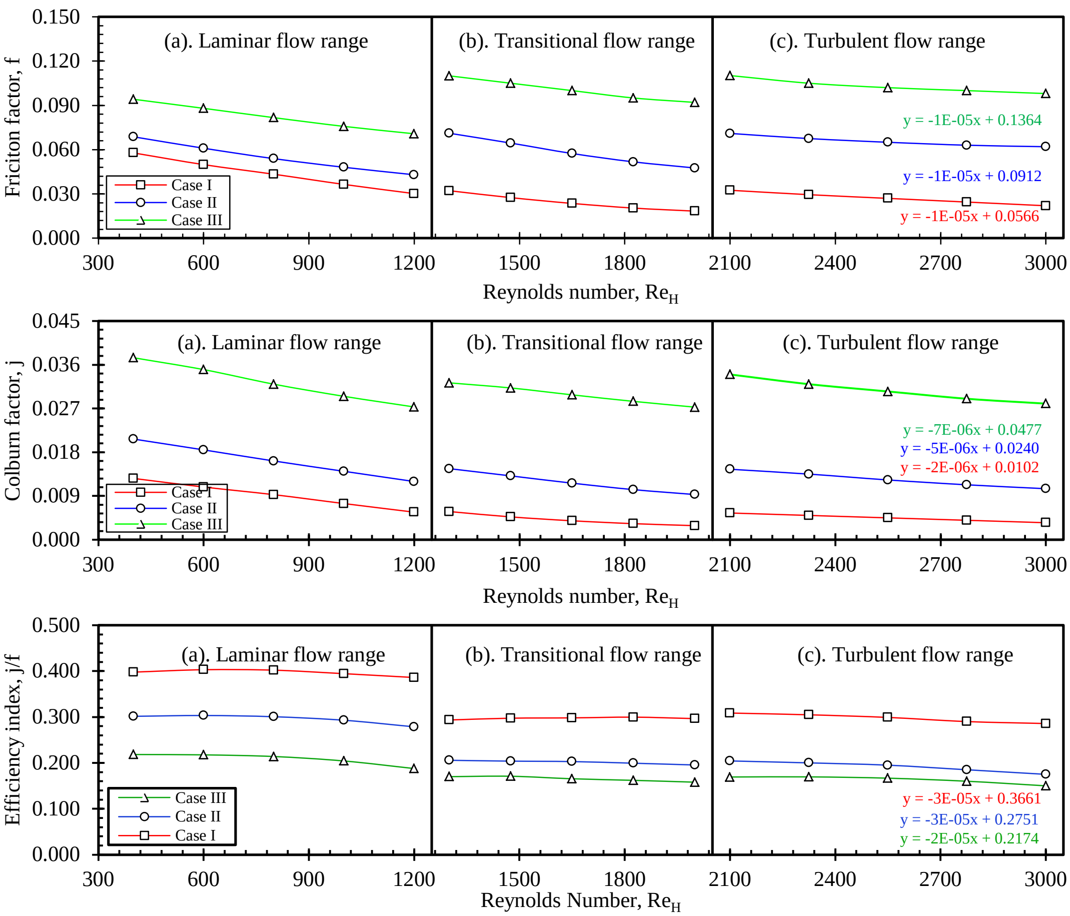

Figure 7: Flow characteristics for the variation of three different wavy angles (Wa) for staggered tube arrangement in (c). Turbulent flow range (2100<Re<3000) compared with the published (a). laminar flow range (400<Re<1200) [16], (b). transitional flow range (1300<Re<2000) [17].

Figure 7 shows the flow characteristics for the variation of three different wavy angles (Wa) for staggered tube arrangement in turbulent flow range (2100<Re<3000) compared with the published laminar flow range (400<Re<1200) [16] and transitional flow range (1300<Re<2000) [17]. It is found that with the increase of wavy angle, heat transfer and pressure drop increases drastically. But efficiency curves shows opposite trends. For the increase of Wa from 8° to 17.5° and 17.5° to 35°, heat transfer and pressure drop increases more than 50% in each cases. While comparing the flow model, for laminar to transitional change, f decreases 43.92% for wavy angle 8°, while for transitional to turbulent case, it increases 11.0%.

Conclusion

This numerical study has been conducted as a continuation of author's previous work considering wavy fin and tube heat exchanger for the modeling of heat transfer and pressure drop performance in different tube arrangements. Commercial CFD Code ANSYS CFX 12.0 is employed, coupled with user defined program. Code was validated with experimental results from literature and a reasonable matching has been observed. Simulated results were presented for turbulent flow range (2100<Re<7000) comparing previously published laminar (400<Re<1200) and transitional (1300<Re<2000) flow ranges. There is clear difference in the performance of staggered and in-lined tube arrangement. Comparatively better performance is observed in staggered case. Detailed parametric study is carried out considering important pitches and wavy angles. The trend observed in turbulent flow is in line with the laminar and transitional flows. But heat transfer, pressure drop and efficiency varies with the variation of these parameters. This parametric study provides a clear understanding and guideline for the design of similar type of heat exchanger depending upon requirements.

References

1. Wang, C., W. Fu, and C. Chang, Heat transfer and friction characteristics of typical wavy fin-and-tube heat exchangers. Experimental Thermal and Fluid Science, 1997. 14(2): p. 174-186.
2. Dong, J., et al., Experimental study on thermal–hydraulic performance of a wavy fin-and-flat tube aluminum heat exchanger. Applied Thermal Engineering, 2013. 51(1–2): p. 32-39.
3. Dong, J., et al., Experimental and numerical investigation of thermal -hydraulic performance in wavy fin-and-flat tube heat exchangers. Applied Thermal Engineering, 2010. 30(11–12): p. 1377-1386.
4. Wang, C.-C., Investigation of wavy fin-and-tube heat exchangers: A contribution to databank. Experimental Heat Transfer, 1999. 12(1): p. 73-89.
5. Du, X., et al., Experimental study on heat transfer enhancement of wavy finned flat tube with longitudinal vortex generators. Applied Thermal Engineering, 2013. 50(1): p. 55-62.
6. Kim, N.H., J.H. Youn, and R.L. Webb, Heat transfer and friction correlations for wavy plate fin-and-tube heat exchangers. American Society of Mechanical Engineers, Heat Transfer Division, (Publication) HTD, 1996. 330: p. 43-52.
7. Yan, W.M. and P.J. Sheen, Heat transfer and friction characteristics of fin-and-tube heat exchangers. International Journal of Heat and Mass Transfer, 2000. 43(9): p. 1651-1659.
8. Wang, C.C., Y.M. Hwang, and Y.T. Lin, Empirical correlations for heat transfer and flow friction characteristics of herringbone wavy fin-and-tube heat exchangers. International Journal of Refrigeration, 2002. 25(5): p. 673-680.
9. Wang, C.C., J.S. Liaw, and B.C. Yang, Airside performance of herringbone wavy fin-and-tube heat exchangers - Data with larger diameter tube. International Journal of Heat and Mass Transfer, 2011. 54(5-6): p. 1024-1029.
10. Pirompugd, W., S. Wongwises, and C.C. Wang, Simultaneous heat and mass transfer characteristics for wavy fin-and-tube heat exchangers under dehumidifying conditions. International Journal of Heat and Mass Transfer, 2006. 49(1-2): p. 132-143.
11. Kim, N.H., J.H. Ham, and J.P. Cho, Experimental investigation on the airside performance of fin-and-tube heat exchangers having herringbone wave fins and proposal of a new heat transfer and pressure drop correlation. Journal of Mechanical Science and Technology, 2008. 22(3): p. 545-555.
12. Gong, J., et al., Numerical simulation of flow and heat transfer characteristics in wavy fin-and-tube heat exchanger with combined longitudinal vortex generators. International Communications in Heat and Mass Transfer, 2013. 43: p. 53-56.
13. Glazar, V., A. Trp, and K. Lenic, Numerical Study of Heat Transfer and Analysis of Optimal Fin Pitch in a Wavy Fin-and-Tube Heat Exchanger. Heat Transfer Engineering, 2012. 33(2): p. 88-96.
14. Bhuiyan, A.A., Islam, A K M Sadrul. A numerical investigation on heat transfer and pressure drop performance of typical wavy fin-and-tube heat exchanger. in The 7th Jordanian International Mechanical Engineering Conference (JIMEC'7). 2010.
15. Bhuiyan, A.A., R. Zaman, and A.S. Islam. Numerical Analysis of Thermal and Hydraulic Performance of Fin and Tube Heat Exchangers. in 13th Asian Congress of Fluid Mechanics (13ACFM). 2010. Bangladesh Society of Mechanical Engineers(BSME).
16. Bhuiyan, A.A., A.S. Islam, and M.R. Amin, Numerical Prediction of Laminar Characteristics of Fluid Flow and Heat Transfer in Finned-Tube Heat Exchangers. Innovative Systems Design and Engineering, 2011. 2(6): p. 1-12.
17. Bhuiyan, A., A. Islam, and M. Amin, Numerical study of 3D thermal and hydraulic characteristics of wavy fin-and-tube heat exchanger. Frontiers in Heat and Mass Transfer (FHMT), 2012. 3(3).
18. Bhuiyan, A.A., M.R. Amin, and A. Islam, Three-dimensional performance analysis of plain fin tube heat exchangers in transitional regime. Applied Thermal Engineering, 2012.
19. Bhuiyan, A.A., Karim, Md.Rezwanul, Amin, M Ruhul, Islam, AKM, Plate fin and tube heat exchanger modeling: Effects of performance parameters for turbulent flow regime. International Journal of Automotive and Mechanical Engineering (IJAME), 2014. 9: p. 1768-1781.
20. Tao, Y.B., et al., Numerical design of an efficient wavy fin surface based on the local heat transfer coefficient study. Journal of Enhanced Heat Transfer, 2007. 14(4): p. 315-332.
21. Tao, Y.B., et al., Three-dimensional numerical study of wavy fin-and-tube heat exchangers and field synergy principle analysis. International Journal of Heat and Mass Transfer, 2007. 50(5-6): p. 1163-1175.
22. Jang, J.Y. and L.K. Chen, Numerical analysis of heat transfer and fluid flow in a three-dimensional wavy-fin and tube heat exchanger. International Journal of Heat and Mass Transfer, 1997. 40(16): p. 3981-3990.
23. Lu, C.-W., et al., A numerical investigation of the geometric effects on the performance of plate finned-tube heat exchanger. Energy Conversion and Management, 2011. 52(3): p. 1638-1643.
24. Aslam Bhutta, M.M., et al., CFD applications in various heat exchangers design: A review. Applied Thermal Engineering, 2012. 32: p. 1-12.
25. Sohr, H., The Navier-Stokes equations: An elementary functional analytic approach. 2012: Springer.
26. Bhuiyan, A.A., et al., Plate fin and tube heat exchanger modeling: Effects of performance parameters for turbulent flow regime. International Journal of Automotive and Mechanical Engineering, 2014. 9(1): p. 1768-1781.
27. Amin, M.R. and S.K. Ramachandran. Numerical Analysis of Airside Characteristics in Plain and Wavy Heat Exchangers in the Turbulent Flow Regime. in ASME 2011 International Mechanical Engineering Congress and Exposition. 2011. American Society of Mechanical Engineers.
28. Menter, F.R., Two-equation eddy-viscosity turbulence models for engineering applications. AIAA Journal, 1994. 32(8): p. 1598-1605.
29. Reddy, J.N. and D.K. Gartling, The finite element method in heat transfer and fluid dynamics. 2010: CRC press.
30. Yang, L.C., et al., Numerical Prediction of Transitional Characteristics of Flow and Heat Transfer in a Corrugated Duct. Journal of Heat Transfer, 1997. 119(1): p. 62-69.

ELSEVIER

Available online at www.sciencedirect.com

ScienceDirect

Procedia Engineering 00 (2015) 000–000

Procedia Engineering

www.elsevier.com/locate/procedia

6th BSME International Conference on Thermal Engineering (ICTE 2014)

Experimental investigation of transient heat transfer on a solid surface, with fire retardant fabric under hot air impinging jet

A.K.M. Nazrul Islam[a,] *, Md. Ashraful Islam[a], Manabendra Saha[b]

[a]*Department of Mechanical Engineering, Bangladesh University of Engineering and Technology, Dhaka-1000, Bangladesh*
[b]*Centre for Energy Technology, School of Mechanical Engineering, The University of Adelaide, SA 5005, Australia*

Abstract

This paper represents an experimental investigation of the transient heat transfer on a solid base plate (mimic to skin) covered by fire retardant fabric (Kevlar® 49), under hot air jet impingement. The study was carried out by a fabricated attachment with an axial flow wind tunnel for horizontal hot air jet impingement. The hot air jet was impinged on a vertical base plate at different velocities and temperatures. A set of experimental conditions was considered to understand the various heat transfer phenomenon. The hot air jet temperatures were 115 and 125 ^{o}C respectively and jet velocities were 12, 15, and 19 ms^{-1} respectively at the exit point of the nozzle. The surface temperatures of the solid base plate are used to calculate the heat flux, local heat transfer coefficient, and Nusselt numbers. The maximum heat transfer is found on base plate, whilst the maximum decrease of heat flux is observed on fire retardant fabric. This experimental model can enhance the understanding and insights of the heat transfer process through permeable fabric.

Peer-review under responsibility of organizing committee of the 6th BSME International Conference on Thermal Engineering (ICTE 2014).

Keywords: Heat transfer; jet impingement; fire retarding fabric; Nusselt number.

---

1. Introduction

Every year, a large number of people are injured even burnt in the whole world as a result of fire incident. Most often, high heat flux exposures in the industrial accident is severe. To rescue the people from fire and high heat

---

* Corresponding author. Tel. : +88-01752 881199
E-mail address: akmnazrul@gmail.com

Peer-review under responsibility of organizing committee of the 6th BSME International Conference on Thermal Engineering (ICTE 2014).

exposure, fire personnel come forward to fight in the high heat flux environment. The realistic tests have become essential to determine how much thermal protection can provide to the fire workers after wearing the fire protective clothing [1]. Consequently, extensive research have been conducted for better understanding about the mechanisms involved in heat transfer through thin fibrous layers and the thermal performance of protective clothing has been a point of interest for several decades. In 1954, Perry [2] conducted a research on convective heat transfer to a plane surface from a hot gas jet and Chen [3] conducted a research on transient heat and moisture transfer through thermally irradiated cloth in 1959. Fire retardant fabric (FRF) properties has steadily improved over the years for designing and creating a new fire protective fabric in order to prevent and minimize tissue burns that result from the radiant energy produced by fire as well as from the localized contact flame exposure. However, their performance had not been studied systematically in details for the safe keeping of their users yet. The aims of the current work are to study in depth of protective clothing and test protocols which are used in the evaluation of materials, clothing and protective equipments. Despite the existence of numerous tests for evaluating fire protective/ flame retardant clothing, there are still many unanswered questions considering the heat transfer response. This investigation focuses on the experimental evaluation of transient heat transfer through thin fibrous layers from an impinging heated air jet. The goal is to broaden the understanding of the spatial heat transfer distribution of the solid plate as well as FRF.

NASA conducted a research [4] for the Apollo service module propulsion system to find out the transient heat transfer behavior in 1965. In the same year Gardon and Akfirat [5] did another research to find out the role of turbulence in heat transfer characteristics of impinging jets. They discussed about the local heat transfer and flow conditions. Mohanty and Tawfek [6], and Goldstein et al. [7] kept constant both of the flat plate and the air jet to generate steady state solutions. Mohanty and Tawfek [6] used heat flux sensors to obtain local heat transfer measurements of a round air jet impinging normal to a flat surface. Goldstein et al. [7] studied the distribution of recovery factor and local heat transfer for an impinging jet on a flat isothermal plate under steady state conditions. Ukponmwan [8] and Torvi [9] studied and provided review of some of the works done for comfort and flammability of the FRF including the work of the government industry research committee (GIRC) [10]. Stoll et al. [11-12] discussed about the analytical, mathematical techniques and experimental method of method to determine the thermal radiation exposure on skin as well as heat transfer through fabrics as related to thermal Injury. Torvi [13] developed a model to simulate the heat transfer for bench top testing apparatus. Torvi et al. [14] used flow visualization methods to study the heat transfer in horizontal air spaces between solid boundaries. Anguiano [15] performed a study on skin stimulant material by a vertical hot jet. Islam et al. [16] conducted an experimental study on a solid bare plate by horizontal hot jet. However the study is not sufficient to understand the real situation at cotton fabric (CF) as well as different jet temperatures and velocities. Although a considerable amount of research has been carried out, but more effective research is essential to investigate results on heat transfer of horizontal hot air jet impingement on a flat surface through FRF fibrous layer. Even though few studies which dealt with heat transfer of impinging jet, did not focus on local heat transfer characteristics. In this study, an experimental facility has been fabricated to find the transient heat transfer phenomena on a vertical bare solid plate.

2. Experimental setup

The experimental study has been carried out by a co-axial wind tunnel and a heating attachment to the wind tunnel. The overall length of the wind tunnel is 9.0 m. It consists of an axial flow fan unit, two settling chambers, two diffusers, a silencer and a nozzle which are shown in Fig. 1(a) - (b). The fan unit consists of three axial wooden aerofoil shape fans in the same series. The fan unit receives air through the butterfly valve and discharges it into the silencer of the flow duct. Flow from the silencer passes on to the settling chamber through a diffuser. The jet velocity of the nozzle is controlled by regulating control unit of the fan. The temperature of the jet is regulated by controlling the supply voltage of the heater. The whole setup is mounted on rigid frames of mild steel pipes and plates and these frames are securely fixed with the ground. At the tip of the second settling chamber, the diameter of the flow facility is reduced from 475 mm to 88.9 mm where the heating section is placed. The heating section consists of a round nozzle. After that a vertical flat plate is placed in-front of the nozzle. The heated air allowed to pass through the long settling chamber to the nozzle having a diameter of 25.4 mm. Air from the wind tunnel is passed through the entrance section, heating section and settling chamber. Detailed explanation of the facility can be found in the studies of Hasan [17]. For the present investigation, a nozzle diameter of 25.4 mm is used. The test has been performed for different jet velocities 12, 15, 19 m/s respectively. Seven K-Type (Ni-Cr/ Ni-Al) thermocouples are placed on the base plate to measure the temperatures. One thermocouple is placed at the stagnation point, and 3 others on both top and bottom side of the stagnation point. A wooden frame is used to hold the fabric and the base plate as per provisions outline in ASTM standard [18]. All temperature measurements were recorded by using Picosoft data acquisition system.

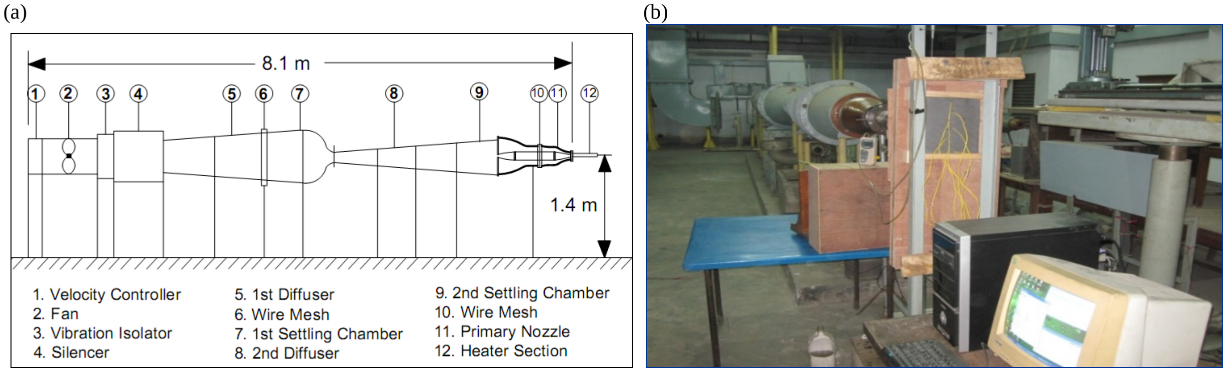

Fig. 1. (a) Schematic diagram of the wind tunnel, (b) Complete experimental setup with data acquisition system.

3. Experimental procedure

3.1. Methodology

The fan motors of the tunnel are initially started for a particular air flow with the help of butterfly valve and run about 15 minutes. The hot air jet is impinged on the base plate by removing the isolator and the thermo couple readings are recorded at the steady state condition. The same experiments are repeated for different conditions as given in Table -1. To cover all the experimental conditions, total 90 different experiments are performed yielding over 86,400 data points. To reach quasi-steady-state condition it takes about 60 minutes and then the computer controlled data acquisition system is allowed to run to record temperatures of all thermocouples in real time in every 1 sec. The test duration is limited by the semi-infinite solid assumption to 120 seconds. Experiments are performed for nozzle-to-plate separation (*l/d*) 2, 4, and 6. Eight pin type clips on all sides of the flat plate are employed to clamp the fabric with the base plate. In order to study the effects of air gap between fabric and flat plate, a solid wooden frame of 6 mm thick is placed beneath the flat plate. CF and FRF are then placed on the wooden frame and experiments are conducted.

Table 1: Experimental Conditions

Parameters	Value	Unit
Jet Velocity	12, 15, 19	m/s
Jet Temperature	115, 125	°C
Nozzle Diameter	25.4	mm
l/d	2, 4, 6	-
r/d	+ 4.5 ~ - 4.5	-

3.2. Mathematical equations

For the uniform initial temperature distribution, we could suddenly expose the surface to a constant surface heat flux (q_x) then the initial and boundary conditions provides -

$$T(x,0) = T_i$$

$$\frac{q_x}{A} = -K\frac{\partial T}{\partial x}\Big|_{x=0} \tag{1}$$

The solution for this case is

$$T_{(x,0)} - T_i = \frac{2q\sqrt{\alpha t/\pi}}{k} e^{\left(-\frac{x^2}{4\alpha t}\right)} - \frac{q_x}{k}\left(1 - erf\left(\frac{x}{2\sqrt{\alpha t}}\right)\right) \tag{2}$$

On the surface (x = 0) Eq. (2) reduces to,

$$T_{(t)} - T_i = \frac{2q\sqrt{\alpha t/\pi}}{k} \tag{3}$$

The local Nusselt number at each radial location, r/d, is derived from the surface heat flux history. Newton's law of cooling can be used to calculate the local heat transfer coefficient, h.

$$q_x = h(T_{jet} - T_i) \tag{4}$$

A major parameter for evaluating heat transfer coefficients is the Nusselt number,

$$Nu = \frac{h \cdot D}{K} \tag{5}$$

4. Results and discussion

4.1. Surface temperature (T_s) of the solid base plate and change of heat flux (q_s") at various radial locations

Fig. 2(a) represents time dependent surface temperature (T_s) variation on the solid massonite base plate (BP) is in contact with fire protective fabric (FPF), at nozzle-to-plate separation distance (*l/d*) = 6, jet temperature (T_{jet}) = 115 ^{o}C, and jet velocity (v_{jet}) = 12, for different radial locations (*r/d* = –4.5 ~ +4.5). It is observed that the maximum T_s is found at the stagnation point (*r/d* = 0). With the gradual increase of the radial distance (*r/d*) from the stagnation point to outer radial location (0 to ± 4.5) the surface temperatures are gradually decrease. In the same time, Fig. 2(b) represents change of heat flux ($q_s^{''}$) on BP is in contact with FPF, at *l/d* = 6, T_{jet} = 115 ^{o}C, and v_{jet} = 12, for *r/d* = –4.5 ~ +4.5. It is observed that, the maximum $q_s^{''}$ is found at *r/d* = 0. Both T_s and $q_s^{''}$ along with *r/d* are almost symmetric.

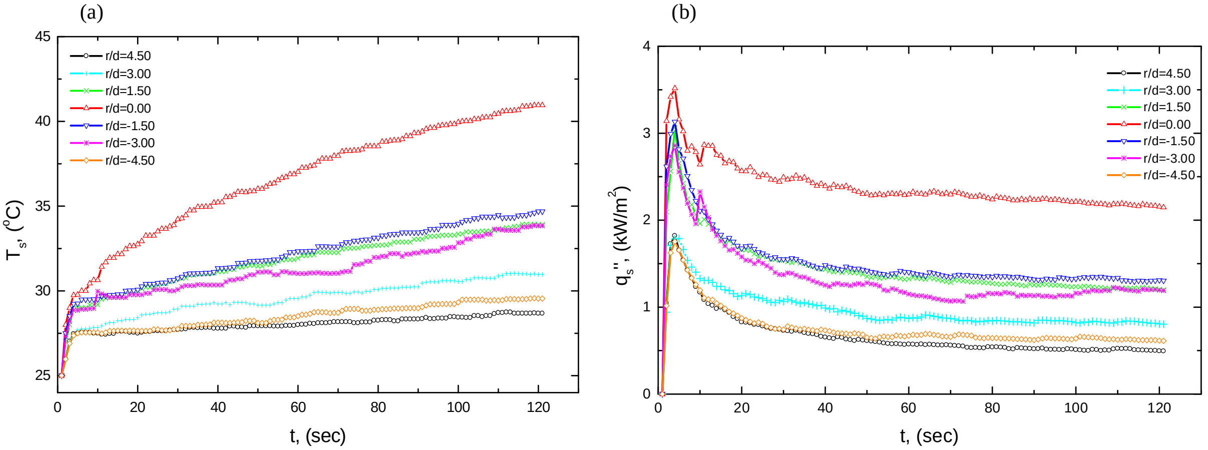

Fig. 2. Variation of surface (a) Temperature (T_s), (b) Heat flux ($q_s^{''}$) at *l/d* = 6; *r/d* = 0 ~ ± 4.5; T_{jet} = 115°C; v_{jet} = 12 m/s; FPF in contact with BP.

4.2. Effect of various nozzle-to-plate separation distance (l/d)of the jet on T_s and respective q_s"

Fig. 3(a) and 3(b) represent time dependent surface temperature (T_s) variation and change of surface heat flux ($q_s^{''}$) respectively of the base plate (BP) in contact CF, at stagnation point, *r/d* = 0, T_{jet} = 125 ^{o}C, v_{jet} = 19 m/s, for different nozzle-to-plate separation distance (*l/d*) = 2, 4, and 6. It is observed that the maximum T_s is found for *l/d* = 2 and decrease with the increase of nozzle-to-plate separation distance. These figures indicate, while the heat source is far from the solid surface, the surface temperature will be lower. For the long distance (*l/d* = 6), certain amount of heat of the jet will be transferred by convection and radiation; thus the temperature of the solid plate surface will be lower. That means, T_s values decrease for various nozzle-to-plate separation distance as per following order: *l/d* (2) > *l/d* (4) > *l/d* (6) > *l/d* (8) and so on.

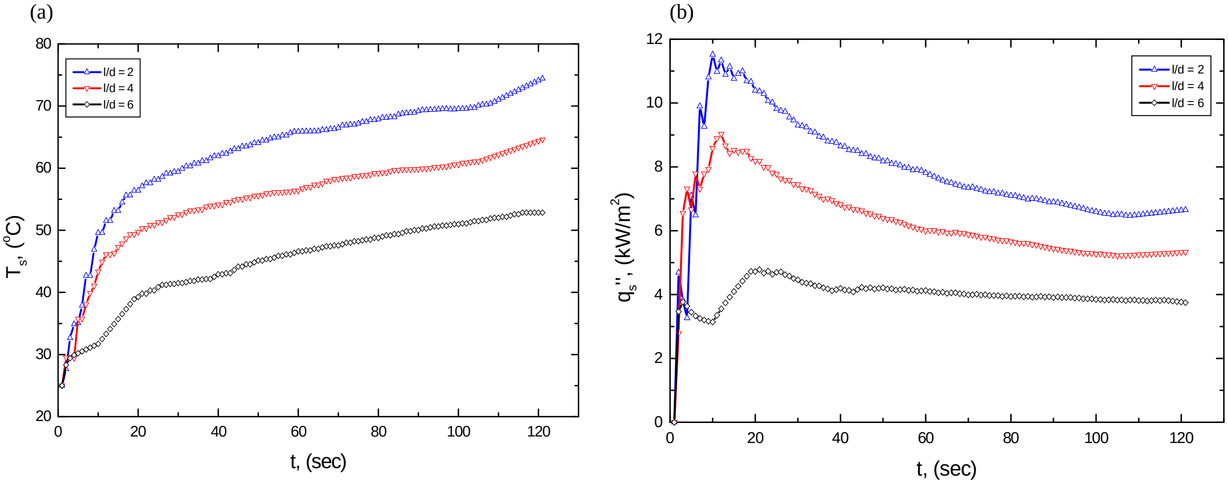

Fig. 3. Variation of surface (a) Temperature (T_s), (b) Heat flux (q_s'') at l/d = 2, 4, 6; r/d = 0; T_{jet} = 125 °C; v_{jet} = 19 m/s; CF in contact with BP.

4.3. Effect of jet velocities on T_s and respective q_s''

Fig. 4(a) and 4(b) represent time dependent surface temperature (T_s) variation and change of surface heat flux (q_s'') respectively of the BP alone, at the stagnation point (r/d) = 0, l/d = 4, T_{jet} = 125 °C, for different jet velocities, v_{jet} = 12, 15, and 19 m/s. It is observed that the maximum T_s and q_s'' are found at v_{jet} = 19 m/s and T_s, whilst q_s'' are decreasing with the decrease of jet velocity.

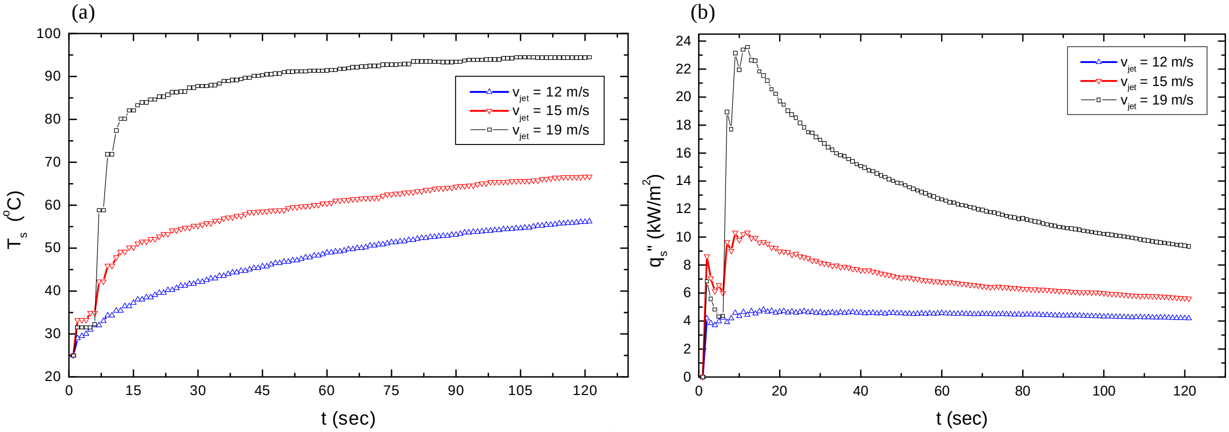

Fig. 4. Variation of surface (a) Temperature (T_s), (b) Heat flux (q_s'') at l/d = 4; T_{jet} = 125 °C; v_{jet} = 12, 15, 19 m/s; r/d = 0 of BP alone.

4.4. Effect of air gap between solid base to the fabric and in contact with the fabric

When a fire fighter wears fabric, there remain some places in contact with the skin to the fabric and due to the structure of the human body, rest of the places of the body create air gaps to the skin with the fabric. For this reason, in this study, experiments are conducted for fabric in contact with BP and 6 mm air gap with the BP. Fig. 5(a) and 5(b) represent T_s and q_s'' variation respectively of the base plate (BP) in contact with the CF and 6 mm air gap between base plate (BP) and cotton fabric (CF), at r/d = 0, l/d = 6, T_{jet} = 125 °C, and v_{jet} = 19 m/s. It is observed that the higher T_s are found for base plate (BP) in contact with the CF and the lower T_s are found for 6 mm air gap between base plate (BP) and cotton fabric (CF). As radiation heat transfer calculation has been neglected from the assumption of the present research, so the heat transfer value is speculated to be different from actual value.

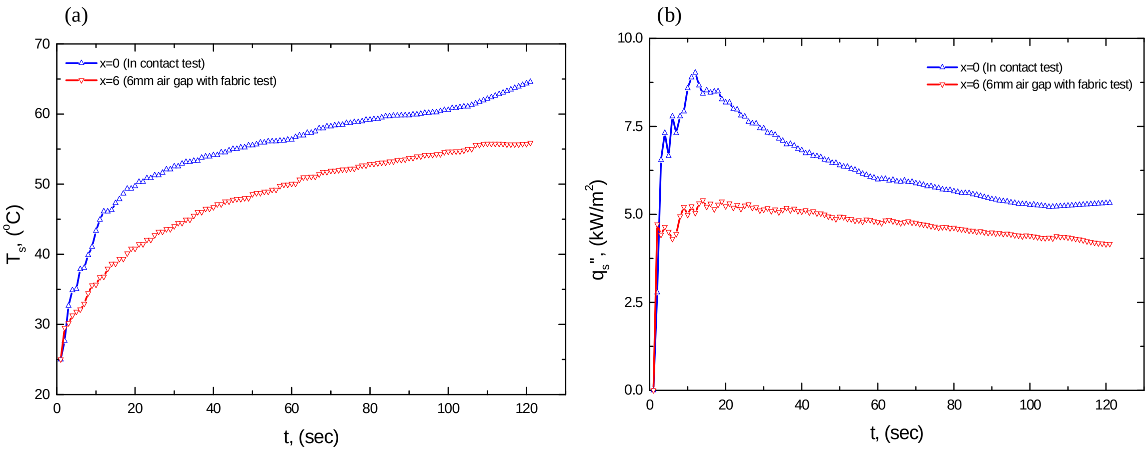

Fig. 5. Variation of surface (a) Temperature (T_s), (b) Heat flux (q_s'') at *l/d* = 6; T_{jet} = 125 °C; v_{jet} = 19 m/s; *r/d* = 0, BP in contact with CF, and 6 mm air gap between BF and CF.

4.5. Transient effect on Nusselt number (Nu)

The effect of transient heat transfer in terms of Nusselt number (*Nu*) with respect to radial distance from the stagnation point (*r/d*) has been shown in Fig. 6(a) and 6(b) for different time, t = 30, 60, 90, 120 seconds. It is found that the *Nu*, decreases with the increase of time (experimental or impinging time) for all type fabric conditions.

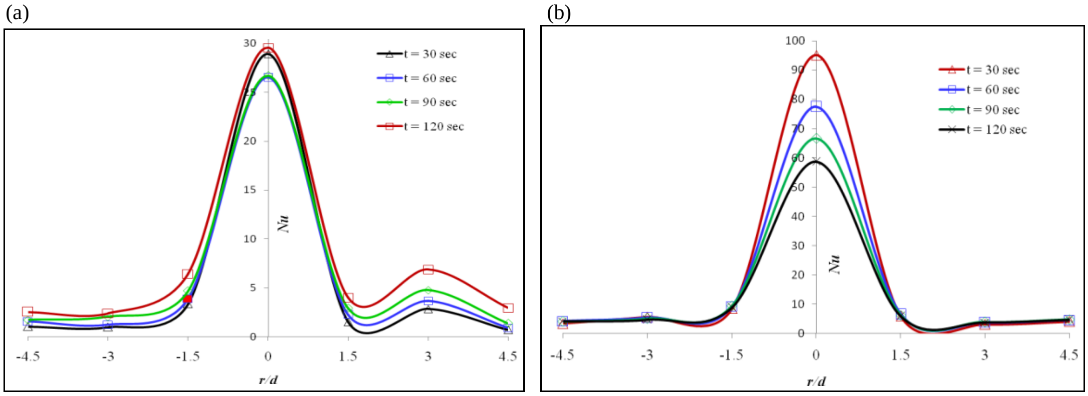

Fig. 6. Comparison of *Nu* at different t; *r/d*=0; T_{jet} = 125 °C; v_{jet} = 19 m/s; *l/d* = 6; (a) CF with BP, (b) BP alone.

The effect of transient heat transfer in terms of *Nu* with respect to radial distance from the stagnation point (*r/d*), and for different fabric conditions (FPF, CF, BP alone) has been shown in Fig. 7(a) - (d) in terms of t = 30, 60, 90, 120 seconds respectively. The highest value of *Nu* is found for base plate alone and lowest for FPF for all type fabric condition. The maximum value of *Nu* is found at *r/d* = 0. At *r/d* = 0, all the kinetic energy transformed into pressure energy. As a result the velocity air at the stagnation point is zero. But at stagnation point the temperature of the air is very high, thus the heat transfer coefficient is higher at stagnation point than the other radial position. So, the maximum pick of Nusselt number occurs at the stagnation point. After the stagnation point the velocity of air start to increase due to the pressure different between the surroundings and the stagnation point. But still the velocity of air is lower and the temperature of the jet decreases as the heat transferred to the base plate and the surroundings. For lower velocity and air temperature, the heat transfer coefficient also decreases, as well as *Nu*. With the increasing velocity the heat transfer coefficient of the air also increases. Although the temperature of the air is now very low then at the stagnation point, but due to the increase in velocity the Nusselt number is again increasing.

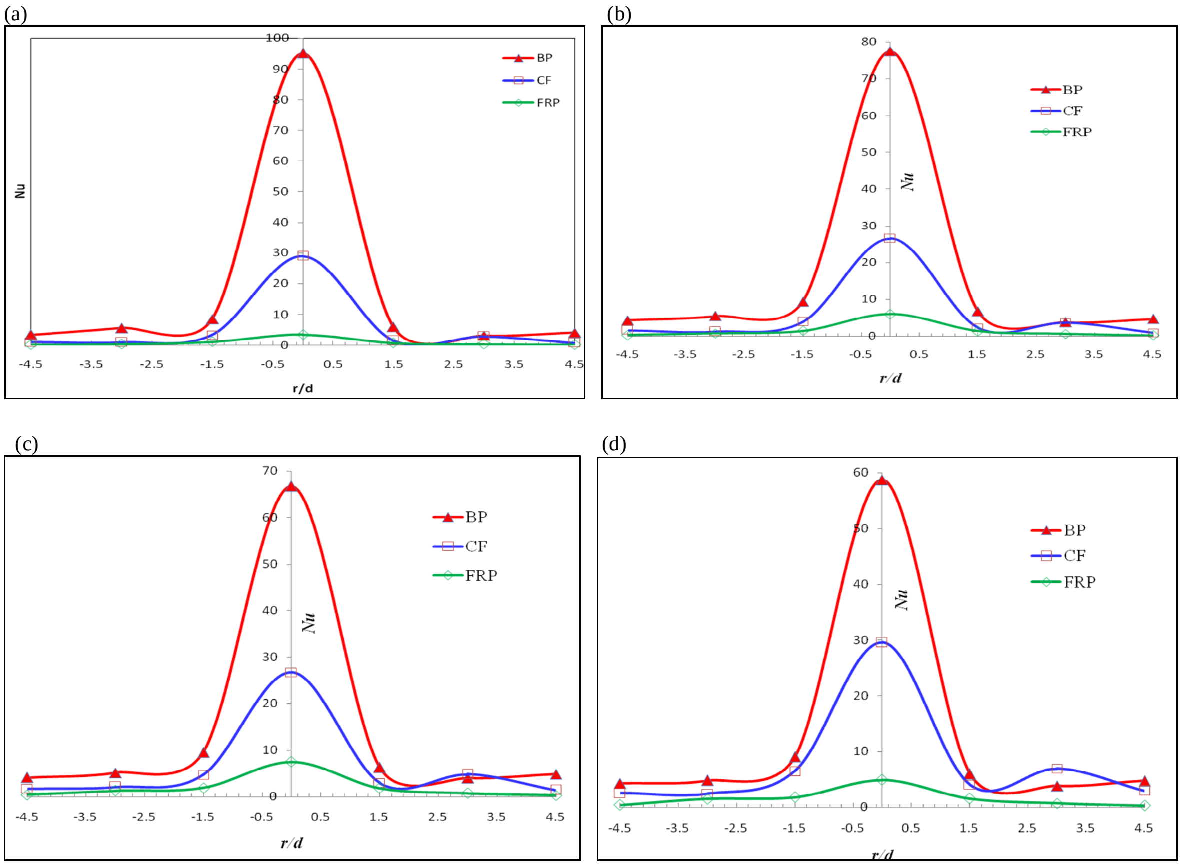

Fig. 7. Variation of *Nu* at different fabrics, at *r/d*=0; T_{jet} = 125 °C; v_{jet} = 19 m/s; *l/d* = 6; (a) t = 30, (b) t = 60, (c) t = 90, (d) t = 120 seconds.

4.6. Heat transfer comparison of the fabrics

Fig. 8(a) and 8(b) represents the surface temperature and change of heat flux for different fabric conditions, at the stagnation point (*r/d*), T_{jet} = 125 °C, v_{jet} = 19 m/s, *l/d* = 6 respectively. It is found that the lowest heat transfer occurred for FPF and the CF shows poor performance to resist heat transfer through the fabric.

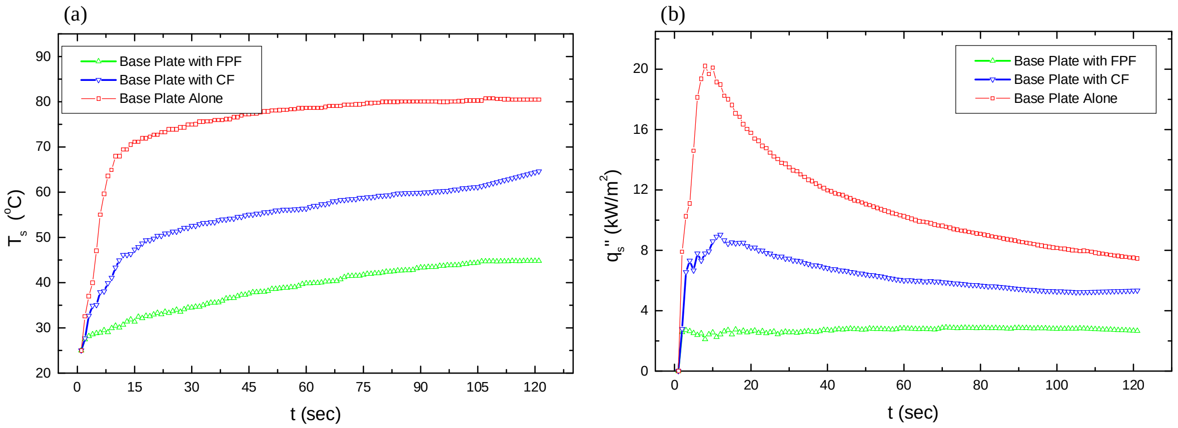

Fig. 8. Variation of surface (a) Temperature (T_s), (b) Heat flux (q_s'') at T_{jet} = 125 °C; v_{jet} = 19 m/s; *l/d* = 6; *r/d* = 0 for different fabric conditions.

5. Conclusions

An experimental setup is built to measure the thermal response of the fire retardant fabric system. The jet velocities are varied 12, 15, and 19 ms^{-1} respectively and temperatures are 115 and 125 °C respectively. Two permeable fabrics (Kevlar® 49 and cotton fabric) are considered. From the local heat transfer history, it is found that the surface heat flux (q_s'') is dependent on time, radial location (*r/d*) or nozzle to plate separation distance (*l/d*), and jet velocity (v_{jet}). The experimental results represent that the maximum heat transfer is occurred for base plate alone at 125 ^{o}C. From the experimental results, it can be concluded that the model can be used to determine various fabric/clothing design parameters for an optimum thermal protection and to estimate skin burn coupled with a fabric system under the jet impingement heating condition. It is also found that the surface heat flux history is dependent on the radial location (*r/d*) distances. The surface temperature and heat flux are almost symmetric along radial location and maximum values are found at the jet stagnation point ($r/d = 0$) for all cases. Initially, the heat transfer occurs as in transient mode and the surface temperature increases very rapidly and after a certain time, the surface heat transfer becomes steady. With the time increment, the rates of heat transfer to the base plate from the jet decreases. The fire resistance capacity of the cotton fabric (CF) is found to very poor comparing to the fire protective fabric (FPF). The FRF Kevlar® shows excellent performance to protect the heat transfer through the fabric. As the FRF Kevlar® has the potential to protect the heat transfer through the fabric, so it can be used as suit for the fire fighters at a certain condition of temperature and time.

References

[1] Islam, A.K.M. N., Study of heat transfer of a solid with protective fabric under hot air jet impingement, *M.Sc. thesis*, Department of mechanical engineering, Bangladesh University of Engineering and Technology, Dhaka, Bangladesh, (2013) 1-127.

[2] Perry, K. P., Heat transfer by convection from a hot gas jet to a plane surface, *proceeding of mechanical engineering inst.*, Vol. 168 (1954) 775 – 784.

[3] Chen, N. Y., Transient heat and moisture transfer through thermally irradiated cloth, *Ph.D. thesis*, Massachusetts Institute of Technology, Cambridge, Massachusetts, USA, 1959.

[4] NASA CB65579, LR 18900, A transient heat transfer and thermodynamic analysis of the apollo service module propulsion system, *Summary report*, Manned spacecraft center, Primary propulsion branch, Houston, Texas (1965) 1 – 15.

[5] Gardon, R. and Akfirat, J. C., The role of turbulence in determining the heat transfer characteristics of impinging jets, *International journal of heat and mass transfer*, Vol. 8 (1965) 1261 – 1272.

[6] Mohanty, A. K. and Tawfek, A. A., Heat transfer due to a round jet impinging normal to a flat surface, *International jomurnal of heat and mass transfer*, Vol. 36 (1993) 1639 – 1647.

[7] Goldstein, R. J., Behbahani, A. I., and Heppelmann, K. K., Stream wise distribution of the recovery factor and the local heat transfer coefficient to an impinging circular air jet, *International journal of heat and mass transfer,* Vol. 29 (1986) 1227 – 1235.

[8] Ukponmwan, J. O., The thermal insulation properties of fabrics, *Textile progress*, Vol. 24, Number 4 (1993)

[9] Torvi, D. A., A finite element model of heat transfer in skin subjected to a flash fire, *M.Sc. thesis*, Department of mechanical engineering, University of Alberta, Edmonton, Alberta, Canada (1992).

[10] Backer, S., et al., Textile fabric flammability, *The MIT Press*, Cambridge, Massachusetts, 1976.

[11] Stoll, A. M. and Chianta, M. A., Method and rating system for evaluation of thermal protection, *Aerospace medicine*, Vol. 40, (November 1969) 1232 – 1238.

[12] Stoll, A. M. and Weaver, J. A., Mathematical model of skin exposed to thermal radiation, *Aerospace Medicine*, Vol. 40, (1969) 24 – 30.

[13] Torvi, D. A., Heat transfer in thin fibrous materials under high heat flux conditions, *Ph.D. thesis*, Department of mechanical engineering, University of Alberta, Edmonton, Alberta, Canada (1997) 1 – 277.

[14] Torvi, D. A., and Sawcyn, C. M. J., Flow visualization in air spaces between protective fabrics and sensors in protective clothing tests, Department of mechanical engineering, University of Saskatchewan, Saskatoon, Alberta, Canada (2004) 1 - 6.

[15] Anguiano, R. M., Transient heat transfer through thin fibrous layer, *M.Sc. thesis*, Department of mechanical engineering, University of Alberta, Emonton, Albarta, Canada (2006) 1-92

[16] Islam, MA, Rezwan, AA, Hossain, S, and Islam, AKM N, Study of transient heat transfer of a solid with protective fabric under hot air jet impingement, *Proc. Int. Conf. on mechanical engineering (ICME2011),* Dhaka, Bangladesh (December 2011), ICME11-TH-042, 1-6.

[17] Hasan, M. N., Experimental study of flow characteristics in the near field of a thermally stratified co-axial free jet, *M.Sc. thesis*, Department of mechanical engineering, Bangladesh University Of Engineering and Technology, Dhaka, Bangladesh, (2008) 1-159.

[18] ASTM F2703-08, Standard test method for unsteady-state heat transfer evaluation of flame resistant materials for clothing with burn injury prediction.

Available online at www.sciencedirect.com

ScienceDirect

Procedia Engineering 00 (2015) 000–000

Procedia Engineering

www.elsevier.com/locate/procedia

6th BSME International Conference on Thermal Engineering (ICTE 2014)

Natural Convection Flow and Heat Transfer in an Enclosure Containing Staggered Arrangement of Blockages

Draco Iyi[a] and Reaz Hasan[b]

[a]*Department of Mechanical Engineering, School of Engineering Robert Gordon University, Aberdeen, AB10 7GJ, United Kingdom*
[b]*Department of Mechanical and Construction Engineering, Northumbria University at Newcastle upon Tyne, NE1 8ST, United Kingdom*

Abstract

The work reported in this paper is a numerical study of airflow and heat transfer for low turbulence buoyancy-driven flow in a rectangular cavity partially filled with solid objects. The two vertical walls were maintained at constant temperatures giving a temperature differential of 42.2 °C resulting in a characteristic Rayleigh number of 1.45×109. Two different types of blockage arrangements were considered for analysis, and these consist of In-line and Staggered arrangements of 12×6 and 12×3 objects. In all cases, steady state flow and wall heat transfer data at the mid-height and mid-width of the cavity are presented. The flow domain displayed a stable core region and the average core temperature was found to be strongly influenced by different stacking arrangement of solid objects. In general, the staggered arrangement resulted in lower heat transfer through the surfaces which is linked with the suppression of turbulence within the boundary layers close to the surfaces.

Peer-review under responsibility of organizing committee of the 6th BSME International Conference on Thermal Engineering (ICTE 2014).

Keywords: Low turbulenc, Natural convection, Heat transfer, CFD, Product stacking and arrangement

---

1. Introduction

Buoyancy driven heat transfer inside cavities has been the subject of extensive research for the last two decades due to the growing demand for detailed quantitative knowledge of the transfer processes and also due to its relevance in many practical applications [1, 2]. The basic set up for such flows, which has also attracted most attention from researchers, is a rectangular cavity filled with dry air whose opposing vertical walls are heated differentially [3-6]. In the case of a rectangular cavity of height H, the natural convection heat transfer from hot to cold walls is characterized by the formation of a slow moving vortex. This vortical motion is often interpreted as an 'engine'

Peer-review under responsibility of organizing committee of the 6th BSME International Conference on Thermal Engineering (ICTE 2014).

which transfers heat from the heated surface (source) to the cold surface (sink). The intensity of flow is conveniently expressed by the Rayleigh number, $Ra = g\beta\Delta TH^3/\alpha\nu$, where, H is the height of the cavity, β is coefficient of thermal expansion, ΔT is the temperature difference between the vertical walls and α and ν are the thermal and molecular diffusivities of the fluid respectively. Depending on the Rayleigh number the flow can be categorized as turbulent or laminar [7-9]. Rayleigh numbers less than 10^8 indicate a buoyancy-induced laminar flow, with transition to turbulence occurring over the range of $10^8 < Ra < 10^{10}$ [10].

Another trend in buoyancy driven flow research has been focused on the examination of enclosures partially filled with solid products [2, 11]. The flows in such confined spaces develop as a result of temperature gradient which is further complicated by the interactive effects of solid products on the airflow and heat transfer. This interest has grown due to the relevance in the design of a wide range of practical applications such as thermal management of indoor environments, cooling of electronic panels, thermal management of agricultural blockages, stacking of items in cold storage etc. Unlike porous media, these obstacles are not in contact with each other but are close enough to influence the transfer processes significantly. The majority of studies in this category are concentrated on steady state laminar flow of Rayleigh number over the range 10^4 to 10^8 [12] investigating the flow induced by temperature gradient. Typical examples of studies in this category are the works by Das and Reddy [13], Desrayaud and Lauriat [12], and Yoon et al. [14], all of which are limited to steady state two dimensional laminar natural convection flow of Rayleigh number ranging from 10^5 to 10^8.

Work has been done for empty box and box full of isolated solid products but none has been reported for isolated solid products arranged in clusters in different parts of the chamber. This may be relevant for storage, design and determining the optimum location of clustered heating elements. The aim of this paper is to explore the heat transfer and flow field inside a rectangular cavity for different arrangements and stacking of these solid blockages and, in particular, to address the influences of in-line and staggered arrangement on the heat transfer, airflow and turbulence quantities. To achieve the above aims, a systematic two-dimensional numerical investigation of low turbulence natural convection flow and heat transfer in a rectangular confined space containing such isolated solid cylindrical objects has been conducted.

Nomenclature

H	height of the cavity (m)
L	width of the cavity (m)
x, y	displacement in x and y direction
Nu_{local}	local Nusselt number, (= hL/k)
Ra	Rayleigh number, $(= (g\beta\Delta TH^3)/\nu\alpha)$
y^+	non-dimensional wall distance
LR k-ε	Low Reynolds number turbulence model

2. Flow Domain

In this study, particular emphasis is placed on quantifying the airflow, turbulence quantities and heat transfer due to various arrangements of solid objects. The geometrical configurations used in these investigations are shown in Fig.1 for 12×6 blockages and are similar to the cavities used in previous investigations [15-17]. As can be seen, the objects are stacked as in-line and staggered. The rectangular cavity has an internal dimension of height, H = 1000 mm and width, L = 500 mm and the cylindrical objects are of diameter 40mm. For this arrangement, the volume occupied by the solid objects is about 18.1% of the total cavity.

Another set of stacking was considered by choosing 12×3 objects for three different cases of staggered arrangement as shown in Figs.2. These are identified as Case 1, Case 2 and Case 3. Exactly similar cases were considered for in-line stacking and an example of Case 3 is shown in Fig. 2. The volume occupied by blockages for 12×3 arrangements represents about 9% of enclosure volume.

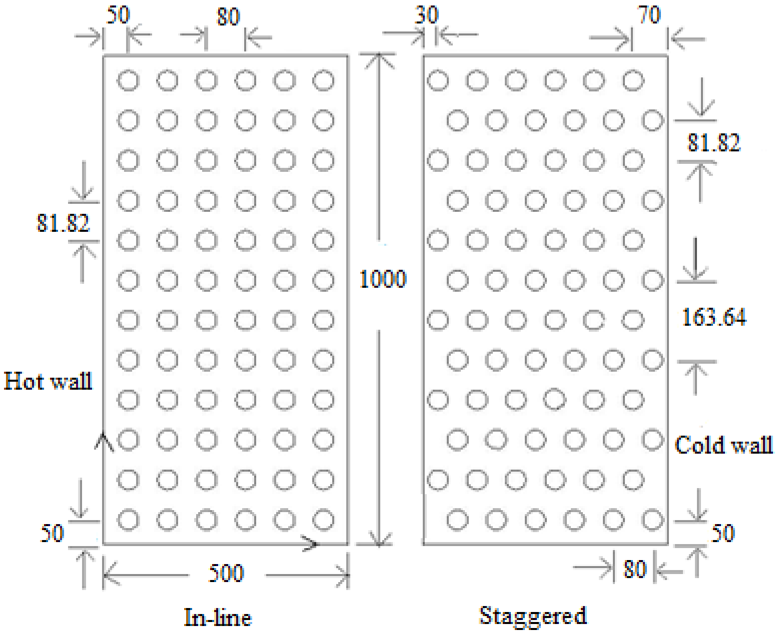

Figure 1: Schematic of the 12 × 6 flow domain arrangement and coordinate system

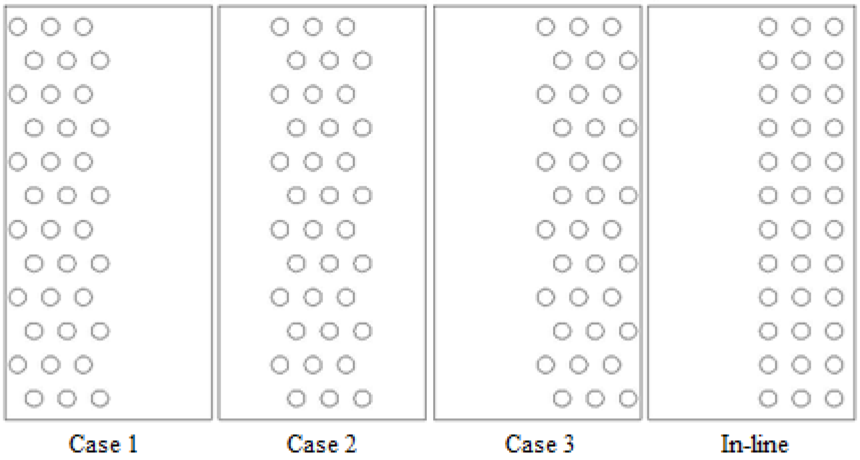

Figure 2: Schematic of the 12x3 arrangement of blockages for staggered and in-line stacking

3. Numerical Method

Calculations were performed for all test cases using the commercial CFD package of ANSYS FLUENT 14.5 [18]. Turbulent fluxes of momentum and heat were modelled by low Reynolds number k-ε eddy viscosity model of Launder-Sharma with the inclusion of the buoyancy terms in the energy equation. This model has been used for greater stability and superior results for blockage flow as reported by Draco et al. [15].

Systematic grid dependency tests were carried out for all cases and the final results were obtained with $y^+ \approx 2$. It is worthwhile to note that the process of computing a steady-state solution using very fine mesh has been quite challenging because of the oscillations associated with higher-order discretization schemes. As a result, a number of steps were taken to achieve a steady-state solution. Initially, low value of Rayleigh number (10^6) was adopted for the solution using an incompressible unsteady solver with a time step of 0.002s with the first-order scheme for convection terms. The resulting data files for the three cases were then used as an initial guess for the higher Rayleigh number simulation using the higher-order discretization schemes. This method helped to create a more realistic initial field for the LR *k*-*ε* runs. All simulations were performed using a single Intel core 2Duo E6600 2.4 GHZ processor and a typical run took about 0.5 hours of computing time.

Zero heat flux (W/m²) was used as the boundary condition for the passive horizontal walls, while the active vertical walls were maintained at 65.5 °C and 23.3 °C for the hot and cold walls respectively. At the surface of the cylinders, zero heat flux (adiabatic surface temperature) was used as the thermal boundary condition. However, radiation heat transfer between the surfaces was taken into consideration. No slip boundary conditions have been imposed for all the solid surfaces. All walls have a fixed emissivity of 0.09, except for the blockages whose emissivity was fixed at 0.9. Thermal properties of the air were estimated at the mean temperature of the isothermal walls of the rectangular enclosure (44.4 °C). Boussinesq approximation was used to specify air density variation due to temperature [19]. The relative variation of density is less than 3% inside the enclosure. To simulate radiation, Discrete Ordinate Method (ANSYS, 2013) has been chosen.

4. Results and Discussion

The numerical results and analyses are presented in this section. At steady state, heat transfer and flow parameters such as the temperature, velocity and turbulence profiles along the mid-height (y/H=0.5) and mid-width (x/L=0.5) were collected and analysed. For all cases, temperature data for the mid-height and mid-width displays a stable core region and hence emphasis is placed on profiles near the walls. The numerical results using the current methodology has already been thoroughly scrutinised and validated against reliable experimental data [17, 18] and hence excluded from this paper.

4.1. The 12×6 arrangements

The influence of staggered arrangement of blockages on the flow and heat transfer is analysed by comparing the results with in-line arrangements. Figure 3 shows the temperature profile at mid-width and near the bottom part of the cavity. A nearly similar pattern is observed for the top part and hence is omitted to avoid repetition. The change in temperature between the two configurations is significant especially near the passive horizontal walls, with a maximum of about 2.5 °C and is found to occur within the boundary layer. The effect due to staggering is more prominent up to y/H=0.15 after which a stable core region can be seen. The turbulence intensity for the two configurations is shown in Fig. 4. It can be observed that the effect is very prominent on turbulence intensity. The average Nusselt number for the two configurations presented in Table 1 shows that the staggering reduces the heat transfer by a modest 7%.

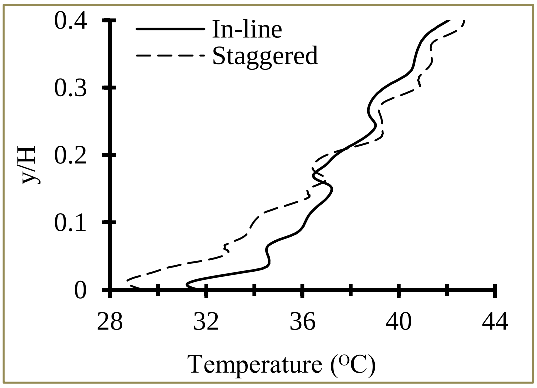

Figure 3: Near bottom wall temperature profile at mid-width

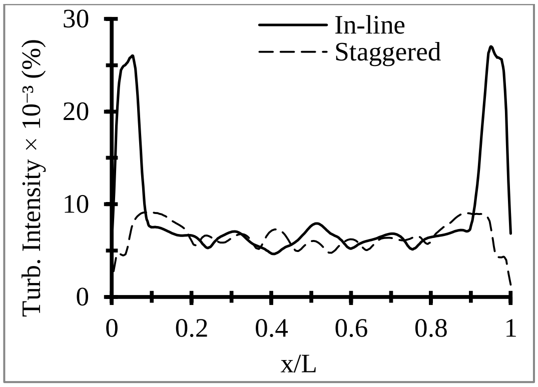

Figure 4: Turbulence intensity profiles at mid-height

Table 1: Average Nusselt number comparison

	Average Nusselt number (12×6)	
	In-line	Staggered stacking
Hot wall	75.30	69.57
Cold wall	73.99	68.38

4.2. The 12×3 arrangements

The results for the in-line and staggered 12×3 arrangement of blockages are presented in this section. For both arrangements, three different cases have been considered as shown in Fig. 2. Firstly, results are presented for in-line stacking and secondly, the effects due to staggering are specifically addressed by suitable plots.

4.2.1. In-line stacking arrangement

Figures 5 show the temperature profiles at mid-height of the cavity, with Case 3 showing the maximum temperature. The average temperature difference between Case 3 and Case 1 is about 2.4 ^{O}C for the most part of the mid-height plane. Similar plot in Fig.6 shows the turbulence intensity profiles highlighting the fact that the proximity of blockages is closely linked to the suppression of turbulence and is also in conformity with the heat transfer through the active walls as presented in Table 2. It is hence reasonable to imply that the different stacking of blockages within an enclosed space can lead to a significant change in the heat transfer, and in our case, the average change in heat transfer is about 10.5%.

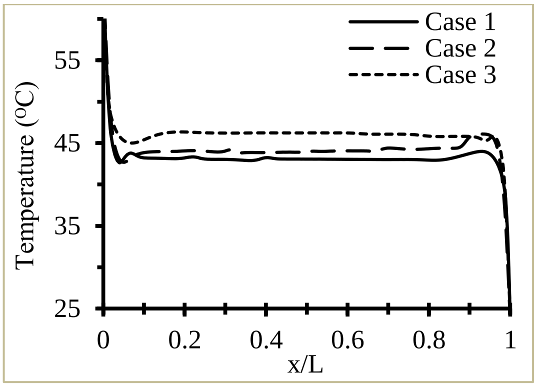

Figure 5: Temperature profile at mid-height

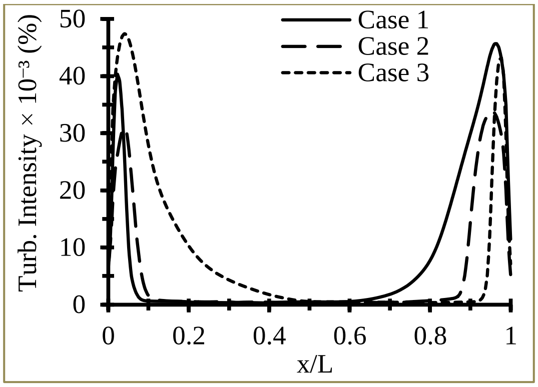

Figure 6: Turbulence intensity profile at mid-height

Table 2: Average Nusselt number comparisons (In-line stacking)

	Average Nusselt number (12×3)		
	Case 1	Case 2	Case 3
Hot wall	78.01	77.80	87.16
Cold wall	87.47	76.75	77.07

4.2.2. Comparison of in-line and stacking 12×3 arrangements

In this section, we compare the results for in-line and staggered stacking of 12×3 blockage arrangements. Figure 7 shows a sample of the flow pattern in the form of a stream function plots for the three different stacking conditions. Overall, the flow field is dominated by stacking arrangement with the main fluid motion taking place near the walls. As expected, the stacking arrangement of Case 1 and Case 3 shows a diagonally symmetric flow pattern. On the other hand, Case 2 displays a rather trapezoidal core region with the higher flow velocities squeezed toward the top right hand and bottom left hand corners of the enclosure.

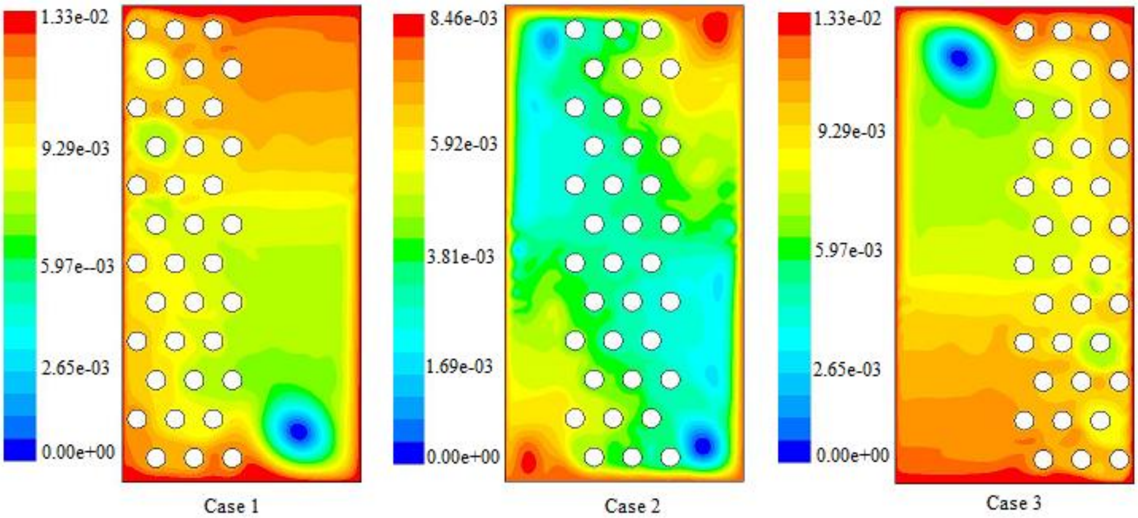

Figure 7: Stream function plots for the three cases of stacking conditions.

Figures 8-9 compare the vertical component of velocity, Vy, and turbulence intensity profiles at the mid-height for Cases 2 and 3. For Case 2, the maximum velocity does not show any significant variation due to arrangement. However, turbulence intensity shows sensitivity which is similar to the previous situation. For Case 3, the velocity magnitude is found to be affected and is due to the very different vortex pattern thanks to the particular stacking arrangement. Again, the turbulence intensity can be seen to be drastically reduced due to the staggering of blockages.

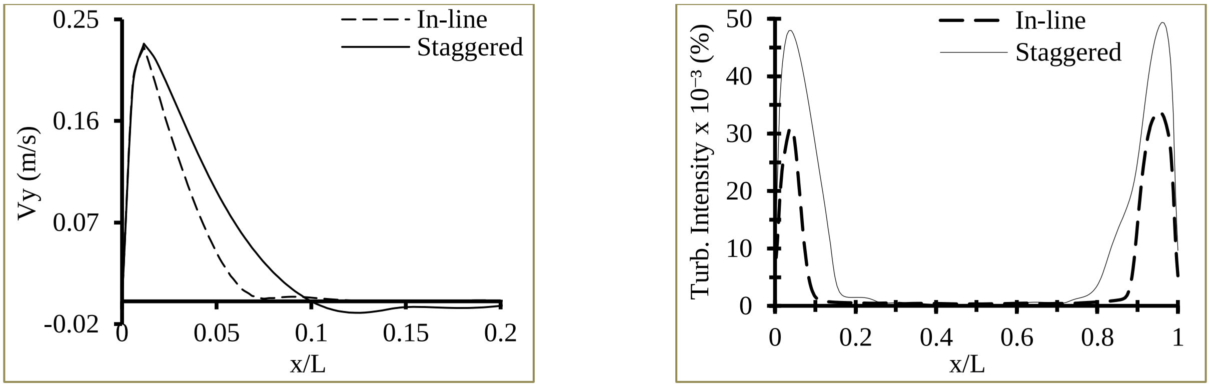

(a) (b)

Figure 8: (a) Vertical velocity and (b) turbulence intensity at mid-height for Case 2

The relative influence on wall heat transfer in terms of local Nusselt numbers within the enclosure are shown in Fig.10. For the case of the blockage stacking near the active vertical walls (Case 3), the in-line configuration shows a higher heat transfer as compared to the staggered configuration. It was also calculated that the average heat transfer for the staggered arrangements were lower by up to 16% in comparison with the in-line stacking.

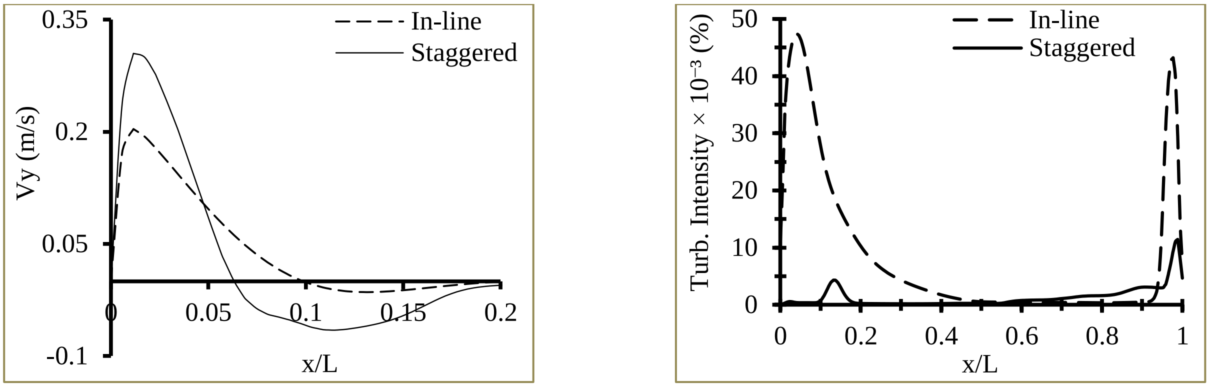

(a) (b)

Figure 9: (a) Vertical velocity and (b) turbulence intensity at mid-height for Case 3

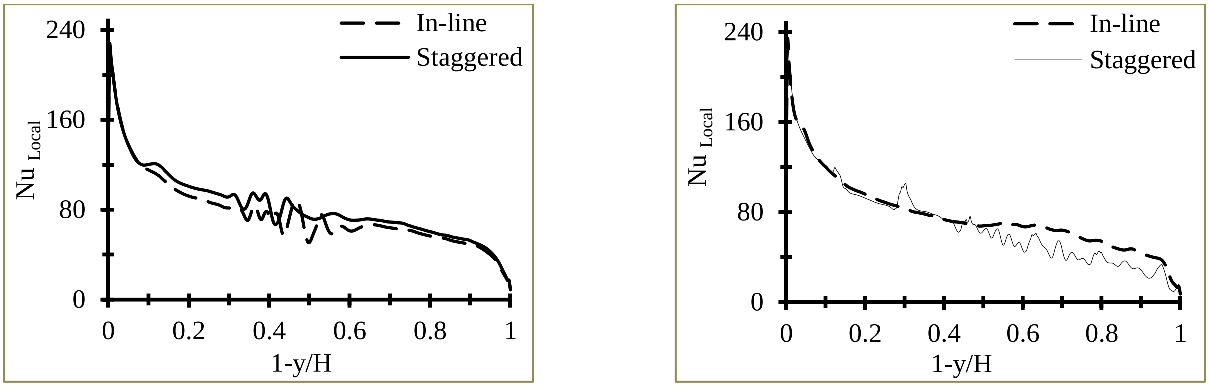

(a) (b)

Figure 10: Local Nusselt number comparisons at cold wall (a) Case 2 (b) Case 3

5. Conclusion

Based on the calculations carried out in this research programme, the numerical results allow a better understanding on the influence of blockages arrangement within a low turbulent natural convection flow in an enclosure. The influence on fluid flow and heat transfer for the different stacking of arrangement of the blockages within the enclosure was identified and detailed profiles at the mid-height and mid-width of the rectangular enclosure have been analyzed. Some general conclusions are presented below:

a) Temperature stratification was observed in all cases, high temperature at the top and low temperature at the bottom region of the enclosure.
b) The flow in such a low temperature enclosure is sensitive to the different stacking arrangement of products and hence a detailed understanding of the flow physics is important for an enhanced design of such applications.
c) The average heat transfer in the enclosure can be reduced to about 16% due to the pattern of arrangement. The stacking pattern was found to affect the flow and heat transfer fairly modestly which is probably dominated by

the suppression of turbulence near the walls. The variation of temperature and heat transfer is modest and hence may be very important in the design of practical applications where long term exposure is in place.

6. References

[1] S. Kadem, A. Lachemet, R. Younsi, and D. Kocaefe, "3d-Transient modeling of heat and mass transfer during heat treatment of wood," *International Communications in Heat and Mass Transfer,* vol. 38, pp. 717-722, Jul 2011.

[2] O. Laguerre, S. Benamara, D. Remy, and D. Flick, "Experimental and numerical study of heat and moisture transfers by natural convection in a cavity filled with solid obstacles," *International Journal of Heat and Mass Transfer,* vol. 52, pp. 5691-5700, Dec 2009.

[3] B. Calcagni, F. Marsili, and M. Paroncini, "Natural convective heat transfer in square enclosures heated from below," *Applied Thermal Engineering,* vol. 25, pp. 2522-2531, Nov 2005.

[4] Y. S. Tian and T. G. Karayiannis, "Low turbulence natural convection in an air filled square cavity - Part II: the turbulence quantities," *International Journal of Heat and Mass Transfer,* vol. 43, pp. 867-884, Mar 2000.

[5] F. Ampofo and T. G. Karayiannis, "Experimental benchmark data for turbulent natural convection in an air filled square cavity," *International Journal of Heat and Mass Transfer,* vol. 46, pp. 3551-3572, Sep 2003.

[6] A. A. DafaAlla and P. L. Betts, "Experimental study of turbulent natural convection in a tall air cavity," *Experimental Heat Transfer,* vol. 9, pp. 165-194, Apr-Jun 1996.

[7] F. Penot, O. Skurtys, and D. Saury, "Preliminary experiments on the control of natural convection in differentially-heated cavities," *International Journal of Thermal Sciences,* vol. 49, pp. 1911-1919, Oct 2010.

[8] W. Chen and W. Liu, "Numerical and experimental analysis of convection heat transfer in passive solar heating room with greenhouse and heat storage," *Solar Energy,* vol. 76, pp. 623-633, 2004.

[9] D. Saury, N. Rouger, F. Djanna, and F. Penot, "Natural convection in an air-filled cavity: Experimental results at large Rayleigh numbers," *International Communications in Heat and Mass Transfer,* vol. 38, pp. 679-687, Jul 2011.

[10] G. Barakos, E. Mitsoulis, and D. Assimacopoulos, "Natural-Convection Flow in a Square Cavity Revisited - Laminar and Turbulent Models with Wall Functions," *International Journal for Numerical Methods in Fluids,* vol. 18, pp. 695-719, Apr 15 1994.

[11] G. D. McBain, "Natural convection with unsaturated humid air in vertical cavities," *International Journal of Heat and Mass Transfer,* vol. 40, pp. 3005-3012, Sep 1997.

[12] G. Desrayaud and G. Lauriat, "Heat and mass transfer analogy for condensation of humid air in a vertical channel," *Heat and Mass Transfer,* vol. 37, pp. 67-76, Jan 2001.

[13] M. K. Das and K. S. K. Reddy, "Conjugate natural convection heat transfer in an inclined square cavity containing a conducting block," *International Journal of Heat and Mass Transfer,* vol. 49, pp. 4987-5000, Dec 2006.

[14] H. S. Yoon, D. H. Yu, M. Y. Ha, and Y. G. Park, "Three-dimensional natural convection in an enclosure with a sphere at different vertical locations," *International Journal of Heat and Mass Transfer,* vol. 53, pp. 3143-3155, Jul 2010.

[15] D. A. Iyi, R. Hasan, and R. Penlington, "Interaction effects between surface radiation and double-diffusive turbulent natural convection in an enclosed cavity filled with solid obstacles," *ICHMT Digital Library Online,* 2012.

[16] D. Iyi, R. Hasan, and R. Penlington, "Numerical Simulation of 2D Turbulent Natural Convection of Humid Air in a Cavity Filled with Solid Objects," *Procedia Engineering,* vol. 56, pp. 538-543, // 2013.

[17] D. Iyi, R. Hasan, and R. Penlington, "Effect of Emissivity on Heat and Mass Transfer of Humid Air in a Cavity Filled with Solid Obstacles," *Numerical Heat Transfer, Part A: Applications,* vol. NHT13/5995, 2014.

[18] ANSYS Inc., "ANSYS Fluent 14.5.," 2013.

[19] H. K. Versteeg and W. Malalasekera, *An introduction to computational fluid dynamics: the finite volume method*: Pearson Education, 2007.

Available online at www.sciencedirect.com

ScienceDirect

Procedia Engineering 00 (2015) 000–000

Procedia Engineering

www.elsevier.com/locate/procedia

6th BSME International Conference on Thermal Engineering (ICTE 2014)

Experimental Study on Heat Transfer and Friction Factor in Laminar Forced Convection over Flat Tube in Channel Flow

Tahseen Ahmad Tahseen[a,c], M.M. Rahman[a,b,]* and M. Ishak[a]

[a] *Faculty of Mechanical Engineering, University Malaysia Pahang*
26600 Pekan, Pahang, MALAYSIA
Phone : +609-424-2246; Fax : +609-424-2202
[b]*Automotive Engineering Centre, Universiti Malaysia Pahang*
26600 Pekan, Pahang, MALAYSIA
[c] *Department of Mechanical Engineering, College of Engineering*
Tikrit University, Tikrit, IRAQ

Abstract

The heat transfer and fluid flow over a flat tube in the channel with laminar forced convection is experimentally investigated. The experiments were conducted at a flat tube in the flow direction, the five air velocity between 0.2 and1.0 m/s, and Reynolds number based on the hydraulic diameter (Re_{Dh}) was considered from 124.5 to 622.5. The uniform heat flux supplies are at the surface of the tube are 354.9, 1016.3 and 1935.8 W/m^2 respectively. The experimental results indicate that the average Nusselt numbers ($\overline{Nu}_{Dh}$) for the flat tube increased with increase of Re_{Dh} at fixed of the heat flux supply. The $\overline{Nu}_{Dh}$ increased with an increase of heat flux supply at fixed Re_{Dh}. On the other hand, the friction factor decreased with increases of the front free stream velocity. The $\overline{Nu}_{Dh}$ relationship with Re_{Dh} in the power law, the$\overline{Nu}_{Dh}$–Re_{Dh} correlation was found to be $\overline{Nu}_{Dh} = C \times (Re_{Dh})^m$. The correlation achieved good predictions of the measured data with the minimum root mean square value is 99.70%.

Peer-review under responsibility of organizing committee of the 6th BSME International Conference on Thermal Engineering (ICTE 2014).

Keywords: Laminar forced convection; heat transfer; fluid flow; Reynold's number; heat flux; Nusselt number.

1. Introduction

The cylinders with different shapes of the cross section (e.g., circular, elliptic, flat) are the basic construction blocks of several engineering applications as an example heat exchangers, automotive radiators and nuclear reactors.

---

* Corresponding author. Tel.: +609-424-62439 fax: +609-424-6222
E-mail: mustafizur@ump.edu.my

Peer-review under responsibility of organizing committee of the 6th BSME International Conference on Thermal Engineering (ICTE 2014).

The heat exchangers played a pivotal role in energy applications for a long time ago. The issue of heat transfer by forced convection from flat tube shape is significantly due to its essential nature, in addition to that numerous direct, applications energy conservation, heat exchanger and numerous others [1–4]. Flat tubes the fact that the playing a vital role in many engineering applications (e.g. automotive radiators, modern heat exchangers). It is a design has recently been presented using air conditioning for automotive condensers and evaporators. The recent developments in automobile industry aluminium manufacturing technology made the cost of the flat tube heat exchanger building more convenient [2]. In the other hand, the flat tube heat exchangers are expecting to be the better air-side heat transfer coefficients and less than air-side of pressure drop compared with a circular shape heat exchangers, the pressure drop in a flat tube is required to be less of circular tubes, due to a smaller wake area. For the same reason, the expected noise and vibration is less than in flat tube shape compared to the circular shape of tube heat exchangers.

The many studies of heat transfer by forced convection from circular tube on the cross-flow. For the examples, the comprehensive convective heat transfer from circular tube shape was studied [1, 5]. Ota et al. [6] have experimental study heat transfer by forced convection of air flow over the elliptic tube. It was shown that the local Nusselt number was completely various for those that circular tube shape. Baughn et al. [7] presented investigate experimentally heat transfer by forced convection from the single circular cylinder, the tube in tandem with tube in the inlet region of the tube bundle under the uniform heat flux condition. It has been observed that, for together staggered and in-line tube configuration, the local Nusselt number distribution depends on row location of the tubes. Stanescu et al. [8] Studies experimentally the optimum space of circular tube shape in cross-flow of heat transfer by forced convection, the study followed given by Bejan et al. [9] on the optimum of configuration of circular tubes in free convection. Together the two studies deem only equilateral triangle at the staggered arrangement and not investigated of the geometry of the tube. Khan et al. [10] Investigated experimentally of the heat transfer by forced convection of air cross flow over one in-line elliptical tube configuration with the minor-to-major axis ratio of 0.33 and at the horizontal plane of attack. The results indicated that the increased heat transfer rate with an increase of both air and water flow. The heat transfer by forced convection from a circular tube on cross-flow to liquids and air has been studied experimentally may be found in Sanitjai and Goldstein [11]. The measurement of heat transfer shows three zone flows around the tube: recurrent vortex flow zone, reattachment of the shear layer zone and the boundary layer zone of the laminar flow. Chang and Mills [12] have experimental studies of the impact of aspect ratio on heat transfer by forced convection from a circular tube in the air cross-flow. The result of the study shows that the mean heat transfer coefficient raises with reduction the aspect ratio. The heat transfer and pressure investigation experimental both in-line and staggered flat tube configuration by Tahseen et al. [13], Ishak et al. [14]. From the studies shows the effect of heat flux supply, the front free-stream velocity of air flow on the heat transfer coefficient. In the other hand, show the effect of Reynolds number on the pressure drop of cross flow. The results indicate the Nusselt number increase always with an increase of Reynolds number. Three dimension experimental and numerical forced convection study for optimum staggered configuration of finned circular and elliptic cross section of tubes by Matos et al. [15]. The results of the study showed the presence of a relative increase heat transfer up to 19% in the optimal configuration of elliptical tube compared with the optimal circular tube.

Forced convection numerical and experimental of air flow over the elliptic tube bank in cross-flow was reported by Ibrahim and Gomaa [16]. The many design parameters effects of Reynolds number range 5600 to 40000, axis ratios of tube (0.25, 0.33, 0.5 and 1) and the attack angle of the flow range 0 to 150^o. The results revealed that, enhance the heat transfer coefficient frequently at the increase of attack angle clockwise into 90^o. In addition, the was qualified for the best thermal performance of an elliptical tube heat exchanger the small values of the Reynolds number, attack angle and ratio of an axis. Tahseen et al. [17,18] have 2–D numerical studies incompressible, steady state flow and using the body fitted coordinate (BFC). The first study heat transfer over a two flat tube staggered and second study the heat transfer over series in-line flat tube between parallel plate channel. The two studies show effects of the Reynolds number on the heat transfer coefficient. The results revealed that the heat transfer coefficient increase with an increase of Reynolds number always.

In this study, an experimental investigation on heat transfer and pressure drop over flat tube in air cross flow. The external flow of fluid Reynolds number based on the mean free stream air velocity and outer hydraulic of the tube, changed from 124.5 to 622.5. As well as, the three different heat flux supply at the outer surface of tube (354.9, 1016.3 and 1935.8) W/m^2, respectively, with a view to examine the effects of Reynolds number and heat flux on the air pressure drop and heat transfer rate across the flow of a flat tube.

2. Experimental investigation and techniques

The flat tube arrangement was made from aluminium with the transverse diameter, d_T = 11–mm and longitudinal diameter, d_L = 18.5–mm with the thickness of tube 1 mm. The outer hydraulic diameter D_h = 13.5–mm with the length of 200 mm the photograph and dimensions presented in Fig. 1. The perimeter of the flat tube equal 1.54 times for the perimeter round tube which the diameter equal the small diameter (transverse) for flat tube. The double electric heaters were inserted the inside of the tube to simulate the heat flux originated from a hot fluid. The flat tube was then assembled according to the design in a drawer from Teflon plate type (PTFE), which is the test module. Losses minimized by holding the end of the flat tube between two Teflon walls separated by the distance L = 200 mm.

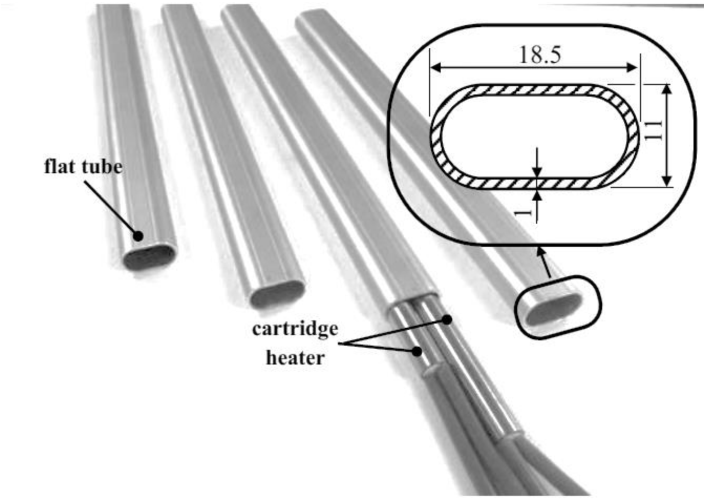

Fig. 1. The photographs of the cross-section flat tube and assembly the heater elements; all dimensions (mm).

Two heating elements, the consisted of cylindrical electric heaters each rated at 50 W up to 850 W with 220 V AC. The outside diameter for the electric heaters is 8 mm and the length of 200 mm the diameter small enough to be inserted in the aluminum tubes see Fig. 1. The heaters were connected in parallel and AC voltage source variables that produced voltages range 0 to 125 V. The maximum power supply 220 V and maximum current of 2.5 A the AC voltage source variable models LOADSTAR 850. The current (I) and voltage (E) measurements were performed with a current clam meter and volt measurement meter with a resolution of 0.05 A and 0.05 V, respectively. Eight thermistors of type EPCOS B57164K0102J NTC (resistance 1000 Ω at 25 ^{o}C) were placed in the test module. The thermistors locations at before, inlet and outlet test rig were placed in the center between the side walls of the wind tunnel and on the midline of the elemental channels. Two thermistors were placed at the arrangement inlet ($T_{in,1}$ – $T_{in,2}$), three at the surfaces of tubes ($T_{s,1}$ –$T_{s,3}$) and two at the outlet ($T_{out,1}$ –$T_{out,2}$) in one elemental channel. An additional thermistor (T_{bef}) was placed on the extended region at 400 mm before the test module to measure the temperature of free stream. Thermistors at the surfaces of the tube showed that the difference between the tubes in one element channel is negligible, and are within ±0.57 °C margin with respect to average three thermistors. Finally, the thermistor put in the extended region for measuring free stream temperatures within ±0.22 °C margin with respect to the average temperature measured inlet arrangement, in all the tests carried out in this work. The velocity measurements were taken with a vane type hot wire anemometer; model YK-2004AH which was placed in the extended flow region, as shown in Fig. 2, in the range of 0.2 m/s–20 m/s. The resolution 0.1 m/s of reading and uncertainty in free stream velocity U_∞ was ±(1–5% +0.1 m/s). The velocity of free stream U_∞ was varied 0.6 m/s–1.0 m/s in this study. The pressure drop measurements were taken using the differential pressure meter model TESTO 510. The operation range of 0–100 kPa with the resolution 1 Pa of reading and the accuracy ±0.3 Pa. The differential pressure measurements had the finality of measuring the pressure drop across each of change the free stream velocity in all experiments as shown in Fig. 2. The experimental work includes the attainment of temperature data using TESTO highly accurate thermometer, model TESTO 110 the nominal range of -50 °C to +150 °C the temperature thermometer resolution is 0.1°C and the accuracy around ±0.2 °C. The thermistors were calibrated in the laboratory for the purpose of finding the deviation limits. The details of the calibration are given in Ishak et al. [14].

Started each run by selecting the voltage and current supply to the cartridge heaters. The selected air velocity of free stream, then we waited for 1.5–2.0 hour while monitor the changes in voltage, current, T_{bef}, $T_{in,1}$–$T_{in,2}$, $T_{s,1}$–$T_{s,3}$ and $T_{out,1}$–$T_{out,2}$. The relative deviation in the voltage, current and temperature were range 0.3%-2.6%, 1.7%–3.6% and 0.16%–0.7%, respectively. These changes were estimated relatively by repeating the same value Re_{Dh} value within 7.5–8.0 hours. It should be noted that these relative changes are small when compared with the uncertainties in the relevant measurements.

3. Data reduction

In this experiment, it is assumed steady state flow. To investigate in the following relations for the relevant air properties and used in the following calculations. They are based on data and valid in the range of temperature. $250\text{K} \leq 0.5(\overline{T_{in}} + \overline{T_{out}}) \leq 275\text{K}$ [19];

$$\left.\begin{aligned}
\rho_a &= 2.209 - 3.414 \times 10^{-3}\left(\frac{\overline{T_{in}} + \overline{T_w}}{2}\right), && \text{kg/m}^3 \\
c_{P_a} &= \left[9.848 + 6.76 \times 10^{-4}\left(\frac{\overline{T_{in}} + \overline{T_w}}{2}\right)\right] \times 10^{2}, && \text{J/(kg K)} \\
k_a &= \left[3.479 + 7.58 \times 10^{-2}\left(\frac{\overline{T_{in}} + \overline{T_w}}{2}\right)\right] \times 10^{-3}, && \text{W/(m K)} \\
\mu_a &= \left[4.475 + 4.564 \times 10^{-2}\left(\frac{\overline{T_{in}} + \overline{T_w}}{2}\right)\right] \times 10^{-6}, && \text{kg/(m s)}
\end{aligned}\right\} \tag{1}$$

in expression,

$$\overline{T_{in}} = \frac{1}{n}\sum_{i=1}^{n}(T_{in})_i\ , \quad n = 2\ ; \quad \overline{T_w} = \frac{1}{n}\sum_{i=1}^{n}(T_w)_i\ , \quad n = 3$$

The electrical heat gain rate [voltage (E) × current (I)], is uniform heat flux (UHF) from the outer tube surface can be evaluated as:

$$q_{sup} = I \times E \tag{2}$$

The steady state heat balance of the electrical heat test surface can be written as:

$$q_{convection} = q_{sup} - q_{conduction} - q_{radiation} \tag{3}$$

Heat transfer from the system may be;

i) Conduction between lab and the wall of the tubes was neglected because of the extremely low thermal conductivity of air (0.23 W/(m °C)) of Teflon and negligible temperature difference between the lab outer walls of the Teflon.

ii) Radiation heat transfer between surfaces of tubes and surrounding were also neglected. Based on the measurement of $0.5(\overline{T_{in}} + \overline{T_{out}})$ and mean $\overline{T_s}$ was estimated the radiation transfer coefficients as [10];

$$\overline{h_{\mathrm{rad}}} = \varepsilon \times \sigma \times \left[\left\{\left(\frac{\overline{T_{\mathrm{in}}} + \overline{T_{\mathrm{out}}}}{2}\right)^2 + (\overline{T_{\mathrm{s}}})^2\right\} \times \left\{\left(\frac{\overline{T_{\mathrm{in}}} + \overline{T_{\mathrm{out}}}}{2}\right) + \overline{T_{\mathrm{s}}}\right\}\right] \tag{4}$$

here

$$\overline{T_{\mathrm{s}}} = \frac{1}{n}\sum_{i=1}^{n}(T_{\mathrm{s}})_{\mathrm{i}}\ , \quad n = 3$$

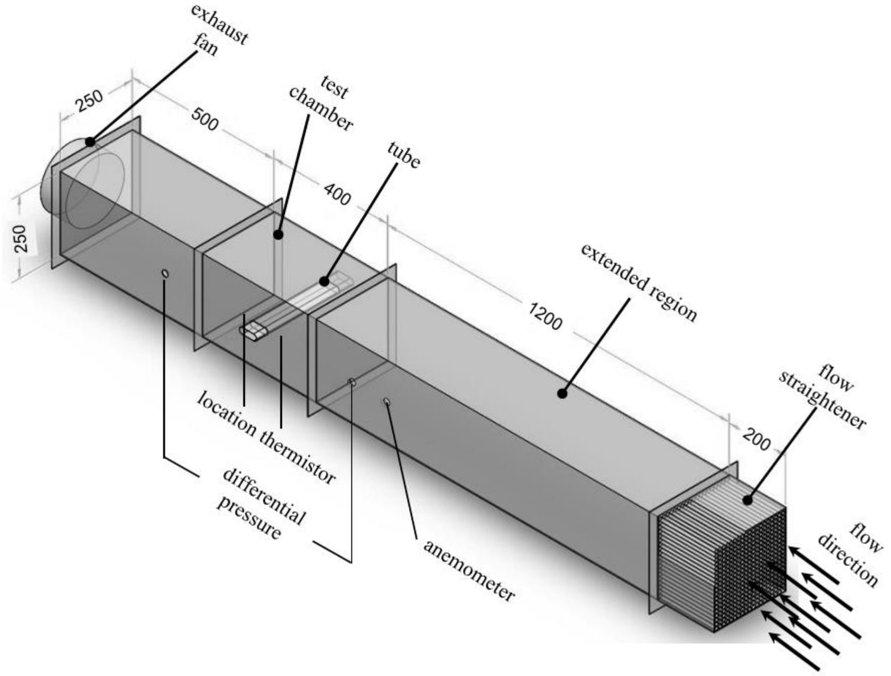

Fig. 2. The schematic diagram of the experimental setup, all dimensions (mm).

For a commercial aluminum tube with emissivity, $\varepsilon \cong 0.028$ [19], $\overline{h_{\mathrm{rad}}}$ was found in a range between (0.174–0.205) W/m^2 $^{\circ}$C, in approximately 0.0102%–0.15% of the air side convection heat transfer coefficient, $\bar{h}$. Thus, the heat transfer between the air and the surface of the tubes was actually due to the convection and the mechanism of the Equation (3) was rewritten [20]:

$$q_{\mathrm{convection}} \cong q_{\mathrm{sup}} = \bar{h}\, A_{\mathrm{s}}\left[\overline{T_{\mathrm{s}}} - \left(\frac{\overline{T_{\mathrm{in}}} + \overline{T_{\mathrm{out}}}}{2}\right)\right] \tag{5}$$

Can be employed with

$$A_{\mathrm{s}} = [\pi d_{\mathrm{T}} + 2(d_{\mathrm{L}} - d_{\mathrm{T}})] \times L$$

The definition $\overline{T_{\mathrm{in}}}$ the inlet air temperature was the variable (24.5–25.3) $^{\circ}$C and the average temperature of the surfaces of tube, $\overline{T_{\mathrm{s}}}$. For the steady state condition, the overall heat transfer rate, $q_{\mathrm{convection}}$ was equal to the electrical heat supply, q_{sup}. From Equation (3), the average heat transfer coefficient was determined as:

$$\bar{h} = \frac{q_{\mathrm{sup}}}{A_{\mathrm{s}}\left[\overline{T_{\mathrm{s}}} - \left(\frac{\overline{T_{\mathrm{in}}} + \overline{T_{\mathrm{out}}}}{2}\right)\right]} \tag{6}$$

And is usually used in the average Nusselt number which is defined via Equation (7);

$$\overline{\mathrm{Nu}_{D_\mathrm{h}}} = D_\mathrm{h}\frac{\overline{h}}{k_\mathrm{f}} \tag{7}$$

in the expression, k_f is the thermal conductivity of air and the hydraulic diameter;

$$D_\mathrm{h} = 4 \times \frac{\left[\frac{\pi}{4}(d_\mathrm{T})^2 + (d_\mathrm{L} - d_\mathrm{T})d_\mathrm{T}\right]}{\pi d_\mathrm{T} + 2(d_\mathrm{L} - d_T)} \tag{8}$$

The Reynolds number based on the hydraulic diameter is defined;

$$\mathrm{Re}_{\mathrm{D}_h} = U_\infty \times D_\mathrm{h} \times \frac{\rho}{\mu} \tag{9}$$

The friction factor is calculated as follows [21];

$$f = \frac{2\Delta P}{\rho U_\infty^2}\left(\frac{D_\mathrm{h}}{4L}\right) \tag{10}$$

The experimental uncertainty issues were dealt by Editorial [22] and Holman [23]. There is more than one way to estimate the uncertainty in the experimental results and has presented by Kline and McClintock. The few sample calculations here. The independent parameters (such as tube dimensions, temperature, velocity, etc.) and the dependent parameters (like $\mathrm{D}_h, \mathrm{Re}_{\mathrm{D}_h}, q_{\mathrm{sup},}\, \overline{\mathrm{Nu}_{\mathrm{D}_h}}$, etc.). Which are independent functions of other measured parameters, an uncertainty for the independent variable spreads them, according to their functional relationship. The example, in case of the Reynolds number, $\mathrm{Re}_{\mathrm{D}_h}$;

$$\mathrm{Re}_{\mathrm{D}_h} = U_\infty \times D_h \times \frac{\rho}{\mu} \tag{11}$$

The uncertainties of density, free stream velocity; viscosity and hydraulic diameter propagate into $\mathrm{Re}_{\mathrm{D}_h}$, and can be estimated in terms of absolute values (%) as follows:

$$U_{\mathrm{Re}_{\mathrm{D}_h}} = \left[\left(\frac{\partial \mathrm{Re}_{\mathrm{D}_h}}{\partial \rho}U_\rho\right)^2 + \left(\frac{\partial \mathrm{Re}_{\mathrm{D}_h}}{\partial U_\infty}U_{U_\infty}\right)^2 + \left(\frac{\partial \mathrm{Re}_{\mathrm{D}_h}}{\partial \mu}U_\mu\right)^2 + \left(\frac{\partial \mathrm{Re}_{\mathrm{D}_h}}{\partial D_h}U_{D_h}\right)^2\right]^{1/2} \tag{12}$$

The entire description of the uncertainty calculation can be found in Ishak et al. [14]. The uncertainties in finding the$\mathrm{D}_h, \mathrm{Re}_{\mathrm{D}_h}, q_{\mathrm{sup},}\, \overline{\mathrm{Nu}_{\mathrm{D}_h}}, f$ were estimated and found to remain approximately within ±5.68%, ±2.19%, ±5.67%, ±4.10% and ±1.10%, respectively.

4. Results and discussion

In the present experimental work, the effects of the front free-steam velocity and heat flux supply on the air flow and heat transfer over flattened tube in the channel. The relationship $\overline{\mathrm{Nu}_{\mathrm{D}_h}} - q_\mathrm{sup}$for several $\mathrm{Re}_{\mathrm{D}_h}$number was plotted in Fig. 3. The results reveals that the $\overline{\mathrm{Nu}_{\mathrm{D}_h}}$ number increased nearly linear always with an increasing $q_{\mathrm{sup},}$ as was expected. The heat transfer coefficient depended on the temperatures difference between the tube surface and free stream of air flow. In other words, increasing $q_{\mathrm{sup},}$ a leads to increased temperature gradient thus increase further in $\overline{\mathrm{Nu}_{\mathrm{D}_h}}$ number.

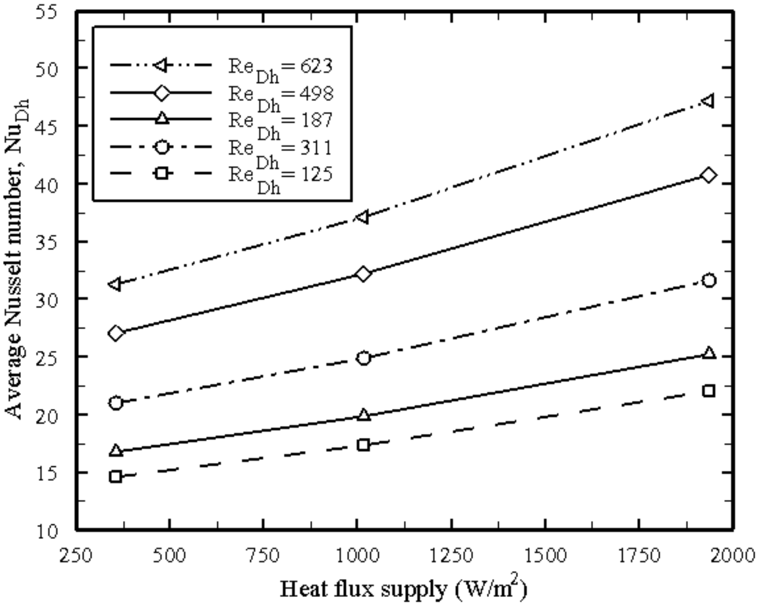

Fig. 3. The $\overline{\mathrm{Nu}_{\mathrm{D}_h}}$ number variation with q_{sup} at different $\mathrm{Re}_{\mathrm{D}_h}$ number.

The $\overline{\mathrm{Nu}_{\mathrm{D}_h}}$number various with $\mathrm{Re}_{\mathrm{D}_h}$ number at a different heat flux supply is plotted in Fig. 4. As might be expected, the $\overline{\mathrm{Nu}_{\mathrm{D}_h}}$ number increases with increasing of the $\mathrm{Re}_{\mathrm{D}_h}$ number. The reason for this issue to the reduction in thickness of a boundary layer and the powerful periodical vortices of air flow in the detached zones near to the behind wall of the tube. In general, $\overline{\mathrm{Nu}_{\mathrm{D}_h}}$ number increases with $\mathrm{Re}_{\mathrm{D}_h}$number. The heat transfer coefficient is largest at the stagnation point and increase with a long time contact of fluid with the surface of tube because of the increased thermal boundary layer. On the other hand, when $\mathrm{Re}_{\mathrm{D}_h}$ number increases the level of turbulence strength caused by secondary flow was increased. This enables be construed increase $\overline{\mathrm{Nu}_{\mathrm{D}_h}}$ number. In this regard, the $\overline{\mathrm{Nu}_{\mathrm{D}_h}} - \mathrm{Re}_{\mathrm{D}_h}$ correlation was using a non–linear regression analysis of the empirical data is defined as:

$$\overline{\mathrm{Nu}_{\mathrm{D}_h}} = C \times \left(\mathrm{Re}_{\mathrm{D}_h}\right)^m \tag{13}$$

The constant (*C*) and (*m*) are estimated by statistical processing for experimental results, can be seen in Table 1. Corresponding trends are given in Fig. 5. It is evident from the figure, the experimental data of Žukauskas [1] with circular tube, the analytical solution by Khan et al. [24] for elliptic tube and for $100 \leq \mathrm{Re} \leq 5000$ and the numerical study by Bahaidarah et al. [25] using flat tube shape for $100 \leq \mathrm{Re} \leq 350$. In general, current work satisfactorily agreed with trends of the previous studies. For the sake of comparison, the trends of result near to the experimental result by Žukauskas [1] are illustrated in the same figure. Noticeable, there was a deviation of about 4.4–16.7% between current results and numerical results from Bahaidarah et al.[25].

Table 1. Summary of estimated parameters in Eq. (13).

q_{sup}, W/m^2	*C*	*m*	R^2 (%)
354.90	1.313	0.500	100
1016.32	1.557	0.500	100
1935.84	1.921	0.503	99.7

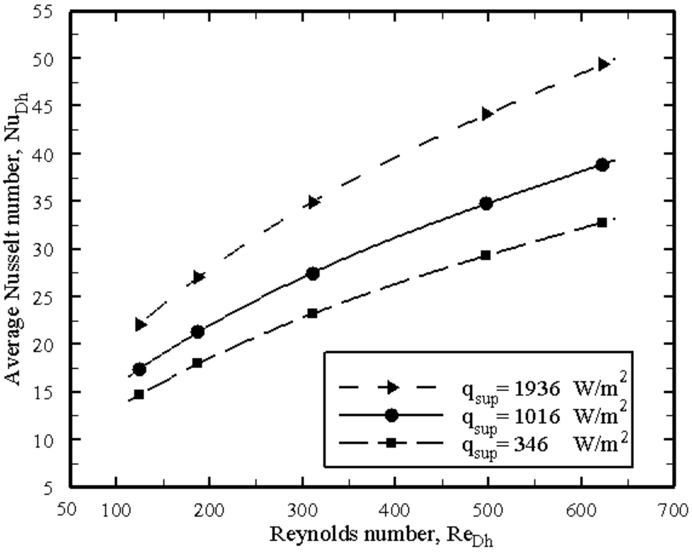

Fig. 4. The $\overline{\mathrm{Nu}_{\mathrm{D}_h}}$ number versus with $\mathrm{Re}_{\mathrm{D}_h}$ number at several q_{sup}.

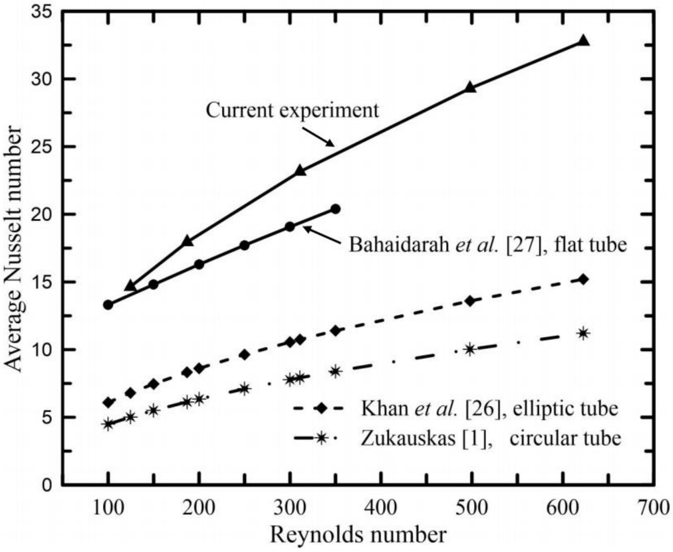

Fig. 5. Comparison of the present results and foretelling with published literature [27].

The pressure drop and friction factor, *f* for isoflux flat tube in the air versus free stream velocity are illustrated in Fig. 6. It is clear that ΔP increased nearly linearly and *f* decreased with increase the free stream velocity. Although, the *f* is directly proportional with the output the ΔP decrease with increase air velocity. With the rise in free stream velocity, relatively contributes to increase the inertial forces whereas was decreases of the *f* (that is the control factor on the friction). This can be attributed for a reason, to the preferable aerodynamic shape for the flat tube which generates less drag force. The friction factor value appears to reduction approximately to 0.018 according to the maximum velocity is 1 m/s.

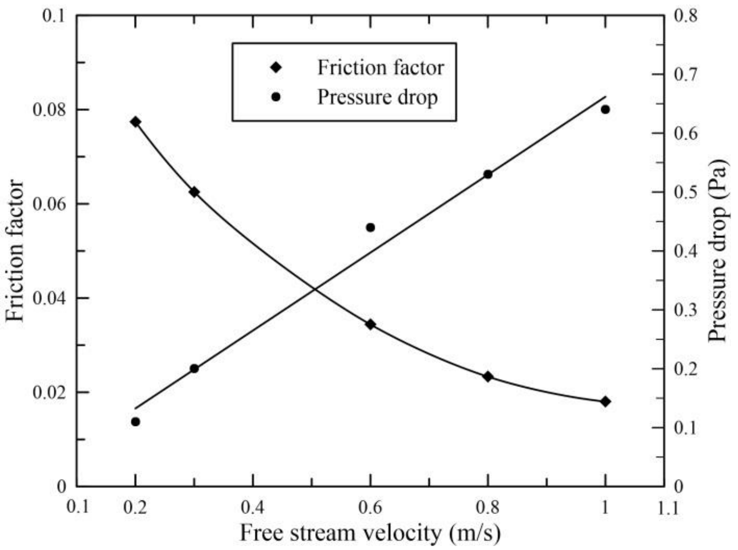

Fig. 6. Variation of ΔP parameter and f with free stream velocity of air.

5. Conclusions

The heat transfer and pressure drop a flat tube in a cross flow of air have been experimentally study. A heat flux supply in the range of 354.9 W/m^2 –1935.84 W/m^2 with the Reynolds number ranging are $125 \leq \mathrm{Re}_{\mathrm{D}_h} \leq 623$. This paper examines the impact of two parameters on the average heat transfer coefficient and friction factor for air flow over single flat tube. It can be summarized that the experimental results are drawn:

i) The heat transfer coefficient increase almost linear with increase heat flux supply for all free stream velocity.
ii) The average Nusselt number increase with increase Reynolds number with any heat flux supply tested.
iii) The pressure drop increased and friction factor decrease with increasing of free stream velocity.
iv) The compared of the results with similar earlier studies as though the good approximation to the similar trends.
v) Lastly, this study clearly show that the flat tube has the pressure drop is small and the heat transfer coefficient is higher compare with circular and elliptic shapes of tube.

Acknowledgements

The authors would like to acknowledgements Ministry of Education Malaysia and Universiti Malaysia Pahang for providing laboratory facilities and financial support under project no. RDU120103 .

References

[1] A. Žukauskas, Heat transfer from tubes in crossflow, Adv. Heat Transfer. 8 (1972), 93–158.
[2] R.L. Webb, Principles of enhanced heat transfer, 2nd Edition, Wiley, USA, 1993.
[3] E. Buyruk, M.W. Johnson, I. Owen, Numerical and experimental study of flow and heat transfer around a tube in cross-flow at low reynolds number, Inter J Heat Fluid Flow 19(3) (1998), 223–232.
[4] F.P. Incropera, D.P. DeWitt, T.L. Bergman, A.S. Lavine, Fundamentals of heat and mass transfer, 6th Edition, John Wiley & Sons Inc., USA, 2007.
[5] V.T. Morgan, The overall convective heat transfer from smooth circular cylinders, Adv Heat Transfer 11(1975), 199–264.
[6] T. Ota, H. Nishiyama, Y. Taoka, Heat transfer and flow around an elliptic cylinder, Inter J Heat Mass Transfer 27(10) (1984), 1771–1779.
[7] J.W. Baughn, M.J. Elderkin, A.A. McKillop, Heat transfer from a single cylinder, cylinders in tandem, and cylinders in the entrance region of a tube bank with a uniform heat flux, J Heat Transfer 108(2) (1986), 386–391.
[8] G. Stanescu, A.J. Fowler, A. Bejan, The optimal spacing of cylinders in free-stream cross-flow forced convection, Inter J Heat Mass Transfer 39(2) (1996), 311–317.

[9] A. Bejan, A.J. Fowler, G. Stanescu, The optimal spacing between horizontal cylinders in a fixed volume cooled by natural convection, Inter J Heat Mass Transfer 38(11) (1995), 2047–2055.

[10] M.G. Khan, A. Fartaj, D.S.K. Ting, An experimental characterization of cross-flow cooling of air via an in-line elliptical tube array, Inter J Heat Fluid Flow 25(4) (2004), 636–648.

[11] S. Sanitjai, R.J. Goldstein, Forced convection heat transfer from a circular cylinder in crossflow to air and liquids, Inter J Heat Mass Transfer 47(22) (2004), 4795–4805.

[12] B.H. Chang, A.F. Mills, Effect of aspect ratio on forced convection heat transfer from cylinders, Inter J Heat Mass Transfer 47(6–7) (2004), 1289–1296.

[13] T.A. Tahseen, M. Ishak, M.M. Rahman, An experimental study air flow and heat transfer over in-line flat tube bank, Inter J Automot Mech Eng 9 (2014) 1487-1500.

[14] M. Ishak, T.A. Tahseen, M.M. Rahman, Experimental investigation on heat transfer and pressure drop characteristics of air flow over a staggered flat tube bank in cross-flow, Inter J Automot Mech Eng 7 (2013), 900–911.

[15] R.S. Matos, T.A.J. Laursen, V.C. Vargas, A. Bejan, Three-dimensional optimization of staggered finned circular and elliptic tubes in forced convection, Inter J Thermal Sci 43(5) (2004), 477–487.

[16] T.A. Ibrahim, A. Gomaa, Thermal performance criteria of elliptic tube bundle in crossflow, Inter J Thermal Sci 48(11) (2009), 2148–2158.

[17] T.A. Tahseen, M. Ishak, M.M. Rahman, Analysis of laminar forced convection of air for crossflow over two staggered flat tubes, Inter J Automot Mech Eng 6(2012), 753–765.

[18] T.A. Tahseen, M. Ishak, M.M. Rahman, A numerical study of forced convection heat transfer over a series of flat tubes between parallel plates, J Mech Eng Sci 3(2012), 271–280.

[19] C.V. Collett, A.D. Hope, Engineering measurements, ELBS, Singapore, 1983.

[20] S. Naik, S.D. Probert, M.J. Shilston, Forced-convective steady-state heat transfers from shrouded vertical fin arrays, aligned parallel to an undisturbed air-stream, Appl Energ 26(2) (1987), 137–158.

[21] R.K. Shah, D.P. Sekuli'c, Fundamentals of heat exchanger design, John Wiley & Sons, Inc. Hoboken, New Jersey, USA, 2003.

[22] Editorial, Journal of heat transfer policy on reporting uncertainties in experimental measurements and results, J Heat Transfer 115(1) (1993), 5–6.

[23] J.P. Holman, Experimental methods for engineers, McGraw-Hill, New York, 2012.

[24] W.A. Khan, R.J. Culham, and M.M. Yovanovich, Fluid flow around and heat transfer from elliptical cylinders: analytical approach, J. Thermophys. Heat Transfer. 19(2) (2005), 178–185.

[25] H.M.S. Bahaidarah, M. Ijaz, N.K. Anand, Numerical study of fluid flow and heat transfer over a series of in-line noncircular tubes confined in a parallel-plate channel, Numer. Heat Transfer. Part B, 50(2) (2006), 97–119.

Available online at www.sciencedirect.com

ScienceDirect

Procedia Engineering00 (2015) 000–000

Procedia Engineering

www.elsevier.com/locate/procedia

6th BSME International Conference on Thermal Engineering (ICTE 2014)

Analysis of Heat Transfer in Channel Flow Subject to Sine-Bump Heating

Umera Sarjana[a], M. Zakir Hossain[b], AKM Monjur Morshed[a]
[a]Department of Mechanical Engineering, Bangladesh University of Engineering and Technology (BUET), Dhaka.
[b]Department of Mechanical and Materials Engineering, University of Western Ontario, Ontario, Canada.
umera.sarjana@gmail.com[a] zakir92@yahoo.com[b] mmmsumon@gmail.com[a]

Abstract

Convection in a channel subject to a distributed sinusoidal bump like heating applied at the lower wall has been studied. It is found that small wave number heating provides large plumes whereas large wave number heating provides a uniform temperature distribution at the upper part of the channel. Heat transfer is more efficient at low Reynolds number with small wave number heating.

Peer-review under responsibility of organizing committee of the 6th BSMEInternational Conference on Thermal Engineering (ICTE 2014).

Keywords: Convection; Heating; Reynolds number; sinusoidal bump;

1.Introduction

A fluid layer bounded by two parallel plates heated uniformly from below represents a classical system known as Rayleigh-Benard (RB) convection [1]. It is known that this convection motion starts when the temperature difference between the plates reaches a critical value. Below this critical point the heat is transported between the plates by conduction and the temperature changes linearly across the layer. Above this critical point the heat transfer rate is increased by the thermal instability and the temperature field is strongly influenced by the presence of convective roll vortices.

* AKM Monjur Morshed. Tel.:+8801795075520;
*E-mail address:*monjur_morshed@me.buet.ac.com

Peer-review under responsibility of organizing committee of the 6th BSME International Conference on Thermal Engineering (ICTE 2014).

These roll vortices assists to augment the heat transfer process in the case of forced convection [2]. In some applications, the bump-like heating is combined with a forced motion resulting in a mixed convection. Such convection is most likely to occur in many system of practical importance.Some of the examples of spatially distributed heating are included in the presence of ocean and land in the earth, presence of local lakes, a set of local fires, a set of computer chips, a set of electrically heated wires inserted on a surface etc [3]. Such systems are modeled using an infinite slot subjected to periodic variation of the temperature defined by sinusoidal-bump-like function at the bottom wall.

Convection driven by a periodic heating, defined by a simple sinusoidal function, in the absence of mean temperature gradient has been studied by Hossain and Floryan [4]. Fluid motion is driven by horizontal density gradients and occurs regardless of the intensity of the heating. Its pattern is determined by the externally imposed heating pattern unless transition to secondary states is encountered. The net heat transfer between the walls is driven by the nonlinear effects. The same heating applied to the moving fluid results in the reduction of drag experienced by this fluid. This so-called super-thermo-hydrophobic effect has been described in detail by Hossain et al. [5], where they demonstrate that spatially periodic heating helps to form small separation bubbles that isolate the moving stream from direct contact with the solid wall and thus reduce the shear stress acting on the fluid. The fluid movement inside separation bubbles is partially driven by the buoyancy gradients associated with the heating, which further contributes to the reduction of the required pressure drop.

Instead of simple sinusoidal heating, distributed bump like heating which occurs more frequently is focused in this study. This type of heating is introduced with a presumption that the heating would create separation bubbles in the flow system so that these bubbles help to enhance the heat transfer process. The lower wall is subjected to a spatially non-uniform heating distributed in the longitudinal direction so that it represents a sinusoidal-bump-like heating. The forcing generated by the heating is characterized by a wave number and amplitude, resulting in a two-parameter problem.

2. Problem formulation

A two-dimensional channel with height 2h as shown in Fig. 1 is considered in this study. The lower wall of the channel is subject to a spatial periodic sine-bump heating with temperatures of the lower (T_L) and upper (T_U) walls are specified as,

$$\begin{aligned} T_L(x) &= 0.5\cos(\alpha x) && 0 \le x \le \lambda/4 \\ &= 0 && \lambda/4 \le x \le 3\lambda/4 \qquad \mathrm{T_U(x)} = 0 \\ &= 0.5\cos(\alpha x) && 3\lambda/4 \le x \le \lambda \end{aligned} \tag{1}$$

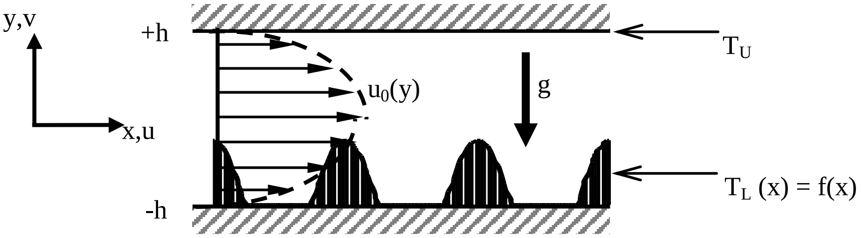

Figure 1.Sketch of the system configuration. Here, f(x) is a sinusoidal bump function as (1).

The velocity and pressure fields in the absence of any heating have the form of Poiseuille flow, and have the following form,

$$V(x,y) = [U_0(y),0] = [1-y^2,0], \qquad p_0(x,y) = -2x/\mathrm{Re} \tag{2}$$

Where **V**=(u,v) denotes the velocity vector scaled with the maximum of the x-velocity U_{max}, p_0 stands for the pressure scaled with ρU_{max}^2, half-channel height h has been used as the length scale and the Reynolds number is defined as $Re=U_{max}h/\nu$.

The applied heating produces flow modifications that can be represented in the form

$$u_2(x,y) = \mathrm{Re}\, u_0(y) + u_1(x,y), \qquad v_2(x,y) = v_1(x,y),$$
$$T_2(x,y) = \mathrm{Pr}^{-1}\, T_0(x,y) + T_1(x,y), \quad p_2(x,y) = \mathrm{Re}^2\, p_0(x,y) + p_1(x,y) \tag{3}$$

where (u_1,v_1), p_1 and T_1 stand for the velocity, the pressure and the temperature modifications due to the applied heating.

The dimensionless non-uniform conductive temperature field T_0 in (3) can be determined from the following problem

$$\partial^2 \mathrm{T}_0 / \partial \mathrm{x}^2 + \partial^2 \mathrm{T}_0 / \partial \mathrm{y}^2 = 0 \qquad \text{with boundary conditions (1).} \tag{4}$$

Solution of (4) has the form,

$$T_0(x,y) = \sum_{n=-\infty}^{+\infty} T_0^{(n)}(y) e^{in\alpha x}$$
$$= \sum_{n=-\infty}^{+\infty} \left[\frac{(T_U^{(n)} - T_L^{(n)})\sinh(n\alpha y)}{2\sinh(n\alpha)} + \frac{(T_U^{(n)} + T_L^{(n)})\cosh(n\alpha y)}{2\cosh(n\alpha)} \right] e^{in\alpha x} \tag{5}$$

With $T_L^{(0)} = 2/\pi, T_L^{(\pm n)} = 1/\pi(n^2-1)$ for $n \geq 0$ and $T_U^{(n)} = 0$ for $n \geq 1$

The dimensionless field equations describing motion of the incompressible-Newtonian fluid and changes in the temperature field have the form,

$$(\mathrm{Re}\, u_0 + u_1)\frac{\partial u_1}{\partial x_1} + \mathrm{Re}\, v_1 \frac{du_0}{dy} + v_1 \frac{du_1}{dy} = -\frac{\partial p_1}{dy} + \nabla^2 u_1 \tag{6a}$$

$$(\mathrm{Re}\, u_0 + u_1)\frac{\partial v_1}{\partial x} + v_1 \frac{dv_1}{dy} = -\frac{\partial p_1}{dy} + \nabla^2 u_1 + R\alpha T_1 + R\alpha\, \mathrm{Pr}^{-1}\, T_0 \tag{6b}$$

$$\mathrm{Pr}((\mathrm{Re}\, u_0 + u_1)\frac{\partial T_1}{\partial x} + v_1 \frac{dT_1}{dy}) + (\mathrm{Re}\, u_0 + u_1)\frac{\partial T_0}{\partial x} + v_1 \frac{dT_0}{dy} = \nabla^2 T_1 \tag{6c}$$

$$\frac{\partial u_1}{\partial x} + \frac{\partial v_1}{\partial y} = 0 \tag{6d}$$

where Ra = gΓh3Td/νk is the Rayleigh number, ∇^2 denotes the Laplace operator. The system is modeled with Boussinesq approximation which accounts the variation of density with temperature considering all other fluid properties to be constant [6].

The boundary conditions take the form

$$u_1(\pm 1) = 0, v_1(\pm 1) = 0, T_1(\pm 1) = 0, \tag{7}$$

The flow with or without the heating has to carry the same mass flow rate, i.e., fixed mass flow rate constraint. This constraint can be expressed as

$$Q = \int_{-1}^{1} u_2 dy = \int_{-1}^{1} (\mathrm{Re} u_0 + u_1) dy = \frac{4\mathrm{Re}}{3} \tag{8}$$

The complete problem, which consists of the field equations (6), the boundary conditions (7) and constraint (8), needs to be solved numerically.

3.Numerical Solution

To solve numerically we define the stream function ψ (x,y) in the usual manner, i.e., $u_1 = \frac{\partial \psi}{\partial y}$

$v_1 = -\frac{\partial \psi}{\partial x}$, and eliminate pressure from the momentum equations bringing the governing equations to the following form

$$\mathrm{Re} u_0 \frac{\partial}{\partial x}(\nabla^2 \psi) - \mathrm{Re} \frac{d^2 u_0}{dy^2} \frac{\partial \psi}{\partial x} + N_\psi = \nabla^4 \psi - Ra \frac{\partial T_1}{\partial x} - Ra \mathrm{Pr}^{-1} \frac{\partial T_0}{\partial x} \tag{9a}$$

$$\mathrm{Pr} \mathrm{Re} u_0 \frac{\partial T_1}{\partial x} + \mathrm{Pr} N_{T_1} + \mathrm{Re} u_0 \frac{\partial T_0}{\partial x} + N_{T_0} = \nabla^2 T_1 \tag{9b}$$

where the nonlinear terms are written in the conservative form, i.e.

$$N_\psi = \frac{\partial}{\partial y}\left(\frac{\partial}{\partial x}\langle u_0, u_1 \rangle\right) + \left(\frac{\partial}{\partial y}\langle u_1, v_1 \rangle\right) - \frac{\partial}{\partial x}\left(\frac{\partial}{\partial x}\langle u_1, v_1 \rangle + \left(\frac{\partial}{\partial y}\langle v_1, v_1 \rangle\right)\right),$$

$$N_{T_1} = \frac{\partial}{\partial x}\langle u_1, T_1 \rangle + \frac{\partial}{\partial y}\langle v_1, T_1 \rangle, \quad N_{T_0} = \frac{\partial}{\partial x}\langle u_1, T_0 \rangle + \frac{\partial}{\partial y}\langle u_1, T_1 \rangle$$

The solution is assumed to be in the form of Fourier expansions, i.e.

$$\psi(x,y) = \sum_{n=-\infty}^{+\infty} \psi^{(n)}(y) e^{in\alpha x}, T_1(x,y) = \sum_{n=-\infty}^{+\infty} \psi^{(n)}(y) e^{in\alpha x}, \tag{10a}$$

$$u_1(x,y) = \sum_{n=-\infty}^{+\infty} u_1^{(n)}(y) e^{in\alpha x}, v_1(x,y) = \sum_{n=-\infty}^{+\infty} v_1^{(n)}(y) e^{in\alpha x}, \tag{10b}$$

$$p_1(x,y) = A_p x + \sum_{n=-\infty}^{+\infty} p_1^{(n)}(y) e^{in\alpha x} \tag{10c}$$

Where, $u_1^{(n)}=D\varphi^{(n)}$ and $v_1^{(n)} = in\alpha\varphi^{(n)}$ and A_p denotes pressure gradient modification.

Substitution of (10) into (9) and separation of Fourier components result in the following system of ordinary differential equations for the modal functions

$$D_n^2 \varphi^{(n)} - in\alpha \mathrm{Re}\left(u_0 D_n - \frac{d^2 u_0}{dy^2}\right)\varphi^{(n)} - in\alpha Ra \varphi^{(n)} = in\alpha Ra \mathrm{Pr}^{-1} T_0^{(n)} + N_\psi^{(n)} \tag{11a}$$

$$D_n \varphi^{(n)} - in\alpha \mathrm{Pr} \mathrm{Re} u_0 \varphi^{(n)} = in\alpha \mathrm{Re} u_0 T_0^{(n)} + N_{T_0}^{(n)} + \mathrm{Pr} N_{T_1}^{(n)} \tag{11b}$$

where $-\infty < n < +\infty, D = \dfrac{d}{dy}, D^2 = \dfrac{d^2}{dy^2}, D_n = D^2 - n^2\alpha^2$

$$N_{\psi}^{(n)} = in\alpha D\langle u_1, u_1\rangle^{(n)} + D^2\langle u_1, v_1\rangle^{(n)} + in^2\alpha^2\langle u_1, u_1\rangle^{(n)} - in\alpha D\langle v_1, v_1\rangle^{(n)}$$

$$N_{T_1}^{(n)} = in\alpha\langle u_1, T_1\rangle^{(n)} + D\langle v_1, T_1\rangle^{(n)},\ N_{T0}^{(n)} = in\alpha\langle u_1, T_0\rangle^{(n)} + D\langle v_1, T_0\rangle^{(n)}.$$

The linear terms have been placed on the left hand side, and the nonlinear and the known terms have been placed on the right hand side. The required boundary conditions for the modal functions have the form

$$D\varphi^{(n)}(\pm 1) = 0, \varphi^{(n)}(\pm 1) = 0, \text{ for } -\infty < n < +\infty \tag{12a,b}$$

$$\varphi^{(n)}(\pm 1) = 0, \text{ for } n \neq 0 \tag{12c}$$

$$\varphi^{(0)}(1) = M_1, \varphi^{(0)}(-1) = M_2, \tag{12d,e}$$

Where the constants M_1, M_2 can be selected arbitrarily [7]

In the case of the fixed mass flow rate constraint these constants have been selected in the form

$$\varphi^{(0)}(1) = 0, \varphi^{(0)}(-1) = 0, \tag{13a,b}$$

The system (11) together with the boundary conditions (12a-c) and either constraint (13a,b) needs to be solved numerically. For the purpose of numerical solution, expansions (10) have been truncated after N_M Fourier modes. The discretization method uses Chebyshev collocation technique based on N_T collocation points [8]. Gauss-Chebyshev-Lobatto points (Trefethen 2000) are used as the collocation points and their locations are computed from the following expression

$$y_k = \sin\left(\frac{\pi(N_T + 1 - 2k)}{2(N_T - 1)}\right), k = 0,1,2,....,N_T \tag{14}$$

The resulting nonlinear algebraic system of equation is solved using an iterative technique combined with under-relaxation in the form

$$\Phi_{j+1} = \Phi_j + RF(\Phi_{comp} - \Phi_j) \tag{15}$$

Where $\Phi=\{\varphi^{(n)},\varphi^{(n)}\}$, Φ_{comp} denotes the current solution, Φ_j denotes the previous solution, and Φ_{j+1} stands for the accepted value of the next iteration and RF denotes the relaxation factor. Once solution of this problem has been completed, the first approximation of the nonlinear terms is computed on the basis of the available approximation of the velocity and temperature fields and system (11) is resolved with the new approximation of the nonlinear terms used on the RHS. This process is continued, with the update of the nonlinear terms taking place after each iteration, until a convergence criterion in the form

$$\max(|\Phi_{comp} - \Phi_j|) < TOL \tag{16}$$

is satisfied. TOL in denotes tolerance at two consecutive iterations. TOL set at 10^{-8} is found to be sufficient in most of the computations.

4. Results and discussions

Due to the presence of the external flow the present problem becomes a three-parameter problem, and the parameters are (i) the heating wave number α which dictates the spatial distribution of the heating, (ii) the Rayleigh number Ra which defines the intensity of the heating, and (iii) the Reynolds number Re which describes the strength of the external flow.

The structure of the conductive temperature field shown in **Fig. 2** demonstrates presence of large plumes at heating wave number α =1 occupying almost the whole channel height. With the increase of heating wave number the height of this plume gradually reduces, and temperature distribution at the upper part of the channel becomes uniform which can easily be observed in Fig.2B. The conduction field creates non-uniform distribution of the buoyancy force along the length of the channel.

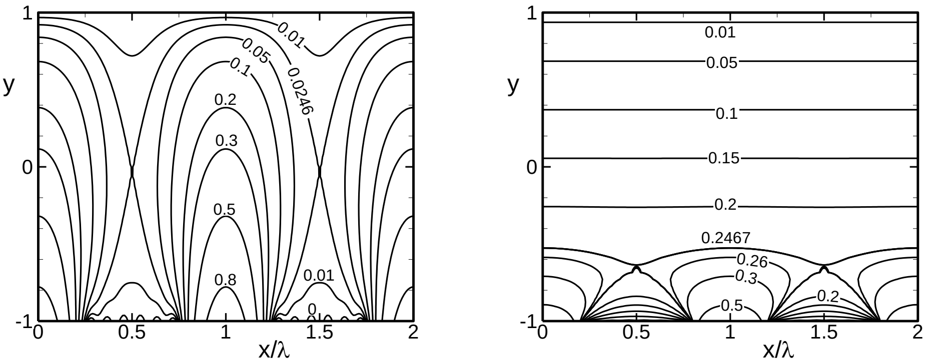

Figure 2.Isotherms of the conductive temperature field for the heating wave number α= 1(left) and α =10 (right).

With the presence of the above conduction field, when convection kicks in, the flow topology starts to evolve as shown in Fig. 3. For purely natural convection, (i.e. Re=0) the flow topology consists of counter rotating rolls (Fig. 3A). The fluid rises above the hot zones in the lower wall and descends above the non-heated zones forming pairs of counter-rotating rolls. When the external flow is introduced, flow topology starts to evolve away from the counter-rotating rolls, and streams of fluid starts to pass between the rolls. Figure 3B displays results for a weak external flow with Re = 1. The clock-wise rotating rolls are contained in the separation bubbles at the lower wall whereas the counter-clock-wise rolls are contained in the separation bubbles at the upper wall. This type of flow structure is usually observed at low Re, and when the intensity of heating is sufficiently high.

Further increase of flow strength washes away the upper-wall bubbles, retaining only the lower wall bubbles (Fig 3C). This type of flow structure occurs when the strength of flow Re is moderate, and intensity of heating Ra is sufficient to alter the bulk parallel motion of the fluids. In the lower wall some cold heavy fluids are trapped near the lower wall and isolated from the main stream flow and start to rotate.

When flow strength is sufficiently high and intensity of heating is sufficiently small, the lower-wall bubbles also disappear, and the flow becomes simple parallel flow (Fig. 3D). In this case, the intensity of heating cannot modify the bulk parallel motion of the fluid too much therefore we obtain very weak waviness in the flow stream. If the shear is further increased then the flow streamline becomes perfectly parallel.

The main quantity of interest is the heat transfer between the walls resulting from the convection. This heat transfer can be expressed in terms on the average Nusselt number Nu and defined as

$$\mathrm{Nu} = \frac{\mathrm{Pr}}{\lambda}\int_0^{\lambda}\left(-\left.\frac{d\theta_1}{dy}\right|_{y=-1}\right)dx = -\mathrm{Pr}\left.\frac{d\phi^{(0)}}{dy}\right|_{y=-1} \qquad (17)$$

Figure 4 shows the effect of heating intensity Ra on the heat transfer. It is evident that heat flow increases as the Rayleigh number Ra increases. Heat transfer is less for higher value of heating wave number (e.g., α=10). At higher α, convection prevails only near to the lower-heated wall, and at the upper part of the channel temperature changes linearly (see Fig. 2B) causing the heat to transport by conduction.

Figure 5 demonstrates the effect of strength of external flow Re on the heat transfer. Small Re flow is more efficient in heat transfer as Nu is higher in this region. Presence of upper and lower wall separation bubbles causes the hotter fluid to come in contact with the colder fluid easily thereby causes more heat to transport. With the increase of Re the size of the separation bubbles gradually reduces and eventfully disappear for high enough Re. The external flow dominates the bulk parallel motion of the fluid, and the transverse heat transfer is limited to conduction only.

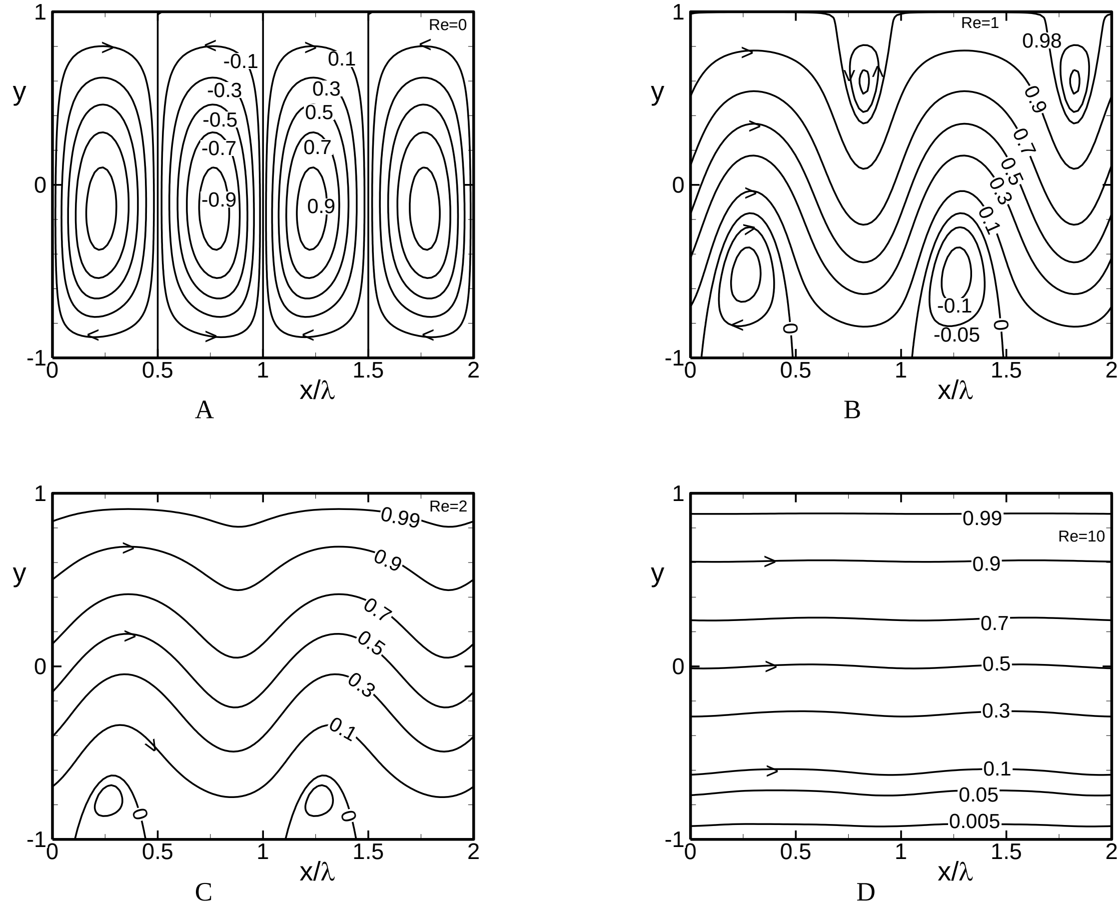

A

B

C

D

Figure 3. Flow topology for the Rayleigh number Ra = 100 and the heating wave number α = 2. Figures 3A-D correspond to the Reynolds number Re = 0, 1, 2, 10, respectively.

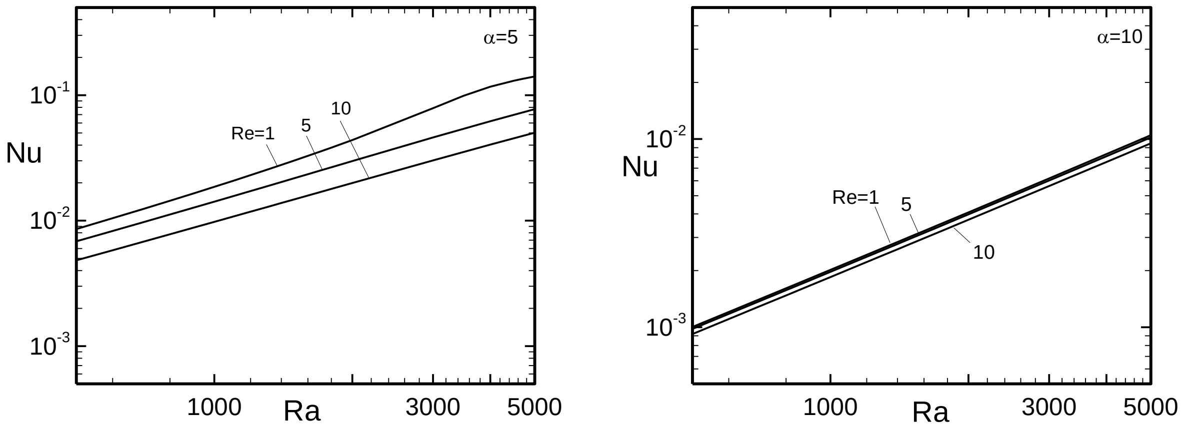

Figure 4. Variation of heat flow as a function of Rayleigh number Ra at selected values of the Reynolds number Re for the heating wave number α = 5 (left) and α = 10 (right).

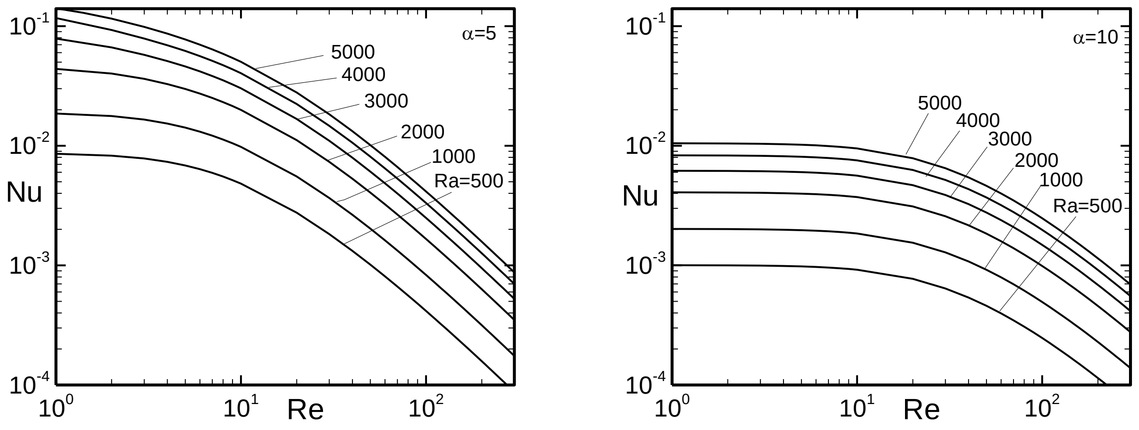

Figure 5: Variation of heat flow as a function of Reynolds number Re at selected values of the Rayleigh number Ra for the heating wave number $\alpha = 5$ (left) and $\alpha = 10$ (right).

To identify the heating pattern (i.e., the heating wave number α) which leads to the Maximum heat transfer, we refer to the plot shown in Fig.6. This figure shows that lower values of the heating wave number α provides more heat transfer than the higher values of α. When α is sufficiently high, Nu decreases proportional to α^{-3}, similar co-relation also reported by [3].

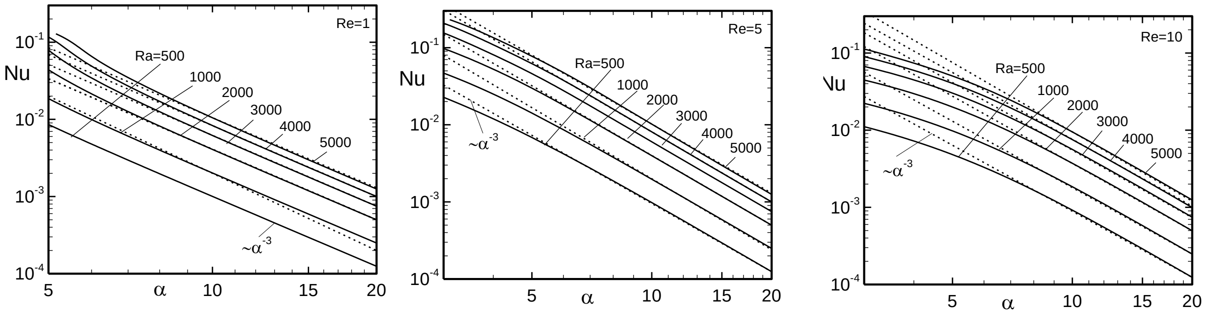

Figure 6: Variation of heat flow as a function of the heating wave number α at selected values of the Rayleigh number Ra for Reynolds number Re=1(left), 5(middle), and 10 (right).

5. Conclusion

Heat transfer characteristics due to the presence of spatially periodic sine-bump heating applied at the lower wall has been investigated. The convective flow structures provide separation bubbles either at upper wall, at lower wall or at both walls, depending on the heating wave number, intensity of heating, and strength of external flow. These separation bubbles are more active at low Reynolds number and at low heating wave number, thereby causing more heat transfer in this zone.

6. References

[1] Bodenschatz, E., Pesh, W. and Ahlers, G., “Recent developments in Rayleigh-Benard convection”, Ann. Rev. Fluid Mech., 32, 709-778, 2000.

[2] Kelly, R. E., "The Onset and Development of Thermal Convection in Fully Developed Shear Flows", Advances In Applied Mechanics, vol31, pp. 35-112, 1994.

[3] Hossain, M. Z., "Convection due to spatially distributed heating", PhD Dissertation, The University of Western Ontario, London, ON, 2011.
[4] Hossain, M. Z., &Floryan, J. M., "Instabilities of Natural Convection in a Periodically Heated Layer". J. Fluid Mech., vol 733, pp. 33–67, 2013.
[5] Hossain, M. Z., Floryan, D. &Floryan, J. M., "Drag Reduction due to Spatial Thermal Modulations", J. Fluid Mech., vol 713, pp. 398–419, 2012.
[6] Chandrasekhar, S., Hydrodynamic and Hydromagnetic Stability. Oxford University Press, 1961.
[7] Floryan, J.M., 1997, Stability of wall bounded shear layers with simulated distributed surface roughness, J. Fluid Mech., 335, 29-55.
[8] Canuto, C., Hussaini, M.Y., Quarteroni, A., Zang, T.A., Spectral Methods, Springer, 1996.

Available online at www.sciencedirect.com

ScienceDirect

Procedia Engineering 00 (2015) 000–000

Procedia Engineering

www.elsevier.com/locate/procedia

6th BSME International Conference on Thermal Engineering (ICTE 2014)

Effect of a DC Field on Temperature Distribution in a Thin FGM Metal Line Subjected to Distributed Local Heating Sources

Abhishek Kumar Ghosh*, Md. Rejaul Haque and S. Reaz Ahmed

Bangladesh University of Engineering and Technology, Dhaka- 1000, Bangladesh

Abstract

The effect of a direct-current field on the temperature distribution in a thin, non-uniform functionally graded metal line subjected to distributed local heat sources is investigated. The material properties of the metal line are assumed to vary over the span following a linear functional relationship. Bump-like heat sources of different profiles are considered to simulate the condition of distributed local heating of the metal line. The governing differential equations associated with the electrical and thermal problems are derived in terms of variable thermal and electrical conductivity of the material. The solution of the coupled boundary-value problem is then obtained using a finite-difference computational scheme. The temperature distributions in the FGM line are determined for different environmental conditions as a function of intensity of the DC field.

Peer-review under responsibility of organizing committee of the 6th BSME International Conference on Thermal Engineering (ICTE 2014).

Keywords: Functionally-graded metal line; distributed heat source; temperature distribution; direct-current field.

1. Introduction

The information revolution and enabling era of ultra-large-scale integration (ULSI) have spawned an ever-increasing level of functional integration on chip, driving a need for more reliable circuit design and higher performance. The increasing density, performance and reliability requirement in circuit design has created significant process integration challenges for future interconnect systems. Several recent analysis [1-3] have highlighted interconnect performance issues for future design of circuit in microelectronic devices. Traditionally aluminum is being considered as one of the suitable candidates for designing metal lines in interconnects; etched

---

* Tel.: +8801816925531;
*E-mail address:*abhishek.ghosh053@gmail.com

Peer-review under responsibility of organizing committee of the 6th BSME International Conference on Thermal Engineering (ICTE 2014).

aluminum alloy with damascene tungsten plugs is still the most predominant interconnect system. While copper conductors reduces Joule heating effects through improved reliability performance, integration of low-dielectrics with copper brings new integration concerns such as copper CMP (chemical mechanical polishing).

Nomenclature

L, w, t	length, width, thickness of line (m)	G	volumetric heat generation (Wm^{-3})
A, C	area (m^2), perimeter (m)	g_{ext}	heat generation by heat sources (Wm^{-3})
J	current density (Am^{-2})	A_m	mechanical equivalent of heat ($Jcal^{-1}$)
k	thermal conductivity ($Wm^{-1}K^{-1}$)	T	temperature (K)
H	convective co-efficient ($Wm^{-2}K^{-1}$)	φ, ρ	electric potential (V), electrical resistivity ($\Omega\ m$)

Copper metallization offers significant performance and reliability improvement but presents numerous integration and reliability challenges. The electro-migration behavior of copper also differs from aluminum in that surface diffusion tends to dominate over grain boundary diffusion, especially for narrow lines exhibiting bamboo grain structure [4]. This difference may be one reason preliminary data shows deterioration of copper reliability at smaller feature sizes [4]. Copper resistivity has also been projected to increase dramatically with smaller feature size due to electron scattering from grain boundaries and conductor walls [5]. Now-a-days, pure metals are of little use in engineering applications because of demand of conflicting property requirements and thus are being replaced by various kinds of advanced materials. Among the various combination processes of materials functionally graded material (FGM) are now treated as the most promising candidate for such materials. FGM belongs to a class of advanced material characterized by variation in properties as the dimension varies. The overall properties of FGM are unique, and are clearly different from any of the constituent materials that form it [6].

Accurate and reliable prediction of electro-thermal behaviour of conducting materials is of great importance for improved performance as well as integrity assessment of microelectronic devices. When an electrical conducting material is subjected to a current flow, Joule heating is induced, which eventually leads to generation of heat in the conductor and thus causes thermal stresses, which is considered to be one of the major reasons of metal line failure in electronic packaging. The problem of heat conduction in a wire under the influence of current flow has been explained theoretically by Carslaw and Jaeger [7]. Introducing a new Joule heating residue vector, heat conduction in symmetrical electro-thermal problems has been analyzed under the influence of direct current passing through symmetrical regions of the boundary [8]. The resulting temperature field of a 2D electro-thermal problem near the corner composed of two dissimilar materials in an angled metal line has been analyzed under a direct current flow [9]. Recently, electro-thermal responses of non-uniform functionally graded metal lines under a direct current field have been analyzed by Ghosh *et al.* [10]. The computational scheme has been extended to develop a simple procedure to determine the optimum material composition distribution of FGM metal lines under a dc field [11].

The present paper is on the analysis of the effect of an electrical field on the temperature distribution in a thin non-uniform FGM metal line subjected to distributed local heat sources. The electrical and thermal properties of the *Cu-Al* FGM line are assumed to vary over the line following a linear relationship. Different profiles of bump-like periodic heating sources are considered along with that of a uniform one. The numerical solutions of the present coupled multi-physics problem are obtained using a finite-difference computational algorithm. The temperature distributions in the FGM line are presented for different profiles of periodic heat sources as well as for different environmental conditions.

2. Mathematical modelling

2.1. Electrical problem

The differential equation that governs the distribution of electric potential in a non-uniform metal line with variable electrical resistivity, is

$$\frac{d^2\varphi}{dx^2} = -\left(\frac{d\rho(x)}{dx} J(x) + \rho(x) \frac{d\,J(x)}{dx} \right) \tag{1}$$

For uniform cross-sectional area and constant electrical resistivity, the derivatives in the right hand side of the Eq. (1) can be neglected. Equation (1) will then be reduced to the standard one dimensional Laplace equation. The end conditions of the metal line are simulated by the following relation of potential gradient:

$$\frac{d\,\varphi}{dx}=\pm\,\rho\left(\frac{I}{A}\right) \qquad (2)$$

The negative sign of the equation (2) applies to the line end where current is being injected and the positive sign corresponds to the current outlet port.

2.2. Thermal problem

The general governing equation for steady state heat transfer in a metal line, the surface of which losses heat by convection to the surrounding atmosphere ($T_\propto$) is

$$\frac{1}{A(x)}\;\frac{\partial}{\partial x}\left[A(x)k(x)\frac{\partial T}{\partial x}\right]-\frac{H\,C(x)}{A(x)}[T-T_\propto]+G(x)=0 \qquad (3)$$

For the present electro-thermal problem, the heat generation rate per unit volume (*G*) is related to Joule heating caused by the current flow and heat supplied by the external heat sources. For steady-state heat transfer in the metal line with variable thermal conductivity *k*(*x*), subjected to an electric field and distributed local heat sources, the governing equation becomes

$$\frac{1}{A(x)}\;\frac{d}{dx}\left[A(x)k(x)\frac{dT}{dx}\right]-\frac{H\,C(x)}{A(x)}[T-T_\propto]+\frac{1}{A_m\,\rho(x)}\left(\frac{d\varphi}{dx}\right)^2+g_{etx}(x)=0 \qquad (4)$$

For the thermal problem, the temperatures at the two ends of the line are assumed to be known. It is mentioned that all possible physical conditions at the ends can readily be accommodated in the present program.

3. Statement of the thermal problem coupled with an electrical field

Figure 1 shows the analytical model of a variable cross-section FGM metal line with overall dimensions, L = 200 mm, w_1 = 5 mm, w_2 = 1 mm, t = 100 μm, which is subjected to a steady direct current field. The current flow is assumed to be, I = 2 A. The FGM line is assumed to be composed of two metals (for example, *Cu* and *Al*), the composition of which varies linearly over the line span.

The entire metal line is assumed to be electrically insulated except for the two ends. For the solution of electrical problem, in addition to the given current densities at the two ends of the line, the zero potential condition is also satisfied at its mid-length position. For the thermal problem, the elevated temperature condition of the metal line was simulated by assigning a fixed temperature (313K) at two ends of the metal line. The surface of the line is assumed to transfer heat by convection to the surrounding environment which is kept at a temperature of 310K. The convection heat transfer co-efficient is assumed to be constant (10 Wm^{-2}K^{-1}) for the entire span of the FGM line.

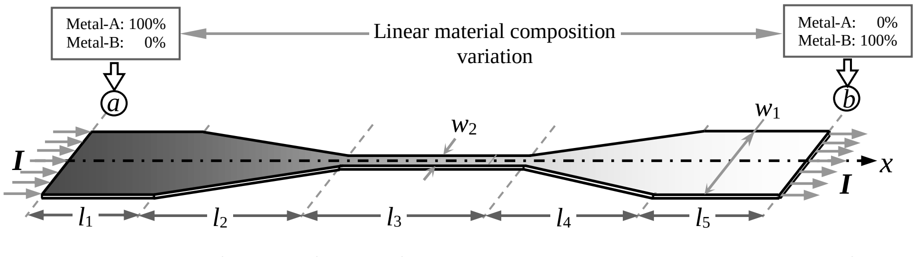

Fig. 1. Model of a non-uniform thin functionally graded metal line under a direct current field.

The individual electrical resistivity and thermal conductivity of the two constituent metals (*Cu* and *Al*) assumed for the present analysis are listed in Table 1. The distribution of material composition of the FGM line is assumed to be linear, as illustrated in Fig. 1; the corresponding variable material properties of the line are obtained following linear laws, which are depicted in Fig. 2.

Table 1: The assumed electrical resistivity and thermal conductivity of Copper and Aluminum at room temperature

Metal	Electrical resistivity, ρ (Ω-m)	Thermal conductivity, *k* (Wm^{-1}K^{-1})
Copper (*Cu*)	1.71×10^{-8}	400.35
Aluminum (*Al*)	2.65×10^{-8}	238.97

The distributed local heat sources considered for the problem are assumed to be of three types, the profiles of which are, respectively, bump-like sinusoidal, bump-like rectangular and an average uniform one. The variations of the heat sources over the metal line are illustrated in Fig. 2(c).

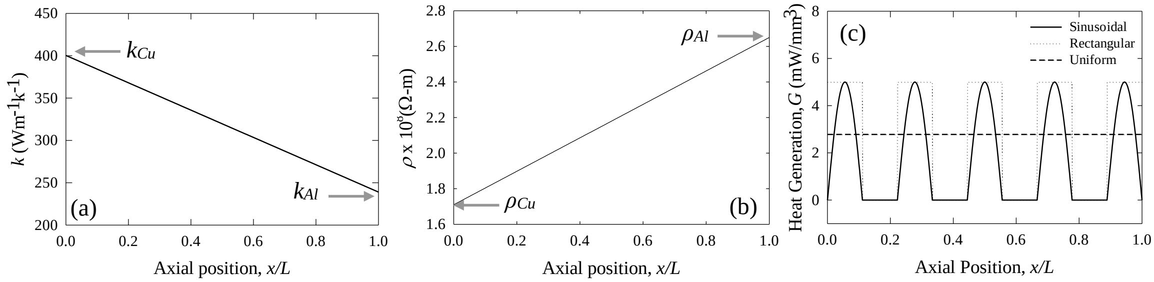

Fig. 2: Distribution of (a) thermal conductivity; (b) electric resistivity; (c) profiles of heating sources over the metal line.

4. Method of solution

The present steady-state heat conduction-convection boundary value problem has been solved numerically by using finite-difference technique. Both the governing differential equations associated with the electrical and thermal problems are discretized using the standard three-point central-difference scheme. The difference equations so developed for the electrical (Eq. (1)) and thermal problems (Eq. (4)) are, respectively, as follows:

$$\varphi_{i+1}-2\varphi_i+\varphi_{i-1}=-\frac{h}{2}\left[J_i\left(\rho_{i+1}-\rho_{i-1}\right)+\rho_i\left(J_{i+1}-J_{i-1}\right)\right] \tag{5}$$

$$\begin{aligned}&[4k_i+k_iA_i^{-1}\left(A_{i+1}-A_{i-1}\right)+\left(k_{i+1}-k_{i-1}\right)]T_{i+1}-[8k_i+4A_i^{-1}H\,C_ih^2]\,T_i+[4k_i-k_iA_i^{-1}\left(A_{i+1}-A_{i-1}\right)\\&-\left(k_{i+1}-k_{i-1}\right)]\,T_{i-1}=-4A_i^{-1}H\,C_ih^2T_\infty-\rho_i^{-1}A_m^{-1}\left(\varphi_{i+1}-\varphi_{i-1}\right)^2-4h^2g_{ext(i)}\end{aligned} \tag{6}$$

A MATLAB based computer code has been developed to solve the coupled problem. The resulting tri-diagonal systems of algebraic equations are solved for the nodal temperatures by the matrix decomposition method. For the calculation of secondary parameter of interest, namely, electrical heat generation, both the three-point forward and backward as well as central differencing schemes were adopted to keep the overall order of error the same (O(h^2)). A total of 1000 nodal points have been used to discretize the computational domain. The convergence as well as the stability of the numerical solution has however been verified by varying the nodal points from 10 to 3000.

5. Analysis of the thermal behavior

In this section, first, the thermal behavior of the FGM line is demonstrated together with those of the constituent metals, without the influence of any electrical field. Fig. 3 shows the distribution of temperature along the metal line for three different types of heating sources namely, sinusoidal, rectangular and uniform heat source under no current flow. For all three cases *Al* shows maximum temperature elevation whereas *Cu* shows the minimum. Temperature distribution of FGM metal line resides in between these two metal lines. Moreover the rise of temperature for sinusoidal heat source is found to be the minimum among three, which is due to the fact that overall heat generation for sinusoidal heat source is minimum among three as seen from figure 2(c). Finally, though the temperature profile is different, the maximum temperature rise for rectangular and uniform heating source is found to be same since the overall heat generation is equivalent for these two cases.

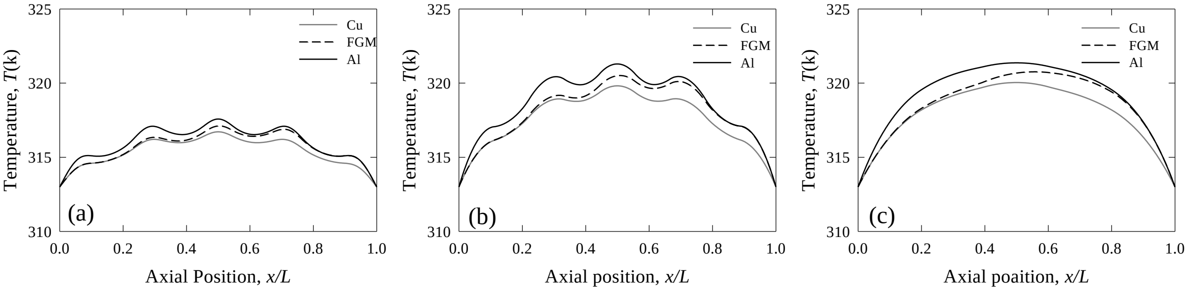

Fig. 3: Temperature distribution along the metal line for different heat sources (I = 0): (a) Sinusoidal; (b) Rectangular; (c) Uniform.

Fig. 4(a) shows the variation of electric potential along the axis of the FGM as well as the constituent metal lines. The potential distribution for the FGM metal line resides in between those of the parent metals, and maintains higher similarities with that of *Cu* for the starting section and *Al* for the end section. This is because the proportion of *Cu* is higher for the first half section and *Al* is higher for the last half section. Fig. 4(b) represents the volumetric heat generation for the FGM metal line subjected to dc current field under three different external heat sources. For all three cases the maximum heat generation is found near the mid-section of the metal line where the cross-sectional area in minimum.

The effect of electric field on the distribution of temperature over the FGM metal subjected to distributed local heating sources is shown in Fig. 5 for two different environmental conditions of the line, namely, bare and buried conditions. Both the conditions show a significant increase in temperature with the increase of current flow. It is also found that temperature rise under buried condition (Fig. 5(b)) is much higher compared to that of bare line (Fig. 5(a)). This is because of the fact that, in case of buried lines, no heat loss is allowed from the surfaces through convection to surroundings, thereby causing the overall state of temperature to assume a higher level compared to the bare lines.

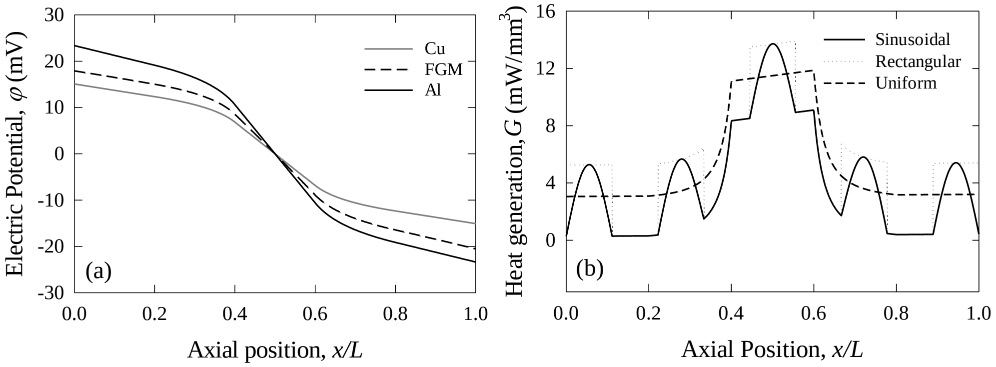

Fig. 4: Distribution of (a) electric potential, (b) resulting heat generation along the metal lines for different heat sources (I = 2A).

.

.

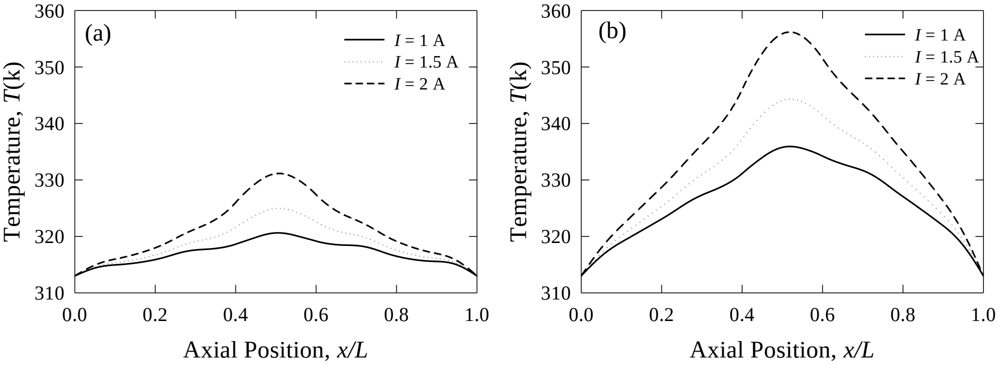

Fig. 5: Effect of dc fields on the temperature distribution caused by periodic sinusoidal heating source: (a) bare line; (b) buried line.

6. Conclusions

Temperature distribution in a thin, non-uniform FGM metal line composed of two metals (*Al* and *Cu*) is investigated under the influence of a direct current field and distributed local heating sources. The distributions of material composition as well as the resulting material properties of the metal line are assumed to be linear functions of spatial coordinate. The distributions of electric potential as well as temperature along the FGM line are found to differ significantly from those of the individual constituent metal lines. The effect of electric field on the temperature distribution is also found to be quite significant even with the presence of local distributed heating sources. The results are claimed to be highly accurate and reliable, which are expected to provide a valuable design guide to functionally graded metal lines in modern electronic devices.

References

[1] M. Bohr, Interconnect scaling–The real limiter to high performance ULSI, Tech. Dig. IEEE Int. Electron Devices Meeting, 1995, pp. 241–244.
[2] A. Deutsch, H. Harrer, C. W. Surovic, G. Hellner, D. C. Edelstein, R. D. Goldblatt, G. A. Biery, N. A. Greco, D. M. Foster, E. Crabbe, L. T. Su, and P. W. Coteus, Functional high-speed characterization and modeling of a six-layer copper wiring structure and performance comparison with aluminum on-chip interconnections, Tech. Dig. IEEE Int. Electron Devices Meeting, 1998, pp. 295–298.
[3] S. Takahashi, M. Edahiro, and Y. Hayashi, Interconnect design strategy: Structures, repeaters and materials toward 0.1 μm ULSI's with a giga-hertz clock operation, Tech. Dig. IEEE Int. Electron Devices Meeting, 1998, pp. 833–836.
[4] C.-K. Hu, R. Rosenberg, H. S. Rathore, D. B. Nguyen, and B. Agarwala, Scaling effect on electromigration in on-chip Cu wiring, Tech Dig. IEEE Int. Interconnect Tech. Conf., 1999, pp. 267–269.
[5] T. S. Kuan, C. K. Inoki, G. S. Oehrlein, K. Rose, Y.-P. Zhao, G.-C. Wang, S. M. Rossnagel, and C. Cabral, Fabrication and performance limits of sub-0.1 micrometer Cu interconnects, Proc. of Mat. Res. Soc. Symp., 2000, vol. 612, no. D7.1.1.
[6] R. M. Mahamood, E. T. Akinlabi, M. Shukla, and S. Pityana, Functionally Graded Material: An Overview, Proc. of the W. Cong. on Eng., London, U.K., July, 2012.
[7] H. S. Carslaw, and J. C. Jaeger, Conduction of Heat in Solids, Second Ed., (1959) Clarendon, Oxford,
[8] M. Saka, Y. X. Sun, and S. R. Ahmed, Heat conduction in a symmetric body subjected to a current flow of symmetric input and output, Int. J. Therm. Sci., Vol. 48 (2009), pp. 114-121.
[9] M. Saka, and X. Zhao, Analysis of the temperature field near a corner composed of dissimilar metals subjected to a current flow, Int. J. Heat and Mass Transf., Vol. 55 (2012), pp. 6090-6096.
[10] A. K. Ghosh, A. Adhikary, and S. R. Ahmed, Prediction of electro-thermal responses of non-uniform functionally graded metal lines under a direct current field, Procedia Eng., Vol. 56 (2013), pp. 807-813.
[11] A. K. Ghosh, M. R. Haque, and S. R. Ahmed, Effect of material composition distribution on the electro-thermal response of a non-uniform functionally graded metal line under a direct current field, Proc. of ICME 2013, Dhaka, Bangladesh, June, 2014.